

# Detector Characterisation and Searches for Gravitational Waves Using GEO 600

Thomas. S. Adams



Submitted for the degree of Doctor of Philosophy  
School of Physics and Astronomy  
Cardiff University

March 2014

# Declaration of Authorship

---

- DECLARATION:

This work has not been submitted in substance for any other degree or award at this or any other university or place of learning, nor is being submitted concurrently in candidature for any degree or other award.

Signed: ..... (candidate) Date: .....

- STATEMENT 1:

This thesis is being submitted in partial fulfillment of the requirements for the degree of Doctor of Philosophy (PhD).

Signed: ..... (candidate) Date: .....

- STATEMENT 2:

This thesis is the result of my own independent work/investigation, except where otherwise stated. Other sources are acknowledged by explicit references. The views expressed are my own.

Signed: ..... (candidate) Date: .....

- STATEMENT 3:

I hereby give consent for my thesis, if accepted, to be available for photocopying and for inter-library loan, and for the title and summary to be made available to outside organisations.

Signed: ..... (candidate) Date: .....

- STATEMENT 4: PREVIOUSLY APPROVED BAR ON ACCESS

I hereby give consent for my thesis, if accepted, to be available for photocopying and for inter-library loans **after expiry of a bar on access previously approved by the Academic Standards & Quality Committee.**

Signed: ..... (candidate) Date: .....

# Summary of Thesis

---

We are currently on the brink of the first direct detection of gravitational waves (GWs) with a new generation of GW detectors currently being commissioned. In the period before the advanced detectors come online we must prepare techniques for detector characterisation and advanced data analysis methods to improve our sensitivity to potential sources of GWs.

We begin with an outline of GW theory, derived from Einstein’s general theory of relativity. We introduce each of the main classes of GW signals, as distinguished by the GW community, focusing mainly on GW bursts. A short outline is also given for compact binary coalescences, continuous waves, and stochastic background. An introduction to GW interferometers is then given, focusing mainly on the GEO 600 detector. The stationary noise sources that limit the frequency dependent sensitivity of current GW detectors are discussed: optical readout noise, thermal noise, and seismic noise.

We discuss transient noise events (glitches) and the veto methods that are used to remove these events from the GW data channel. Details are given for *glitch hunting* that was performed at GEO 600 to identify and understand sources of transient noise. We demonstrate a cost-benefit analysis method that could be used for increasing the number of observable sources, by assessing the severity of detector noise sources to efficiently guide commissioning.

We introduce X-PIPELINE, a coherent search pipeline for GW bursts associated with astrophysical transients such as gamma-ray bursts, and give details of pipeline line development that we were involved in. Results from a search for GW associated with 78 gamma-ray bursts that occurred while only GEO 600 and one of the LIGO or Virgo detectors were taking data are presented; these events have not previously been analysed.

The sensitivity of searches for GW bursts is often critically limited by non-Gaussian noise fluctuations that are difficult to distinguish from real signals. We utilised the boosted decision tree multivariate analysis classifier to probe the full space of measured properties of events in an attempt to maximise the power to accurately classify events as signal or background, compared to the standard X-PIPELINE.

While the LIGO and Virgo detectors are undergoing intense commissioning, GEO 600 is the only GW detector taking observations. Therefore, we demonstrate the feasibility of performing a single detector analysis for GW bursts using GEO 600 in preparation for any exceptional astrophysical events (such as a Galactic supernova).

To Mum, Dad, and Natasha.



# Acknowledgements

---

Firstly, thanks to my parents for your continued encouragement and endless support, I couldn't have done this without you. Natasha, Bertie, Freddie, and Jemima, thank you for inspiring me to try hard in everything I do and for always making me laugh, I'm sorry I don't get to see you all more. I hope I can tell you all at some point what I have been doing these past few years.

To Patrick Sutton, firstly thank you for taking me on as your student. You have been a great supervisor, mentor, and friend throughout my PhD. You have taught me a lot and have always had an open door when ever I had a question. Thanks for many informative and fun meetings and discussions, and for reading this thesis. I hope that we get to work together again in the future.

To the GEODC guys: Jonathan Leong, Jacob Slutsky, and Michał Wąs. Thanks for keeping me busy during my visits to GEO 600, you have all taught me a lot and become great friends. To Hartmut Grote and the other members of GEO 600, thank you for your help during my visits, for making me feel welcome at the site, and for many great BBQs.

I have had the pleasure of meeting many lovely people in the Cardiff Gravitational Waves group, thanks for making my time at the group so enjoyable: James Clark, Thomas Dent, Mark Edwards, Steve Fairhurst, Maxime Fays, Mark Hannam, Ian Harrison, Gernot Heissel, Paul Hopkins, Gareth Jones, Ioannis Karmaretsos, Sebastian Khan, Erin Macdonald, Duncan Meacher, Chris Messenger, Frank Ohme, Valeriu Predoi, Geraint Pratten, Michal Pürrer, Sathyaprakash, Patricia Schmidt, John Vietch, and Andrew Williamson. A special thanks to Ian Harry, Duncan Macleod, and Laura Nuttall for showing me the ropes when I first arrived, helping me improve my programming, working together on GEODC (GEO! GEO! GEO!), the N3.24 Backgammon World Championship, and many good times.

Finally, to the other members of the Cardiff Physics department and the AEI, my friends, and my family. There are too many of you to name, which I am sorry for and also grateful to have met so many amazing people. You have all in some way made the time I have spent doing my PhD some of the best years of my life. I hope to see you all again in the future.

# Contents

---

<b>1</b>	<b>Gravitational Wave Theory and Sources</b>	<b>1</b>
1.1	Introduction . . . . .	1
1.2	Gravitational Wave Theory . . . . .	3
1.3	Gravitational Wave Sources . . . . .	7
<b>2</b>	<b>Gravitational Wave Detectors</b>	<b>13</b>
2.1	Michelson-Morley Experiment . . . . .	13
2.2	Gravitational Wave Detection Principle . . . . .	14
2.3	Limiting Noise Sources . . . . .	23
2.4	Gravitational Wave Interferometer Network . . . . .	30
2.5	The GEO 600 detector . . . . .	31
<b>3</b>	<b>Detector Characterisation</b>	<b>45</b>
3.1	Transient Noise Events . . . . .	46
3.2	Vetoed . . . . .	47
3.3	Diagnostic tools . . . . .	49
3.4	Simplified GEO 600 Layout . . . . .	54
3.5	Glitch hunting . . . . .	55
3.6	Characterisation directed commissioning of the GEO 600 detector	64
<b>4</b>	<b>Gravitational Waves Associated with Gamma-Ray Bursts</b>	<b>87</b>
4.1	Gamma-Ray Bursts . . . . .	87
4.2	X-PIPELINE . . . . .	88
4.3	Leveraging the GEO 600 Detector to Search for Gravitational Waves from Gamma-Ray Bursts . . . . .	97
<b>5</b>	<b>Gravitational Wave Detection Using Multivariate Analysis (XTMVA)</b>	<b>117</b>
5.1	X-PIPELINE Event Variables . . . . .	117
5.2	Toolkit for Multivariate Analysis . . . . .	120
5.3	Boosted Decision Trees . . . . .	120
5.4	Signal Population . . . . .	123
5.5	Multivariate X-PIPELINE Performance . . . . .	124
5.6	Discussion and Conclusions . . . . .	133
<b>6</b>	<b>Gravitational Wave Detection Using a Single Detector</b>	<b>143</b>
6.1	Single Detector Analysis Trigger . . . . .	143
6.2	Single Detector Analysis Procedure . . . . .	144

6.3	Analysis Segments and Veto Methods . . . . .	147
6.4	Analysis Results . . . . .	157
<b>7</b>	<b>Discussion and Conclusions</b>	<b>169</b>
<b>A</b>	<b>Optical Layout of GEO 600</b>	<b>172</b>

# List of Figures

---

1.1	Orbital decay of PSR B1913+16 due to the emission of gravitational waves. . . . .	2
1.2	Effect of a gravitational wave on the proper distance between a circle of free test masses. . . . .	7
2.1	Schematic of basic Michelson interferometer. . . . .	14
2.2	Diagram of the Michelson and Morley experiment. . . . .	15
2.3	Coordinates used to describe the antenna pattern of gravitational wave detectors. . . . .	18
2.4	Directional sensitivity for a gravitational wave detector with arms aligned along the x-axis and y-axis. . . . .	19
2.5	Schematic of a Fabry-Perot cavity. . . . .	22
2.6	Basic layout of control system for cavity length using the Pound-Drever-Hall technique. . . . .	23
2.7	Noise spectral density of initial LIGO showing the limiting noise sources. . . . .	24
2.8	Optical readout noise for GEO 600 . . . . .	25
2.9	Elements of a mirror that cause thermal noise, suspensions, coatings, and substrate. . . . .	28
2.10	Seismic noise at the GEO 600 site . . . . .	29
2.11	Strain sensitivity of GEO 600 in comparison with LIGO and Virgo. . . . .	32
2.12	Schematic of main optics suspension for GEO 600 . . . . .	34
2.13	Schematic of a laser interferometer with power recycling cavity. . . . .	35
2.14	Schematic of a laser interferometer with dual recycling. . . . .	36
2.15	Schematic of the output optics of GEO 600. . . . .	38
2.16	Michelson interferometer heterodyne readout scheme. . . . .	38
2.17	Michelson interferometer dc readout scheme. . . . .	39
2.18	Schematic of Michelson interferometer with field amplitudes at different points along the light path. . . . .	40
2.19	Squeezing error ellipse in the phase ( $P$ ) and amplitude ( $A$ ) space of the light field inside an interferometer. . . . .	41
2.20	Sensitivity of GEO 600 for various stage through the GEO-HF upgrade scheme. . . . .	44
3.1	Cartoon example of veto method to clean up the GW channel data using auxiliary channels. . . . .	48

3.2	Cartoon showing observable volume ( $D^3$ ) against time for a noise investigation. . . . .	51
3.3	Detector characterisation summary pages for GEO 600. . . . .	53
3.4	Simple optical layout of GEO 600. . . . .	54
3.5	Strain noise spectral density verse frequency for GEO 600 for different epochs. . . . .	55
3.6	Omega-scan of a 900 Hz glitch in the GW data channel. . . . .	56
3.7	Omega trigger plot of time versus frequency, showing 900 Hz glitches. . . . .	57
3.8	Schematic of the Michelson differential control loop. . . . .	58
3.9	900 Hz glitch rate dependence with temperature. . . . .	59
3.10	Delay between the auxiliary channel HACR triggers with central frequency between 2800 Hz and 3100 Hz. . . . .	60
3.11	Time-frequency coincidence between HACR triggers kHz in auxiliary channel and the GW data channel. . . . .	61
3.12	PEM_TFE_MAG-Z channel HACR trigger plot of frequency versus time . . . . .	62
3.13	Histograms of number of PEM_TFE_MAG-Z HACR triggers versus time in day, from each glitch band from tank far east. . . . .	63
3.14	Modulation of a high frequency fluctuation by a low frequency variation in alignment of the OMC. . . . .	66
3.15	Strain noise spectral density for the BDO suspension upgrade. . .	68
3.16	Cumulative glitch rate for the BDO suspension upgrade. . . . .	69
3.17	Frequency dependent range for the BDO suspension upgrade. . .	69
3.18	Omega-grams for the BDO suspension upgrade. . . . .	70
3.19	Strain noise spectral density for OMC isolation upgrade. . . . .	72
3.20	Cumulative glitch rate for OMC isolation upgrade. . . . .	72
3.21	Frequency dependent range for OMC isolation upgrade. . . . .	73
3.22	Omega-grams for the output mode cleaner isolation upgrade. . . .	74
3.23	Strain noise spectral density for squeezer glitches. . . . .	76
3.24	Cumulative glitch rate for the squeezer glitches. . . . .	76
3.25	Frequency dependent range for the squeezer glitches. . . . .	77
3.26	Omega-grams for the squeezer glitches. . . . .	78
3.27	Strain noise spectral density for 3.5 Hz squeezer glitches. . . . .	80
3.28	Cumulative glitch rate for 3.5 Hz squeezer glitches. . . . .	80
3.29	Frequency dependent range for 3.5 Hz squeezer glitches. . . . .	81
3.30	Squeezer backscattering stacked triggergrams where all triggers were time shifted to loop over the same 2 seconds to reveal the 3.5 Hz periodicity. . . . .	82
3.31	Omega-grams for the 3.5 Hz squeezer glitches. . . . .	83
4.1	Time-frequency map to show clustering method. . . . .	90
4.2	Space of detector strains. . . . .	92
4.3	Scatter plot of $I_{\text{null}}$ vs. $E_{\text{null}}$ for background events and simulated gravitational wave bursts. . . . .	95
4.4	Procedure for setting upper limits. . . . .	97

4.5	Procedure for the closed box analysis. . . . .	98
4.6	Typical strain sensitivity spectrum of the detectors used in this analysis. . . . .	101
4.7	The 50% and 90% upper limits for 150 Hz sine-Gaussian injections.102	
4.8	The 50% and 90% upper limits for 800 Hz sine-Gaussian injections.103	
4.9	The 50% and 90% upper limits for binary neutron star inspiral injections. . . . .	104
4.10	Comparison of the linear and circular grid for the GW analysis of GRB 080906B. . . . .	108
4.11	Cumulative p-value distribution from the analysis of 78 GRB triggers. . . . .	111
4.12	Exclusion distances for 500 Hz and 1 kHz CSG waveforms for 78 GRBs. . . . .	112
5.1	Processing time verses number of triggers for different MVA classifiers. . . . .	121
5.2	Schematic of a decision tree. . . . .	122
5.3	Time series of waveform used for signal injections. . . . .	125
5.4	Time-frequency spectrograms of waveforms used for signal injections. . . . .	125
5.5	Background rejections against signal efficiency for the BDT test sample in the GRB 060223A analysis. . . . .	127
5.6	Results histogram from multivariate analysis test analyses. . . . .	130
5.7	Time series of “equinox event”. . . . .	132
5.8	Background distribution for the X-PIPELINE and boosted decision tree analyses of the equinox event. . . . .	133
5.9	Simple example decision tree. . . . .	134
5.10	Scatter plot of signal and background events with cuts from simple example decision tree. . . . .	135
5.11	Complex example decision tree. . . . .	135
5.12	Histogram of number of times each variable or variable combination is used at decision tree nodes in the booster decision tree forest for the default GRB 060223A analysis. . . . .	136
5.13	Scatter plot of $I_{\text{circ}}$ versus $E_{\text{circ}}$ for testing data from the default GRB 060223A X-PIPELINE and boosted decision tree analyses. . .	138
5.14	Linear correlation matrix for the event variables in the training sample for signal events. . . . .	140
5.15	Linear correlation matrix for the event variables in the training sample for background events. . . . .	140
5.16	Histogram of BDT response for the CSG signal and background testing samples, overlaid with the signal and background training samples response for the default GRB 060223A analysis. . . . .	141
6.1	Duty cycle histogram of the off source around the Bert trigger. . .	147
6.2	Time versus frequency and time versus SNR triggergrams before applying any vetoes segments. . . . .	148

6.3	Time versus frequency and time versus SNR triggergrams after applying HVeto segments. . . . .	150
6.4	Frequency-SNR triggergram after applying HVeto segments. . . . .	152
6.5	GEO 600 noise amplitude spectral density for the single detector Bert IceCube event analysis. . . . .	153
6.6	Time versus frequency and time versus SNR triggergrams after applying HVeto segments and > 300 Hz low frequency cut-off. . .	154
6.7	Time versus frequency and time versus SNR triggergrams after applying HVeto segments, > 300 Hz low frequency cut-off, and acoustic channel trends. . . . .	155
6.8	Time versus frequency and time versus SNR triggergrams after applying HVeto segments, > 300 Hz low frequency cut-off, acoustic channel, and seismometer trends. . . . .	156
6.9	Time versus frequency and Time versus SNR triggergram after applying HVeto segments, > 300 Hz low frequency cut-off, acoustic channel, seismometer, and east arm power trends. . . . .	157
6.10	Bar chart of number of times each variable is used at decision tree nodes in the BDT forest for the two detector XTMVA analysis. . . .	159
6.11	Bar chart of number of times each variable is used at decision tree nodes in the BDT forest for the single detector XTMVA analysis. .	161
6.12	Histogram of off-source triggers for a number of the different single detector XTMVA test analyses. . . . .	163
6.13	Linear correlation matrix for the event variables in the training sample for signal events. . . . .	164
6.14	Linear correlation matrix for the event variables in the training sample for background events. . . . .	165
6.15	Background rejections against signal efficiency for the BDT test sample in the single detector analysis. . . . .	165
6.16	Histogram of BDT response for the CSG signal and background testing samples, overlaid with the signal and background training samples response for the single detector Multivariate X-PIPELINE (XTMVA) analysis. . . . .	166
A.1	Schematic of GEO 600 optical layout. . . . .	173

# List of Tables

---

3.1	Veto categories . . . . .	48
3.2	Table of <i>before</i> and after <i>after</i> commissioning times used for each investigation, and the duration of the data used in each case. . . .	65
3.3	Commissioning down time, burst like ranges and catch up times for each of the investigations given in section 3.5. . . . .	84
4.1	S5 and S6 science run dates. . . . .	100
4.2	Results from GEO 600 recovered gamma-ray burst analyses. . . . .	114
5.1	X-PIPELINE cluster properties . . . . .	119
5.2	MVA test analyses trigger parameters . . . . .	127
5.3	MVA test analyses results . . . . .	131
6.1	Table of parameters for the Bert IceCube event. . . . .	144
6.2	Set up of test analyses for the Bert IceCube event. . . . .	146
6.3	HVeto results for the Bert IceCube event single detector GEO 600 analysis. . . . .	151
6.4	GEO 600 duty cycle for different combinations of vetoes for the Bert IceCube event single detector analysis. . . . .	158
6.5	Results from test analysis of Bert trigger. . . . .	162



# Co-authored Papers

---

Sections of this thesis include previously published co-authored work, or work that is in preparation for publication as described below.

- [Chapter 3](#) presents a method for effectively directing commissioning to increase the number of observable sources by using detector characterisation. This work is in preparation for publication as “Characterisation directed commissioning of the GEO 600 detector” [[165](#)]. T. S. Adams is the lead author of this paper.
- [Chapter 4](#) gives the results of a search for gravitational waves associated with gamma-ray bursts that occurred while only GEO 600 and one of the LIGO or Virgo detectors were taking data. This work is in preparation for publication as “Methods and Results of a Search for Gravitational Waves Associated with Gamma-Ray Bursts Using the GEO 600, LIGO, and Virgo Detectors” [[153](#)]. T. S. Adams is one of two graduate students who led this analysis, and in particular the GRB results reported in [table 4.2](#) were analysed by T. S. Adams.
- [Chapter 5](#) was published as “Gravitational-wave detection using multivariate analysis” [[204](#)]. T. S. Adams is the lead author of this paper.



# Gravitational Wave Theory and Sources

# 1

## 1.1 Introduction

At the beginning of the twentieth century Einstein formulated the general theory of relativity. Unlike Newtonian mechanics, where gravity is described as a force which acts between two masses, Einstein described gravity as the curvature of spacetime [1, 2]. General relativity (GR) predicts that perturbations of the curvature satisfy a wave equation. These ripples in space time are called gravitational waves (GWs) and they propagate at the speed of light. Similar to how electromagnetic (EM) waves are produced by the acceleration of charge, GWs are produced by the acceleration of matter; another similarity to EM waves is that GWs carry energy away from the source. However, unlike their EM counterparts, GWs interact very weakly with matter and combined with the decreasing amplitude as they travel away from the source, this makes the direct detection of GWs very challenging.

There is a lot of strong indirect evidence of the existence of GWs. In 1974 Hulse and Taylor discovered a pulsar in a binary system with an unseen companion [3]. This system, referred to as PSR B1913+16, has been observed for the last forty years which has yielded precise values of the masses for the two components, and the orbital parameters of the system. It has been found that the orbital period of this binary is decreasing at  $2.4 \times 10^{-12}$  seconds per second [4]. As can be seen in figure 1.1, the observational data matches the prediction from GR of a binary neutron star (BNS) system emitting GWs [5] to within 0.2% [4]. Hulse and Taylor received the 1993 Nobel Prize in physics for their discovery, and the agreement of these observations with the prediction of GR is still the best known indirect evidence supporting the existence of GWs. There is now further evidence from other sources such as PSR B1534+12 [7] and the binary pulsar system PSR J0737-3039A [8]. As of March 2014, the BICEP2 Collaboration announced the first direct detection of a B-mode power spectrum in the cosmic microwave background, this is detection is strong evidence for inflationary GWs [9].

In this chapter, starting in section 1.2, we introduce the theory required for understanding GWs. Section 1.2.1 briefly introduces GR using the weak field

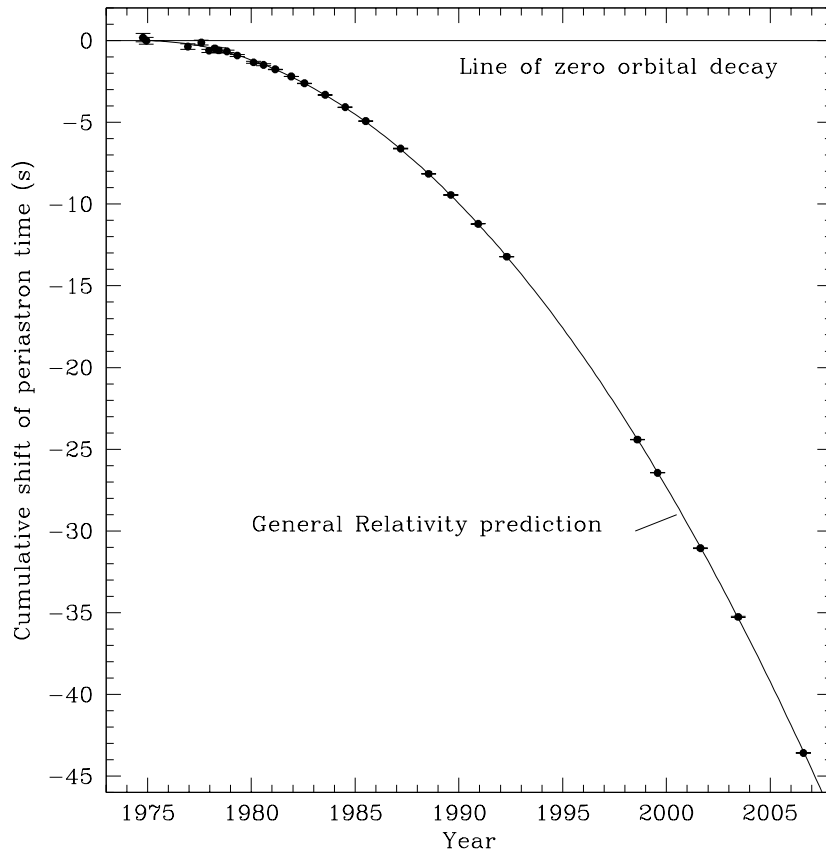


Figure 1.1: Orbital decay of PSR B1913+16 due to the emission of GWs. The solid line is the orbital decay predicted by GR and data points are the observed orbital decay with error bars [6]. The observations match the prediction from GR to within 0.2%.

approximation. [Section 1.2.2](#) describes the plane wave solution for GWs using the transverse-traceless (TT) gauge. [Section 1.2.3](#) explain how GWs interact with matter. [Section 1.3](#) introduces the main classes of sources that are expected to emit GWs that may be detectable by ground-based instruments such as GEO 600.

## 1.2 Gravitational Wave Theory

In this section we give a brief introduction to GW theory. For a more thorough treatment see [[10](#), [11](#), [12](#)], the content of which is closely followed here.

### 1.2.1 Linearised Gravity

In the general theory of relativity GR, gravity is described as the curvature of the four dimensional spacetime. The Einstein equations ([1.1](#)), are a set of 10 equations that relate the curvature of spacetime to the distribution of matter and energy. The Einstein equations are given in tensor notation as

$$G_{\mu\nu} = R_{\mu\nu} - \frac{1}{2}g_{\mu\nu}R = \frac{8\pi G}{c^4}T_{\mu\nu}. \quad (1.1)$$

Here  $G_{\mu\nu}$  is the Einstein tensor,  $T_{\mu\nu}$  is the stress-energy tensor which describes the density and flux of energy and momentum, and  $g_{\mu\nu}$  is the metric which contains all information about the curvature of the spacetime. The metric describes the separation of nearby points in spacetime as

$$ds^2 = g_{\mu\nu}dx^\mu dx^\nu. \quad (1.2)$$

In flat space time using Cartesian co-ordinates we have the simple Minkowski spacetime metric,  $\eta_{\mu\nu} = \text{diag}(-1, 1, 1, 1)$ . In the presence of matter and energy the metric changes from the flat space values according to the Einstein equations ([1.1](#)).  $R_{\mu\nu}$  is the Ricci tensor and  $R$  is the Ricci scalar, we will give explicit formulae for these later.

Here it is worth noting that the convention of explicitly writing  $c$ , the speed of light, and  $G$ , the Newton constant, is used. Greek indices  $[\alpha, \beta, \dots]$  take the values  $[0, 1, 2, 3]$  and are used to denote the four spacetime dimensions. Latin letters  $[i, j, \dots]$  take the values  $[1, 2, 3]$  and are used to denote the three spatial dimensions.

To understand GWs we can simplify the Einstein equations by using the linearised theory of GR. In linearised theory the spacetime metric  $g_{\mu\nu}$  is written as the sum of the flat Minkowski metric  $\eta_{\mu\nu}$  and a small metric perturbation  $h_{\mu\nu}$ , which describes the time varying gravitational field. This is given as

$$g_{\mu\nu} = \eta_{\mu\nu} + h_{\mu\nu}, \quad (1.3)$$

where  $|h_{\mu\nu}| \ll 1$ . This is the weak-field approximation, which we can use to expand the Einstein equation. Due to the metric perturbation being small, we

keep only terms that are linear in  $h_{\mu\nu}$ , and any higher order terms can be discarded. It will be useful to know that indices of  $h_{\mu\nu}$  can be raised or lowered by multiplication with  $\eta_{\mu\nu}$  and its inverse  $\eta^{\mu\nu}$ ,

$$h^{\alpha\beta} = \eta^{\alpha\mu}\eta^{\beta\nu}h_{\mu\nu}. \quad (1.4)$$

The Ricci tensor

$$R_{\mu\nu} = R_{\mu\rho\nu}^{\rho} = \frac{1}{2} \left( \partial_{\rho}\partial_{\nu}h_{\mu}^{\rho} + \partial_{\mu}\partial^{\rho}h_{\nu\rho} - \square h_{\mu\nu} - \partial_{\mu}\partial_{\nu}h \right), \quad (1.5)$$

and Ricci scalar

$$R = g^{\mu\nu}R_{\mu\nu} = \left( \partial_{\rho}\partial^{\mu}h_{\mu}^{\rho} - \square h \right), \quad (1.6)$$

are constructed from derivatives of  $g_{\mu\nu}$ . Here  $\square = \eta_{\mu\nu}\partial^{\mu}\partial^{\nu} = \partial_{\mu}\partial^{\mu} = -\left(\frac{1}{c^2}\right)\partial_0 + \nabla^2$  is the flat space d'Alembertian and  $h = h_{\alpha}^{\alpha}$  is the trace of the metric perturbation.

The Einstein equations (1.1) can be written in terms of the metric perturbation by substituting the Ricci tensor (equation (1.5)) and Ricci scalar (equation (1.6)), keeping only 1<sup>st</sup> order terms of  $h$ ,

$$\begin{aligned} G_{\mu\nu} &= R_{\mu\nu} - \frac{1}{2}g_{\mu\nu}R \\ &= \frac{1}{2} \left( \partial_{\rho}\partial_{\nu}h_{\mu}^{\rho} + \partial_{\mu}\partial^{\rho}h_{\nu\rho} - \square h_{\mu\nu} - \partial_{\mu}\partial_{\nu}h - \eta_{\mu\nu} \left( \partial_{\rho}\partial^{\lambda}h_{\lambda}^{\rho} - \square h \right) \right). \end{aligned} \quad (1.7)$$

This equation can be simplified significantly by using the trace-reversed metric perturbation

$$\bar{h}_{\mu\nu} \equiv h_{\mu\nu} - \frac{1}{2}\eta_{\mu\nu}h. \quad (1.8)$$

This gives us

$$R_{\mu\nu} - \frac{1}{2}g_{\mu\nu}R = \frac{1}{2} \left( \partial_{\rho}\partial_{\nu}\bar{h}_{\mu}^{\rho} + \partial_{\mu}\partial^{\rho}\bar{h}_{\nu\rho} - \square\bar{h}_{\mu\nu} - \eta_{\mu\nu}\partial_{\rho}\partial^{\lambda}\bar{h}_{\lambda}^{\rho} \right). \quad (1.9)$$

This can be further simplified by choosing an appropriate coordinate system, or *gauge*. Here we choose to make the infinitesimal coordinate transformation

$$x^{\mu} \rightarrow x'^{\mu} = x^{\mu} + \xi^{\mu}, \quad (1.10)$$

where  $\xi^{\mu}$  is an arbitrary slowly varying infinitesimal vector field. The transformation in  $h_{\mu\nu}$ , to lowest order, is

$$h_{\mu\nu} \rightarrow h'_{\mu\nu} = h_{\mu\nu} - \left( \partial_{\mu}\xi_{\nu} + \partial_{\nu}\xi_{\mu} \right). \quad (1.11)$$

This coordinate transformation is valid if  $|\partial_{\mu}\xi_{\nu}|$  are at most the same order as  $|h_{\mu\nu}|$ , so that the weak-field approximation still holds in the new coordinates,  $|h'_{\mu\nu}| \ll 1$ . Substituting this into the trace-reversed metric perturbation, equation (1.8) becomes

$$\bar{h}_{\mu\nu} \rightarrow \bar{h}'_{\mu\nu} = \bar{h}_{\mu\nu} - \left( \partial_{\mu}\xi_{\nu} + \partial_{\nu}\xi_{\mu} \right) + \eta_{\mu\nu}\partial^{\rho}\xi_{\rho}. \quad (1.12)$$

Considering the gauge freedom inherent in the choice of  $\xi^\mu$ , we can make a choice of coordinate system to simplify the Einstein equations for the weak field case. From examination of [equation \(1.9\)](#) we can make a further simplification by using the Lorenz gauge, defined by

$$\partial^\nu \bar{h}_{\mu\nu} = 0. \quad (1.13)$$

It is then simple using [equation \(1.12\)](#) and the Lorenz gauge condition from [equation \(1.13\)](#) to show that

$$\partial^\nu \bar{h}'_{\mu\nu} \rightarrow (\partial^\nu \bar{h}_{\mu\nu})' = \partial^\nu \bar{h}_{\mu\nu} - \square \xi_\mu. \quad (1.14)$$

So any arbitrary metric perturbation  $h_{\mu\nu}$  can be put into a Lorenz gauge by making a coordinate transform that satisfies the condition  $\square \xi_\mu = \partial^\nu \bar{h}_{\mu\nu}$ . Using the Lorenz gauge the Einstein tensor from [equation \(1.9\)](#) becomes

$$G_{\mu\nu} = -\frac{1}{2} \square \bar{h}_{\mu\nu}. \quad (1.15)$$

This leaves us with the linearised Einstein equations

$$\square \bar{h}_{\mu\nu} = -\frac{16\pi G}{c^4} T_{\mu\nu}. \quad (1.16)$$

This is a wave equation where  $x^0 = ct$ , which shows that GWs do travel at the speed of light, “c”.

### 1.2.2 Transverse Traceless Gauge

At a point outside of any sources, in a vacuum, we have  $T_{\mu\nu} = 0$ . This simplifies the Einstein equations [\(1.16\)](#) to the vacuum wave equation

$$\square \bar{h}_{\mu\nu} = 0. \quad (1.17)$$

We can now specialise to the space of homogeneous, asymptotically flat solutions of the linearised Einstein’s equations [\(1.16\)](#) [\[12\]](#). We can further specialise the gauge to make the metric perturbations purely spatial, traceless, and with the Lorenz gauge condition also make the metric perturbation transverse [\[10\]](#). We then have the TT gauge conditions

$$h^{0\mu} = 0, \quad (1.18a)$$

$$h^i_i = 0, \quad (1.18b)$$

$$\partial^j h_{ij} = 0. \quad (1.18c)$$

Metric perturbations in the TT gauge will be written as  $h_{\alpha\beta}^{TT}$ . We can use the TT gauge to show that GWs have two polarisations. Consider a GW travelling in the z-direction.  $h_{ij}^{TT} = h_{ij}^{TT}(t - z)$  is a valid solution to  $\square h_{ij}^{TT} = 0$  for any arbitrary function of  $(t - z)$ . The Lorenz condition  $\partial_z h_{zj}^{TT} = 0$  implies that  $h_{zj}^{TT}(z - t) = C$ , where  $C$  is a constant. For the condition that  $h_{\alpha\beta} \rightarrow 0$  as  $r \rightarrow \infty$ , then  $C = 0$ . So

the only non-zero components of the metric perturbation are  $h_{xx}^{TT}$ ,  $h_{xy}^{TT}$ ,  $h_{yx}^{TT}$ , and  $h_{yy}^{TT}$ . Only two of these non-zero components are independent because of the traceless condition [equation \(1.18b\)](#) and the symmetry of  $h_{\mu\nu} = h_{\nu\mu}$ . For a wave propagating in the  $z$ -direction the metric perturbation can therefore be written as

$$h_{\mu\nu}^{TT} = \begin{pmatrix} 0 & 0 & 0 & 0 \\ 0 & h_+ & h_\times & 0 \\ 0 & h_\times & -h_+ & 0 \\ 0 & 0 & 0 & 0 \end{pmatrix}, \quad (1.19)$$

where the wave amplitudes are

$$\begin{aligned} h_+ &= A_+ \cos(\omega_{\text{GW}} t + \phi_+), \\ h_\times &= A_\times \cos(\omega_{\text{GW}} t + \phi_\times), \end{aligned} \quad (1.20a)$$

These are the simple solutions for a monochromatic plane wave with linear polarization. We can see from [equation \(1.19\)](#) that the metric perturbation has only two degrees of freedom  $h_+$  and  $h_\times$ , which are the two independent polarisations of a GW. These are known as the “plus” and “cross” polarisations of the GW which are separated by a rotation of  $45^\circ$ , as can be seen in [figure 1.2](#).

### 1.2.3 Interaction of Gravitational Waves with Matter

So far we have shown how to describe GWs. In this section we will discuss how GWs interact with matter. Here we will look at the effect on the spacetime coordinates of a free falling test mass considering just “plus” polarised GWs. With a spacetime metric  $g_{\mu\nu}$ , and four dimensional spacetime coordinates  $x^\mu$ , the geodesic equation describing the motion of test masses in free fall is

$$\frac{d^2 x^\mu}{d\tau^2} + \Gamma_{\nu\rho}^\mu \frac{dx^\nu}{d\tau} \frac{dx^\rho}{d\tau} = 0, \quad (1.21)$$

where the Christoffel symbols  $\Gamma_{\nu\rho}^\mu$  are defined as

$$\Gamma_{\nu\rho}^\mu = \frac{1}{2} g^{\mu\sigma} \left( \partial_\nu g_{\sigma\rho} + \partial_\rho g_{\sigma\nu} - \partial_\sigma g_{\nu\rho} \right). \quad (1.22)$$

The 4-velocity of a free falling test mass initially at rest is  $\frac{dx^\mu}{d\tau}|_{\tau=0} = (1, 0, 0, 0)$ , and  $\Gamma_{00}^\mu = 0$  for a metric which satisfies the TT gauge conditions in [equations \(1.18\)](#). Substituting this into [equation \(1.21\)](#) we find the initial acceleration of the test mass  $\frac{d^2 x^\mu}{d\tau^2}|_{\tau=0} = 0$ . Therefore, as the test mass begins at rest and has zero acceleration, the spacetime coordinate position of the test mass does not change. Extending this to the case of two test masses, we see that the coordinate distance between two test masses is not affected by the passage of a GW.

However, the proper (physical) distance between free falling test masses does change. The proper distance  $ds$  between two free test masses is given by

$$ds^2 = g_{\mu\nu} dx^\mu dx^\nu = -(cdt)^2 + (1 + h_+)dx^2 + (1 - h_+)dy^2 + dz^2, \quad (1.23)$$



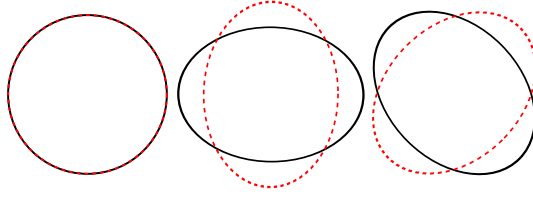


Figure 1.2: Deformation effect of a GW travelling out of the page on proper distance between a circle of free test masses (left). The effect of both “plus” (centre) and “cross” (right) polarised GWs can be seen as a distortion of the space between the free test masses, changing the proper distance between them. The only difference between the plus and cross polarisations is a rotation of  $45^\circ$ .

where we consider only plus polarised GWs travelling in the  $z$  direction. Choosing our coordinates so that the masses are separated along the  $x$ -axis ( $dy = dz = 0$ ) at some time  $t$ , we find the proper distance between the two masses is given by

$$\begin{aligned} ds &= \sqrt{1 + h_+} dx, \\ &\simeq \left(1 + \frac{1}{2}h_+\right) dx, \end{aligned} \quad (1.24)$$

where we used the weak-field limit,  $|h_+| \ll 1$ , and the binomial expansion to find the estimate of the proper distance. Here we can see that GWs cause the proper distance between two points to fluctuate, but as we showed above this does not affect the coordinate distance between the points. We can see this effect for both the  $x$ -axis and  $y$ -axis for both “plus” and “cross” polarised GWs by considering the proper distance between a ring of free falling test masses as shown in [figure 1.2](#). This result is the basis for the modern generation of laser interferometric GW detectors; we will give details on the detection principle in [Section 2.2](#).

### 1.3 Gravitational Wave Sources

GWs can be produced by the acceleration of mass and are most strongly produced in compact, asymmetric, and relativistic objects. If dealing with a self-gravitating system, the motion is dominated by the sources own gravity and we can roughly relate the orbital angular frequency  $\omega$  to mass  $M$  and orbital radius  $R$  by Kepler’s law. It is worth noting that it is not possible to generate a detectable GW in a laboratory. We could consider man made sources of GWs, a good example of this is a centrifuge made of two  $10^3$  kg masses on the ends of a 10 m long pole. If this system were to rotate around the centre of the pole at 10 Hz, GWs with frequency of 20 Hz would be produced. Due to their quadrupole nature, GWs are typically emitted at twice the frequency of the source motion. The wavelength of the waves would be  $\sim 1.5 \times 10^7$  m (roughly the diameter of the Earth). To detect GWs, and not near zone Newtonian gravity, a GW detector must be at least one wavelength away from the source [\[13\]](#). For a detector positioned on the opposite of the Earth to the source, the GWs passing the detector will have an amplitude of  $h \sim 5 \times 10^{-43}$  which is far too small to attempt a detection [\[14\]](#).

We can not produce a detectable GW sources on the Earth, but there are many astrophysical systems that are expected to have the conditions required to produce larger GW strains that could be detectable from Earth. In this section we will describe the expected sources of GWs that may be detectable by ground-based interferometric detectors. These are distinguished into different categories by the GW community so that search methods can be developed and optimised for each separately.

### 1.3.1 Transient / Burst Sources

Transient or “burst” sources are catastrophic astrophysical events such as supernovae (SNe) and gamma-ray bursts (GRBs) which emit a large amount of energy as GWs in a very short time, typically less than a few seconds; this is referred to as a gravitational-wave burst (GWB).

Many potential sources of GWBs are difficult to model because we do not know all of the physics involved (e.g. the neutron star (NS) equation of state (EOS)), or because they are too complex, or more likely a combination of both. For some proposed phenomena, such as stellar core-collapse SN, we have only analytical toy models. The first models for GWs from a rotating stellar core-collapse and bounce were based on the axisymmetric (2D) Newtonian simulations [15, 16]. More recently simulations have been performed with varying degrees of micro-physical detail, but still in 2D [17, 18]. Recently, the first 3D simulations have been performed for a rapidly rotating strongly magnetised core collapse [19]. It was found that the 3D dynamics of rapidly rotating highly magnetised core collapse SNs are fundamentally different from what was anticipated on the basis of previous simulations in axisymmetric (2D) simulations. These results show promise for future simulation in 3D and prompt an extended study into the effect of the initial conditions and numerical resolution of the simulations. Current GW signal models from these simulations are not sufficiently accurate to allow a matched filter analysis, so we are forced to rely on waveform independent detection techniques. Although there are many possible sources for GWBs, here we will only consider SNs and GRBs in depth.

The progenitors for SNs are accreting white dwarfs (type Ia SN) or the collapse of highly evolved stars (type II SN) [20]. Type Ia SN are expected to produce GWs, but below the sensitive frequency band of the ground based detectors [21, 22]. There are many aspects still unknown about the complex physics of type II SN, it has proven difficult to make a reliable prediction of the expected strength of GWs emitted by this process. Simulations that include some, but not all, of the physics of a stellar core-collapse SN have been performed, for a review see [23]. These simulations identify numerous potential emission processes for GWs with up to  $10^{-8} M_{\odot} c^2$  of energy in GWs [23]. The initial laser interferometer gravitational-wave observatory (LIGO) and Virgo detectors have only been sensitive to SN from inside of our own Galaxy [24]. The rate of a Galactic SNs are one per 30–100 years [25, 26].

GRBs are astrophysical events that are observed as an intense flash of gamma rays [27, 28, 29]. Long-soft ( $> 2$  s) GRBs are associated with the stellar core-

collapse SN of massive stars [30, 31, 32, 33]. Short-hard ( $< 2$  s) GRBs are thought to be due to the merger of compact binaries consisting of two neutron stars or a neutron star and a black hole [34, 35]. Both of these progenitor models are highly relativistic and lead to the formation of an accreting black hole (or possibly a magnetar [36]).

While the GWs produced by the inspiral phase of compact binary coalescence (CBC) in short GRBs are well modelled, numerical models of SNs and collapsars often include only approximations of the required physics and simplifications such as handling neutrinos or assuming symmetries to models sources in less than the full 3 dimensions. The expected signal from long GRBs are speculative, but possibly strong. In the extreme stellar core-collapse conditions required to power long GRBs (“collapsars”) alternative GW emission processes can be considered than for SN. One of the most extreme scenarios for GW emission from long GRBs is dynamical fragmentation of a rapidly differentially spinning stellar core-collapse, producing a coalescing system of two protoneutron stars [37, 38]. Although this scenario is unlikely [39], the GW emission would be very strong producing  $10^{-2} M_{\odot} c^2$  to  $10^{-1} M_{\odot} c^2$  of energy in GWs in the 50 Hz–1 kHz frequency band. Other scenarios can also produce up to  $10^{-2} M_{\odot} c^2$  of energy in GWs [37, 40, 38, 41, 36, 42]. Details on possible GW emission processes for short and long GRBs will be given in [section 4.1](#). The current best exclusion distances for GWBs associated with 150 GRBs analysed using the LIGO and Virgo detectors, assuming  $E_{\text{GW}} = 10^{-2} M_{\odot} c^2$  of energy in GWs and a jet opening angle of  $5^\circ$  gives a median exclusion distance of  $\sim 17 \text{ Mpc} (E_{\text{GW}}/10^{-2} M_{\odot} c^2)^{1/2}$  for GW emission around 150 Hz [43]. This is the same order of magnitude as the limits found using a modelled search for CBCs, however this is much smaller than the typical distance to the closest GRB system per year ( $\sim 1 \text{ Gpc}$ ).

Many analyses have been performed for GWBs of various types using the GEO 600, LIGO, TAMA 300, and Virgo GW interferometers. Searches can either be performed for GWBs from any direction arriving at any time, or can be aimed at a “trigger”. These triggers are typically a source detected by EM or neutrino observations, such as a GRB. A triggered analysis can gain up to 20% in distance compared to an all sky search [44].

Details of recent all-sky searches for GWBs can be found in [45, 46, 47, 48, 24]. Details of recent triggered searches for GWBs can be found in [49, 50, 51, 52, 53, 54, 43, 55, 56, 57].

### 1.3.2 Compact Binary Coalescence

CBC are two body systems which emit GWs as they orbit each other, these systems can be binary black hole (BBH), binary neutron star (BNS) or BH–NS binaries. During the last minutes of the inspiral of these binary systems strong GWs are produced in the frequency band of ground-based detectors. For the binary black hole (BBH) and black hole (BH)–NS cases this will only be the case if the BHs have masses of  $1\text{--}1000 M_{\odot}$ . As the system loses energy and angular momentum through the emission of GWs the orbital radius of the system will decay and the orbital frequency will increase, following Kepler’s Law, which causes the

frequency of the emitted GWs to also increase as this is dependent on the orbital mechanics of the binary. The orbital radius will continue to decrease in this manner, until it is small enough that the two objects will collide and merge. When the two bodies merge the frequency and power of the emitted GWs will increase, producing a strong GWB. This inspiral phase of a CBC produces a characteristic chirp signal and is accurately modelled by post-Newtonian expansions [58]. This allows a modelled search to be performed using matched filtering to improve the sensitivity for these signals [59]. The GW signal spectrum for the inspiral phase of a CBC signals is

$$h(f) \sim M^{5/6} f^{-7/6}, \quad (1.25)$$

where  $f$  is frequency and

$$M = \frac{(m_1 m_2)^{3/5}}{(m_1 + m_2)^{1/5}} \quad (1.26)$$

is the chirp mass, where  $m_1$  and  $m_2$  are the component masses [10].

The sky-position averaged observable distance for BNSs, the effective BNS range or *horizon distance*, is often used as a measure of detector performance. Initial LIGO had a design effective BNSs range of 14 Mpc, and the actual best effective BNS range achieved was  $\sim 20$  Mpc [60]. For the advanced LIGO detectors we expect an order of magnitude improvement in the effective BNS range to 200 Mpc [61, 62].

From the most recent search for CBCs LIGO for an optimally orientated source set rate upper limits of  $1.3 \times 10^{-4} \text{ Mpc}^{-3} \text{ yr}^{-1}$ ,  $3.1 \times 10^{-5} \text{ Mpc}^{-3} \text{ yr}^{-1}$ , and  $6.4 \times 10^{-6} \text{ Mpc}^{-3} \text{ yr}^{-1}$  for  $1.4 M_\odot$ – $1.4 M_\odot$  BNS,  $1.4 M_\odot$ – $10 M_\odot$  NS–BH, and  $10 M_\odot$ – $10 M_\odot$  BBH systems respectively [63]. Details of recent analyses for CBCs can be found in [64, 43, 63, 65, 57].

### 1.3.3 Continuous / Periodic Sources

Continuous sources of GWs, also called periodic sources, radiate GWs at a constant or nearly constant frequency. An example of this is a rotating neutron star, or pulsar; these sources emit radio waves which are beamed like a lighthouse crossing our line of sight as they rotate. If this rapidly rotating body were to have a small asymmetry, such as a bump on its surface, then GWs would be emitted from this object. The amount of energy emitted in GWs depends on the size of the asymmetry, but it is unclear which mechanism produces the asymmetry and how large it can get [66].

We would expect an asymmetric pulsar to radiate GWs with characteristic amplitude [12]

$$h = \frac{4\pi^2 G}{c^4} \frac{I f^2 \epsilon}{D}, \quad (1.27)$$

where  $I$  is the rotational moment of inertia of the neutron star,  $f$  is the frequency of rotation,  $D$  is the distance to the source, and  $\epsilon = (I_{xx} - I_{yy})/I$  is the equatorial ellipticity; the amount that the neutron star is distorted. This final parameter is poorly understood but it thought that the crusts of neutron stars are not strong enough to support  $\epsilon$  larger than  $\sim 10^{-6}$  [14], and realistic values could be much

smaller than this limit. A non zero  $\epsilon$  will cause the pulsar to lose energy through the emission of GWs with  $h \sim 10^{-24}$  or smaller [13]. This causes the rotational frequency to decrease, which is referred to as spin-down. Searches for these continuous GWs are done by matched filtering long sequences of data against the expected signal. A large number of templates are required to account for the unknown sky position, frequency of emission, spin down rate, and other parameters [66]. All-sky searches for continuous GWs are strongly computationally limited due to the large number of required templates.

Details of recent analyses for continuous GWs can be found in [67, 68, 69, 61, 70]. Searches have also been performed for specific targets such as the Crab [71] and Vela pulsars [72]. The current best upper limit for the equatorial ellipticity is  $\epsilon \approx 10^6$  [61].

### 1.3.4 Stochastic Background

The stochastic gravitational wave background (SGWB) is the superposition of a large number of independent, uncorrelated GW sources which are individually undetectable [73, 74, 75, 76]. An interesting potential source of these GWs is the early universe, which could produce a background across the entire sky [77]. Stochastic GWs are expected to have a roughly constant amplitude across the frequency band of the ground based detectors. Predictions of the expected amplitude of the SGWB are less robust than for other sources. The strength of the SGWB is usually described in terms of the GW spectrum,

$$\Omega_{\text{GW}}(f) = \frac{f}{\rho_c} \frac{d\rho_{\text{GW}}}{df}, \quad (1.28)$$

where  $d\rho_{\text{GW}}$  is the energy density of gravitational radiation contained in frequency range  $f$  to  $f + df$  and  $\rho_c$  is the critical energy density of the Universe.

Searches for the SGWB with LIGO and Virgo data are performed by cross correlating the data from a network of at least two detectors. While noise in each detector will be un-correlated, a SGWB will appear as correlated “noise” between detectors. The analysis of data from the S5 science run assumed a power-law template for the GW spectrum,

$$\Omega_{\text{GW}}(f) = \Omega_\alpha \left( \frac{f}{100 \text{ Hz}} \right)^\alpha, \quad (1.29)$$

where  $\alpha$  is the spectrum index. This analysis gave an upper limit on the frequency independent GW spectrum ( $\alpha = 0$ ) in a frequency band around 100 Hz of  $\Omega_{\text{GW}} < 6.9 \times 10^{-6}$  with 95% confidence [78]. This result improves on the indirect limits from Big Bang nucleosynthesis [79] and cosmic microwave background [80] at 100 Hz.

Details of recent analyses for SGWB can be found in [81, 78, 82].



# Gravitational Wave Detectors

# 2

In this chapter details of the working principles of GW interferometers will be given. [Section 2.1](#) describes the Michelson Morley experiment, a design which the current generation of ground based interferometer GW detectors are based on. [Section 2.2](#) explains the working principle of an interferometric GW detector. [Section 2.3](#) discusses the main noise sources which limit sensitivity for ground based GW interferometers, focusing on GEO 600. [Section 2.4](#) describes the status of the current global network of interferometric GW detectors, and plans for the future generations of ground and space based GW detectors. [Section 2.5](#) gives a more in-depth description of a number of the sub-systems of GEO 600. For a more thorough introduction to GW detectors see [\[13\]](#), and references therein, which this chapter draws from heavily.

## 2.1 Michelson-Morley Experiment

A simple way to determine the distance between two objects is to measure the light travel time of the round trip between the two objects. A classic example of the use of this concept is the experiment performed by Michelson and Morley in 1887. Using an interferometer they attempted to detect a shift in the speed of light due to the motion of the Earth through the *aether* [\[83\]](#). A null result was obtained from the experiment, which was the first strong evidence against the *aether* theory; instead showing that light travels at a constant speed in all inertial frames of reference. This result triggered a line of research that would eventually lead to Einstein formulating the special theory of relativity.

The Michelson and Morley experiment was performed using a simple interferometer design that is now referred to as a “Michelson interferometer”. The most basic components are a coherent light source (such as a sodium lamp as used by Michelson and Morley or a laser as used in modern interferometers), a beam splitter (BS) (50% transmissive mirror), and two mirrors at equal distance from the BS in two orthogonal directions which make up the “arms”. Finally the light leaving the interferometer must be observed (Michelson and Morley used a telescope while modern interferometers use a photo detector (PD)), see

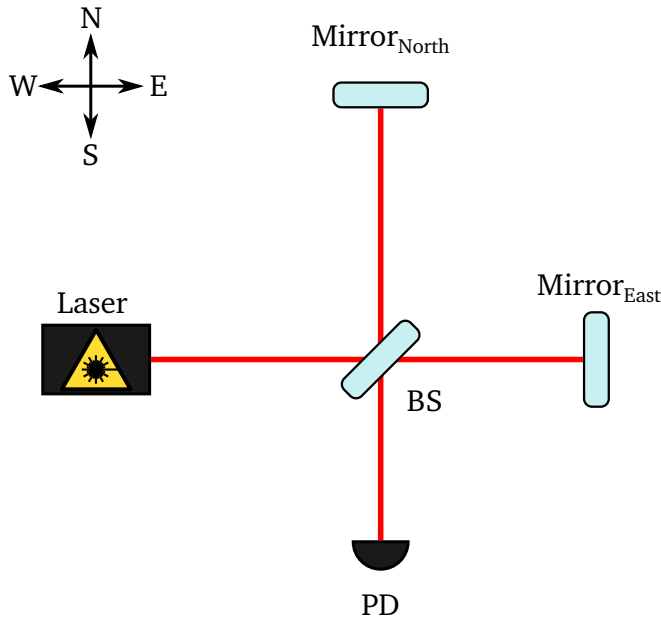


Figure 2.1: Schematic of the basic layout of a Michelson interferometer. The path followed by the laser is shown in red. The input (common) port is shown to the West and the output (differential) port is shown to the South relative to the beam splitter (BS).

figure 2.1. Light from the light source enters the interferometer at the *input port*, it is partially reflected and partially transmitted by the BS and then travels along the arms toward the two end mirrors. This light is then reflected back towards the BS, where it is superimposed. A measurement can then be performed by observing light leaving the *output port* which gives information about the relative travel time of photons in the two orthogonal arms. For *aether*, the expected difference in the speed of light along the two orthogonal arms would have caused light recombining at the BS to be out of phase, which would be observed as a change in the interference pattern at the output port. For GWs the speed of light is a constant but the arm lengths are changed differentially by GWs, which will similarly affect the phase between the light in the two arms and be observable at the output port. Figure 2.1 is the simplest design for a Michelson interferometer; the instrument actually used by Michelson and Morley was more complicated using extra mirrors to increase the arm length as shown in figure 2.2, which as will be shown in Section 2.2 increases the sensitivity of the detector. As we shall see in this chapter, GW interferometers are even more complicated and built on a much larger scale which allows higher precision measurements, but the working principle for detecting differential length changes in the arms remains essentially the same as for the Michelson and Morley instrument.

## 2.2 Gravitational Wave Detection Principle

It was shown in section 1.2.3 that GWs interact with matter, which has the effect of changing the proper distance between two free test masses without changing



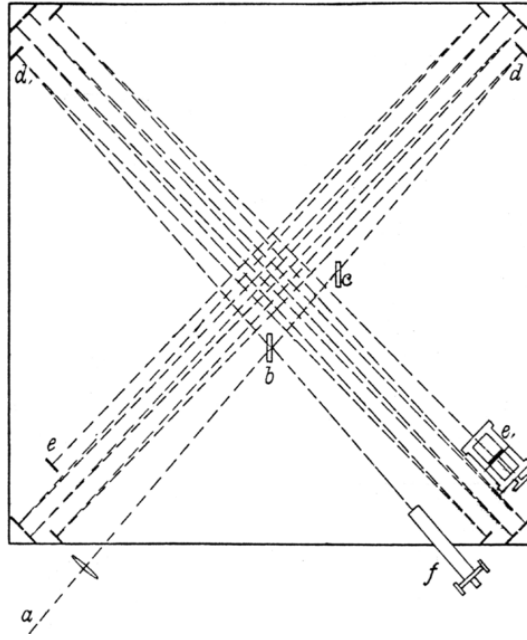


Figure 2.2: Diagram of experimental set up of the Michelson and Morley experiment in 1887. The sodium lamp is positioned at  $a$ , and the BS is positioned at  $b$ .  $e$  are plane parallel mirrors at the ends of the arms, while the other mirrors (which are unlabelled) are used to increase the arm length, and  $f$  is the observing telescope [83].

the coordinate distance between them. Knowing this effect we can consider how a laser interferometer can be used to detect GWs. From equation (1.23), considering a linearly polarised GW ( $h_{\times} = 0$ ) of the form given in equation (1.20), we have the condition  $ds = 0$  for the light path taken between two test masses,

$$ds^2 = -(cdt)^2 + (1 + h_+)dx^2 + (1 - h_+)dy^2 + dz^2 = 0. \quad (2.1)$$

Considering light travelling along the  $x$ -axis (along the East arm of the interferometer shown in figure 2.1) we can use the fact that  $dy = dz = 0$  to simplify equation (2.1), giving

$$dt = \frac{\sqrt{1 + h_+}}{c} dx. \quad (2.2)$$

By integrating this we can find the time taken for light to travel the length of the  $x$  arm,  $L_x$ , from the BS at  $t_0$  to the East end mirror at  $t_1$

$$\begin{aligned} \int_{t_0}^{t_1} dt &= \frac{1}{c} \int_0^{L_x} \sqrt{1 + h_+(t)} dx, \\ &\simeq \int_0^{L_x} \frac{1}{c} \left( 1 + \frac{1}{2} h_+(0) \right) dx, \\ &\simeq \frac{1}{c} \left[ 1 + \frac{1}{2} h_+(0) \right] L_x, \end{aligned} \quad (2.3)$$

where we have used the binomial expansion  $\sqrt{1+h_+} \simeq 1 + \frac{1}{2}h_+$  and keep only term of 1<sup>st</sup> order in  $h$  because  $|h_+| \ll 1$ . We also assume that the period  $T$  of the GW is large compared to the round-trip time,  $T \gg \frac{2L_x}{c}$ , so that  $h(t) = h(0)$  (i.e. the long-wavelength limit). We find the same results for the return trip from the East end mirror to the BS and so can define the round-trip time for the x arm as

$$t_{\text{round-trip } x} \simeq \frac{2}{c} \left[ 1 + \frac{1}{2}h_+(0) \right] L_x. \quad (2.4)$$

The same can be done for light travelling in the y arm, giving the same result with  $h_+ \rightarrow -h_+$  due to the quadrature nature of GWs:

$$t_{\text{round-trip } y} \simeq \frac{2}{c} \left[ 1 - \frac{1}{2}h_+(0) \right] L_y. \quad (2.5)$$

Assuming that  $L = L_x = L_y$ , from [equations \(2.4\) and \(2.5\)](#) we can define the travel time difference between the two arms as

$$t = t_{\text{round-trip } x} - t_{\text{round-trip } y} = \frac{2L}{c} h_+(0). \quad (2.6)$$

It is then simple to define the fractional change in optical path length, which is referred to as the *strain*

$$\frac{\Delta L}{L_{\text{opt}}} = \frac{c \Delta t}{2L} = h_+(0), \quad (2.7)$$

where  $L_{\text{opt}} = 2L$ . This can also be expressed as a phase shift

$$\Delta \phi = \frac{4\pi L f_c}{c} h_+(0), \quad (2.8)$$

where  $f_c$  is the laser carrier frequency. For a GW with  $h_+ = 1 \times 10^{-22}$  in the GEO 600 detector, which has arms of  $L = 1200$  m, this will produce a differential time delay of  $8 \times 10^{-28}$  s. The laser at GEO 600 has  $f_c = 2.8 \times 10^{14}$  Hz, giving a phase shift of  $1.4 \times 10^{-12}$  rad.

The phase change on light travelling in both the x arm and y arm is given by the pair of equations

$$d\phi = \omega_c t_{\text{round-trip}} = \frac{2\omega_c L}{c} \pm \frac{\omega_c}{2} \int_{t_0}^{t_0+2L/c} h_+(t) dt, \quad (2.9)$$

where  $\omega_c$  is the angular frequency of the laser carrier.

Only the second term of these equations depend on the GW; we will refer to this phase shift due to the effect of GWs as  $\delta\phi$ . Again considering a linearly polarised GW ( $h_x = 0$ ) of the form given in [equation \(1.20\)](#), we define the phase shift [\[10\]](#)

$$\begin{aligned} \delta\phi &= \pm \frac{\omega_c}{2} \int_{t_0}^{t_0+2L/c} A_+ \cos(\omega_{\text{GW}} t) dt \\ &\simeq \pm \frac{A_+ \omega_c}{\omega_{\text{GW}}} \sin(\omega_{\text{GW}} L/c) \cos[\omega_{\text{GW}}(t_0 + L/c)], \end{aligned} \quad (2.10)$$

for the light in the  $x$  and  $y$  arms. Therefore a GW will modulate laser light at its frequency,  $\omega_{\text{GW}}$ , in each of the arms of the detector.

Still considering just plus polarised GWs travelling in the  $z$  axis with respect to the interferometer and with amplitude given by  $h_+ = A_+ \cos(\omega_{\text{GW}}t)$ , these GWs will cause a differential length change of the interferometer arms, which in turn will produce a light travel time difference in the two arms [84]. This is a change in the proper length of the arms, but not in the coordinate position of the test masses, so the test masses are not actually moved by GWs.

From this one could think because the phase shift is proportional to  $L$ , the larger the optical path the larger the phase shift due to GWs, and so the better the sensitivity. However, there is an ideal arm length,  $L_{\text{ideal}}$ , and corresponding light storage time that depends on the frequency of the GW being observed,  $f_{\text{GW}} = \frac{\omega_{\text{GW}}}{2\pi}$ . The light in the arms will acquire the largest possible phase shift if the round-trip time equals half the wave period

$$L_{\text{ideal}} = \frac{c}{4f_{\text{GW}}} . \quad (2.11)$$

From this we can see that for a GW with  $f_{\text{GW}} = 1$  kHz the ideal arm length is  $L_{\text{ideal}} \approx 75$  km. It is infeasible to construct a vacuum system large enough to house interferometer arms this long, so advanced interferometric techniques, that will be explained in [sections 2.2.2, 2.5.4 and 2.5.5](#), are used to achieve effective arm lengths of this order within a physically smaller vacuum system of order a few km.

Until this point we have considered the special case of a GW travelling along the  $z$ -axis, but interferometric GW detectors are sensitive to GWs from all directions over the entire sky; there is no pointing like an EM telescope. However, the sensitivity is not uniform for all directions [85]. A GW detector with arms along the  $x$ -axis and  $y$ -axis is most sensitive to signals from directly along the  $z$ -axis, from above or below, as this will produce the largest differential length change between the arms (referred to as optimally positioned signals). GWs from along the direction of one of the interferometer arms will produce a response a factor of two less than the maximum along the  $z$ -axis. There is zero sensitivity to signals from in the plane of the arms along the bisectors of the  $x$  and  $y$  arms, this is because these signals will produce precisely equal length changes in the two arms of the interferometer that will cancel each other out producing no change at the detector output.

The general form of [equation \(2.7\)](#) for a GW from a direction  $\theta, \phi$  in spherical coordinates, and with the polarisation rotated with respect to the detector axes by an angle  $\psi$ , as shown in [figure 2.3](#), with signal components  $h_+$  and  $h_\times$  in the two GW polarisations will produce a strain  $\Delta L/L_{\text{opt}}$  at the detector given by

$$\frac{\Delta L(t)}{L_{\text{opt}}} = F_+(\theta, \phi, \psi) h_+(t) + F_\times(\theta, \phi, \psi) h_\times(t) . \quad (2.12)$$

Here  $F_+$  and  $F_\times$  are the antenna pattern response functions for the two polarisa-

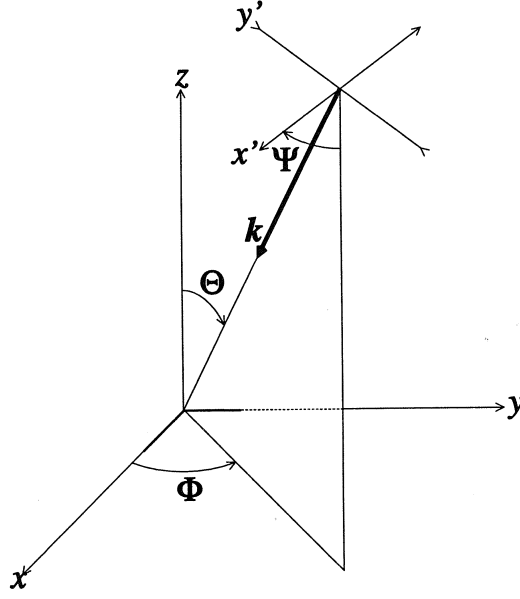


Figure 2.3: Coordinates used to describe the antenna pattern of GW detectors in the x-y plane with arms parallel to the x and y-axes [13].

tions, given by [14]

$$\begin{aligned} F_+ &= \frac{1}{2} (1 + \cos^2 \theta) \cos 2\phi \cos 2\psi - \cos \theta \sin 2\phi \sin 2\psi, \\ F_\times &= \frac{1}{2} (1 + \cos^2 \theta) \cos 2\phi \sin 2\psi + \cos \theta \sin 2\phi \cos 2\psi. \end{aligned} \quad (2.13)$$

Figure 2.4 shows the “peanut diagram” which displays the RMS directional sensitivity  $\sqrt{F_+^2 + F_\times^2}$  of a GW detector, which is independent of angle  $\psi$ .

### 2.2.1 The Sideband View

As was shown in equation (2.10), GWs phase modulate the light in the interferometer arms. This modulation is out of phase in the two arms, which we will show below allows the GW signals to leave the interferometer via the output port. An electric field with angular frequency  $\omega_c = 2\pi f_c$  and amplitude  $E_c$  is given by

$$E(t) = E_c e^{i\omega_c t}. \quad (2.14)$$

If we applied a phase modulation to this electric field with modulation index  $m$  and modulation angular frequency  $\omega_m$ , we find[87]

$$\begin{aligned} E_{\text{pm}}(t) &= E_c e^{i\omega_c t} e^{im \cos(\omega_m t)} \\ &\simeq E_c e^{i\omega_c t} \left[ 1 - \frac{m^2}{4} + i \frac{m}{2} (e^{i\omega_m t} + e^{-i\omega_m t}) \right], \end{aligned} \quad (2.15)$$

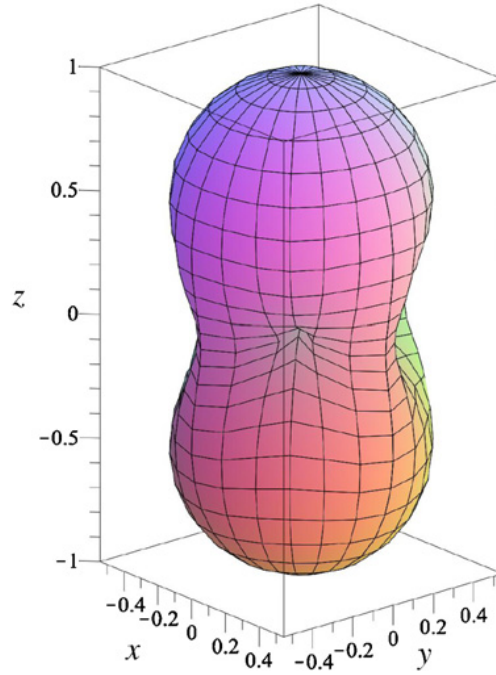


Figure 2.4: The RMS antenna amplitude response  $\sqrt{F_+^2 + F_\times^2}$ . Showing the directional sensitivity for a GW detector with arms aligned along the x-axis and y-axis [86].

where we assume weak modulation, so  $|m| < 1$  and keep terms of up to second order in  $m$ <sup>1</sup>. In [equation \(2.15\)](#) we can clearly see the phase modulation has created two sidebands at frequencies  $\pm\omega_m$  compared to the carrier [87]. The amplitude of the sidebands is  $m/2$ , while the carrier now has the amplitude  $1 - m^2/4$ . The “ $i$ ” in front of the sideband terms shows that there is a phase angle of  $\frac{\pi}{2}$  between the carrier and the sidebands.

As we describe in [section 2.5.7](#), current ground based detectors operate at or near the “dark fringe”; this is the operating point where most of the carrier light that enters the interferometer through the input port is reflected back towards the input port. Also, because of the symmetry of an interferometer the equivalent effect will happen for light entering the interferometer from the output port. As we will now show, this operating point has the benefit of separating the carrier light from signal sidebands which reduces the light power hitting the output photo detector, suppressing common mode noise such as laser power fluctuations. This also allows the use of advanced interferometric techniques such as power recycling ([section 2.5.4](#)) and signal recycling ([section 2.5.5](#)) because of the natural separation of the carrier and signal light.

We shine a laser at the input port of the interferometer with electric field

$$E_{\text{in}} = E_c e^{i\omega_c t}. \quad (2.16)$$

<sup>1</sup>If we were to keep only terms of first order in  $m$  the carrier is unchanged by the modulation, here we chose to keep terms up to second order in  $m$  which is more intuitive and makes the conservation of energy more explicit [87].

We assume the interferometer has a BS with amplitude reflectivity  $\rho = +1/\sqrt{2}$  on one side and  $\rho = -1/\sqrt{2}$  on the other side, amplitude transmissivity  $\tau = 1/\sqrt{2}$ , and perfectly reflective end mirrors with  $\rho = -1$ . Then the power reflected towards the input (common) port and transmitted to the output (differential) port are given by

$$\begin{aligned} P_{\text{common}}/P_{\text{in}} &= \frac{1}{2}(1 - \cos \phi_0) \\ P_{\text{differential}}/P_{\text{in}} &= \frac{1}{2}(1 + \cos \phi_0), \end{aligned} \quad (2.17)$$

where  $\phi_0$  is the phase between the two arms. Operating at or near the dark fringe, where the differential length difference of the arms is controlled so that  $\phi_0 \simeq \pi$ , we have

$$\begin{aligned} P_{\text{common}}/P_{\text{in}} &\simeq 1, \\ P_{\text{differential}}/P_{\text{in}} &\simeq 0. \end{aligned} \quad (2.18)$$

This shows that the majority of light entering the input of a interferometer operating at or near the dark fringe, is reflected back towards the input port.

The phase of the electric field is conserved during free propagation, but acquires factors from reflection and transmission from the optical components of the interferometer. Propagating the input laser  $E_{\text{in}}$  through the BS and into the two arms in the presence of a GW will give the electric fields

$$\begin{aligned} E_{\text{arm}} &= \frac{1}{\sqrt{2}} E_c e^{i\omega_c t} e^{a_{\text{GW}} \cos(i\omega_{\text{GW}} t)} \\ &= \frac{1}{\sqrt{2}} E_c e^{i\omega_c t} \left[ 1 - \frac{a_{\text{GW}}^2}{4} \pm \frac{ia_{\text{GW}}}{2} (e^{i\omega_{\text{GW}} t} + e^{-i\omega_{\text{GW}} t}) \right]. \end{aligned} \quad (2.19)$$

Notice that the effect from the GW has opposite phase in the two arms due to the quadrature nature of GWs. If we then recombine these fields at the BS we find the electric field leaving the input (common) port is given by

$$\begin{aligned} E_{\text{common}} &= (-1) \cdot \frac{1}{\sqrt{2}} \cdot E_{\text{x-arm}} + (-1) \cdot \frac{1}{\sqrt{2}} \cdot E_{\text{y-arm}} \\ &\simeq -\frac{1}{2} E_c e^{i\omega_c t} \left\{ \left[ 1 - \frac{a_{\text{GW}}^2}{2} + \frac{ia_{\text{GW}}}{2} (e^{i\omega_{\text{GW}} t} + e^{-i\omega_{\text{GW}} t}) \right] \right. \\ &\quad \left. + \left[ 1 - \frac{a_{\text{GW}}^2}{2} - \frac{ia_{\text{GW}}}{2} (e^{i\omega_{\text{GW}} t} + e^{-i\omega_{\text{GW}} t}) \right] \right\} \\ &\simeq -E_c e^{i\omega_c t} + \frac{a_{\text{GW}}^2}{4}. \end{aligned} \quad (2.20)$$

This is the reflected carrier, and there are no GW sidebands which leave the input port. As will be shown in [section 2.5.4](#), the fact that the majority of the carrier is reflected by the interferometer can be used to increase the circulating

laser power with power recycling (PR). The electric field leaving the output (differential) port is given by

$$\begin{aligned}
 E_{\text{differential}} &= (-1) \cdot \frac{-1}{\sqrt{2}} \cdot E_{\text{x-arm}} + (-1) \cdot \frac{1}{\sqrt{2}} \cdot E_{\text{y-arm}} \\
 &\simeq \frac{1}{2} E_c e^{i\omega_c t} \left\{ \left[ 1 - \frac{a_{\text{GW}}^2}{2} + \frac{ia_{\text{GW}}}{2} (e^{i\omega_{\text{GW}} t} + e^{-i\omega_{\text{GW}} t}) \right] \right. \\
 &\quad \left. - \left[ 1 - \frac{a_{\text{GW}}^2}{2} - \frac{ia_{\text{GW}}}{2} (e^{i\omega_{\text{GW}} t} + e^{-i\omega_{\text{GW}} t}) \right] \right\} \\
 &\simeq \frac{ia_{\text{GW}}}{2} (e^{i\omega_{\text{GW}} t} + e^{-i\omega_{\text{GW}} t}) E_c e^{i\omega_c t}. \tag{2.21}
 \end{aligned}$$

There is no carrier component in this signal, only the GW sidebands leave the output port. To sense the GW sidebands with a photodiode, a local oscillator must be introduced to produce power variations that are detected by the photodiode; we will discuss the available signal readout schemes in [section 2.5.7](#). As will be shown in [section 2.5.5](#), the fact that only the signal sidebands leave the output port and they are separated from the carrier can be used to increase the interaction time of the signal sidebands in the interferometer arms with signal recycling (SR).

### 2.2.2 Fabry-Perot cavities and control systems

As we saw from [equation \(2.11\)](#) the optimal arm length for audio frequency GWs, which the ground-based interferometers are sensitive to, is of order 100 km. One technique that is used to achieve an effective arm length of this size in a vacuum tube which is only a few km long is Fabry-Perot (FP) cavities in the arms.

A FP cavity is formed by two parallel highly reflecting mirrors, the *input* mirror and *end* mirror, separated by a distance  $L$ , see [figure 2.5](#). Light entering this cavity will be reflected and transmitted by the cavity and power builds up inside due to the light being reflected back and forth inside the cavity. Consider a cavity of length  $L$  with lossless mirrors and a perfectly reflective end mirror ( $\rho_{\text{end}} = 1, \tau_{\text{end}} = 0$ ), then the reflection coefficient of light at frequency  $\omega_c$  is [\[13\]](#)

$$R = -\rho_{\text{in}} + \frac{\tau_{\text{in}}^2 e^{\frac{-i2\omega_c L}{c}}}{1 - \rho_{\text{in}} e^{\frac{-i2\omega_c L}{c}}}, \tag{2.22}$$

where  $\rho_{\text{in}}$  and  $\tau_{\text{in}}$  are the reflection and transmission coefficients for the input mirror. In our model no light is transmitted by the FP cavity because  $\tau_{\text{end}} = 0$ . This reflected light is the sum of the light reflected directly off the input mirror plus the light reflected inside the cavity  $n$  times and transmitted back through the input mirror. The cavity is said to be resonant when the length is a multiple of half carrier wavelengths,  $L = n\lambda_c/2$ , so that  $e^{\frac{i2\omega_c L}{c}} = 1$ . The storage time for a FP cavity is defined by

$$t_{\text{storage}} = \frac{L}{c} \frac{r_{\text{in}}}{1 - \rho_{\text{in}}}. \tag{2.23}$$

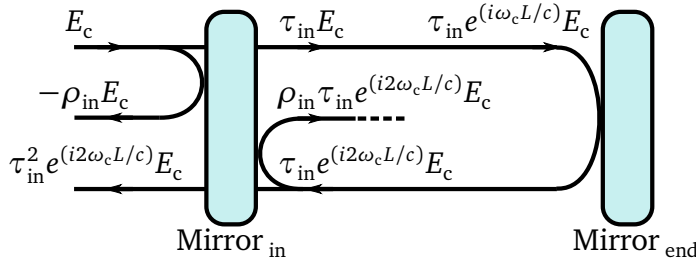


Figure 2.5: Schematic of a Fabry-Perot cavity, for clarity the spatially superposed beams are shown separated.  $E_c$  is the incoming laser incident on  $\text{Mirror}_{\text{in}}$  from the left. This light is partially reflected giving the beam with amplitude  $-\rho_{\text{in}} E_c$ . The transmitted beam propagates along the interferometer arm with amplitude  $\tau_{\text{in}} e^{(i\omega_c L/c)} E_c$  when it is incident on  $\text{Mirror}_{\text{end}}$ . This beam is reflected by  $\text{Mirror}_{\text{end}}$  and has amplitude  $\tau_{\text{in}} e^{(i2\omega_c L/c)} E_c$  when it is incident on  $\text{Mirror}_{\text{in}}$ . This beam is then partially transmitted giving the beam with amplitude  $\tau_{\text{in}}^2 e^{(i2\omega_c L/c)} E_c$ . The remainder of the light is reflected giving the beam with amplitude  $\rho_{\text{in}} \tau_{\text{in}} e^{(i2\omega_c L/c)} E_c$ . This continues, and subsequent beams reflected by the cavity have extra factors of  $\rho_{\text{in}} e^{(i2\omega_c L/c)}$ . Here we have assumed that  $\rho_{\text{end}} = 1, \tau_{\text{end}} = 0$ . We choose to define  $\rho_{\text{in}}$  so that external reflections acquire the negative term [13].

For a FP cavity to work in practice we need a control scheme to hold the system at resonance. The Pound-Drever-Hall (PDH) technique [88] was originally invented for stabilising the frequency of a laser by locking it to a cavity, however the technique is often used the other way around to lock a cavity to a laser. Doing this allows very precise measurement of length changes of the cavity [89].

The optical and control layout shown in figure 2.6 is used to lock the cavity to the laser. Laser light is sent into the cavity through the input mirror. The light reflected by the cavity is sent to a photo detector which sends a signal to the actuator attached to the end mirror which controls the cavity length. If operating correctly this system will hold the cavity in resonance for the laser light. However, the operation technique described above would not be able to distinguish between the cavity getting longer or shorter, therefore the system would not know whether to push or pull with the actuator to move the cavity length back towards resonance. This is because the photo detector only detects changes in the reflected beam power, which changes in the same way on either side of the resonance.

To solve this problem the laser light is phase modulated with a modulation signal from a local oscillator before it enters the cavity, and the photo detector signal is demodulated with the local oscillator modulation signal. Consider modulating the laser frequency, then above the resonant frequency increasing the frequency will increase the reflected power. Below the resonant frequency increasing the frequency will decrease the reflected power. This allows the control system to determine which side of the resonance the cavity is on. In figure 2.6 the demodulation occurs at the mixer, which outputs an *error signal* which has a different sign of each side of the resonance and is zero when the cavity is



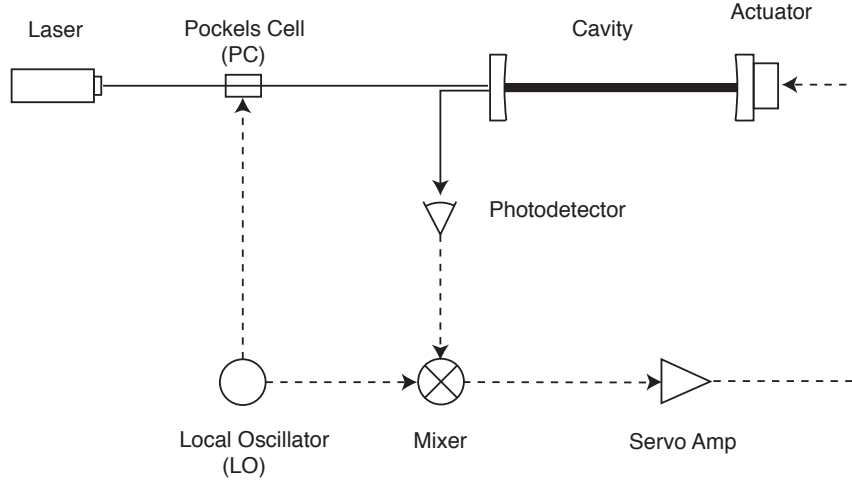


Figure 2.6: Basic layout of the control system for cavity length using the PDH technique [89]. Solid lines show optical paths while dashed lines show signal paths.

resonant. Finally the error signal may need amplification or a phase change so a servo is used to modify the error signal before it is sent to the actuator.

The phase change of light in a FP cavity, in the long-wavelength limit, in the vicinity of resonance is [10]

$$\Delta\phi = \frac{2\sqrt{\rho_{\text{in}}}}{1 - \rho_{\text{in}}} \frac{4\pi L f_c}{c} h_+(0). \quad (2.24)$$

This is the same phase change a Michelson interferometer with arms of length  $\frac{2\sqrt{\rho_{\text{in}}}}{1 - \rho_{\text{in}}} L$  would experience, and so this does not effect the working principle of our simple Michelson interferometer.

## 2.3 Limiting Noise Sources

Expected GW strains from astrophysical sources are very small,  $\leq 10^{-22}$ , so we need to be able to understand the noise sources that limit the sensitivity of GW detectors at these scales.

From figure 2.7 we can see that the sensitivity of the initial LIGO detectors were limited by shot noise (quantum-uncertainty in number of photons, see section 2.3.1) above  $\sim 200$  Hz. The mid frequency sensitivity is limited by thermal noise from the test masses and suspensions (see section 2.3.2), while the low frequency sensitivity is limited by seismic noise (see section 2.3.3). Here we will consider the GEO 600 detector which has a higher frequency sensitivity band than the LIGO detectors and is instead shot noise limited over  $\sim 500$  Hz and is limited by seismic noise at mid and low frequencies. Here a brief overview of each of these noise sources is presented; this section draws heavily from the treatment of interferometer noise sources in [13].

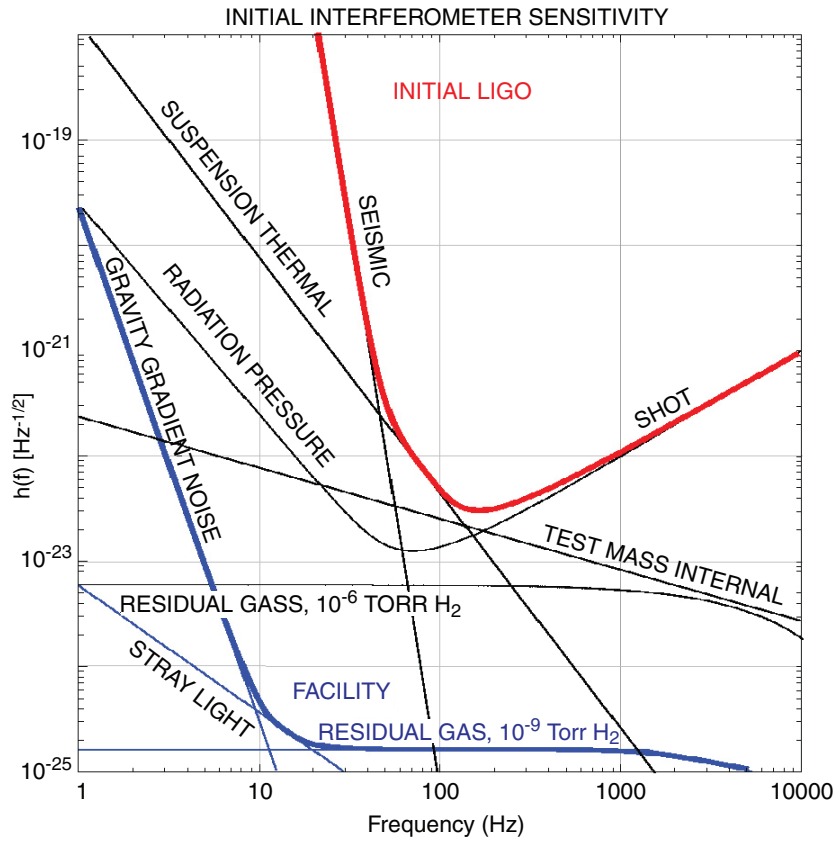


Figure 2.7: Noise spectral density of initial LIGO showing the limiting noise sources. The dominant noise sources for LIGO are seismic ( $\lesssim 60$  Hz), suspension and test mass thermal (60 Hz–200 Hz), and shot noise ( $> 200$  Hz). [12].

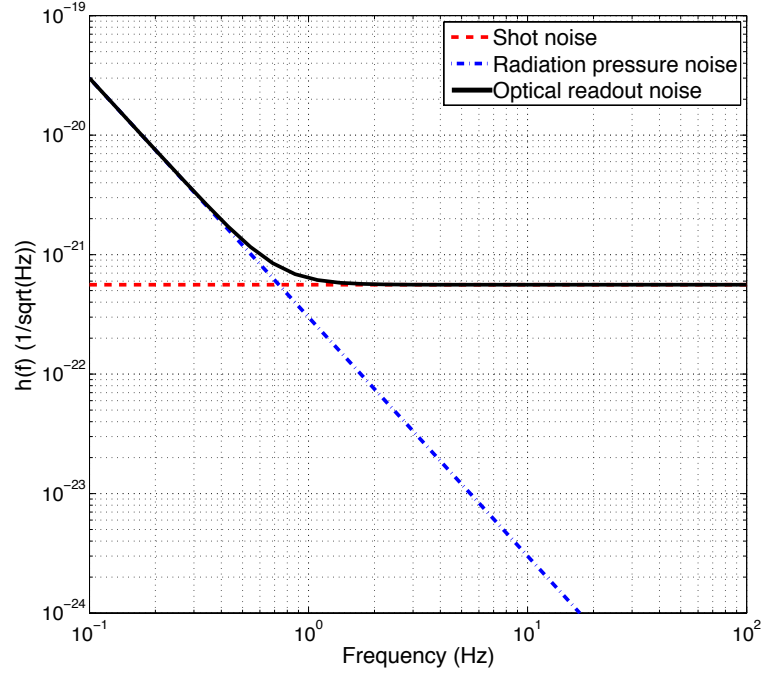


Figure 2.8: Optical readout noise for GEO 600 using the results from [equation \(2.28\)](#) and [equation \(2.33\)](#). As the laser power is increased the shot noise will decrease and the radiation pressure noise will increase.

### 2.3.1 Optical readout noise

#### Photon Shot Noise

Light can be modelled as finite photon packets, so measuring the optical power at the output port is equivalent to counting the number of photons that arrive during the measurement [\[90\]](#). A fluctuation in the rate of arrival of photons at the output port is indistinguishable from a change in the phase of the interferometer arms caused by a GW. When counting a series of discrete independent events with a mean number  $\bar{N}$  per counting interval, we find a Poisson distribution from repeated measurements,

$$p(N) = \frac{\bar{N}^N e^{-\bar{N}}}{N!}. \quad (2.25)$$

When  $\bar{N} \gg 1$ , the Poisson distribution can be approximated by a Gaussian distribution with a standard deviation  $\sigma = \sqrt{\bar{N}}$ . If there is a power  $P_{out}$  at the output port of an interferometer then the photon flux at the output will be

$$\bar{n} = \frac{\lambda_c}{2\pi\hbar c} P_{out}, \quad (2.26)$$

where  $\lambda_{laser}$  is the wavelength of the laser. Following the derivation in [\[13\]](#) we find that statistical power fluctuations produce the same effect as a GW on the

output signal. The resulting effective photon shot noise is given by

$$h_{\text{shot}}(f) = \frac{1}{L_{\text{opt}}} \sqrt{\frac{\hbar c \lambda_c}{2\pi P_{\text{in}}}}, \quad (2.27)$$

where  $L_{\text{opt}}$  is the optical arm length,  $\hbar$  is the Planck constant, and  $P_{\text{in}}$  is the laser power into the interferometer. From this we can see that the photon shot noise can be reduced by increasing the input laser power or by increasing the light storage time by increasing  $L_{\text{opt}}$ .

For GEO 600 using  $L_{\text{opt}} = 2400$  m and an effective  $P_{\text{in}} = 3$  kW using power recycling (see [section 2.5.4](#)) at 1064 nm, we find a shot noise of

$$h_{\text{shot}}(f) = 5.6 \times 10^{-22} \text{ Hz}^{-1/2}, \quad (2.28)$$

as shown in [figure 2.8](#). This white noise is the limiting noise source for interferometers at high frequency, for GEO 600 above  $\sim 500$  Hz. It is worth mentioning here that the shot noise in the detector noise spectral density, as shown in [figure 2.7](#), has a  $\sqrt{S} \propto f$  dependence. This is because the response of interferometers to GWs at high frequencies falls off as  $\partial \phi \propto \frac{1}{\omega_{\text{GW}}}$  ([equation \(2.10\)](#)) and by convention plots such as [figure 2.7](#) are in terms of effective GW amplitude.

### Radiation Pressure Noise

Photons reflected by a surface will transfer momentum to the surface. This happens in an interferometer when photons are reflected by the mirrors in the arms. If there is an uncorrelated fluctuation in the number of photons in the two arms of the interferometer this can cause a differential motion of the mirrors [91]. The force exerted on a mirror from a normally reflecting electromagnetic wave of power  $P$  is given by

$$F_{\text{rp}} = \frac{P}{c}. \quad (2.29)$$

The fluctuations of this force due to the quantised nature of light give a frequency independent fluctuation in this force of

$$F_{\text{rp}}(f) = \sqrt{\frac{2\pi\hbar P_{\text{in}}}{c\lambda_c}}. \quad (2.30)$$

This affects each of the masses that the light interacts with in the arms. For the simplest Michelson interferometer, when assuming that the beam splitter is massive enough to be treated as stationary, the radiation pressure noise in each of the arms from a power  $P_{\text{in}}/2$  will cause the length of the arms to change as

$$\partial L(f) = \frac{1}{m(2\pi f)^2} F(f) = \frac{1}{mf^2} \sqrt{\frac{\hbar P_{\text{in}}}{8\pi^3 c \lambda_c}}, \quad (2.31)$$

where  $m$  is the mass of the end test masses. From the full quantum mechanical treatment of radiation pressure noise [91], power fluctuations will be anti-correlated in the two arms of the interferometer which doubles the effect of this

noise at the output, producing the radiation pressure noise

$$h_{\text{rp}}(f) = \frac{1}{mf^2 L_{\text{opt}}} \sqrt{\frac{\hbar P_{\text{in}}}{2\pi^3 c \lambda_c}}. \quad (2.32)$$

For GEO 600 which has  $L_{\text{opt}} = 2400$  m and an effective  $P_{\text{in}} = 3$  kW with power recycling (see [section 2.5.4](#)) at 1064 nm, and end test masses with  $m = 5.6$  kg [\[92\]](#), we find a radiation pressure noise

$$h_{\text{rp}}(f) = 3.0 \times 10^{-26} \text{ Hz}^{-1/2} \left( \frac{100 \text{ Hz}}{f} \right)^2, \quad (2.33)$$

as shown in [figure 2.8](#).

### Standard Quantum Limit

Shot noise scales inversely with laser power, while radiation pressure noise scale with laser power. At low frequencies the radiation pressure noise is the dominant optical readout noise source and at higher frequencies shot noise will be the dominant optical readout noise source. We could improve the shot noise limited sensitivity at higher frequencies by increasing the laser power, but this would increase the radiation pressure noise so a balance of the two noise sources must be found [\[13\]](#). The total optical readout noise is the quadrature sum of [equation \(2.27\)](#) and [equation \(2.32\)](#):

$$h_{\text{optical readout noise}} = \sqrt{h_{\text{shot}}^2(f) + h_{\text{rp}}^2(f)}. \quad (2.34)$$

For a given frequency there is an optimum circulating laser power  $P_{\text{opt}}$  which will minimise the optical readout noise, this is found by equating [equation \(2.27\)](#) and [equation \(2.32\)](#), and is given by

$$P_{\text{opt}} = \pi c \lambda_c m f^2. \quad (2.35)$$

If we substitute this power into [equation \(2.34\)](#) then we find the lowest possible optical readout noise known as the “standard quantum limit” (SQL),

$$h_{\text{SQL}} = \frac{1}{\pi f L} \sqrt{\frac{\hbar}{m}}. \quad (2.36)$$

For GEO 600  $m = 5.6$  kg [\[92\]](#),  $\lambda_c = 1064$  nm, and optimising for sensitivity at  $f = 1$  kHz we find  $P_{\text{opt}} \approx 15$  MW. As we will see in [section 2.5.2](#), even after the GEO high frequency (GEO-HF) upgrades the maximum circulating power in GEO 600 will be  $\sim 30$  kW so GEO 600 will have a shot noise larger than the optimum level. This motivates other solutions to reduce the shot noise besides increasing the laser power, one of which, squeezing, will be discussed in [section 2.5.8](#).

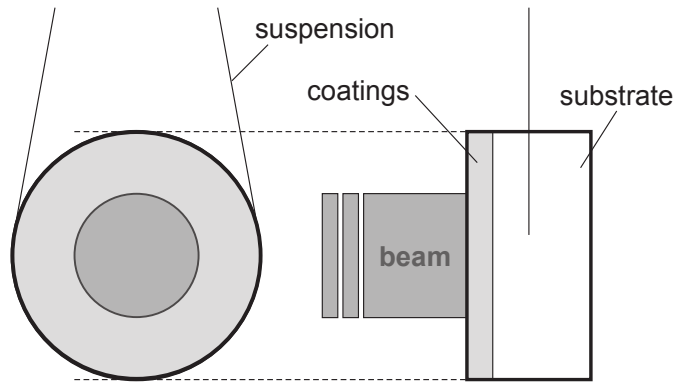


Figure 2.9: Elements of a mirror that cause thermal noise, suspensions, coatings, and substrate. The dominant thermal noise source is the coating thermal noise. Modified from [96].

### 2.3.2 Thermal Noise

The limiting noise source for LIGO at mid frequencies around a few hundred Hz is thermal noise, this is not currently a limiting noise source for GEO 600. However it is important to consider as the shot noise will be reduced during the GEO-HF program, and then the thermal noise could begin to make a significant contribution to the detector noise spectrum.

Thermal noise was first discovered by the microscopist Robert Brown in 1828 [93]. He observed the motion of small dust grains and pollen suspended in water, and attributed this motion to the action of a universal “vital force”. Einstein explained the true cause of Brownian motion as fluctuations in the rate of impact of individual water molecules on a dust grain [94]. Due to the motion of particles at non-zero temperatures, the particles of the optics and suspension in an interferometer will always move randomly at the atomic level [95]. This will limit the accuracy to which we can determine the positions of the optics as the surface of the optics and the optics centre of mass will be moving due to thermal oscillations of the coatings and suspensions.

The thermal noise of the optics is limited by the coatings that are used on the reflective surfaces, see figure 2.9. Following the derivation from [97] for GEO 600 we find a spectral density noise due to random thermal fluctuations in the coatings of the mirrors of

$$h_{\text{BR}}(f) \simeq 9.5 \times 10^{-23} \text{ Hz}^{-1/2} \left( \frac{100 \text{ Hz}}{f} \right)^{1/2}, \quad (2.37)$$

which can be seen in figure 2.20. To improve the sensitivity that is limited by this noise new coating materials and coating methods are being developed [98].

The thermal noise of the suspensions (see figure 2.9) is loudest around the vibrational resonant frequency and its harmonics [99, 100], therefore suspensions are designed to position these resonant frequencies away from the detection band of the detector as much as possible, or to cluster these together to limit

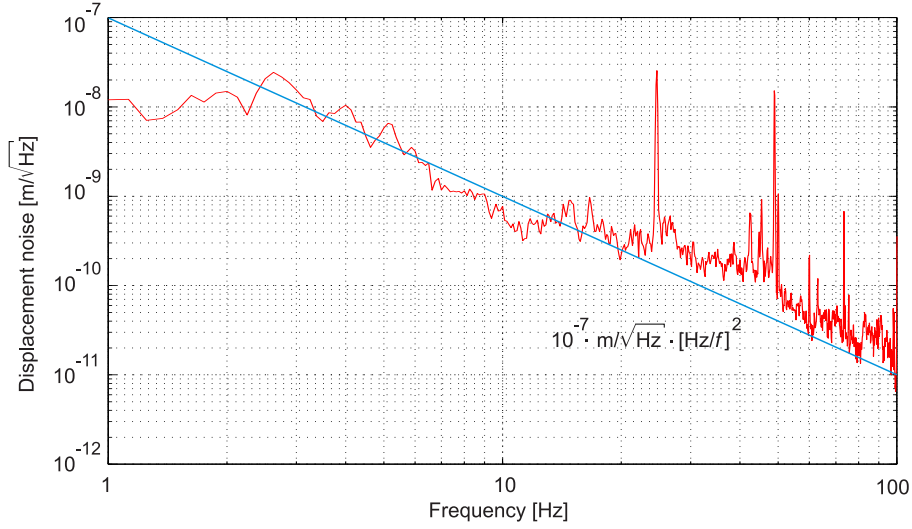


Figure 2.10: Seismic noise at the GEO 600 site. Measurement of horizontal motion measured on the detector foundation in the central building. The motion roughly fits the model  $10^{-7} \text{ m}/\sqrt{\text{Hz}} \left(\frac{1 \text{ Hz}}{f}\right)^2$  [92].

the noise to a small frequency band. This is exactly what has been done for the resonant (“violin”) modes of the main optics suspensions at each of the detectors. The large amplitude violin modes produce noise at specific frequencies, however the suspensions were designed to cluster these together into a small frequency band. For GEO 600 this is around 700 Hz, see figure 2.11.

During transmission of the beam splitter light power is absorbed by the BS ( $\sim 16 \text{ ppm}$  [101]) which causes a number of different types of thermal noise. The dominant noise source from the BS in the sensitive band for ground-based GW detectors is transmissive substrate thermorefractive noise, see figure 2.9. Temperature fluctuations in the BS substrate from the absorption of the transmitted laser power causes changes in the refractive index of the BS substrate, and this causes the optical path length for the transmitted light to change. The noise spectral density of the thermorefractive noise at GEO 600 due to the BS is [102]

$$h_{\text{TR}}(f) \simeq 6.5 \times 10^{-23} \text{ Hz}^{-1/2} \left( \frac{100 \text{ Hz}}{f} \right), \quad (2.38)$$

which can be seen in figure 2.20.

### 2.3.3 Seismic Noise

At low and mid frequencies, up to a few hundred Hz, GEO 600 is limited by mechanical motion of the main detectors optics, which is caused by seismic noise at frequencies below 50 Hz. At the GEO 600 site above 3 Hz an ambient seismic noise of  $10^{-7} \text{ m}/\sqrt{\text{Hz}} \left(\frac{1 \text{ Hz}}{f}\right)^2$  has been measured in both the vertical and horizontal directions, see figure 2.10 [103, 92].

The simplest way to reduce the effect of seismic noise on a GW detector is to build the detector in a seismically quiet location [104, 105]. In densely popu-

lated areas the dominant source of seismic noise is anthropogenic noise (human activity), for this reason GW detectors are often build at isolated locations to reduce this effect. The location for future generation detector will be chosen carefully to minimise ambient seismic noise.

To reduce the seismic noise below that of the ground the detector is build on, passive and active isolation systems are used in the suspension systems for the main optics. For the main interferometer optics GEO 600 uses vibration isolation stacks which are made of alternating layers of soft rubber springs and stainless steel masses. On top of these stacks are triple layer pendulum suspensions. Pendula are good mechanical filters for frequencies above their resonant frequency, giving a  $f^{-2}$  attenuation for frequencies above the resonance. This passive seismic isolation system gives a  $f^{-8}$  attenuation from 30 Hz to 50 Hz [106].

To improve beyond the performance of passive isolation systems, one must employ active isolation systems. An example of active isolation is seismic feed forward, where an array of seismometers is used to measure the motion of the ground or suspension system due to seismic noise. This information is then fed-forward to actuators in the suspension system which can in principle subtract the effect of the seismic noise. Active isolation will be used in advanced LIGO [107].

There are no planned improvements for the seismic isolation system for GEO 600 while effort is focused on the high frequency sensitivity above  $\sim 500$  Hz during the GEO-HF upgrade scheme; see [section 2.5.9](#).

## 2.4 Gravitational Wave Interferometer Network

The concept of using an interferometer as a GW detector didn't come until the 1960's and was pushed for by Drever et al. [10]. In the early 1980's three prototype GW interferometers were constructed in Glasgow, in Garching near Munich, and at MIT [108]. There is now a worldwide network of ground-based GW laser interferometers which are sensitive to GWs in the frequency range between a few tens of Hz to a few thousand Hz. In the USA there are two interferometer sites, one in Hanford, Washington, and the other in Livingston, Louisiana, which are collectively referred to as the LIGO detectors [109]. The Hanford site has two co-aligned detectors referred to as H1 and H2, with 4 km and 2 km long arms respectively, and the Livingston site has one detector referred to as L1 which has 4 km long arms. Near Pisa, Italy, is the French-Italian detector Virgo which is referred to as V1 and has 3 km long arms [110, 111, 112]. The LIGO and Virgo detectors are all power recycled interferometers (see [section 2.5.4](#)) with Fabry-Perot cavities (see [section 2.2.2](#)) in the arms. Just south of Hanover, Germany, is the British-German detector GEO 600, which is referred to as G1, this detector has 1200 m long arms in 600 m long vacuum tubes [113]. The GEO 600 detector is a dual recycled interferometer (see [section 2.5.4](#) and [section 2.5.5](#)) with single fold delay lines in the arms. More information about GEO 600 is given in [section 2.5](#). The TAMA 300 detector is about 20 km from the centre of Tokyo



and has 300 m long arms [114, 115]. This is a prototype detector which began taking data in 1999, but is not currently operating as an observing instrument.

At the time of writing the LIGO and Virgo detectors are being upgraded from their enhanced configurations to advanced LIGO [116, 117, 118, 119] and advanced Virgo [120, 121, 122]. The upgrade program takes these detectors out of commission from 2011 until 2015 when the detectors will begin to come back online [123]. The advanced detectors have design sensitivities that will give a factor of  $\sim 10$  improvement in BNS range compared to the initial detectors [116, 120]. While these detectors are out of commission they are no longer able to perform astrophysical observations due to severe hardware and infrastructure upgrades and commissioning. The GEO 600 detector has also begun a program of upgrades referred to as GEO-HF [124]. This program, unlike that for LIGO and Virgo, does not require GEO 600 to go off line for extended periods of time. More details on the GEO-HF program will be given in [section 2.5.9](#). Because of this, during the period of upgrades to the LIGO and Virgo detectors between 2011–2015, GEO 600 will be the only operating large scale GW laser interferometer performing astrophysical observations.

Other detectors are already being planned for the future using advanced interferometric techniques and building on the experiences gained from the first generation of detectors. There is the possibility of moving optics from the H2 advanced LIGO detector to India where they could be used to build another 4 km LIGO style detector [104]. All of the previously mentioned detectors are on Earth’s surface, which imposes a limit to the low frequency sensitivity due to seismic noise. In Japan construction has begun for KAGRA [125], which will have 3 km long arms and is being built underground to reduce the effects of seismic noise. It will also use cryogenics to cool down the main optics to reduce thermal noise effects. This detector will also use resonant side-band extraction (RSE) which will be explained in [section 2.5.5](#). Another solution to the problem of seismic noise is to construct a GW interferometer in space; one proposal is the evolved laser interferometer space antenna (eLISA) [126]. Without the limit of seismic noise at low frequencies eLISA will be able to observe GWs at lower frequencies than the ground based detectors. There has also been a conceptual design study for a third generation ground based detector, the Einstein telescope [105]. This detector will use advanced interferometric techniques and combine multiple interferometers with sensitivity optimised to a particular frequency range into a single detector; this method is referred to as the “xylophone” technique.

## 2.5 The GEO 600 detector

In this section details will be given about the GEO 600 detector and its sub-systems. These details will be useful for understanding the investigations performed in [section 3.5](#).

GEO 600 is a British-German GW interferometer located near Ruthe, south of Hannover, Germany [127, 128, 129]. The arms of GEO 600 are contained inside

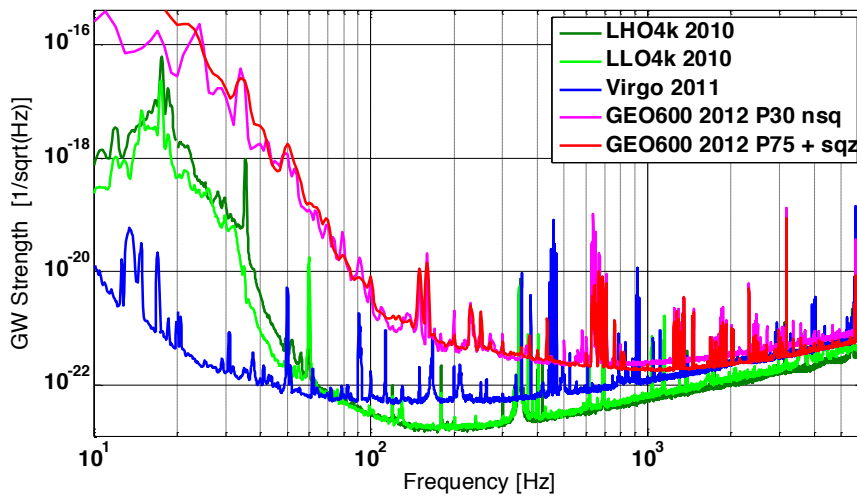


Figure 2.11: Strain sensitivity of GEO 600 in comparison with LIGO and Virgo best sensitivities from S6. The two lines for GEO 600 show the improvement on the shot noise limited sensitivity due to increasing the input laser power and the use of squeezed light.

of 600 m vacuum tubes and use a four-beam delay line. This means that the arms have physical length 1200 m from the BS to the end mirrors which are located in the central building, while the end stations of the vacuum tubes contain the folding mirrors. The full optical layout of GEO 600 can be seen in [Appendix A](#). Construction started in 1995 and since 2001 GEO 600 has been operational and taking part in a number of science runs with the LIGO and Virgo interferometers [130]. Between these science runs GEO 600 also operates in “Astrowatch” mode, taking observational data on weekends and evenings, while commissioning work is performed during the working week. In 2004 the detector reached its design sensitivity [113], after which further work is being continued to remove the remaining noise sources.

GEO 600 uses a number of advanced interferometric techniques and technologies to achieve sensitivity comparable to the LIGO and Virgo detectors. Unlike the LIGO and Virgo detectors, which undergo large upgrade programs during long periods of downtime between science runs, the GEO collaboration has decided to implement a number of sequential upgrades during short periods of down time, of order a few days to a few weeks, while the detector is commissioned to be kept at optimal sensitivity due to the limited infrastructure of GEO 600. The GEO-HF upgrade program aims to increase the sensitivity of GEO 600 above  $\sim 500$  Hz which is limited by shot noise [131, 132, 124].

This is being done by the implementation of a number of advanced interferometric techniques which are listed in [section 2.5.9](#). We will give a brief summary of some of the key elements and sub-systems of GEO 600 and details on the upgrades that have been performed or are planned in the GEO-HF program. For a more in depth explanation of the GEO 600 detector see [133].

### 2.5.1 Laser source

The laser source used at GEO 600 is a Nd:YAG (Neodymium- doped Yttrium-Aluminum-Garnet) laser, which produces light with wavelength 1064 nm. All of the current generation of ground-based GW detectors use this type of laser as they are well tested and stable, and because of the availability of high quality optics for light at this wavelength.

As part of the GEO-HF program the original GEO 600 laser system which was only capable of producing up to 15 W [134] was replaced with a new system, the same type used in the enhanced LIGO (eLIGO) detectors, which can produce up to 35 W [135].

### 2.5.2 Input mode cleaners

The input mode cleaner (IMC) for GEO 600 is a pair of triangular ring cavities which the light travels through in sequence. This improves the frequency stabilisation of the light from the laser before the light enters the main interferometer. These cavities are designed to only be resonant for the  $TEM_{00}$  spatial mode of the laser, this means that higher order modes are suppressed by the IMC.

With the new laser system for the GEO-HF program the light resonating inside of the IMC cavities builds up sufficient energy that the radiation pressure noise becomes too loud for the cavities length control system to keep the cavities locked and resonant. To stop this the IMC coupling mirrors were replaced in August 2013 with lower reflectivity mirrors. This reduced the finesse of the IMCs, and therefore reduced the circulating laser power and radiation pressure noise inside of the cavities, enabling stable locking of the cavities for larger input laser powers.

The combined changes to the laser system and input mode cleaners aim to increase the circulating laser power inside the main interferometer from  $\sim 3$  kW to  $\sim 30$  kW. With this increase in circulating laser power GEO 600 requires a thermal compensation system to correct for thermal distortions of the optics that are heated by absorbing laser light. Unlike the LIGO and Virgo detectors which have Fabry-Perot cavities in the arms, all the circulating laser power in the arms of GEO 600 passes through the BS. This causes thermal lensing effects which limit the maximum power that can be used as the detector will become unstable [136].

### 2.5.3 Main optics suspensions

To suppress seismic noise GEO 600 uses a triple pendulum isolation system with fused silica suspensions and 5.6 kg test masses. This suspension system provides a  $f^{-8}$  attenuation above the resonant frequency of the pendulum, from 30 Hz to 50 Hz. A similar system has been implemented at Virgo [137] and will be implemented for the advanced LIGO detectors [138].

Figure 2.12 shows the GEO 600 seismic isolation that incorporates a three-stage pendulum for the main interferometer test masses and beam splitter [106]. The upper level is controlled using shadow sensors and actuated with magnetic

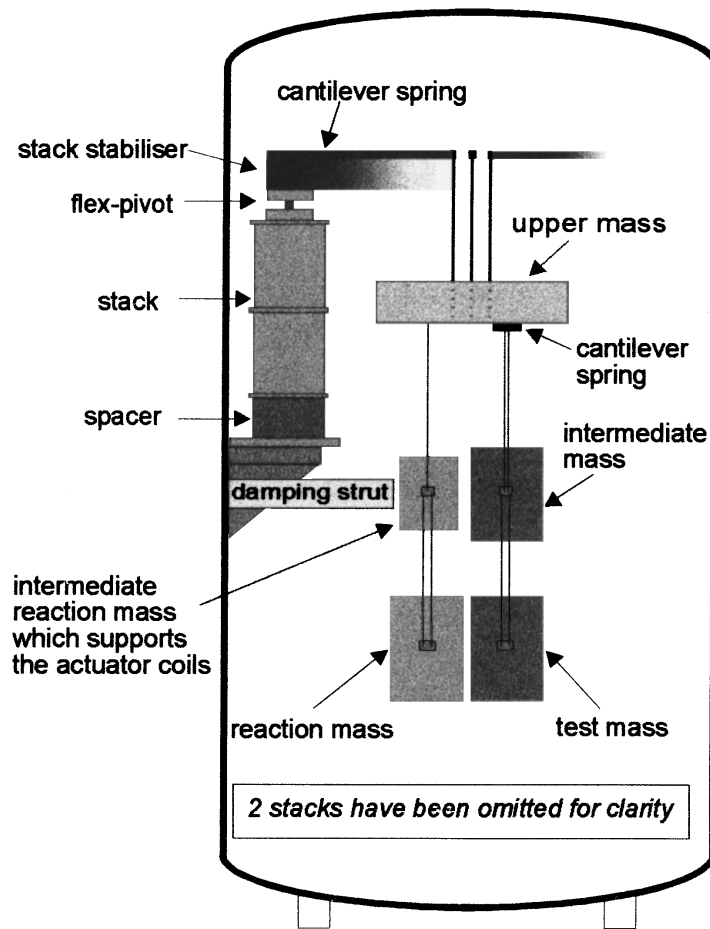


Figure 2.12: Schematic of the main optic suspension for GEO 600. The triple pendulum isolation system is comprised of the upper mass, intermediate mass, and test mass. Here we also show the reaction mass, which is used for actuation on the test mass [106].

coils. There are then two chains of masses attached to the upper level, one ends in a test mass, which is one of the main optical components in GEO 600 such as the BS or one of the end test masses; the other ends in a “reaction mass”, this chain is used to actuate on the lower levels of masses from a damped platform. This is done, because if the actuators are not sufficiently isolated from seismic noise then they will introduce noise back into the system, by-passing the seismic isolation. The intermediate mass is actuated on with magnetic actuators attached to the intermediate reaction mass, while the test mass is actuated on with electrostatic actuators from the reaction mass. This sequential actuation gives both a broad range of actuating force and also delicate control of the main optical components.

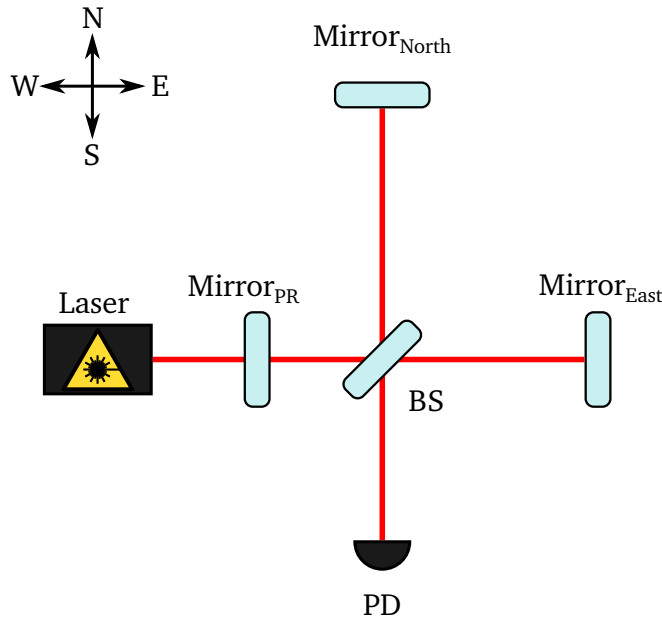


Figure 2.13: Schematic of a laser interferometer with PR cavity. The power recycling mirror (MPR) is added to the interferometer between the laser source and the BS at the input port of the detector.

### 2.5.4 Power Recycling

The sensitivity of a shot noise limited GW interferometer, such as all of the ground based detectors, can in theory be simplified to the dependence on two things: the amount of energy stored in the arms and the storage time of the GW induced signal sidebands [139]. Power recycling (PR) addresses the first limit to interferometer sensitivity by increasing the energy stored in the interferometer arms.

As was explained in section 2.3.1 shot noise is caused by the quantised nature of light in photon packets, which arrive at random intervals causing fluctuations in the light intensity. As a random process the shot-noise limited sensitivity is proportional to the square root of the number of photons and so the light power stored in the interferometer arms [13]. Therefore increasing the stored light power in the interferometer arms will reduce the shot noise.

The advanced interferometer technique of PR was first proposed by Drever. PR is used in all current ground-based GW detectors to increase the light power stored in the interferometer arms [140]. As explained in section 2.2, when an interferometer is operating at or near to the dark fringe, light which enters the detector through the input port is reflected by the interferometer back towards the input port; i.e, the Michelson interferometer appears as a highly reflective mirror. By adding an additional mirror called the PR mirror  $M_{PR}$  between the laser and the beam splitter, see figure 2.13, this forms a Fabry-Perot cavity with the Michelson interferometer which is referred to as the PR cavity. This cavity must be kept resonant with the laser light, so that the stored energy is resonantly increased [89], details on the length control system can be found here [133]. The PR mirror in GEO 600 has a transmissivity of  $\tau_{MPR} = 0.1\%$ , which will give a

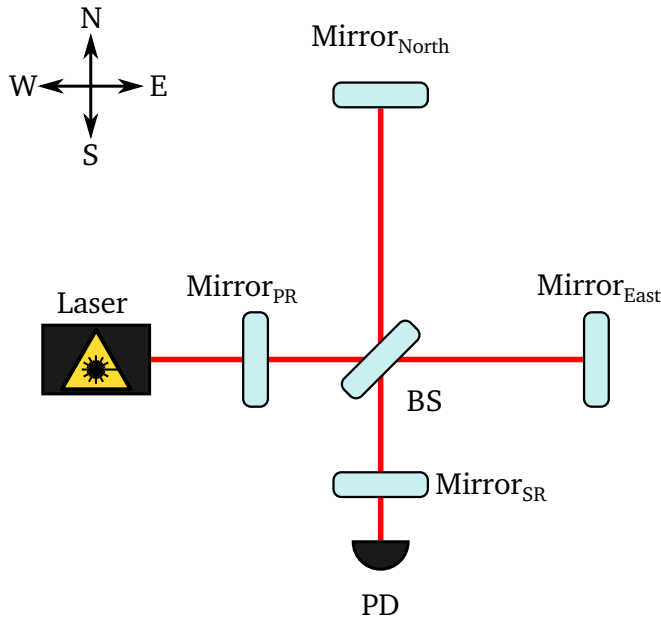


Figure 2.14: Schematic of a laser interferometer with dual recycling. The signal recycling mirror (MSR) is added to the interferometer between the BS and the PD at the output port of the detector.

power enhancement of up to a factor of  $P_{\text{cavity}}/P_{\text{in}} = 1000$ , depending on losses inside the cavity.

### 2.5.5 Signal Recycling

Signal recycling (SR) addresses the second limit to interferometer sensitivity, by increasing the storage time of the GW induced signal sidebands.

The effect of a GW on an interferometer can be described as a modulation of the light in the arms. This has the effect of producing signal sidebands as explained in [section 2.2](#). As a GW passes an interferometer, the interaction time of the GW with the photons in the arms is given by the round trip light travel time  $2L_{\text{opt}}/c$ . As we showed with [equation \(2.11\)](#), the optimal light storage time in the arms of the interferometer is half the period of the GW. This will allow the GW to have a maximum effect and produce the largest signal. For a GW in the sensitive frequency band of ground-based detectors at 1000 Hz, the required storage time is 0.0005 s which would require an interferometer with 75 km long arms. For a ground based interferometer arms this long would be too expensive and impractical to build. Therefore alternative methods are used to extend the laser storage time in the interferometer arms by effectively increasing the arm length while keeping the physical arm lengths at the km scale.

One solution to this problem is the use of an additional mirror at the output port of the detector between the BS and the PD, the so called MSR, which forms a FP cavity with the Michelson interferometer which is referred to as the SR cavity. If used in conjunction with PR like at GEO 600, this configuration is referred to as a dual recycled interferometer. The optical layout for dual recycling can be seen in [figure 2.14](#). GEO 600 is the first km scale GW interferometer to implement SR,

but this technique is being adopted by both the advanced LIGO and advanced Virgo detectors.

SR is used to resonantly enhance GW signals inside the interferometer arms by sending the signal sidebands back into the interferometer arms a number of times, thus increasing the interaction time with GWs [141]. This has the same effect as increasing the physical size of the arms.

Depending on the microscopic position of the signal recycling mirror (MSR), the SR cavity can be “tuned” to maximise the sensitivity of the interferometer for a certain signal frequency. The peak of the sensitivity is at the resonant signal frequency for the SR cavity. By moving the microscopic position of the MSR, detuning the SR cavity, the shot noise limited sensitivity can be improved for certain GW signal frequencies. Tuned SR is obtained when the SR cavity is made resonant for the carrier frequency  $f_c$ , which gives maximum sensitivity at 0 Hz, the so-called “DC” offset. Detuned SR is obtained when the SR cavity is resonant for the signal sideband frequency  $f_c + f_{\text{GW}}$ .

Reduction of the MSR reflectivity widens the sensitive bandwidth of GEO 600 which improves the high frequency shot noise sensitivity at the expense of the mid frequency shot noise sensitivity. As GEO 600 is not limited by shot noise below a few hundred Hz this only affects the noise slightly at these frequencies. As part of the GEO-HF program the MSR was changed in October 2010 to decrease the reflectivity from 98% to 90%, the effect of this can be seen in figure 2.20.

Resonant side-band extraction (RSE) [142, 143] is the equivalent method to SR for interferometers with high finesse Fabry-Perot cavities in the arms. RSE is being implemented in both advanced LIGO and advanced Virgo.

### 2.5.6 Output mode cleaner

As part of the GEO-HF program an OMC was installed at GEO 600 in December 2009 [144]. This is a “bow tie” filter cavity which suppresses higher order spatial and temporal modes leaving the detector from the output port before it reaches the PD. By removing the higher order modes from the output beam the OMC reduces the detection noise and therefore improves the shot noise limited sensitivity.

To couple the output beam from the output port of the interferometer to the OMC a number of beam directional optics (BDOs) were installed. The position of the beam directional optic 1 (BDO1), beam directional optic 2 (BDO2), and beam directional optic 3 (BDO3) can be seen in figure 2.15, as well as the OMC.

### 2.5.7 Readout scheme

As was shown in section 2.2.1 GWs produce signal sidebands on the carrier light at  $f_{\text{sig}} = f_c \pm f_{\text{GW}}$ , where  $f_c$  is the carrier frequency of the input laser and  $f_{\text{GW}}$  for ground-based GW detectors is a few Hz to a few kHz, in the audio band. Therefore,  $f_{\text{sig}}$  will be at a few hundred THz where the PD can not directly detect the GW signal, unless using a local oscillator [146].



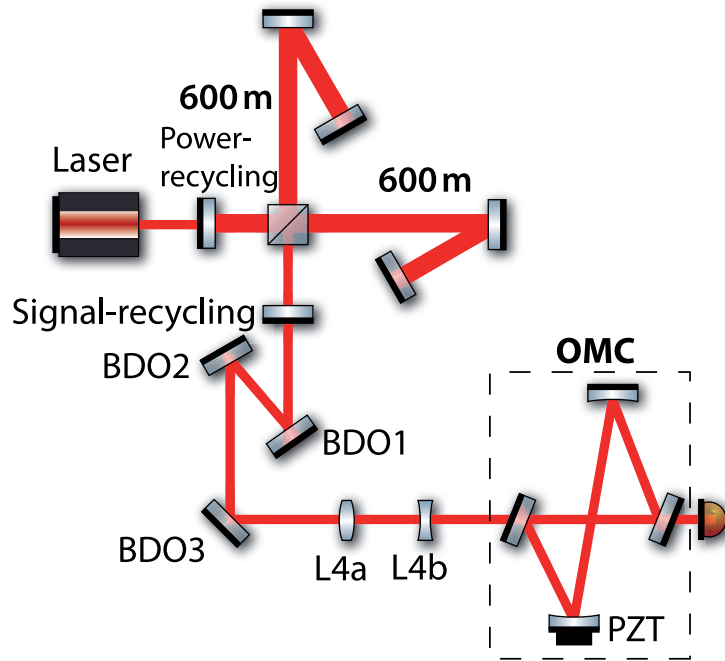


Figure 2.15: Schematic of the output optics of GEO 600. The output mode cleaner (OMC) is between the output port of the Michelson and the PD. It is a bow tie cavity which is used to remove higher order modes from the output beam, the cavity length is controlled to keep the cavity resonant with the carrier laser [144].

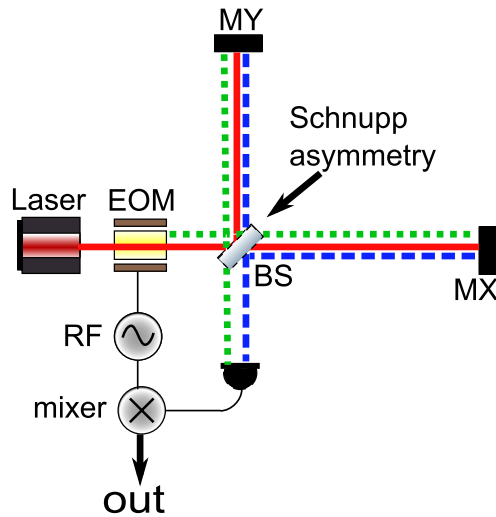


Figure 2.16: Michelson interferometer heterodyne readout scheme. Heterodyne readout was the readout scheme originally used at GEO 600. The carrier is shown in red, the modulation sidebands are shown in green (dotted), and the signal sidebands are shown in blue (dashed). The modulation signal is generated at RF, and applied to the carrier at the electro-optic modulator (EOM). The signal at the PD is then demodulated with the mixer. The Schnupp asymmetry is a small difference in the length of the interferometer arms, at GEO 600 this was 69 mm. Modified from [145].



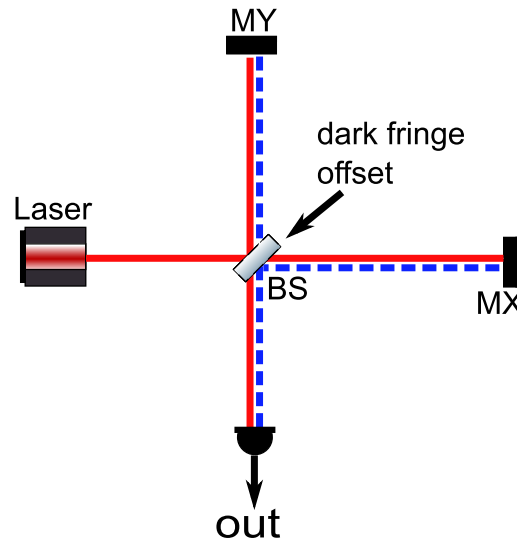


Figure 2.17: Michelson interferometer DC readout scheme. As part of the GEO-HF program direct current (DC) readout was implemented at GEO 600. The carrier is shown in red and the signal sidebands are shown in blue (dashed). Modified from [145].

GEO 600 was originally operated at the dark fringe, in which as was explained in section 2.2 the differential arm length is controlled to give destructive interference at the output port ( $\phi_0 = \pi$ ) in figure 2.17, so that carrier light is reflected back towards the input port and ideally no light is transmitted to the PD. At GEO 600 a heterodyne readout scheme [147] was originally used to observe differential arm motion, see figure 2.16. Radio frequency (RF) sidebands are modulated on the carrier light before it enters the interferometer (Schnupp modulation [87]), and a macroscopic difference in the length of the arms of 69 mm (the so called Schnupp asymmetry) allows the modulation sidebands to be transmitted by the interferometer to the PD where they can be used as a local oscillator for the GW signal. By demodulating the PD signal at the local oscillator frequency we can obtain a signal stream which will contain GW signals at  $f_{\text{GW}}$ . This scheme is essentially the same as the Pound-Drever-Hall (PDH) technique for measuring cavity length as described in section 2.2.2.

As part of the GEO-HF program, to allow for future upgrades such as the implementation of squeezed light (see section 2.5.8), the readout scheme for GEO 600 was changed to DC readout in September 2009 [148], see figure 2.17. A DC readout scheme [149] uses a small offset from the dark fringe ( $\phi = \pi + \eta$  where  $|\eta| \ll 1$ ), so that a small amount of the carrier lights exits the output port of the detector which is used as a local oscillator for the GW signal. This change was only possible due to improvements in the stability of laser power noise, which was the reason this readout scheme was not originally used in the ground-based detectors. A summary of the advantages and disadvantages of using DC readout over heterodyne readout is given in [145].

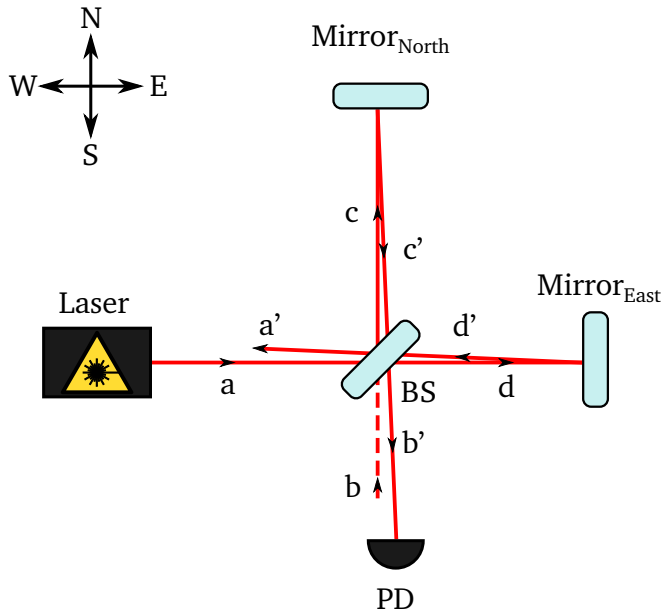


Figure 2.18: Schematic of Michelson interferometer with field amplitudes at different points along the light path.  $a$  is a strong input beam from the laser, and  $b$  is a vacuum or a squeezed light source. The amplitudes of the field in the arms after transmission, or reflection, of the beam splitter are given by  $c$  and  $d$ .  $c'$  and  $d'$  are the amplitudes of the fields just before they are recombined at the beam splitter to produce the output beams  $a'$  and  $b'$ .

### 2.5.8 Squeezing

GEO 600 is the first large scale interferometric detector to implement squeezing [90, 91] to improve the shot noise limited sensitivity [150, 151, 152], and the first detector using squeezing to be used in an astrophysical search [153] as shown in section 4.3. To understand how squeezing can be used to reduce the shot noise of an interferometer we follow closely the “visual” formalism of [154], which is a rederivation of the result originally proposed by Caves [155].

The standard shot noise limit (see section 2.3.1) corresponds to the limit of the smallest phase that we can measure

$$\delta\phi \geq 1/\sqrt{n}, \quad (2.39)$$

where  $n$  is the number of photons reaching the PD at the output port of an interferometer during our measurement time. To obtain this result, we consider the interferometer shown in figure 2.18, where the letters denote the field amplitudes at different point along the light path (quantum mechanically, the annihilation operators for the modes of the field at different points along the light path, in the propagation direction given).

The output signal that is used to detect GWs with a Michelson interferometer is simply the relative phase between  $c'$  and  $d'$ . These are related to  $c$  and  $d$  by a simple phase change as the light propagates through the arms. So the limit of how well defined the relative phase between  $c'$  and  $d'$  is, can be phrased as how well defined the phase between  $c$  and  $d$  was originally.

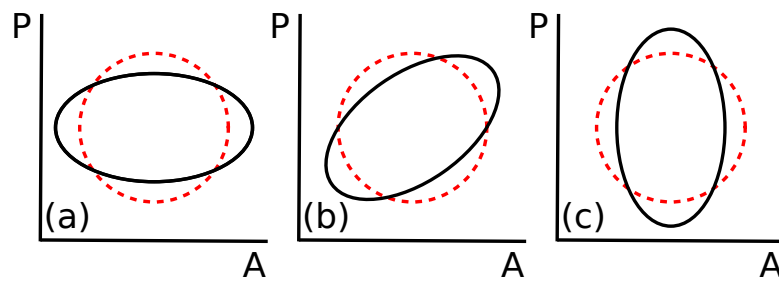


Figure 2.19: In the phase ( $P$ ) and amplitude ( $A$ ) space (the axes do not lie along lines of zero  $P$  and  $A$ ) of the light field inside an interferometer we show the error ellipses for quantum fluctuations of a coherent vacuum state in red compared to those of squeezed states in black. The three plots show different example directions in which quantum fluctuations can be suppressed by squeezing. A Michelson interferometer makes measurements in the phase quadrature of the light field so that we can represent the level of shot noise of the beam at the output of the interferometer schematically by the width of the ellipse in the  $P$  direction. In the region where the interferometer's sensitivity is limited by shot noise the best sensitivity improvement is then achieved by squeezing the ellipse in the  $P$  direction as shown in (a). (b) shows squeezing along a direction which gives the same shot noise as the coherent vacuum state, i.e. where there is no effect from the squeezing. (c) shows squeezing along the  $A$  direction which ends up increasing the shot noise level in the interferometer output and thus decreases its sensitivity to GWs.

Firstly we treat our interferometer classically and assume no field is coming from the direction of  $b$  in [figure 2.18](#). In this case  $c$  and  $d$  have been split from the same incident beam  $a$  at the beam splitter, and so classically all their fluctuations would be perfectly correlated. But this is not the case for a quantum-mechanical field. At the beam splitter, some amount of decorrelation between the phase fluctuations in  $c$  and  $d$  is introduced. The origin of this decorrelation can be understood by taking into account the beam  $b$  in [figure 2.18](#). Classically we assumed no field was entering the interferometer from this direction, but quantum mechanically this corresponds to a electromagnetic field in a vacuum state entering the interferometer from this direction. The beam splitter combines the two fields  $a$  and  $b$ , giving us the annihilation operators for modes  $c$  and  $d$ ,

$$c = (a + b)/\sqrt{2}, \quad (2.40a)$$

$$d = (a - b)/\sqrt{2}. \quad (2.40b)$$

From this we can see that fluctuations in the field  $a$  are correlated in  $c$  and  $d$  (they cancel when the two fields are subtracted), while fluctuations in  $b$  are anticorrelated in  $c$  and  $d$  (they add when the two fields are subtracted). So no combination of  $c$  and  $d$  can be made free from fluctuations. We can think of the fluctuations in the difference between  $c$  and  $d$  as being caused entirely by the fluctuations in  $b$ , which is roughly the case when operating at or near to the dark fringe. It is this difference between  $c$  and  $d$  (and the difference between  $c'$  and  $d'$ ) that is of interest when using an interferometer to search for GWs. Therefore if we add a light source entering the interferometer along the direction  $b$  which has less fluctuations than the vacuum state, the difference between  $c$  and  $d$  (and therefore between  $c'$  and  $d'$ ) is more sharply defined, effectively reducing the shot noise [\[90\]](#).

The fluctuations of a beam are separated in the two conjugate quadratures amplitude, and phase. We can picture the quantum state uncertainty of a beam by drawing an ellipse in a plane spanned by these two conjugate variables, see [figure 2.19](#). The minimum area of this ellipse is set by the uncertainty principle. Squeezed states of light are quantum states that have a reduced uncertainty in one of the field quadratures compared to a coherent state, and an increased uncertainty in the conjugate quadrature. A squeezed state of light is injected into the output port of the interferometer (see [figure A.1](#)) to replace the coherent vacuum state that would otherwise be entering this port. If the squeezing is oriented correctly in relation to the electric field inside the interferometer it will improve the shot noise limited sensitivity of the interferometer [\[90\]](#); see [figure 2.19](#). The orientation of the squeezing error ellipse with relation to the electric field inside the interferometer is controlled to optimise the improvement for the shot noise limited sensitivity as shown in [figure 2.19](#), this error point is recorded.

### 2.5.9 GEO-HF

As was explained in the previous sections, the GEO-HF incrementally improves the shot noise limited sensitivity of GEO 600. The main elements of the GEO-HF program are,

1. Tuned SR and moving to DC readout. (September 2009)
2. Installation and implementation of OMC. (October 2009)
3. Implementation of squeezed light. (April 2010)
4. Installation of new signal recycling mirror. (October 2010)
5. Input laser power increase. Operating with higher powers requires the input mode cleaner coupling mirrors to be replaced and the installation and implementation of a thermal compensation system. (On going work as of 2014)
6. Increase squeezer performance (On going work as of 2014)

The effect of these sequential upgrades can be seen in the modelled noise spectra shown in [figure 2.20](#).

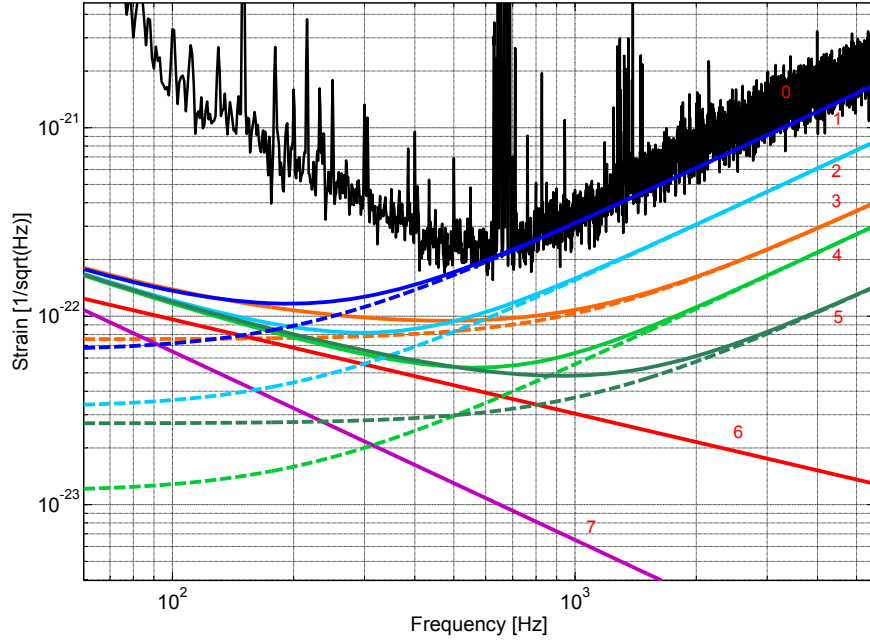


Figure 2.20: Sensitivity of GEO 600 for various stage through the GEO-HF upgrade scheme [132]. Here we only show the model shot and thermal noise components; low frequency sensitivity is limited by mechanical noise, such as seismic motion of the mirrors. Dashed lines represent shot noise models, while solid lines represent the combination of shot and thermal noise.

(0) Sensitivity of GEO 600 in 2009 before GEO-HF upgrades began,

(1) DC, tuned SR,  $\tau_{\text{SR}} = 2\%$ ,  $P_{\text{laser}} = 3.2 \text{ W}$ ,

(2) DC, tuned SR,  $\tau_{\text{SR}} = 2\%$ ,  $P_{\text{laser}} = 3.2 \text{ W}$ , 6 dB squeezing,

(3) DC, tuned SR,  $\tau_{\text{SR}} = 10\%$ ,  $P_{\text{laser}} = 3.2 \text{ W}$ , 6 dB squeezing,

(4) DC, tuned SR,  $\tau_{\text{SR}} = 2\%$ ,  $P_{\text{laser}} = 20 \text{ W}$ , 6 dB squeezing,

(5) DC, tuned SR,  $\tau_{\text{SR}} = 10\%$ ,  $P_{\text{laser}} = 20 \text{ W}$ , 6 dB squeezing,

(6) Coating thermal noise model,  $h_{\text{BR}}(f)$ ,

(7) Thermo-refractive noise of the beam splitter,  $h_{\text{TR}}(f)$ .

# Detector Characterisation

---

# 3

Detector characterisation is an important step in commissioning GW detectors and in maintaining optimal sensitivity.

The frequency-dependent sensitivity of a GW detector is limited by a stationary noise floor overlaid with non-stationary transient noise artefacts. These components limit the sensitivity to GWs signals in two ways: a high noise floor masks GWs in the data (reducing the signal-to-noise ratio (SNR) of signals), while transients can mimic GWs. These transients produce a substantial background of events that limit the confidence of GW identification; therefore, we require higher amplitude GWs for confident identification. The goal of detector characterisation is to identify the components of the noise floor and causes of non-stationary noise.

There are two standard methods to eliminate non-stationary transients: removing the physical cause of the noise, and removing the data contaminated by the noise, which is referred to as a “veto”. Vetoing is simply ignoring candidate GW events that lie in a time period or frequency band of data around a noise event. The level of the stationary noise floor can be reduced by commissioning to remove the physical causes of noise.

GW detectors are complicated instruments made up of many subsystems and control loops; our current understanding of the instrument behaviour is incomplete. Characterising the detector behaviour works to aid both analysis and commissioning groups. The GEO 600 detector characterisation (GEODC) group has focused mainly on aiding commissioning work, through clear and frequent communication with the commissioning team, which is assisted by having GEODC members on-site at the detector. The GEODC group investigate noise artefacts in order to understand and eliminate the physical causes. Information is fed back to the on-site commissioning team who carry out investigations, fix hardware issues, and therefore improve the detector sensitivity. The efforts of the GEODC group have played a major role in investigations of instrumental artefacts and the removal of their sources, but it has not been possible to remove all artefacts.

We aim to increase the number of GW signals that are observable in our data. This number is proportional to both the volume of space containing canonical

signals we are sensitive to and the amount of time for which we are observing. By commissioning the detector we aim to increase the sensitive range, and therefore increase the volume of space we are observing. However, commissioning interrupts the data taking which reduces the time spent observing, this time is referred to as “down time”. Every investigation costs observing time, so it is important to select investigation directions intelligently to maximise the probability of GW detection.

In this chapter we report on the detector characterisation work that was done at GEO 600 to improve the detector sensitivity. [Section 3.1](#) discusses transient noise in GW detectors. [Section 3.2](#) describes how vetoes to remove transient noise events are classified into “veto” categories and how these vetoes are used in GW data analysis. [Section 3.3](#) gives a description of the diagnostic tools used for the detector characterisation investigations in this thesis. [Section 3.4](#) gives a brief description of the key elements of GEO 600 that are referred to in the investigations described in later sections. [Section 3.5](#) gives details of specific noise hunting investigations that were performed at GEO 600. [Section 3.6](#) gives an explanation of several noise sources observed at GEO 600 to demonstrate how a close relationship between the characterisation team and commissioning team can be used to improve the scientific output of the detector.

## 3.1 Transient Noise Events

Transient noise events, commonly referred to as “glitches”, are clusters of time-frequency pixels that have excess power above the background in an auxiliary channel of the GW detector or in the GW data channel but are not caused by a GW. Glitches in the main GW output of an interferometer are indistinguishable from GWBs, in the absence of a signal model for the GWB; short duration signals with *a priori* unknown waveforms. Because of this it is important to reduce the rate at which glitches with large values of SNR occur, as this will lower the false alarm probability associated with a large SNR GW signal.

The first step in eliminating glitches is to identify them. To do this there are a large number of auxiliary channels which record information about the state of the detector components and the surrounding environment. Some of these auxiliary channels include microphones, seismometers, thermometers, vacuum levels in tanks, magnetometers, signals from control loops, optical components position and alignment, light powers transmitted by optics and the injected laser power. Data from these auxiliary channels and the GW data channel are processed by algorithms that look for transient glitch events. One such algorithm is hierarchical algorithm for curves and ridges (HACR). This is a time-frequency excess power algorithm which takes in data from any of the interferometer channels and locates clusters of time-frequency pixels with power in excess of the typical stationary background noise level [156]. The central frequency, time, SNR, and other parameters of each cluster represents a single glitch in the data. These clusters are referred to as “triggers”.

Another algorithm is the Omega-pipeline which is a multi-quality-factor time-



frequency excess power algorithm. It uses a sine-Gaussian wavelet basis and performs a matched filter search for sine-Gaussian-like glitches over a range of durations, frequencies, and quality-factors [157, 158, 159, 160].

Both of these event trigger generators are used to produce a variety of glitch property maps for the GW data channel and auxiliary channels at GEO 600. These two algorithms complement each other, as they generate comparable plots for the same piece of data using different techniques. Examples of these are time-frequency, frequency-SNR, and time-SNR maps, which all give different, complementing, and useful insights into the glitch background of the GW data channel and auxiliary channels. These tools are regularly used for detector characterisation and monitoring the status of the detector.

## 3.2 Vetoes

It is common practice in GW data analysis to apply “vetoes” to the GW output of detectors to remove glitches caused by noise sources. A veto is a short time, or frequency, window that removes an interval of data or candidate GW events found in that interval from any analysis that is performed. A cartoon example of this process can be seen in figure 3.1. Vetoes are ordered according to the level of understanding that we have of the glitch class that they remove. Details of these are given in table 3.1.

In an analysis performed by X-PIPELINE, the GW search algorithm employed in chapters 4 to 6 of this thesis, category 1 vetoes are not analysed. The remaining segments, after applying category 1 vetoes, are referred to as *science* segments. Science is defined as when the detector is operating in the design configuration which is the optimal state for GW observation. After event lists have been produced from the science segments, category 2 vetoes are applied to remove known glitch classes. Simulated GW signals are sometimes added into the detectors (referred to as hardware injections); these are used to test the performance of GW search pipelines and the ability to detect real signals in the detectors. In X-PIPELINE analysis category 4 vetoes are applied to the event list produced by the analysis to remove events corresponding to hardware injections. Category 3 vetoes are used for computing upper limits to make the data set as clean as possible during follow up in the case of a detection candidate, but they do not automatically veto detection candidates.

### 3.2.1 HVeto

At GEO 600 the HVeto [162] algorithm is used to generate veto segments automatically online. HVeto is a hierarchical veto algorithm which looks for coincidence between GW data channel triggers and triggers from an auxiliary channel. At GEO 600 the Omega-pipeline [158, 159, 160] is used to generate trigger lists for the GW data channels and a large number of auxiliary channels. HVeto tests the statistical significance of the number of time coincidences between triggers

Veto categories	Description
1	Times when the detector is not taking data in the design configuration. The inverse of science segments.
2	Generated when there is a clear statistical correlation between glitches in an auxiliary channel and glitches in the GW data channel, and the physical coupling is understood.
3	Generated when there is a clear statistical correlation between glitches in an auxiliary channel and glitches in the GW data channel, but the physical coupling is not understood.
4	Time of hardware injection of a simulated GW signal.

Table 3.1: Veto categories used in GW searches to tag times of poor data quality. This is the same classification as used by LIGO and Virgo when performing transient searches [161].

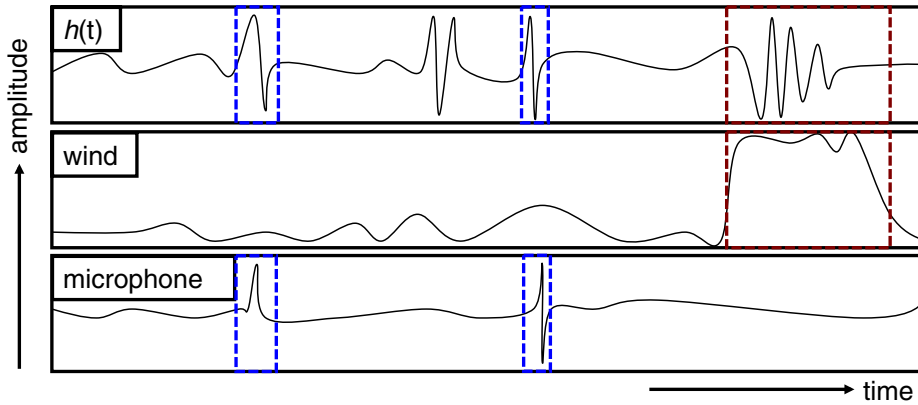


Figure 3.1: Cartoon example of veto method to clean up the GW data channel using auxiliary channels. The top trace shows  $h(t)$ , the GW data channel. The middle trace shows wind speed, while the bottom trace is from a microphone located near the detector. The blue dotted lines show vetoes applied due to association with excess noise in the microphone, while the red dotted lines show a veto due to high local wind speed [162].

in the GW data channel and an auxiliary channel, for each of the auxiliary channels. Then the channels are ranked based on how likely it is that their observed number of coincidences occurred due to the intersection of two Poisson distributions of triggers (i.e. due to random chance, with no physical correlation). This is done for a range of time coincidence windows and SNR thresholds which are defined for each channel depending on the expected trigger duration and the time for coupling between the auxiliary channel and the GW data channel. For each channel the most significant combination of time coincidence window and SNR threshold is selected, and the most significant channel is selected as the “winner”. Using the winning channel veto segments are generated with duration given by the time coincidence window around all triggers in the winning auxiliary channel with SNR above the SNR threshold. These veto segments are then applied to the GW data channel and are removed from the analysis of further “rounds”. The process is repeated for another round to select additional winning channels until the significance of the winning channel is below a pre-set significance threshold.

We demonstrate the use of this algorithm in [section 6.3.2](#) when performing a methods study for the feasibility of performing a single detector burst search using GEO 600. We include a table of the results for all rounds from this HVeto analysis in [table 6.3](#), and a discussion of the results in [section 6.3.2](#).

### 3.3 Diagnostic tools

In this chapter we use a variety of software tools to investigate the noise sources that are observed in the detector. These tools are used to compare a period *before* commissioning, when the noise is present, with a period *after* commissioning when the noise has been removed. This gives us a measure of the commissioning performance at removing the noise source. We also compare the same period *before* commissioning with vetoes applied, if available, to the *after* commissioning period. This gives a comparison of the relative performance of the vetoes and commissioning for each noise source.

**Strain noise spectral density** is a representation of the noise floor of the detector as a function of frequency, which is an estimate of the stationary noise that is present in the detector. The spectrum is stable on the hour to day time scale but changes as the detector configuration is changed. See [figure 3.5](#) for an example.

**Omega-grams** give a multi quality-factor time-frequency representation of the detector data, similar to a spectrogram (see [figure 3.18\(a\)](#)) [[157](#)]. However, unlike a spectrogram Omega-grams can simultaneously show information about both short broadband and long narrow-band structure. At GEO 600 we found that this visualisation method is particularly useful when coupled with an audio output of the data, so that the ears can pick out features visible in the Omega-grams.

**Cumulative glitch rate histograms** illustrate the SNR distribution of transient

noise event triggers (for example [figure 3.16](#)). This quantifies the non-stationary noise in the detector.

**Fixed false-alarm probability range** is a measure of the sensitive range of the detector to GWBs as a single number that accounts for both the stationary noise floor and transient noise events in the detector, see [\[163\]](#) for a full description.

In general the formulation of the range at a given frequency  $f$  is [\[164\]](#)

$$D(f) = \left( \frac{GE_{\text{GW}}}{2\pi^2 c^3} \right)^{1/2} \frac{1}{\rho \sqrt{S(f)f}}, \quad (3.1)$$

where  $E_{\text{GW}}$  is the energy released in GWs isotropically by a target source,  $\rho$  is an SNR threshold determined by the distribution of transient noise events, and  $S(f)$  is the strain noise spectral density.

To find the range for a particular frequency band, for example the band in which we expect GWs for a particular source, we integrate the range. For a frequency band  $f_1$  to  $f_2$  we define the integrated range [\[163\]](#) as

$$D \equiv \left[ \frac{1}{f_2 - f_1} \int_{f_1}^{f_2} D(f)^3 df \right]^{1/3}, \quad (3.2)$$

where  $\rho$  is set using background triggers that overlap the frequency range  $f_1$  to  $f_2$  in order to obtain a required background trigger rate.

Here we also use the frequency dependent range, in order to visualise the contributions at different frequencies to the range integrated over a frequency band  $f_1$  to  $f_2$ . This frequency dependent range  $D(f)$  is given in [equation \(3.1\)](#), but with  $\rho$  as a function of frequency  $\rho(f)$ .  $\rho(f)$  is found using background triggers whose frequency extent at half maximum overlaps with the frequency  $f$ . Note that taking the frequency extent at half maximum of a trigger is only an approximation of how the sensitivity at a given frequency is affected by a trigger. Because of this sharp edge in the affected frequency range and the very discrete determination of frequency range by event trigger generators like Omega-pipeline, we observe jumps in  $D(f)$  as a function of frequency (see e.g. [figure 3.29](#)).

In practice we use parameters corresponding to two possible sources for GWs: from a Galactic core-collapse SN and a nearby GRB. For the SN case we assume an emission of  $E_{\text{GW}} = 10^{-8} M_{\odot} c^2$  in the frequency band of [500 Hz–4 kHz]. For the GRB case we assume an emission of  $E_{\text{GW}} = 10^{-2} M_{\odot} c^2$  in the frequency band of [100 Hz–500 Hz]. In both cases we use an SNR threshold corresponding to a false-alarm probability of  $\sim 10^{-3}$  in a few seconds long search window around the SN core bounce time or GRB observation. These two astrophysically motivated ranges allow us to assess the low and high frequency sensitivity of the detector.

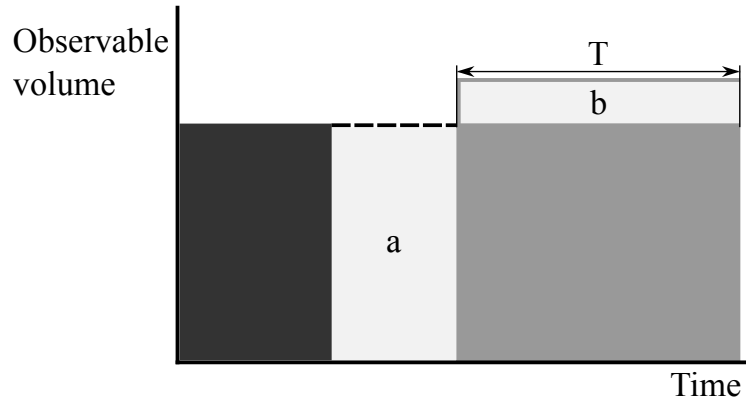


Figure 3.2: Cartoon showing observable volume ( $D^3$ ) against time for a noise investigation. Before (dark grey) is a period of detector performance while the problem was present with or without vetoes applied. After (grey) is a period after the problem was removed. Commissioning (light grey) incurs a down time from investigating and removing a problem. The number of observable sources is proportional to area, so  $T$  is the time such that  $\text{area}_a = \text{area}_b$ .

**Catch up time** is defined as the time required, running at the improved range after commissioning, to make up the deficit in the number of observable sources due to the commissioning down time lost at the previous range.

To find the catch up time we first define the number of observable sources, which is estimated using a combination of the fixed false-alarm probability range [163] and the detector duty cycle. Assuming that observable sources are uniformly distributed in volume and frequency with rate density  $B$ , we define the number of observable sources as

$$N_{\text{GW}} = \frac{4\pi}{3} D^3 T B, \quad (3.3)$$

where  $T$  is the observation time [163]. The rate density  $B$  can be for instance an estimate of the Galactic SN rate, but its actual value is irrelevant for the catch up time, which only compares the relative performance of the detector between two periods.

The catch up time can be found from a simple rearrangement of equation (3.3) and equating the areas  $a$  and  $b$  as shown in figure 3.2, as

$$T_{\text{catch up}} = \frac{D_{\text{before}}^3 t_{\text{comm}}}{D_{\text{after}}^3 - D_{\text{before}}^3}. \quad (3.4)$$

The quantity  $t_{\text{comm}}$  is the down time due to commissioning, while  $D_{\text{after}}$  and  $D_{\text{before}}$  are the ranges before and after commissioning, respectively. This measure of the performance of the commissioning at removing the noise source is shown schematically in figure 3.2. For this calculation we assume the detector performance is stable before and after commissioning, and that the detector could have maintained the performance before the

commissioning for the duration of the commissioning down time; this is shown in [figure 3.2](#). We estimate the down time for the commissioning in each investigation and treat it as a single block of time between the before and after commissioning times. We also assume that the commissioning only affects the noise source being investigated, and that this removal of the noise is the only difference between the before and after commissioning times. However, this does not always hold, we will see in [section 3.6](#) (for example, in the infinite catch up times in [table 3.3](#)).

This same procedure is also used to measure the relative performance of the vetoes and commissioning. In this case the range before commissioning is found after applying vetoes to the before commissioning period,  $D_{\text{vetoes before}}$ . More discussion of interpretation of this range can be found in [section 3.5](#).

**Summary pages** give an overview of the current and historical state of an interferometer. Information is displayed for the current day and is updated every minute, as well as being saved in an archive displaying data on day, week, month, and year times scales. In [figure 3.3](#) we give an example of the “day summary” from the GEO 600 summary pages for the 3<sup>rd</sup> July 2012. In the centre of this page are the most useful figures from each of the monitors being run to produce the summary page. From top left and across these are time-frequency distribution of GW data channel HACR triggers, time-frequency distribution of GW data channel Omega-pipeline triggers, a variety of burst-like ranges, a spectrogram of the GW data channel, the duty cycle histogram for the different detector states, the data quality vector<sup>1</sup>, calibration information, effect of HVeto on the cumulative glitch rate, laser power at different points throughout the detector, and squeezing level. Each of these figures is a link to a more in depth page. This can also be accessed using the navigation bar along the top, where each tab provides more plots and information for each of these monitors. On the left of the page is a navigation bar to move between different days or months and access the archive of past day pages.

These pages have proved extremely useful for noise characterisation in the GEO600 group and are continuously evolving. This concept has been implemented for LIGO, Virgo, and GEO 600 individually, but the summary pages shown in [figure 3.3](#) are developed to be run on any of the detectors and to show useful information that is needed by both the commissioning and characterisation teams. This allows comparison between detectors using the same plots and comparison of the same detector at different times. These pages are currently being implemented for the advanced LIGO detectors.

---

<sup>1</sup>The channel which records the status of the detector lock, hardware and software maintenance, squeezer status, hardware injection times, as well as some simple vetoes.



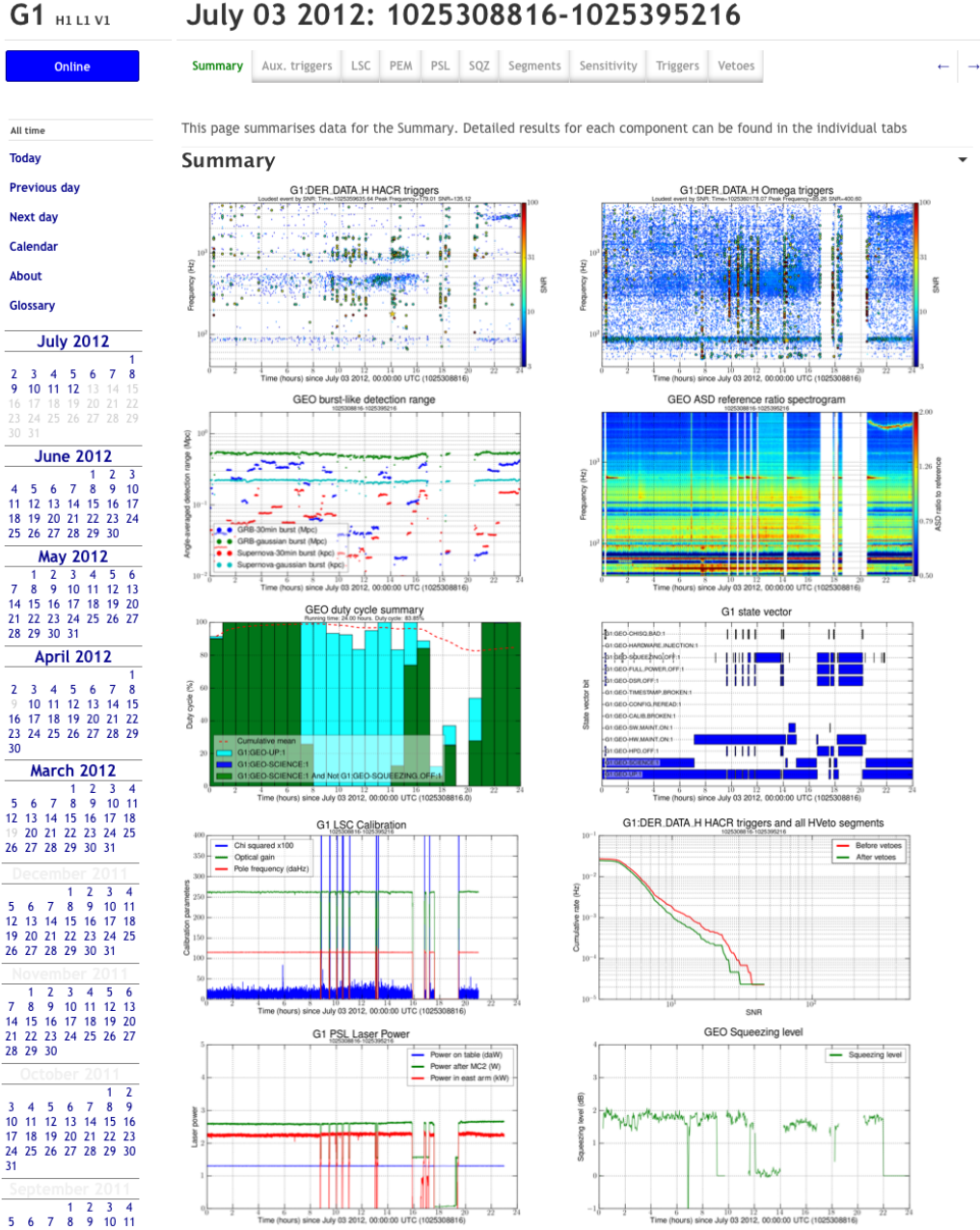


Figure 3.3: Detector characterisation summary pages for GEO 600. We show the summary tab for the 3<sup>rd</sup> July 2012, each image is a link to a separate tab with more plots and information from each of the monitors. From top left and across these are time-frequency distribution of GW data channel HACR triggers, time-frequency distribution of GW data channel Omega-pipeline triggers, a variety of burst-like ranges, a spectrogram of the GW data channel, duty cycle histogram for the different detector states, the data quality vector, calibration information, effect of HVeto on the cumulative glitch rate, laser power at different points throughout the detector, and squeezing level.

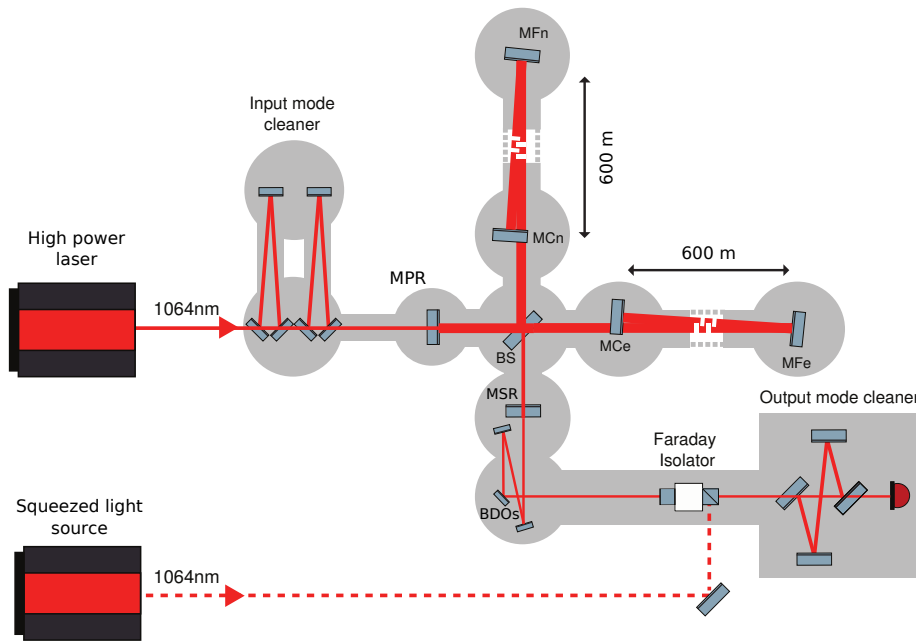


Figure 3.4: Simple optical layout of GEO 600, see [section 3.4](#) for details. Here we show the BDOs, OMC, and squeezer which are relevant for the investigations in [section 3.5](#).

### 3.4 Simplified GEO 600 Layout

This section gives a brief description of some elements of GEO 600 that are relevant to the investigations performed in [section 3.5](#). [Figure 3.4](#) is a simple schematic of the optical layout of GEO 600. Laser light is fed into the vacuum system by a pre-stabilised laser at a wavelength of 1064 nm. It first passes through two suspended triangle cavities that remove higher order spatial modes of the laser light and to reduce amplitude noise, these are called the input mode cleaners.

The interferometer itself is composed of seven large suspended main optics, which form a Michelson interferometer with 1200 m long folded arms. The light split by the BS passes underneath the two end mirrors of the Michelson (MCe and MCn for close-east and close-north) and is then folded back towards those mirrors by folding mirrors (MFe and MFn for far-east and far-north) at the end of the 600 m long vacuum tubes. The Michelson interferometer is operated close to the dark fringe so most of the light is reflected by the interferometer back towards the laser at the input port. The MPR is used to reflect the light back towards the BS which increases the light circulating in the interferometer arms by about a factor 1000, see [section 2.5.4](#). Relative changes in the two arm lengths allow a small amount of light to escape towards the output port where MSR is placed. MSR resonantly enhances this signal by allowing it to circulate in the interferometer multiple times, see [section 2.5.5](#).

At the output of the interferometer, three mirrors (the BDO mirrors) are used to direct the light into a Faraday isolator and through an OMC. The purpose of the BDOs is twofold: they form a beam telescope which reduces the large beam



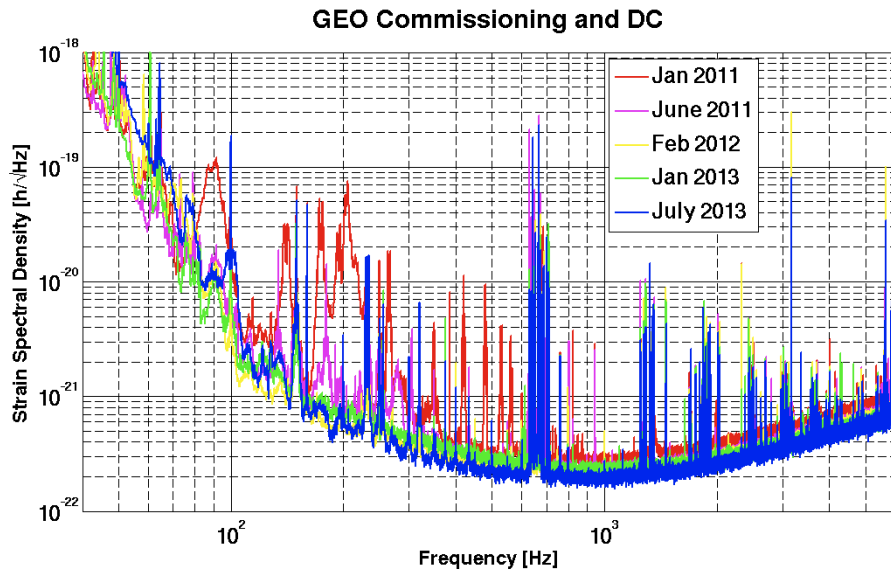


Figure 3.5: Strain noise spectral density verse frequency for GEO 600 for different epochs.

waist of the interferometer to match the small waist of the output optics while also serving as alignment actuators.

The OMC rejects radio frequency side-bands of the laser light that are used for interferometer control and also rejects higher order spatial modes coming from defects of the main optics. The power in this *cleaned* light exiting the OMC is detected by the photo-diode shown in [figure 3.4](#). This signal is used to measure changes in the relative arm length inside the interferometer, the GW channel.

The purpose of the Faraday isolator is to prevent light back-scattered by the OMC and the photo-diode from being injected back into the interferometer. It is also used in the injection of a squeezed vacuum state into the output side of the interferometer. This decreases the shot noise at the photo-diode, the dominant source of noise in the relative arm length sensing at high frequencies (see [section 3.6.2](#) for details). The sensitivity of GEO 600 can be seen in [figure 3.5](#) where the noise spectral density is plotted for a number of different epochs which span the work reported in this chapter.

### 3.5 Glitch hunting

In this section we give details of investigations (“glitch hunting”) performed by the author for several transient noise classes that were observed in GEO 600. These noise sources were investigated in depth to gauge the effect that they have on the GW data channel, and therefore any potential searches. The aim of glitch hunting is to find the source of a glitch type and remove it, so that the glitches no longer occur. But this is not always possible, in this case we will then try to understand the glitch and determine the conditions that produce the glitches so that these can be minimised to reduce the number of glitches that occur. If it is not possible to remove the glitches or reduce them sufficiently

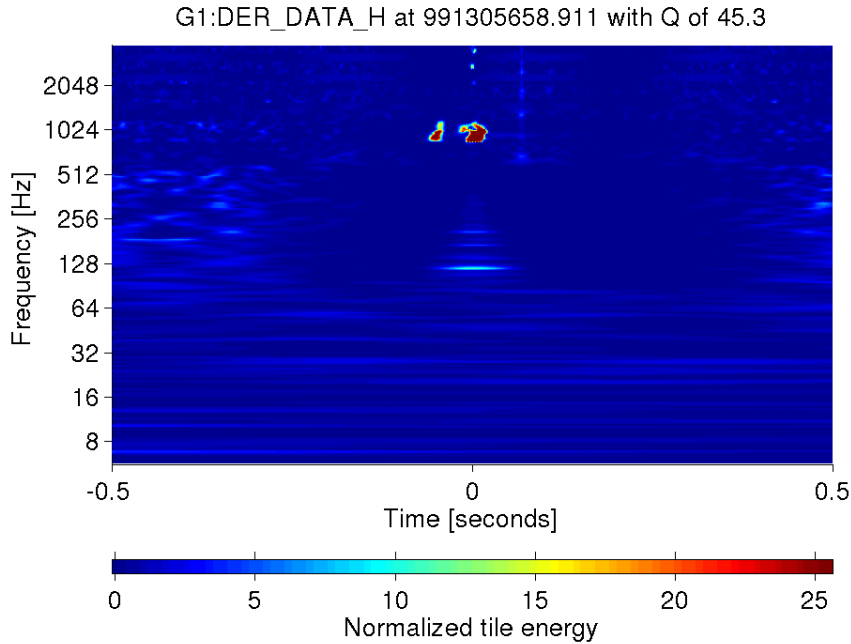


Figure 3.6: Omega-scan of a 900 Hz glitch in the GW data channel, found using the GEODC online tools. As can be seen here, and as is seen when producing a time series of these glitches, the glitches are of order a tenth of a second in duration and they are narrow band around 900 Hz.

then the final solution is to veto times when the glitches occur and this requires some way of determining when the glitches occur. The section highlight the procedures used and the outcome from glitch hunting, which is performed at GEO 600 throughout the Astrowatch period to clean the detector data in case of an extraordinary astrophysical event.

### 3.5.1 900 Hz Glitches

The “900 Hz glitches”, or “sine-Gaussian glitches” as they have been referred to in the past, are sine-Gaussian in shape and occur around 900 Hz in the GW data channel, as their name suggests. These events can have some of the largest SNR  $\mathcal{O}(1000)$  of any events in the GW data channel during science segments, and occur in the most sensitive frequency band of the GEO 600 noise spectral density. The rate of these glitches has varied over time, but at their worst they were occurring tens of times per day. All of these reasons make these events important to understand as these will be indistinguishable from an unmodelled GWB, and so will limit the false-alarm probability we can assign to a real GW event in the case of a detection.

In [figure 3.6](#) we can see a 900 Hz glitch in the GW data channel, DER\_DATA\_H. This channel is calibrated to show us the detector strain  $\Delta L/L$ . The glitch is large in amplitude compared to the background noise and occurs at  $\sim 900$  Hz.

In [figure 3.7](#) we see the time versus frequency and frequency versus SNR distributions of Omega triggers respectively, for June 5<sup>th</sup> 2011; the beginning of

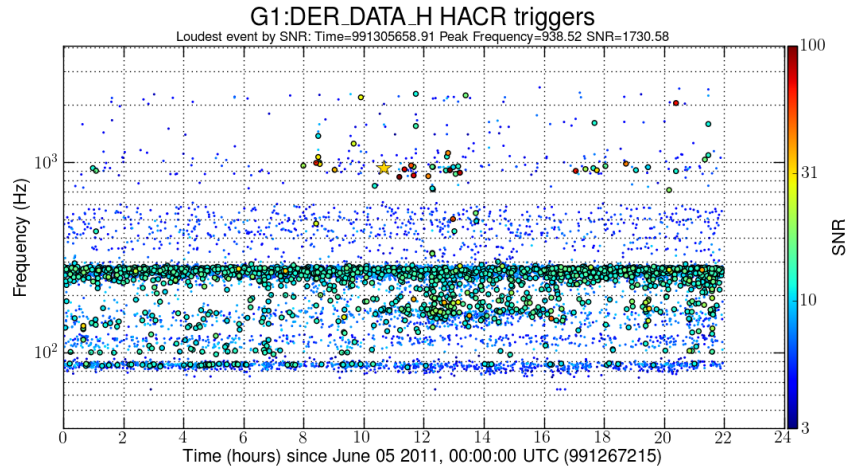


Figure 3.7: Omega trigger plot of time versus peak frequency, from one of the first days of the S6E/VSR4 science run June 5<sup>th</sup> 2011. The high SNR 900 Hz glitches stand out clearly (in red) above a background of lower SNR glitches. The yellow star represents the loudest trigger.

S6E/VSR4 science run. The sample of 900 Hz glitches shown here were common features in the glitch background for that period, i.e. these are not extraordinary events in the glitch population.

These events do not appear in auxiliary channels which monitor common mode length changes in the arms, and appear strongly in auxiliary channels which monitor differential mode length changes in the arms. Therefore it was thought that these glitches were originating in the MID\_VIS control loop to the differential electrostatic drive (ESD) feedback. To test this we performed a number of injections of sine-Gaussian signals at 920 Hz at two different points in the feedback loop, see [figure 3.8](#).

The amplitude of the injections were compared in the feedback and MID\_VIS channels,  $V_{\text{feedback}}$  and  $V_{\text{MID\_VIS}}$  respectively, finding the ratio of these two channels  $V_{\text{feedback}}/V_{\text{MID\_VIS}}$ . Comparing this ratio to the relationship seen for 900 Hz glitches we test the two hypothesis that the glitches either originate in the suspensions and optics of the interferometer or in the electronics of the Michelson differential control loop.

Injections upstream of the electronics of the control loop (X in [figure 3.8](#)) gave the ratio

$$V_{\text{feedback}}/V_{\text{MID\_VIS}} = 0.1,$$

while injections upstream of the suspensions and optics of the interferometer (Y in [figure 3.8](#)) gave the ratio

$$V_{\text{feedback}}/V_{\text{MID\_VIS}} = 5.1.$$

The observed ratio for 900 Hz glitches was consistently measured as

$$V_{\text{feedback}}/V_{\text{MID\_VIS}} \simeq 0.1.$$

This is consistent with the hypothesis that the glitches originate in the electronics of the Michelson differential control loop.

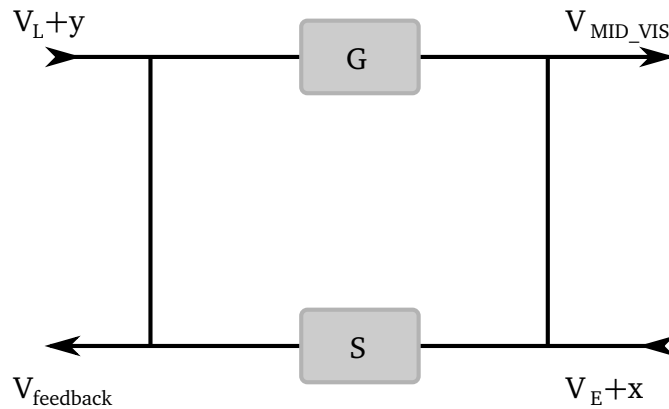


Figure 3.8: Schematic of the Michelson differential control loop.  $G$  represents the suspensions and optics of the interferometer and  $S$  represents the electronics of the control loop.  $V_{\text{MID\_VIS}}$  is the voltage from the Michelson differential mode visibility.  $V_{\text{feedback}}$  is the voltage from the Michelson differential mode feedback point to ESDs on the MCE and MCN mirrors.  $V_L$  is the voltage of a channel used for injections between the MID\_FEEDBACK and MID\_VIS channels, to test the hypothesis of the 900 Hz glitches originating from the suspensions and optics of the interferometer.  $V_E$  is the voltage of a channel used for injections between the MID\_VIS and MID\_FEEDBACK channels, to test the hypothesis of the 900 Hz glitches originating from the control loop electronics. Injections were performed at  $X$  or  $Y$  by adding the injection to the relevant channel.

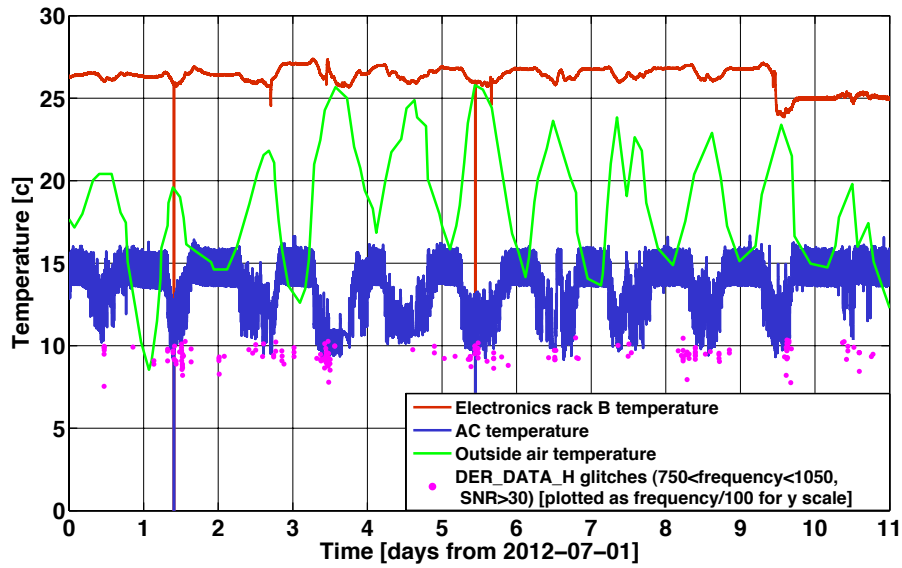


Figure 3.9: 900Hz glitch rate dependence with temperature. The outside air temperature (green) rises during the day, the air conditioning unit (blue) responds to cool the central building. The effect of this extra cooling can be seen in the electronics rack B temperature (red) which decreases during the day. 900Hz are most frequent during the hottest part of the day.

A dependence on the outside air temperature was found for the 900Hz glitches. This dependence can be clearly seen in [figure 3.9](#), which shows glitches in the GW data channel with  $\text{SNR} > 20$  in the 750Hz–1050Hz band, as well as a number of different temperature measurements. As the air temperature increases during the day time, the air conditioning unit temperature decreases to control the temperature inside of the central building, the electronics rack B temperature follows the same daily trend, due to its location inside of the central building. From the time distribution of the 900Hz glitches, we see that they occur most frequently during the hottest part of the day.

We do not currently know the exact source of these glitches, and so we have no commissioning solution to remove them. We also do not have a reliable veto to automatically remove these glitches, as they primarily show up in auxiliary channels which observe the differential mode of the detector; these channels are not “safe” as glitches in these channels are indistinguishable from events caused by true GWBs due to the close relationship to the GW data channel. However, through these investigations we now have some understanding of the environmental conditions in which they are most frequent and we now know the time-frequency shape of these events, as shown in [figure 3.6](#). This is an example of a glitch class that can not be removed with standard blind vetoes but which is recognisable using a variety of different data visualisation methods. Using this information these events could be removed from data in the case of a detection

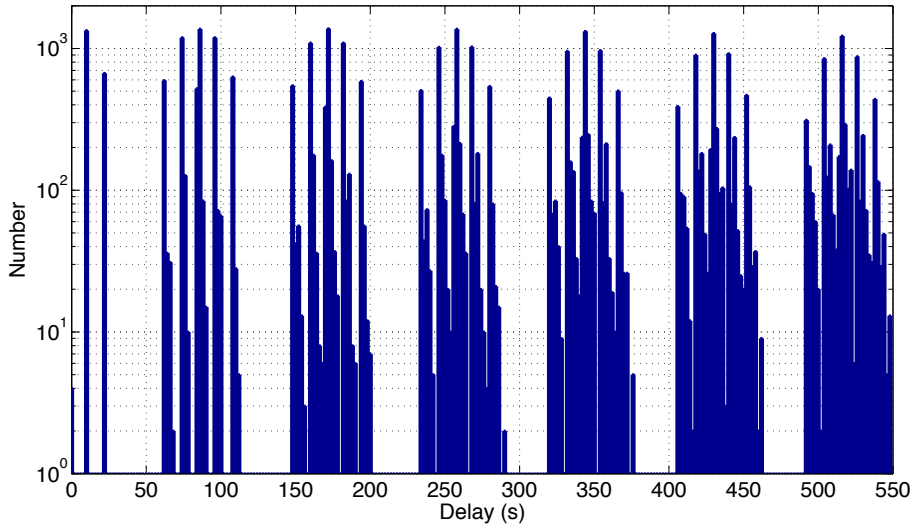


Figure 3.10: Delay between the HACR triggers with  $\text{SNR} > 300$  and central frequency from 2.8 kHz–3.2 kHz in VOID\_CHANNEL0001.

candidate during a detection candidate event follow up investigations, this would result in making GEO 600 insensitive to signals with similar characteristics to these glitches.

### 3.5.2 “ting” glitches

There were a class of glitches that were first observed in February 2010 which had large SNR ( $> 300$ ) in DER\_DATA\_H with frequencies around 3 kHz. These glitches also showed up in an auxiliary channel which was at the time monitoring an accelerometer attached to the tank centre output b (TCOb) vacuum tank (VOID\_CHANNEL0001), see [figure A.1](#). The glitches came in groups of three separated by 11 s–12 s every 86 s. To find the cause of these glitches we looked for coincidence with other auxiliary channels, and found glitches matching in time and frequency in a microphone in the central building, near to TCOb. Taking data from the microphone, we produced a sound file and listened to the glitches to try to identify the cause of the noise. The glitches were very clear “tings” which sounded like they were being produced by a mechanical source, and specifically something hitting against something else, when listening to both the GW data channel and auxiliary channel.

To test the suspected periodicity of these glitches, we used one day of HACR triggers from February 17<sup>th</sup> 2011 from the accelerometer auxiliary channel and selected out just these “ting” glitches. This was done by looking at time-frequency and frequency-SNR plots of the glitches from that day, and selecting cuts in frequency (2.8 kHz–3.2 kHz) and  $\text{SNR} > 300$ . This left just over 2000 glitches. We computed the delay time between each glitch and the next 200 glitches following. These times were then collected with 2 second bins to find any periodicity in the glitches, the results are shown in [figure 3.10](#).

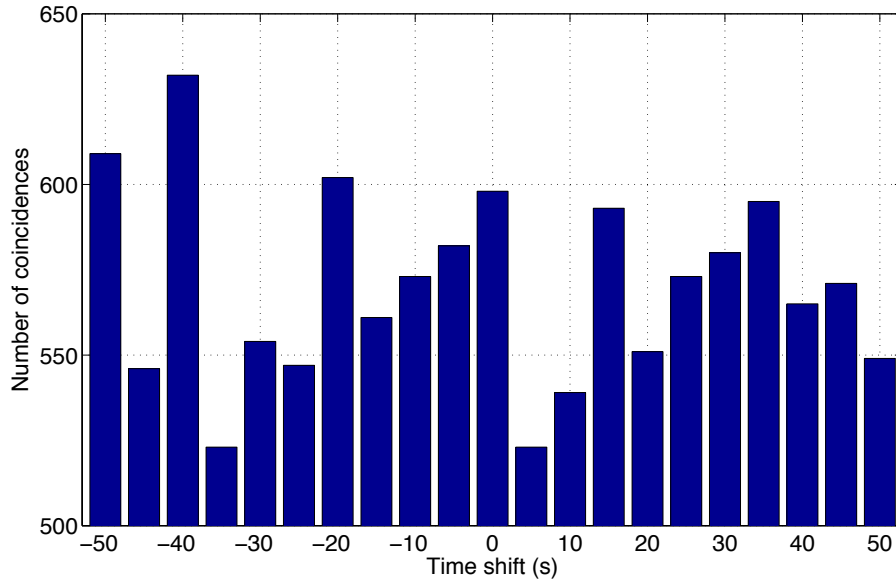


Figure 3.11: Time-frequency coincidence between HACR triggers with SNR > 300 and central frequency from 2.8 kHz–3.2 kHz in VOID\_CHANNEL0001 and the GW data channel.

It is clear from [figure 3.10](#) that there is a periodicity of the glitches in the accelerometer auxiliary channel. The 10 s–12 s bin peak is the difference between consecutive triggers within a group, the 22 s–24 s bin peak is the difference between the first and last triggers of a group. Then there are peaks for the differences between the triggers in neighbouring groups at 62 s–64 s, 74 s–76 s, 86 s–88 s, 96 s–98 s, and 108 s–110 s bins and so on.

The coincidence of these glitches with glitches in the GW data channel were then checked using the triggers selected for the investigation shown in [figure 3.10](#). We measured the number of coincidences, and then repeat this after artificially time shifting the time stamps of the glitches by multiples of 5 seconds. This allows us to compare the significance of any coincidences to the background caused by random coincidences. [Figure 3.11](#) shows the results of this test, that there is no significant difference between the zero lag coincidence and the background coincidence which means that these are random coincidences and not causal.

While these glitches are loud and frequent in the auxiliary channels, they do not seem to contaminate the GW data channel, so they are low priority to eliminate. There glitches were still present after the BDO suspension upgrade which is detailed in [section 3.6.1](#), and the exact cause has not been tracked down to date. This is an example of a glitch class that can not be removed but which does not effect the GW data channel, and therefore is not a concern when performing searches for GWs. Noise sources of this sort, which do not contaminate the GW data channel and do not have an available veto or commissioning solution, can be left in place and monitored until a solution is found to remove the noise source.

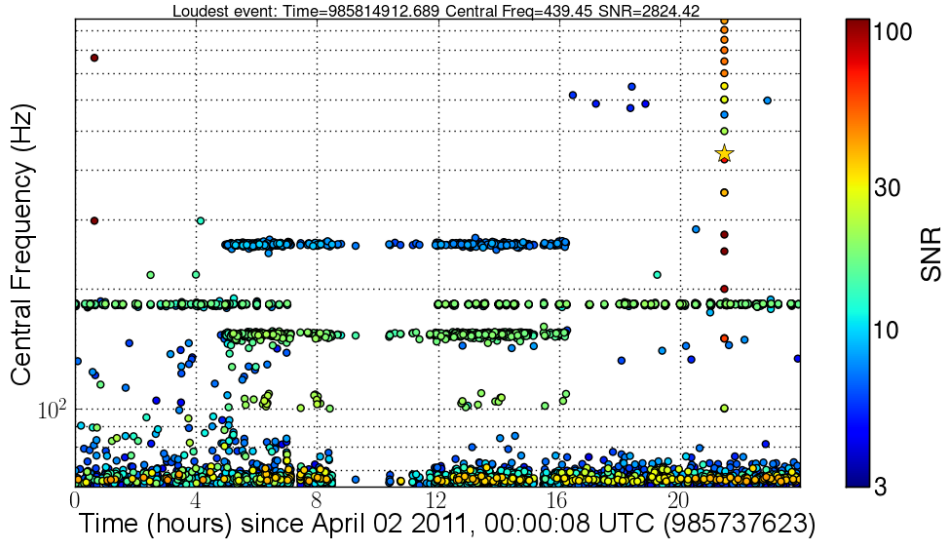


Figure 3.12: PEM\_TFE\_MAG-Z channel HACR trigger plot of frequency versus time for 02/04/2011. This shows the two periodic glitch bands that are being investigated at 145 Hz–160 Hz and 250 Hz–265 Hz.

### 3.5.3 Far East Tank Magnetometer Glitches

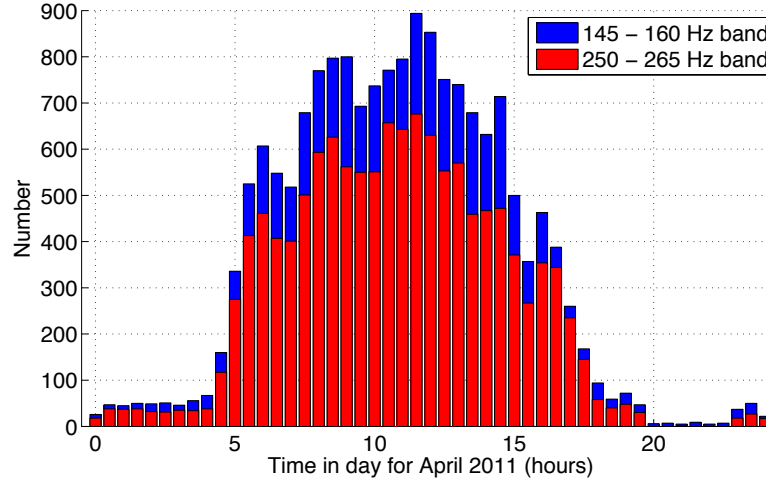
There were two transient glitch bands in the east end tower (see [figure A.1](#)) magnetometer channel (PEM\_TFE\_MAG-Z) at 145 Hz–160 Hz and 250 Hz–265 Hz which would appear during the day time. These glitches were first observed in April 2011 and can be seen clearly in [figure 3.12](#), where glitches appear in these bands around 05:00 and then disappear around 16:00 coordinated universal time (UTC).

Using all of the HACR triggers from when these glitches were first noticed (April 2011) and an earlier time (September 2007) we tested if this was a new feature, or if it had gone unnoticed up until April 2011. All the glitches in these frequency bands were stacked and a histogram was produced of the time of the glitches in the day, using 30 min bins, for both of the periods. The results of this test can be seen in [figure 3.13](#).

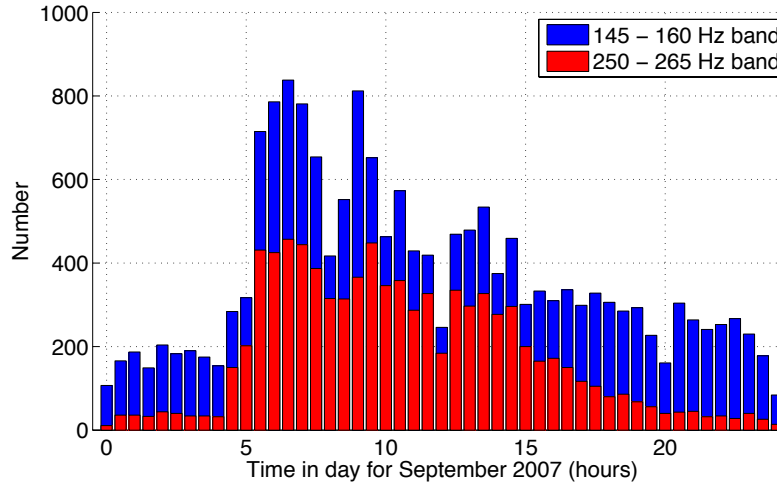
In [figure 3.13\(a\)](#) (April 2011) the glitches in both bands follow the same trend, and occur mainly between 5 and 16 hours. In [figure 3.13\(b\)](#) (September 2007) both bands increase at 5 but the decrease is more gradual, but still clear in the 250 Hz–265 Hz band. This shows that these glitch bands were both present in September 2007, but the periodicity was not as clear as in April 2011. [Figure 3.13\(b\)](#) also shows that there was a larger trigger background at quiet times in the 145 Hz–160 Hz band, of  $\sim 200$  triggers per 30 min. As the background rate of glitches in these bands is less in April 2011, as seen in [figure 3.13\(a\)](#), the effect of these glitches is more visible over the background. Using the triggers from April 2011, a time-frequency coincidence test was performed with the GW data channel, and it was found that there was no correlation.

Therefore, these glitches were not significant for GW searches and so this noise source is low priority to eliminate. No more time was spent investigating





(a) April 2011



(b) September 2007

Figure 3.13: Histograms of the number of PEM\_TFE\_MAG-Z HACR triggers versus time in day, from each glitch band using 30 minute bins in the PEM\_TFE\_MAG-Z. We can see that the triggers occur mainly between 5 and 16 hours. This behaviour is present in both figures but is more pronounced in April 2011.

these events, and the source of this noise was not tracked down. This is another example of a glitch class that can not be removed but which does not effect the GW data channel, and therefore is not a concern when performing searches for GWs.

The investigations in this section are an example of the sort of work that can be done on-site to characterise glitch classes and to measure the urgency of commissioning to remove the source of each noise source by looking at the effect they have on the GW data channel. Investigations of this sort are performed throughout the GEO 600 Astrowatch period. As can be seen in this section it is not always possible to remove a glitch class with either vetoes or a commissioning solution. In this case, as much information is gathered for a glitch class and it is monitored as the detector configuration changes.

## 3.6 Characterisation directed commissioning of the GEO 600 detector

In this section we will give details of a handful of investigations into noise sources that occurred at GEO 600. This section draws from Ref. [165] which is in preparation. The author was the lead for these detector characterisation investigations in collaboration with the GEODC group, the commissioning activities were performed by the GEO 600 commissioning team.

This is not an exhaustive summary of the work done by either the detector characterisation or commissioning teams. Rather, these investigations were chosen to display a variety of noise sources that require different solutions from either vetoes or commissioning. The “before” and “after” commissioning times for each investigation were chosen to highlight the problems clearly, so ideally only the effects of the noise sources being investigated are present. However, GW detectors are complex instruments and so this is not perfect.

A key element for why these investigations were chosen is their ability to demonstrate how a close relationship between the characterisation team and commissioning team can improve the scientific output of the detector. At GEO 600 we were unable to perform these investigations at the time these noise sources were first observed, due to the GEODC group being manpower limited. Here we show that if such investigations were performed, the detector characterisation team could contribute significantly to the decision making for commissioning solutions to noise sources; resulting in an overall increase in the number of observable sources compared to commissioning without this guidance.

For any instrumental issue there are two standard techniques available to remove the noise from the data. The first option is to veto the data at the times when the issue is occurring or apply a notch filter to remove the noisy frequency band, whichever is most appropriate. The second option is to remove the source of the noise through commissioning the detector. There are pros and cons for each of these methods. Vetoes can be applied after the fact and do not require larger periods of down time due to commissioning. However, they do not remove the source of the noise; instead they just remove the affected data. Sometimes

Investigation	Before time GPS (UTC)	After time GPS (UTC)	Duration (hours)
BDO suspension upgrade	988315215 (02-05-11 20:00:00)	990993615 (01-06-11 20:00:00)	12
OMC isolation upgrade	1007510415 (10-12-11 00:00:00)	1008439215 (20-12-11 18:00:00)	12
Squeezer glitches	1010808015 (17-01-12 04:00:00)	1010872815 (17-01-12 22:00:00)	2
3.5 Hz dither squeezer glitches	994788015 (15-07-11 18:00:00)	997552815 (16-08-11 18:00:00)	4

Table 3.2: Table of *before* and *after* commissioning times used for each investigation, and the duration of the data used in each case.

effective vetoes are not available (e.g. if the glitches are not seen in an auxiliary channel). Commissioning removes the source of the noise, which means that there is no lost data after the initial down time for commissioning activities. However, the down time required for investigations and commissioning can be substantial and commissioning does not always work.

To compare these two methods we define the catch up time in [equation \(3.4\)](#). If the catch up time is small compared to the commissioning down time, this means that the commissioning gave a significant increase in range which makes the commissioning worth while. If the catch up time is large compared to the commissioning down time, then the decision to perform commissioning must be considered more carefully. For example, if a problem arose during a science run, then the commissioning should only be performed if you expect the catch up time to be smaller than the remaining observational time of the science run. If this is not possible then the commissioning should be delayed until after the end of the science run. These two choices will maximise the number of observable sources during the science run.

Four investigations into different noise sources observed at GEO 600 follow. Each investigation discussion describes the noise phenomena, veto and commissioning results, compares their performance, and discusses the best solution and lessons learned.

### 3.6.1 OMC auto alignment issues

The three optics that match the main interferometer to the OMC are referred to as the BDOs, see [figures 2.15](#) and [3.4](#). Originally it was thought that the motion of these optics would not couple strongly to the GW data channel so they were hung as single pendulum suspensions from blade springs rigidly connected to the ground. Due to this simple suspension design, ground motion easily excited some of the resonances of this system which then coupled into mirror motion and ultimately a fluctuation of the alignment of the output beam onto the OMC.

The transverse motion of optics suspended as pendula experience high sup-

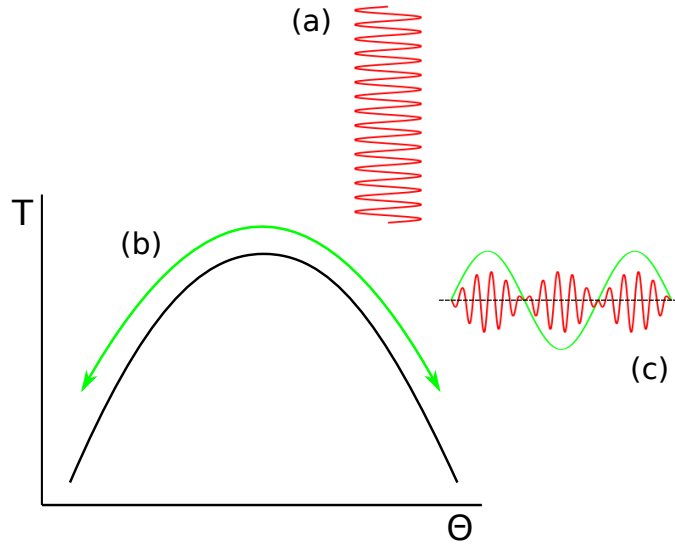


Figure 3.14: The transmission,  $T$ , of a beam impinging on the OMC as a function of an alignment degree of freedom parameter  $\Theta$  is shown as the black curve. A high frequency fluctuation in  $\Theta$  shown in red (a) is modulated by a low frequency variation shown in green (b). This produces a modulated high frequency fluctuation in the transmission (c) shown in red with the low frequency window shown in green.

pression at frequencies well above the resonance frequencies of the pendula. However at frequencies well below the resonance frequencies there is no motion suppression at all and there is even some amplification happening near the resonances. At GEO 600, for the main interferometer the optic's suspensions have resonance frequencies spanning from 0.5 Hz–2 Hz. At these frequencies there are quite a few interferometer degrees of freedom which are uncontrolled. This leads to relatively large motion, for example, of the position and angle of the output beam exiting the interferometer. In turn, this motion causes miss-alignment of the output beam onto the OMC. Any additional high frequency alignment fluctuations are modulated by the low frequency variations, producing a noise source that varies in amplitude as the alignment of the OMC changes. This mechanism is shown schematically in [figure 3.14](#). When the OMC is missaligned, a fluctuation entering the OMC will couple into the photo-diode signal in transmission of the OMC, and thus the observed GW signal, at the frequency of the fluctuation. Conversely, when the OMC is well aligned, the entering fluctuation will couple much less and only to the harmonics of the frequency of fluctuation.

Of particular concern were the violin modes of the steel wires suspending the mirrors which spanned frequencies from 140 Hz–205 Hz. Other important excited resonances spanned a range of frequency from 80 Hz–600 Hz. Through the mechanism described above, the high frequency fluctuation of the alignment of the OMC was modulated by the low frequency variation due to the motion of the main optics. This produced complex noise features in the GW data channel mainly seen from 80 Hz–600 Hz; see [figure 3.15](#). This noise can also be viewed in an Omega-gram of the GW data channel as shown in [figure 3.18\(a\)](#), as compared

to a time without the noise source shown in [figure 3.18\(b\)](#). [Figure 3.18\(a\)](#) shows the frequency jittering of the noise entering the detector through the BDOs. This noise is spread across a broadband of frequencies, with major features around 90 Hz, 140 Hz, 200 Hz, and 350 Hz. The noise at these frequencies is transient, due to the coupling of this noise to the GW data channel changing with the variation of the alignment of the OMC. There are short periods of times when the OMC passes through the correct alignment and all of the jitter line coupling is suppressed.

Although this noise contamination is broadband, notches can be used to remove the major noise features. Notches from 80 Hz–110 Hz, 135 Hz–150 Hz, 160 Hz–250 Hz, and 340 Hz–360 Hz were used which remove  $\sim 30\%$  of the bandwidth between 80 Hz–600 Hz. This is effectively a veto in frequency instead of in time. The effect of this veto on the spectrum, frequency dependent range, and cumulative trigger rate are shown in [figures 3.15](#) to [3.17](#) respectively. The strain noise spectral density is not improved, but the noisy frequency bands are removed; see [figure 3.15](#). The rate of glitches in the 80 Hz–600 Hz band with  $\text{SNR} \geq 10$  is reduced by one order of magnitude, this can be seen in [figure 3.16](#). There is a broadband improvement outside of the notch bands at which we have zero sensitivity; see [figure 3.17](#). This is due to the removal of broadband glitches with central frequencies within the notch bands, as they degrade the range in all frequency bins which they overlap.

To reduce this noise, the BDO suspensions were redesigned such that they would provide of order 100 times better isolation of the ground motion from 50 Hz–1 kHz. The cumulative down time from the commissioning which resulted in the completion of this upgrade was  $\sim 20.83$  days. The effect of this commissioning on the spectrum, frequency dependent range, and cumulative trigger rate are shown in [figures 3.15](#) to [3.17](#) respectively. The amplitude of the noise features in the spectrum at  $\sim 200$  Hz is reduced by up to a factor of 50; see [figure 3.15](#). The rate of glitches in the 80 Hz–600 Hz band with  $\text{SNR} \geq 10$  is reduced by one order of magnitude, this can be seen in [figure 3.16](#). This has a corresponding effect on the frequency dependent range of up to a factor of 100 at the noise band frequencies as well as a broadband improvement due to the removal of broadband glitches; see [figure 3.17](#).

As shown in [table 3.3](#), there is an improvement in both the GRB-like range [100 Hz–500 Hz] and investigation-specific range due to the commissioning. This results in a short catch up time from commissioning of 1.29 days and 1.57 days for the GRB-like and investigation-specific ranges respectively. These catch up times are small compared to the commissioning down time, which shows the improvement in the range is significant. We can also see in [table 3.3](#) that the commissioning gave a larger increase in range, for both the GRB-like and investigation-specific ranges, than the vetoes. The improvement in the range due to the vetoes increases the catch up times to 10.3 days and 13.7 days for the GRB-like and investigation-specific ranges respectively. However, these catch up times are still small compared to the commissioning down time and so the improvement in the range from the commissioning is still significant.

In this investigation, the commissioning resulted in a significant range im-

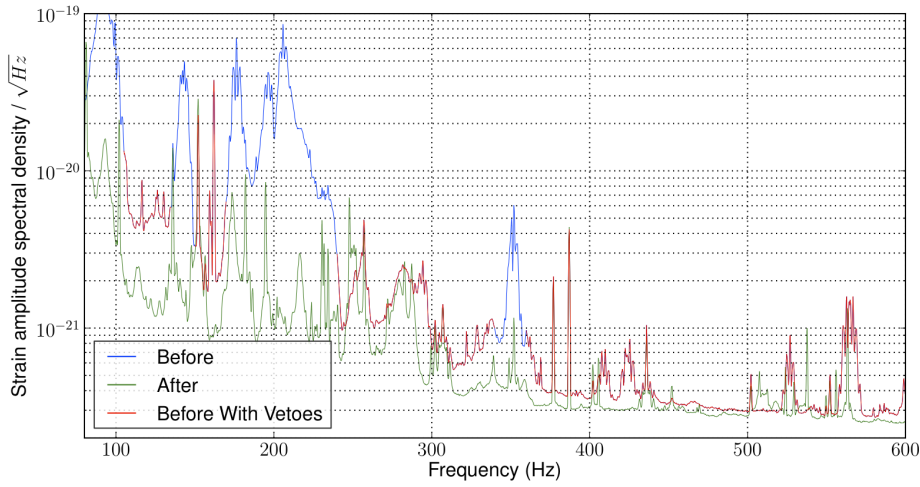


Figure 3.15: Strain noise spectral density for the BDO suspension upgrade. A period of time before the BDO suspension upgrade is shown in blue, while a period of time after the upgrade is shown in green. The improvement from the commissioning can be seen in the removal of the complex noise feature around 20 Hz.

provement even compared to the effective veto. This is due to the loss of bandwidth from a veto of this kind, for though the veto gave similar improvements as the commissioning at some frequencies, there was zero sensitivity at the frequencies of the notches; see [figure 3.17](#).

After the BDO suspension upgrades, a secondary noise source that was caused by the same mechanism was observed, which had previously been buried by the noise caused by the BDO suspensions. This noise source was caused by resonances of elements within the OMC and its suspension. Resonant structures were observed around 255 Hz and 280 Hz in the GW data channel.

The noise can be seen in the Omega-gram of the GW data channel in [figure 3.22\(a\)](#), in comparison to a time without the noise in [figure 3.22\(b\)](#). Comparing the Omega-grams [figure 3.18\(a\)](#) and [figure 3.22\(a\)](#), these noise sources have the same transient behaviour, caused by the variation of the OMC alignment modulating the coupling of the noise into the GW data channel.

As before, a frequency dependent veto could notch out the glitch bands while maintaining sensitivity at other frequencies. The veto applied here is a pair of notches at 245 Hz–265 Hz and 270 Hz–290 Hz. The effect of this veto on the spectrum, frequency dependent range, and cumulative trigger rate are shown in [figures 3.19 to 3.21](#) respectively. The strain noise spectral density is not improved, but the noisy frequency bands are removed; see [figure 3.19](#). The rate of glitches in the 200 Hz–300 Hz band with  $\text{SNR} \geq 10$  is reduced by over one order of magnitude, this can be seen in [figure 3.20](#). A broadband improvement in the frequency dependent range is apparent at frequencies outside of the notch bands, where we have zero sensitivity; see [figure 3.21](#).

To reduce this noise, the OMC isolation was upgraded in a similar manner to the BDO suspension upgrade. In this case, the cumulative down time from the

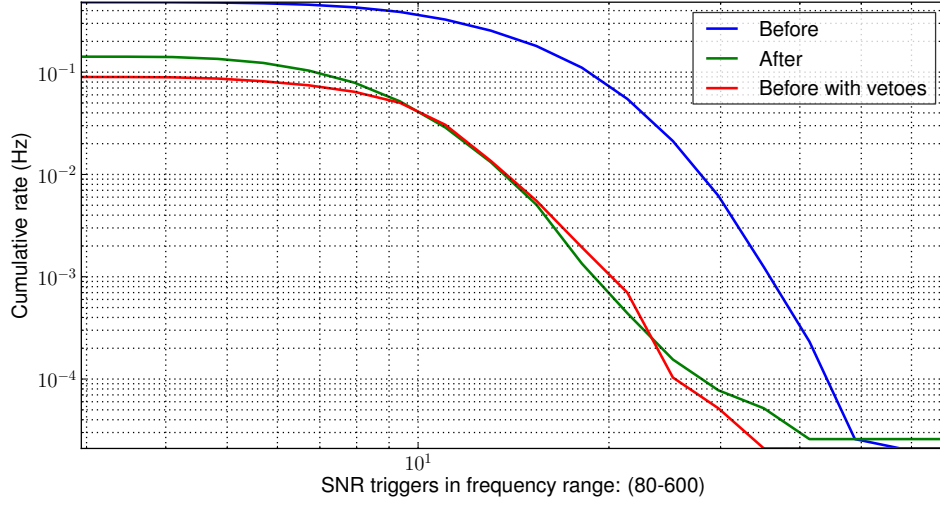


Figure 3.16: Cumulative glitch rate for the BDO suspension upgrade. A period of time before the BDO suspension upgrade is shown in blue, while a period of time after the upgrade is shown in green. There is a decrease in the rate of triggers at all values of SNR in the 100 Hz–60 Hz band.

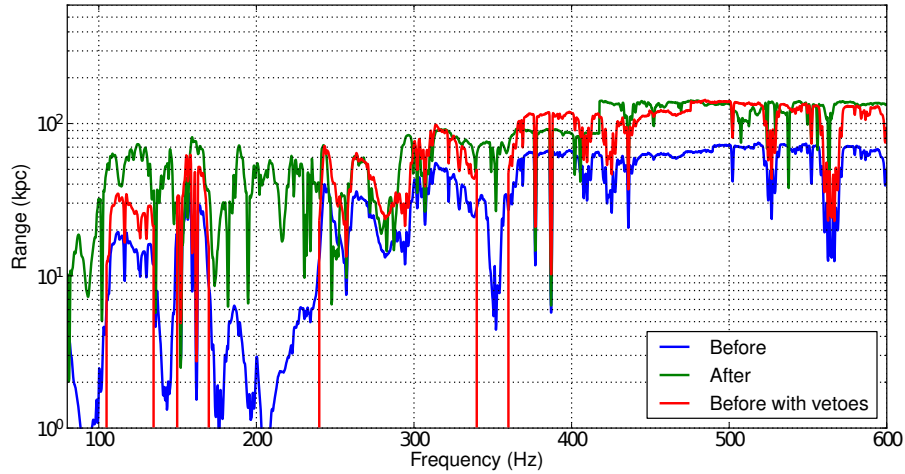
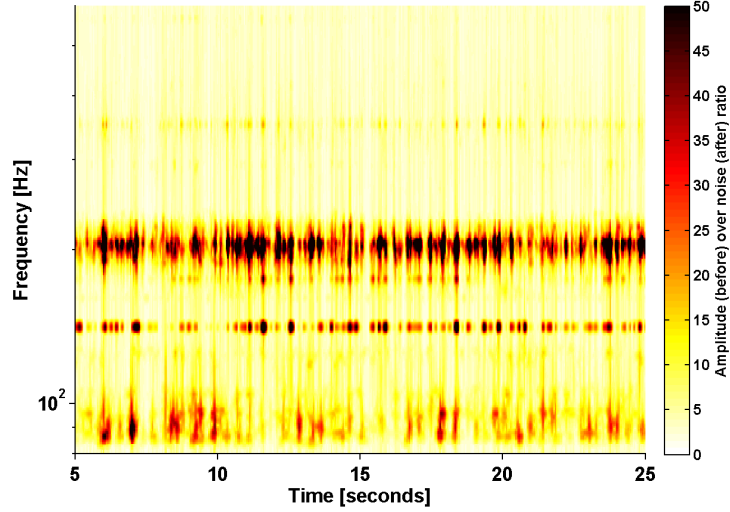
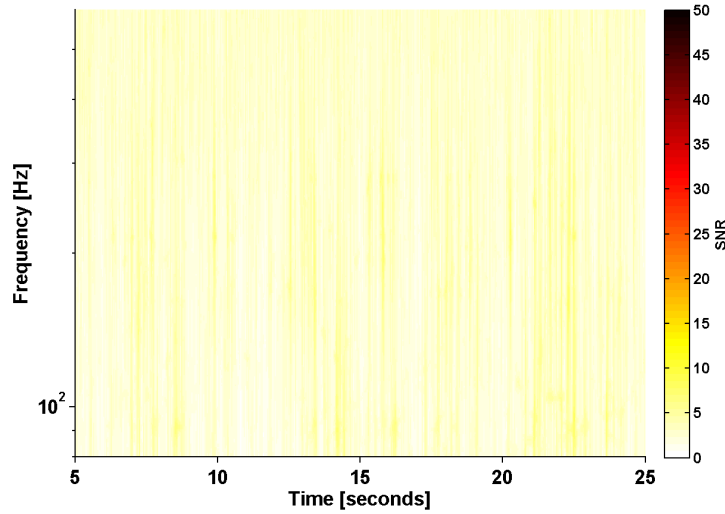


Figure 3.17: Frequency dependent range for the BDO suspension upgrade assuming  $E = 10^{-2} M_{\odot} c^2$ . A period of time before the BDO suspension upgrade is shown in blue, while a period of time after the upgrade is shown in green. The improvement from the commissioning can be seen in the removal of the complex noise feature around 20 Hz.





(a) Before the BDO suspension upgrade



(b) After BDO suspension upgrade

Figure 3.18: Omega-grams for the BDO suspension upgrade. (a) A period of time before the BDO suspension upgrade normalised by a period of time after the BDO suspension upgrade. Variations in the alignment of the OMC from the low frequency motion of the output beam modulates the couple of high frequency noise from the BDO suspension jitter lines into the GW data channel. (b) A period of time after the BDO suspension upgrade, where the improved BDO suspensions have removed the noise source.



required investigations and commissioning work was  $\sim 1.88$  days. The effect of this commissioning on the spectrum, frequency dependent range, and cumulative trigger rate are shown in [figures 3.19 to 3.21](#) respectively. The amplitude of the resonance structures at 255 Hz and 280 Hz are reduced by a factor of at least  $\sim 3$  and  $\sim 1.6$  respectively, see [figure 3.19](#), so that they are buried by the noise floor. The rate of glitches in the 200 Hz–300 Hz band with  $\text{SNR} \geq 10$  is reduced by over one order of magnitude, this can be seen in [figure 3.20](#). The frequency dependent range is improved at all frequencies due to the removal of broadband glitches and the noise features at 255 Hz and 280 Hz are removed, giving an improvement of a factor of  $\sim 4$  and  $\sim 2$  respectively.

As shown in [table 3.3](#), there is an improvement in investigation-specific ranges due to the commissioning. This results in a short catch up time of 0.47 days. These catch up times are small compared to the commissioning down time, which shows the improvement in the range is significant. For the GRB-like range there is no significant improvement in the range due to the commissioning, in fact the GRB range is slightly worse. This effectively gives an infinite catch up time for this commissioning, as the deficit in the number of observable sources will not be recovered. [Table 3.3](#) also shows that the vetoes give a similar improvement for the investigation-specific range as the commissioning. The improvement in the range due to the vetoes increases the catch up times to 3.48 days. This catch up time is larger than the commissioning down time, due to the vetoes giving a similar improvement in range as compared to the commissioning. For the GRB like range, the vetoes give no significant improvement in range in the same way as the commissioning, so again the catch up time when including the vetoes is effectively infinite. The reason that neither of these solutions affected the GRB like range is that the improvement in range in these narrow frequency bands, or the removal of these bands, is negligible compared to the variation in the noise between the before and after commissioning times.

Comparing the BDO suspension upgrade and the OMC isolation upgrade, we can see that although both these noise sources were caused by the same mechanism the severity of the problem greatly affects how we would decide to plan commissioning. The very severe BDO suspension upgrade noise source required immediate commissioning work. Even using a frequency veto to remove the noise, there was still a considerable improvement in both the GRB-like range and investigation-specific range from the commissioning. In comparison, the OMC isolation upgrade noise source did not require immediate commissioning as there is a simple frequency notch veto that removes the narrow band noise features. This frequency veto gave a similar improvement in range compared to the commissioning for the investigation-specific range, and neither solutions gave a significant improvement on the GRB-like range. Using this veto to maintain good data quality, the commissioning work can be delayed and performed at a convenient time to reduce total down time due to commissioning.

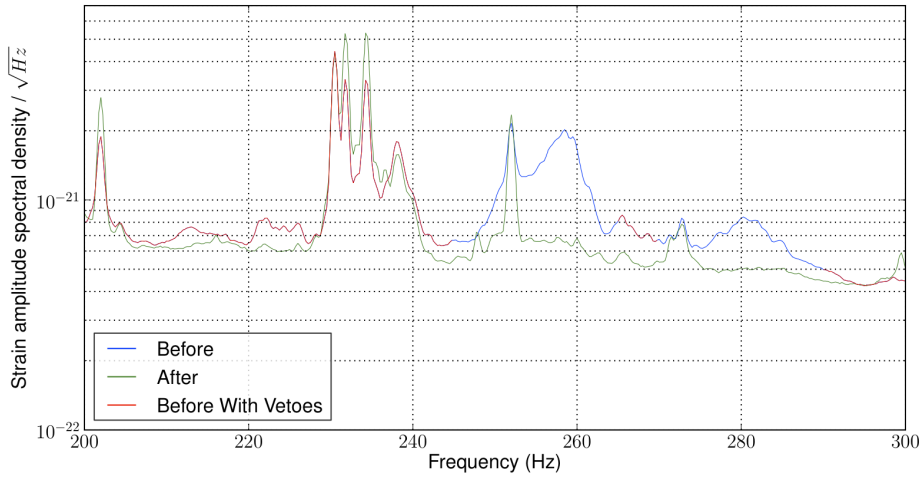


Figure 3.19: Strain noise spectral density for OMC isolation upgrade. A period of time before the OMC isolation upgrade is shown in blue, while the same period with two notch vetoes at 245 Hz–265 Hz and 270 Hz–290 Hz is shown in red. A period of time after the commissioning work was completed is shown in green. The noise features are well confined to two narrow frequency bands around 255 Hz and 280 Hz, the notch vetoes were selected to remove these features from the spectrum.

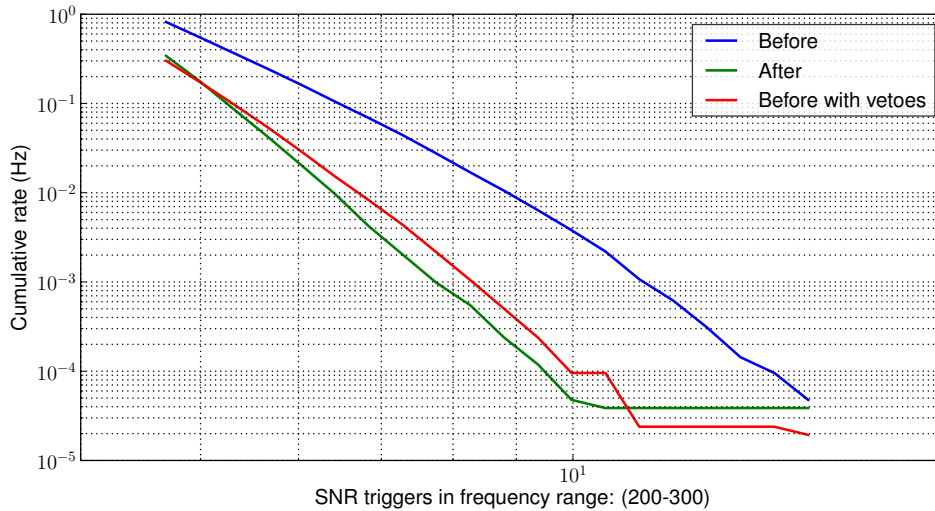


Figure 3.20: Cumulative glitch rate for OMC isolation upgrade. A period of time before the OMC isolation upgrade is shown in blue, while the same period with two notch vetoes at 245 Hz–265 Hz and 270 Hz–290 Hz is shown in red. A period of time after the commissioning work was completed is shown in green. The effect on the glitch rate for the vetoes and commissioning is similar, this shows that both perform well to remove this noise source.

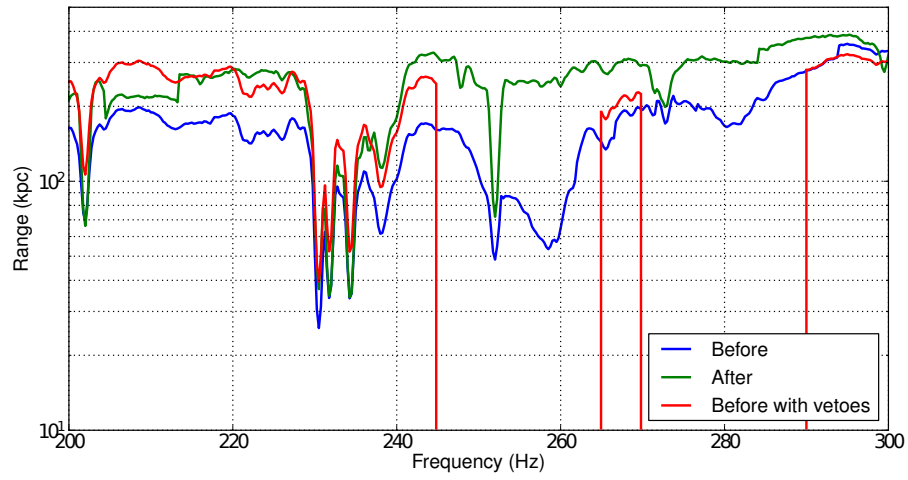
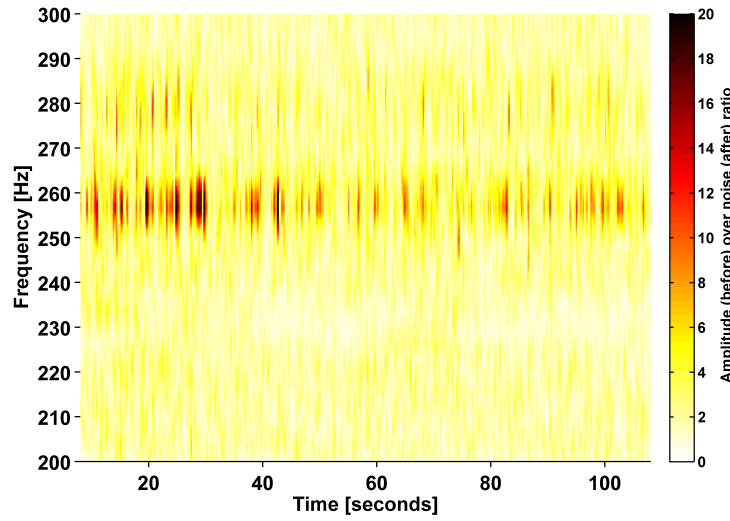
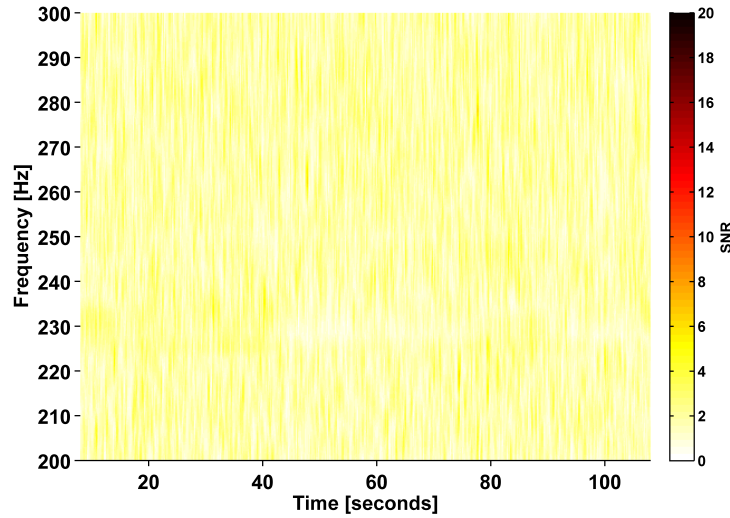


Figure 3.21: Frequency dependent range for OMC isolation upgrade assuming  $E = 10^{-2} M_{\odot} c^2$ . A period of time before the OMC isolation upgrade is shown in blue, while the same period with two notch vetoes at 245 Hz–265 Hz and 270 Hz–290 Hz is shown in red. A period of time after the commissioning work was completed is shown in green. The improvement from the vetoes is at all frequencies because of the removal of broadband glitches, however we have no sensitivity at the frequency of the notch vetoes. The performance of the veto and commissioning work are similar when comparing the range, however the commissioning also gives sensitivity at the frequency of the notch vetoes.



(a) Before OMC isolation upgrade



(b) After OMC isolation upgrade

Figure 3.22: Omega-grams for the OMC isolation upgrade. (a) A period of time before the OMC isolation upgrade normalised by a period of time after the OMC isolation upgrade. We can see the transient noise in the two bands around 255 Hz and 280 Hz. Variations in the alignment of the OMC allow noise entering the detector through the seismic isolation of the OMC to be coupled into the GW data channel. (b) A period of time after the OMC isolation upgrade, where the improved OMC isolation has removed the noise source.

### 3.6.2 Squeezer glitches

GEO 600 is the first large scale interferometric detector to implement squeezing to improve the shot noise limited sensitivity [151]. For an introduction to squeezing and an explanation of how squeezing can be used to reduce the shot noise of a Michelson interferometer see [section 2.5.8](#). A squeezed state of light is injected into the output port of the interferometer (see [figure A.1](#)) to replace the coherent vacuum state that would otherwise be entering this port. If the squeezing is oriented correctly in relation to the electric field inside the interferometer it will improve the shot noise limited sensitivity of the interferometer [90]; see [figure 2.19](#). The orientation of the squeezing error ellipse with relation to the electric field inside the interferometer is controlled to optimise the improvement for the shot noise limited sensitivity as shown in [figure 2.19](#), and this squeezer error point is recorded.

A population of glitches was observed that produced broadband noise in the GW data channel. The noise is short duration and broadband above a few hundred Hz as shown in [figure 3.26\(a\)](#), in comparison to a time without the noise in [figure 3.26\(b\)](#). These glitches only occur during times of squeezing and it was found that these glitches were due to the squeezer malfunctioning and producing noise that was being injected into the interferometer. Although the exact cause of this noise is not well understood, it is thought that this noise source is caused by some element of control system for the squeezer ellipse orientation malfunctioning and allowing the squeezer ellipse to move away from the optimal orientation used to reduce the shot noise.

The squeezer error point RMS increases in coincidence with the periods of broadband glitches in the GW data channel, and so this auxiliary channel could be used to produce vetoes to remove these glitches from the data. An investigation compared the trends of the squeezer error point to the times of the glitches, testing a number of thresholds. A threshold using a sample rate of one second was chosen to produce veto segments; these removed only 0.34% of the science time but vetoed 80% of HACR triggers above 1 kHz with  $\text{SNR} \geq 20$  during the S6E/VSR4 science run. This accounted for 4.1% of all HACR triggers during the S6E/VSR4 science run. The effect of this veto on the spectrum, frequency dependent range, and cumulative trigger rate are shown in [figures 3.23 to 3.25](#) respectively. The strain noise spectral density is not effected, although the transient noise events are loud they do not happen frequently enough to make a significant contribution when averaging over the full 2 hours used for this investigation; see [figure 3.23](#). The rate of glitches in the 100 Hz–3 kHz band with  $\text{SNR} \geq 20$  is reduced by three orders of magnitude, this can be seen in [figure 3.24](#). A broadband improvement in the frequency dependent range can be seen above  $\sim 300$  Hz, as shown in [figure 3.25](#).

This noise source was removed by a period focused commissioning and maintenance on the squeezer bench, lasting  $\sim 1.21$  days. The effect of this commissioning on the spectrum, frequency dependent range, and cumulative trigger rate are shown in [figures 3.23 to 3.25](#) respectively. The commissioning gives the same sensitivity improvement as applying the veto.

In [table 3.3](#) there is an improvement in SN-like range [500 Hz–4 kHz] and

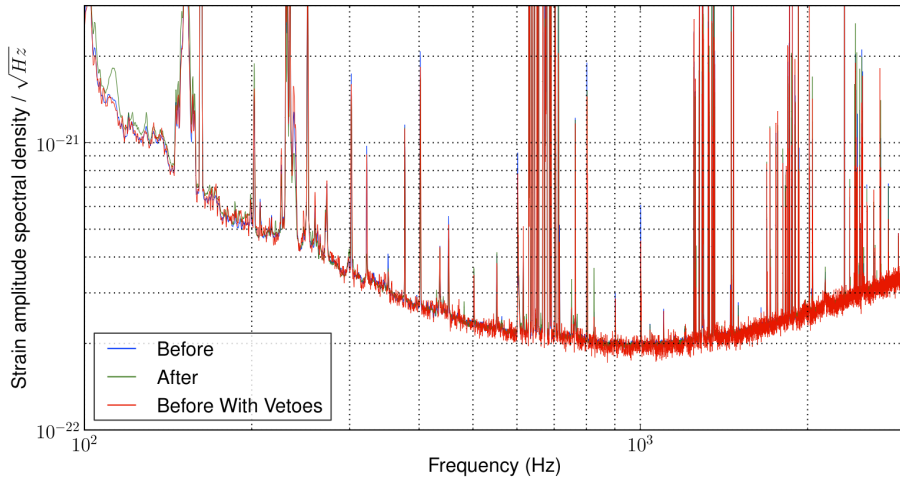


Figure 3.23: Strain noise spectral density for squeezer glitches. A period of time with squeezer glitches is shown in blue, while the same period with vetoes applied is shown in red. A period of time without these glitches is shown in green. The transient noise events are loud, but they do not happen frequently enough to make a significant change to the strain noise spectral density, when averaged over the full 2 hours used for this investigation.

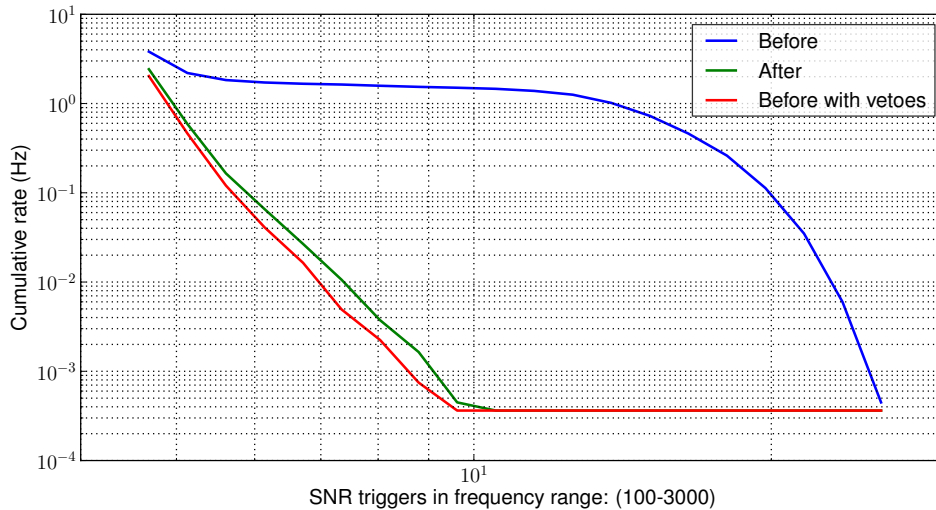


Figure 3.24: Cumulative glitch rate for the squeezer glitches. A period of time with squeezer glitches is shown in blue, while the same period with vetoes applied is shown in red. A period of time without these glitches is shown in green. Both the vetoes and commissioning do well to remove the large number of high SNR glitches that were being produced by this noise source.

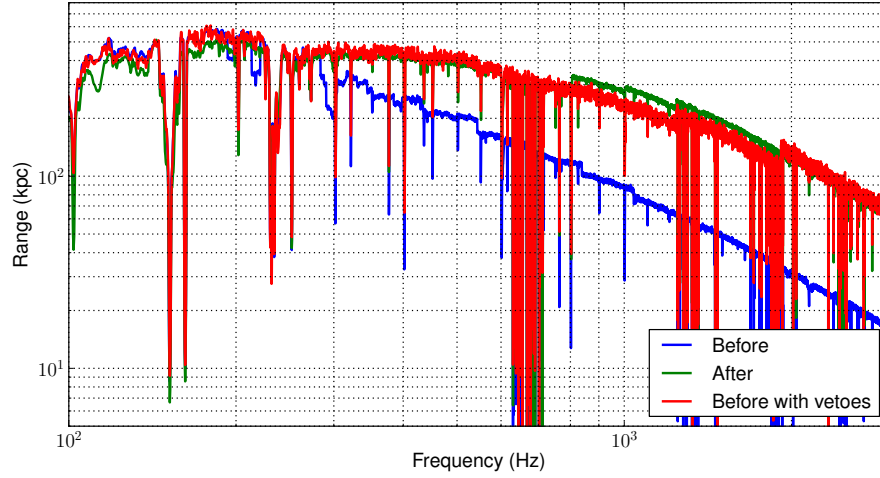
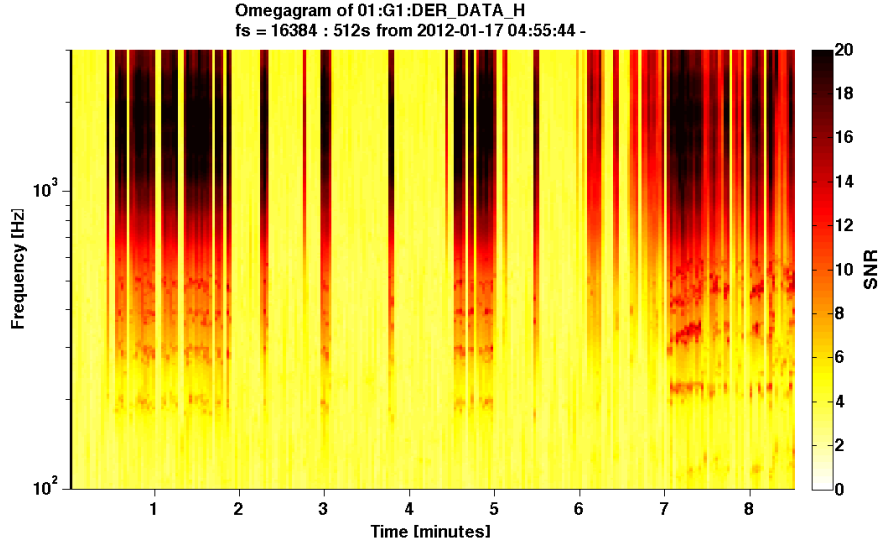


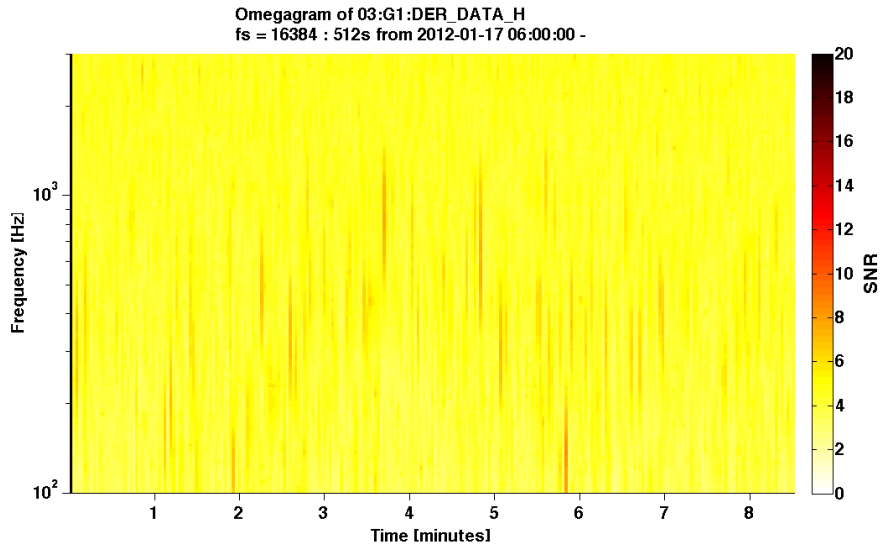
Figure 3.25: Frequency dependent range for the squeezer glitches assuming  $E = 10^{-2} M_{\odot} c^2$ . A period of time with squeezer glitches is shown in blue, while the same period with vetoes applied is shown in red. A period of time without these glitches is shown in green. The glitches produce a decrease of up to a factor of 5 in the frequency dependent range of the detector in the shot noise limited frequency region about a few hundred Hz.

investigation-specific ranges due to the commissioning. This results in a trivial catch up time of 0.05 days and 0.07 days for the SN-like range and investigation-specific range respectively. Also, in [table 3.3](#) the vetoes give a similar improvement in performance for the SN-like and investigation-specific range as the commissioning. In the case of the SN-like range the commissioning performs slightly better, whereas for the investigation-specific range the vetoes perform slightly better. The difference in the improvements for the SN-like range and investigation-specific range between the vetoes and the commissioning is not significant compared to variations in the noise between the two times. This gives us a very large catch up time for the SN-like range of 16.3 days and an infinite catch up time for the investigation-specific range.

From this investigation we can see that for this noise source, the veto and commissioning give the same strong improvement for both the SN-like range and investigation-specific range. Therefore the commissioning here was not necessarily required as the veto gives the same improvement in range and cleanly removes this noise source.



(a) Squeezer glitches



(b) No squeezer glitches

Figure 3.26: Omega-grams for the squeezer glitches. (a) A period of time containing glitches caused by the squeezer. (b) A period of time without these glitches. The squeezer is working well to improve the shot noise limited sensitivity.



### 3.6.3 3.5 Hz dither squeezer glitches

Sinusoidal modulations are applied to two degrees of freedom of each of two of the three BDOs, with all four of these dithers at different frequencies. The purpose of the dithers are to create small misalignment signals that can be used by automatic control processes to maintain the alignment of the interferometer beam to the output mode cleaner. A 3.5 Hz dither specifically modulates the degree of freedom with the largest geometric effect on the squeezer path.

When the 3.5 Hz BDO dither was active and the squeezed light injection was operating the rate of low amplitude glitches in the shot noise limited frequency region increased. As can be seen in [figure 3.28](#), the rate of glitches with SNR of 6 increased by a factor of 5. These glitches were not present while the shutter between the squeezer and the interferometer was closed, nor were they present after the 3.5 Hz dither was deactivated. The glitch mechanism is not entirely clear, however there is a strong correlation of glitch occurrence with the dither period. This can be seen in [figure 3.30\(a\)](#) in comparison to a time without this problem as shown in [figure 3.30\(b\)](#), and there was no drift in this behaviour over several months. These glitches do not show up in the Omega-grams because they tend to be low SNR glitches. A period with these glitches can be seen in [figure 3.31\(a\)](#) in comparison to a period after the dither was removed in [figure 3.31\(b\)](#). There is a slight change in both the spectrum and frequency dependent range, as can be seen in [figure 3.27](#) and [figure 3.29](#), although the difference is minimal. This change is not fully understood and could possibly be due to something unrelated since the reference times were separated by a month.

This noise source has no veto as the glitches have low SNR and do not show correlation with any auxiliary channels, and occur continuously, so the only way to remove it is to remove the noise source. However, because this occurred during the S6E/VSR4 science run in 2011, detector observation time was very valuable and unnecessary commissioning was to be avoided if possible. At the time, only the elevated glitch rate with squeezer operation was known and not the dependence on the 3.5 Hz dither. The question arose, whether or not to turn off the squeezer or to investigate the source of the glitches.

Fortunately during the science run, the ability to carry out studies similar to those described in this chapter were available. Elements of the coherent Wave-Burst all-sky burst search analysis [166] were being run on the GEO 600-Virgo network on a weekly basis. These analyses were providing a figure-of-merit for the non-stationary elements of the network noise similar to  $\rho$  in the integrated fixed false-alarm probability range defined by [equation \(3.1\)](#) and [equation \(3.2\)](#). A directed analysis at the 3.5 Hz dither squeezer glitches which compared time intervals with the squeezer shutter open and closed showed that these glitches were only affecting the network fixed false-alarm probability SNR threshold by less than 10%. In the single interferometer study shown in [figure 3.28](#) we get similar results. Since the squeezing at that time was acting to decrease the noise spectral density of GEO 600 by approximately 20% across the shot noise limited frequency range ( $> 500$  Hz), we decided that no further action was needed. After the S6E/VSR4 science run, there was a commissioning break, during which the optical path from the squeezer to the interferometer was extensively modified to

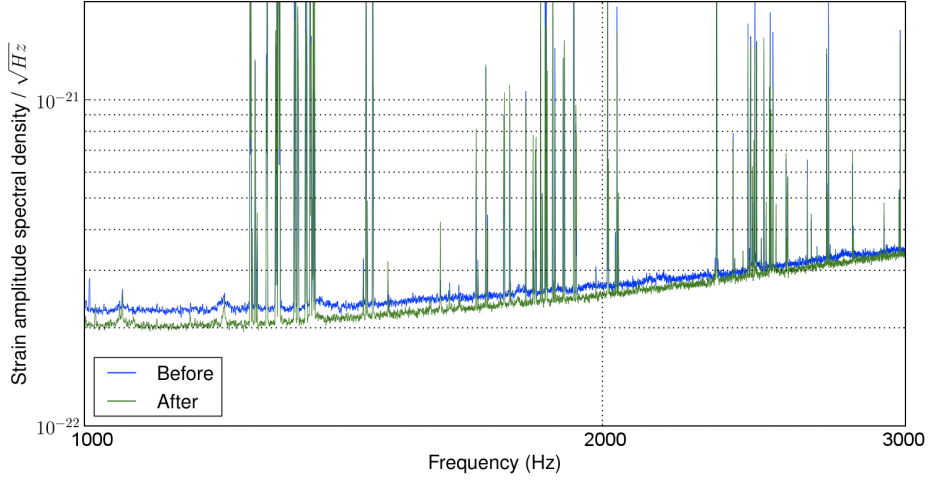


Figure 3.27: Strain noise spectral density for 3.5 Hz squeezer glitches. A period of time with glitches is shown in blue while a time without these glitches is shown in green. These glitches have a small effect on the spectrum, although this difference is not significant.

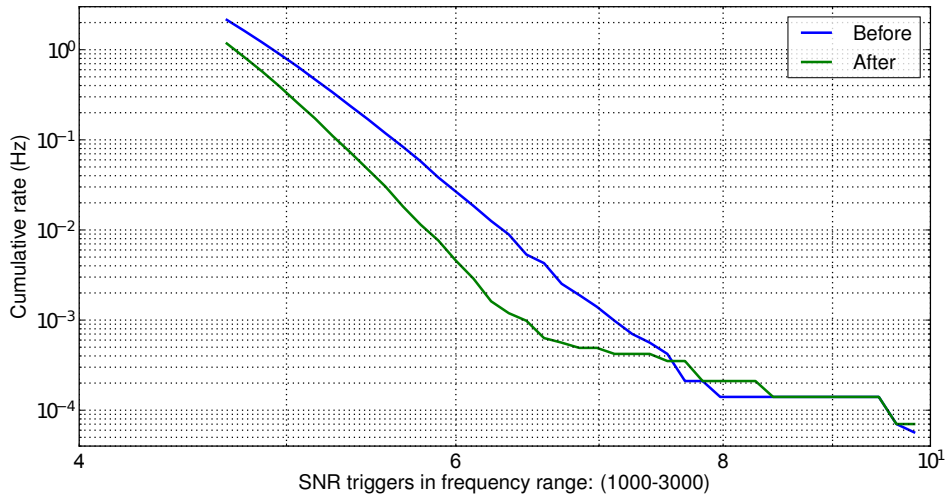


Figure 3.28: Cumulative glitch rate for 3.5 Hz squeezer glitches. A period of time with glitches is shown in blue while a time without these glitches is shown in green. There is a decrease in the rate of low SNR triggers when the 3.5 Hz dither signal has been removed, at SNR 6 the change is a factor of 5.

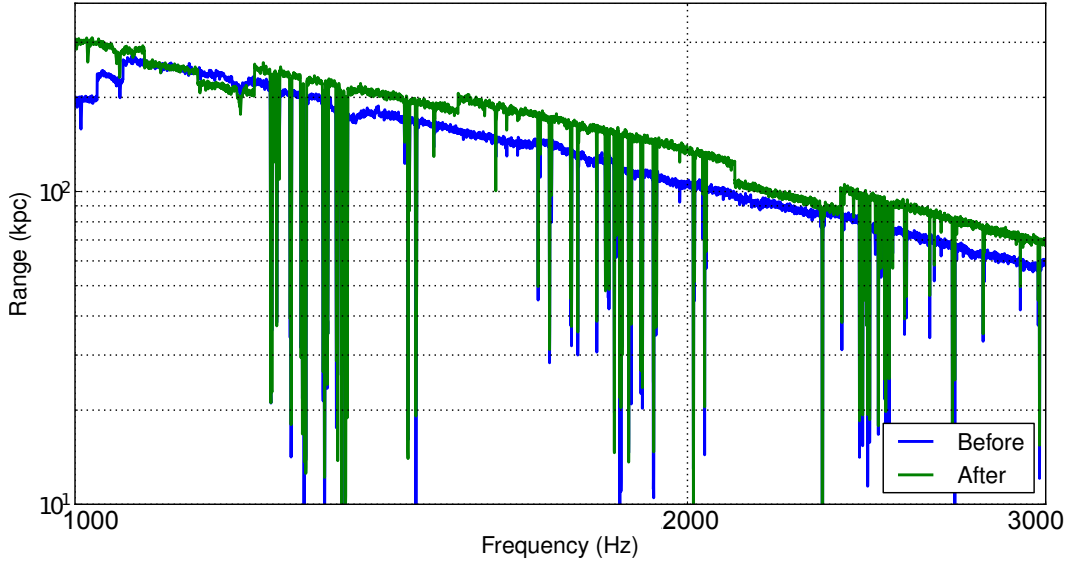
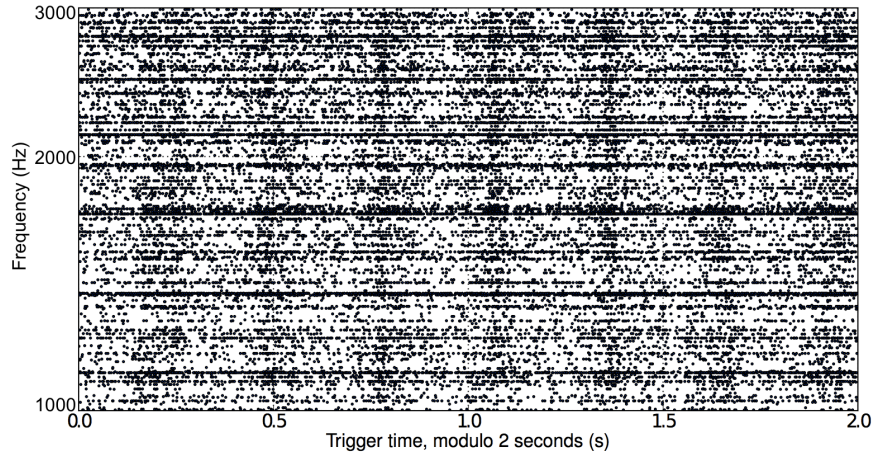


Figure 3.29: Frequency dependent range for 3.5 Hz squeezer glitches assuming  $E = 10^{-2} M_{\odot} c^2$ . A period of time with glitches is shown in blue while a time without these glitches is shown in green. These glitches have a small effect on the frequency dependent range in the shot noise limited frequency region.

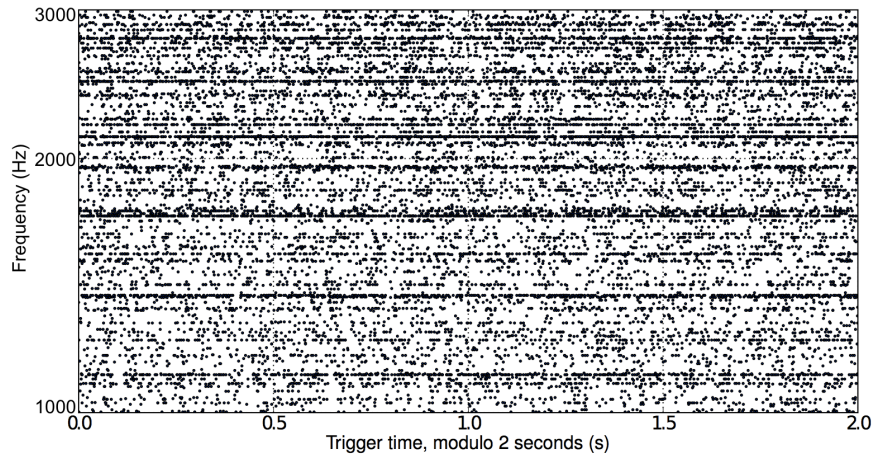
improve the optical isolation and reduce scattered light. After this, the presence of the 3.5 Hz dither was not sufficient to reintroduce the glitches, nor were they seen again.

As shown in [table 3.3](#) we can see that there is no significant improvement in the SN-like range or the investigation-specific range. The difference can be accounted for by the variations in the noise between the before and after commissioning times, here of order 10%. As this noise source was not limiting the sensitivity of the detector any commissioning down time from working on this problem would produce a deficit in the number of observable sources that could not be regained from this commissioning as it will give no improvement in the range. This was particularly important for this noise source, as it was observed during the S6E/VSR4 science run while GEO 600 was taking coincident data with Virgo.

From this investigation we can see that for this noise source, the best solution was to wait until a period of scheduled commissioning when the 3.5 Hz dither signal could be removed without incurring any additional down time.

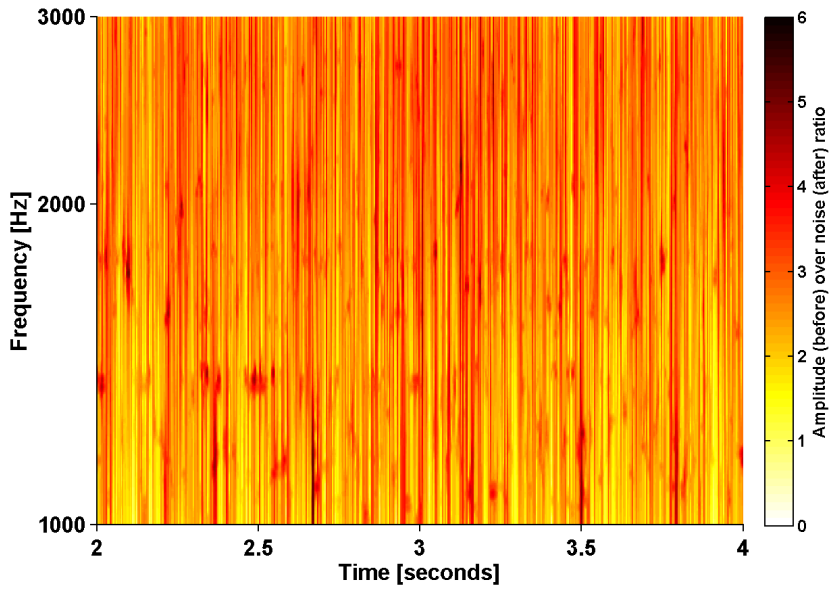


(a) Stacked triggergram with squeezer backscatter glitches

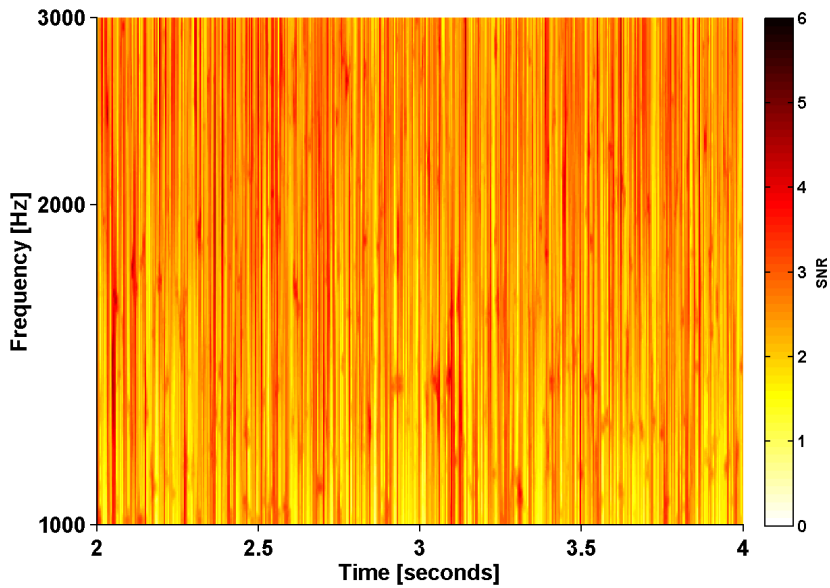


(b) Stacked triggergram without squeezer backscatter glitches

Figure 3.30: Stacked triggergram for the 3.5 Hz squeezer glitches, plotting trigger time modulo 2 seconds to reveal the 3.5 Hz periodicity. (a) A period of time when the 3.5 Hz dither squeezer glitches were happening, seen as a 3.5 Hz periodicity. (b) A period of time after the 3.5 Hz dither signal was removed; there is no 3.5 Hz periodicity observable.



(a) Before the 3.5 Hz dither was removed



(b) After the 3.5 Hz dither was removed

Figure 3.31: Omega-grams for the 3.5 Hz squeezer glitches. (a) A period of time with the 3.5 Hz dither squeezer glitches were happening normalised by a period of time after the 3.5 Hz dither signal was removed. (b) A period of time after the 3.5 Hz dither signal was removed. Glitches from this dither were low SNR and infrequent,  $\sim 10^{-2}$  Hz at SNR 6 so individual events are not clear. As shown in [figure 3.30](#), long stretches of must be stacked to reveal the periodicity of this noise, and so we do not observe individual events in these Omega-grams.

Investigation [Commissioning down time (days)]	Range type [frequency band]	Before range (kpc)	Vetoed before range (kpc)	After range (kpc)	Catch up from commissioning (days)	Catch up with vetoes (days)
<b>Beam Direction Optics (BDO)</b> [20.83]	GRB [100 Hz–500 Hz]	51	93	134	1.29	10.3
	Noise specific [80 Hz–600 Hz]	54	97	131	1.57	13.7
<b>Output mode cleaner (OMC)</b> [1.88]	GRB [100 Hz–500 Hz]	169	170	157	$\infty^\dagger$	$\infty^\dagger$
	Noise specific [200 Hz–300 Hz]	205	304	352	0.47	3.48
<b>Squeezer glitches</b> [1.21]	SN [500 Hz–4 kHz]	62	183	188	0.05	16.3
	Noise specific [1 kHz–3 kHz]	91	254	238	0.07	$\infty^\dagger$
<b>3.5 Hz dither squeezer glitches</b> [0]	SN [500 Hz–4 kHz]	157	-	177	Undefined*	Undefined*
	Noise specific [500 Hz–3 kHz]	144	-	168	Undefined*	Undefined*

Table 3.3: For each investigation in [section 3.5](#) we give the commissioning down time, an astrophysically motivate fixed false-alarm probability range and a noise source specific frequency band fixed false-alarm probability range, see [section 3.3](#); for a period before commissioning, the same period before commissioning with vetoes applied, and for a period after commissioning. We also give the catch up times found using the commissioning solution and found using the veto solution following the method described in [section 3.3](#) and given by [equation \(3.4\)](#).

$\dagger$  The commissioning did not make a significant improvement over the noise. We therefore assume in this case that the range has not changed and so the catch up time is effectively  $\infty$ .

\* The commissioning work for this investigation was done while other work was happening, so the commissioning time is effectively zero and the catch up time is not defined.



### 3.6.4 Summary

Here we have discussed a small selection of noise investigations undertaken at GEO 600. In each case, a different strategy for removing the noise contamination proved optimal.

In [section 3.6.1](#) a frequency dependent veto was used to remove the noise source caused by the BDO suspensions and the OMC isolation. These notches removed the noise sources well from both the spectrum and frequency dependent range, but left these bands with zero sensitivity. There was also a clear understanding of the physical cause for this noise, allowing effective hardware upgrades to be planned and commissioned. For the BDO noise, commissioning performed better than the frequency veto, as can be seen in [table 3.3](#), and so this commissioning was important to effectively remove this noise. On the other hand, for the OMC noise coupling, the veto performed as well as the commissioning at improving the narrow investigation-specific range, but neither affected the GRB-like range, as can be seen in [table 3.3](#). In this case the commissioning could have waited until a convenient opportunity, to reduce total down time.

In [section 3.6.2](#) we consider squeezer glitches. An auxiliary channel was available that was effective at producing veto segments that removed this noise cleanly. This veto performed as well as the commissioning at removing the noise source, as can be seen in the range improvements for this investigation in [table 3.3](#). Therefore the commissioning was not necessarily required. However, to remove this noise completely the commissioning could be performed at a convenient time to reduce the total down time. If this type of noise source appeared during a science run, then commissioning could be delayed if the catch up time was larger than the expected observing time left in the science run.

In [section 3.6.3](#) we considered 3.5 Hz dither glitches. There was no veto available to remove this noise source. This was not a problem however, as this noise source was shown to not limit the sensitivity of the detector, and so could be left in place. This decision was also taken due to the squeezing giving an improvement in noise spectral density of approximately 20% at the time this noise source was observed. There was a commissioning solution to this problem, but without a sensitivity gain available, so this was performed while other commissioning was already planned and in so doing did not cause any additional down time.

At GEO 600 we were unable to do these investigations at the time that the noise sources were first observed due to the GEODC group being manpower limited. This will not be the case for the advanced detectors. The advanced LIGO and advanced Virgo detector characterisation groups have the opportunity to evaluate the sensitivity cost of noise phenomena as they appear, and make recommendations about veto/commissioning solutions based on the expected detector down time versus the possible improvement in sensitivity. This is particularly important in the lead up to and during the first science runs, while the detectors are still being brought up to design sensitivity. This requires predictions about the expected improvements from any commissioning work. A simple way to do this, in the case of noise features like those observed in [section 3.6.1](#), is to remove the glitches in the frequency bands affected using a frequency veto and interpolate over the notch bands, in order to estimate the expected sensitivity

improvement in the commissioned detector. In the case of transient noises, such as discussed in [section 3.6.2](#), then applying vetoes is a good estimate of the expected performance once this noise has been removed. Finally, in the case of a noise source which does not limit the sensitivity of the detector as observed in [section 3.6.3](#), this noise source can be monitored until it is convenient to do the required commissioning without inducing any additional down time. These predictive methods will be discussed further in [\[165\]](#).

When applying this method to advanced LIGO and advanced Virgo, there are many other factors that come into play when planning commissioning. This method is just one way to measure the urgency of performing commissioning to remove a particular noise source, but factors such as commissioning time, commissioning cost, man power, and other possible benefits such as improved detector stability from the commissioning will need to be taken into account. This method is proposed to complement these other factors which must be taken into account when planning commissioning activities. We have shown in this section that by intelligently guiding commissioning decisions using detector characterisation of noise sources as they are discovered in the advanced LIGO and advanced Virgo detectors, we can help to increase the number of observable sources.



# Gravitational Waves Associated with Gamma-Ray Bursts

# 4

In this chapter we present the methods and results of a search for GWBs associated with GRBs using the GEO 600 detector in combination with the LIGO and Virgo detectors. In [section 4.1](#) we outline some of the potential mechanisms for producing GW signals in GRBs that are most interesting for an unmodelled search using GEO 600 data. In [section 4.2](#) we give a brief introduction to the standard package used to search for unmodelled GWs associated with GRBs, the X-PIPELINE analysis package. In [section 4.3](#) we give details of an analysis of 78 GRBs which were detected between 4<sup>th</sup> Nov 2005 and 3<sup>rd</sup> Nov 2011 and which occurred in periods when only GEO 600 and one of the LIGO/ Virgo detectors were operating.

## 4.1 Gamma-Ray Bursts

In this section we outline some of the mechanisms for GW production in GRBs, which are the source for the analyses reported in this chapter. All of the analyses performed here include the GEO 600 detector which has modest sensitivity at low frequencies ( $< 500$  Hz) compared to the LIGO and Virgo detectors, so we mainly focus on sources of GWs at higher frequencies from a few hundred Hz up to a few thousand Hz. There exist several plausible models for GW emission at these frequencies which could be strong enough to be detected by ground based GW detectors.

The progenitors of short GRBs are believed to be associated with the merger of a NS either with another NS or a BH. The recent observation of kilonova associated with GRB 130603B [[167](#), [168](#)] gives support to this progenitor model. The inspiral phase of these mergers is expected to be a bright source of gravitational radiation [[169](#)]. Although most of the GW energy flux from the inspiral occurs at frequencies below 500 Hz, numerical simulations of BNS mergers have shown that substantial GW emission can occur at frequencies greater than 1 kHz [[170](#), [171](#)]. BNS mergers may result in the formation of a hyper-massive neutron star, which can produce strong GW emission as it collapses to a black hole [[172](#), [173](#)]. Up to a few percent of short GRBs with unknown redshifts could be

produced by giant flares from a local population of soft gamma-ray repeaters (SGRs) which are expected to produce some GW energy ( $\lesssim 10^{-8} M_{\odot} c^2$ ) in the 1 kHz range. This is detectable only on Galactic scales [34, 174, 175, 176].

The progenitors of long GRBs are core-collapse supernovae in rapidly rotating massive stars [177, 178, 32, 33]. Simulations of core-collapse supernovae indicate several methods for GW emission at frequencies of several hundred Hz to 1 kHz, but the amplitude of the emission is highly uncertain [23]. The most optimistic emission models arise from the pulsations of a proto-neutron star core, which may release  $\sim 10^{-7} M_{\odot} c^2$  in GWs in a narrow frequency band around 1 kHz [179, 180]. One of the most extreme scenarios for GW emission from long GRBs is dynamical fragmentation of a rapidly differentially spinning stellar core-collapse, producing a coalescing system of two protoneutron stars [37, 38]. Although this scenario is unlikely [39], the GW emission would be very strong producing  $10^{-2} M_{\odot} c^2$  to  $10^{-1} M_{\odot} c^2$  of energy in GWs in the 50 Hz–1 kHz frequency band. The so-called bar mode instability, in the  $l = 2, m = 2$  non-axisymmetric mode, is an optimistic model for GW emission in extreme core-collapse supernovae, producing GWs in the 500 Hz–2 kHz frequency band [40, 38]. If the deformation remains coherent for  $\sim 100$  ms,  $E_{\text{GW}} \sim 0.1 M_{\odot} c^2$  could be emitted at 1 kHz.

SGR are believed to be highly magnetized neutron stars (magnetars). Significant energy could be emitted as GWs in SGR giant flares, this could occur during excitation of the stars non-radial modes, producing GWs with kHz-frequencies [181, 182, 183]. Theoretical upper limits have been set on the emitted energy in GWs from SGRs of  $10^{-7} M_{\odot} c^2$  [182] and  $10^{-6} M_{\odot} c^2$  [184]. Searches for GWs associated with SGRs have been performed [54, 52].

Both short and long GRBs are expected to result in the formation of a black hole with an accretion disk. Instabilities in the accretion disk can emit significant energy in GWs, perhaps  $10^{-2} M_{\odot} c^2$ . Various semi-analytical scenarios have been proposed which produce up to  $10^{-2} M_{\odot} c^2$  in GWs, all of which correspond to some rotational instability developing in the accretion disk or central engine. An accretion disk that cools rapidly enough to become self-gravitating may fragment into one or more smaller bodies and generate an inspiral-like signal that persists to higher frequencies ( $\sim 1$  kHz) [41]. Instead of an accretion disk, a torus may form around the black hole and convert up to  $0.1 M_{\odot} c^2$  of the spin energy of the black hole into GWs in the 1 kHz–2 kHz band [185, 186]. Numerical simulations have produced similar signals [187, 170]. Finally, the in fall of matter from a rapidly-rotating accretion disk could produce GWs in the  $\sim 700$  Hz–2.4 kHz band [188].

## 4.2 X-PIPELINE

In this section we give details of the search algorithm X-PIPELINE [189, 44], which is an externally triggered coherent GWB analysis pipeline. X-PIPELINE has previously been used in a number of LIGO-Virgo searches for GWBs [53, 43, 55, 190, 57]. Section 4.2.1 gives details of the inputs that are required to

run an analysis using X-PIPELINE. Section 4.2.2 gives details on time-frequency map generation and the process for identifying signal and noise transients in the data. Section 4.2.3 gives the formulation used to describe the data streams from a network of GW detectors. Section 4.2.4 gives details on the dominant polarisation frame and the coherent likelihoods. Section 4.2.5 gives details on the coherent veto tests used to separate signal from noise. Section 4.2.7 gives details on the closed box analyses and tuning procedure used by X-PIPELINE. Section 4.2.6 gives details on the procedure for identifying candidate events, and producing upper limits in the case of no detection. This section draws heavily from [189], which gives a full description of X-PIPELINE.

### 4.2.1 X-PIPELINE Analysis Inputs

Externally triggered searches use the known time and sky position of a externally observed event such as a GRB to conduct a focused search in data for GWs consistent with that time and sky position. This reduces the parameter space that has to be analysed, so reducing the computational cost for the search. In principle, as the event has been measured using multiple techniques (GW and EM) we may gain more insight into the nature of the source, than if the detection was made using just GWs. Parameters for a particular event such as time, sky position, sky position uncertainty, and in the case of GRBs the  $T_{90}$ <sup>1</sup> are fed into X-PIPELINE.

Data from GW detectors surrounding the time of a GRB is separated into an *on-source region*, the time in which we would expect to observe a GW signal associated with the GRB, and an *off-source region*, an interval around the trigger time (excluding the on-source) that is used to characterise the detector background. Here we typically use an on-source window of  $[-600, +60]$  s around the trigger time and an off-source window of  $[-1.5, +1.5]$  hr around the trigger time, unless otherwise stated. For very long-lasting GRBs, the off-source window is extended to include the entire  $T_{90}$  time after the trigger time.

### 4.2.2 Time-Frequency Maps and Trigger Identification

Data from each of the GW detectors is whitened, using a linear predictor error filter, and then time-shifted according to the light travel time for the trigger sky position, so that a GW signal is simultaneous in each of the detector data streams. The data is divided into 50% overlapping segments and Fourier-transformed, producing time-frequency maps for each detector. X-PIPELINE then produces linear combinations of the time-frequency maps which maximise or minimise the SNR of GW signals in the data.

To identify candidate GW signals in these time-frequency maps clustering is used. For the pixels in the time-frequency map of the *detection statistic*, such as  $E_{\text{SL}}$  (discussed in section 4.2.4), a threshold is applied to select some percentage of the map pixels, typically 1% of the pixels with the highest value of the detection statistic, which are marked as “black”. Black pixels that share a boundary or

---

<sup>1</sup>the period in which 90% of the energy from the GRB is observed.

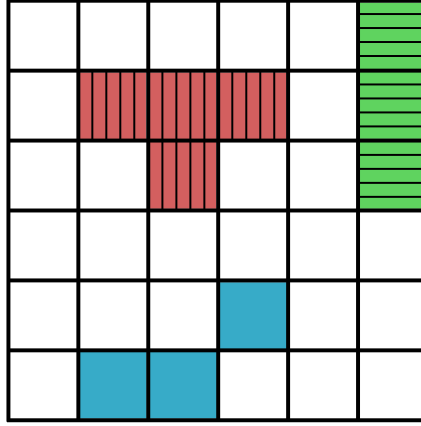


Figure 4.1: Time frequency map with “black” pixels grouped into three clusters. Next-nearest neighbour black pixels are grouped into clusters, here each cluster is give an different hatching pattern.

corner are grouped into clusters, this is called next-nearest neighbour clustering, see [figure 4.1](#). This procedure is appropriate for GWBs which are likely to be continuous in the time-frequency plane. These clusters are assigned a “significance”, which is a measure of the likelihood of the cluster being a GW signal; this is used to compare clusters to determine which is the “loudest”. For most choices of detection statistic, the significance is defined to be the statistic value. It’s different only for the so-called projection likelihoods ( $E_{\text{SL}}, E_+, E_\times, E_{\text{tot}}$  (discussed in [section 4.2.4](#))) where the cumulative probability distribution in Gaussian noise is known analytically; in these cases the significance is defined as the cumulative probability at the measured detection statistic.

This procedure is repeated for a number of different fast Fourier transform (FFT) lengths and for each sky position. We repeat with multiple FFT lengths because the shape of the GW signal is not known *a priori*, and the optimal pixel size is that which contains the signal in the minimum number of pixels, this helps to reduce pollution of the statistics from noise. Once clusters for each FFT length have been produced, they are compared in a second level of clustering where clusters which overlap in the time-frequency plane are discarded keeping only the cluster with the largest significance.

### 4.2.3 Detector Data Streams

In the presence of a GW signal,  $h_+(t, \vec{x})$ ,  $h_\times(t, \vec{x})$  from the direction  $\hat{\Omega}$ , the data streams from a detector  $\alpha = [1, \dots, D]$  can be written as the linear combination of the GW signal and noise  $n_\alpha$ :

$$d_\alpha(t + \Delta t_\alpha(\hat{\Omega})) = F_\alpha^+(\hat{\Omega})h_+(t) + F_\alpha^\times(\hat{\Omega})h_\times(t) + n_\alpha(t + \Delta t_\alpha(\hat{\Omega})). \quad (4.1)$$

Here  $F_\alpha^+(\hat{\Omega}), F_\alpha^\times(\hat{\Omega})$  are the *antenna response functions* which describe the directional sensitivity of the detector to the plus and cross polarisations respectively.  $\Delta t_\alpha(\hat{\Omega})$  is the time delay between the signals arrival at the detector at position

$\vec{r}_\alpha$  and some arbitrary reference position  $\vec{r}_0$ :

$$\Delta t_\alpha(\hat{\Omega}) = \frac{1}{c}(\vec{r}_0 - \vec{r}_\alpha) \cdot \hat{\Omega}. \quad (4.2)$$

The one-sided noise power spectral density  $S_\alpha$  of the noise  $\tilde{n}_\alpha$  is

$$\langle \tilde{n}_\alpha^*[k] \tilde{n}_\beta[k'] \rangle = \frac{N}{2} \delta_{\alpha\beta} \delta_{kk'} S_\alpha, \quad (4.3)$$

where the “ $\sim$ ” denotes the Fourier transform,  $k$  is the discrete Fourier frequency and we use angled brackets to indicate an average over noise instantiations.

In the whitening step, the Fourier transformed data streams  $\mathbf{d}$ , noise  $\mathbf{n}$ , and the antenna factors  $\mathbf{F}$  are divided by the frequency-dependent sensitivity of each detector. It is convenient to define the noise-spectrum weighted quantities

$$\tilde{d}_{w\alpha}[k] = \frac{\tilde{d}_\alpha[k]}{\sqrt{\frac{N}{2} S_\alpha[k]}}, \quad \tilde{n}_{w\alpha}[k] = \frac{\tilde{n}_\alpha[k]}{\sqrt{\frac{N}{2} S_\alpha[k]}}, \quad F_{w\alpha}^{+, \times}[\hat{\Omega}, k] = \frac{F_\alpha^{+, \times}[\hat{\Omega}, k]}{\sqrt{\frac{N}{2} S_\alpha[k]}}, \quad (4.4)$$

in this way the search accounts for differences in detector sensitivity which are frequency dependent. We also define the normalisation of the whitened noise

$$\langle \tilde{n}_\alpha^*[k] \tilde{n}_\beta[k'] \rangle = \delta_{\alpha\beta} \delta_{kk'}. \quad (4.5)$$

Using this notation we can write [equation \(4.1\)](#) in the simple matrix form

$$\tilde{\mathbf{d}} = \mathbf{F} \tilde{\mathbf{h}} + \tilde{\mathbf{n}}, \quad (4.6)$$

where we have dropped the indices for frequency and sky position. The boldface symbols  $\tilde{\mathbf{d}}$ ,  $\mathbf{F}$ ,  $\tilde{\mathbf{n}}$  refer to noise-weighted quantities that are vectors or matrices on the space of detectors:

$$\tilde{\mathbf{d}} \equiv \begin{bmatrix} \tilde{d}_{w1} \\ \tilde{d}_{w2} \\ \vdots \\ \tilde{d}_{wD} \end{bmatrix}, \quad \tilde{\mathbf{h}} \equiv \begin{bmatrix} \tilde{h}_+ \\ \tilde{h}_\times \end{bmatrix}, \quad \tilde{\mathbf{n}} \equiv \begin{bmatrix} \tilde{n}_{w1} \\ \tilde{n}_{w2} \\ \vdots \\ \tilde{n}_{wD} \end{bmatrix}, \quad (4.7)$$

and

$$\mathbf{F} \equiv \begin{bmatrix} \mathbf{F}^+ & \mathbf{F}^\times \end{bmatrix} \equiv \begin{bmatrix} F_{w1}^+ & F_{w1}^\times \\ F_{w2}^+ & F_{w2}^\times \\ \vdots & \vdots \\ F_{wD}^+ & F_{wD}^\times \end{bmatrix}. \quad (4.8)$$

Note that these are for a single frequency bin of the data from the network and for a fixed sky position. So each of these quantities is both a function of frequency and sky position, and all information about the sensitivity of the network as a function of both frequency and sky position is contained in the matrix  $\mathbf{F}$ .

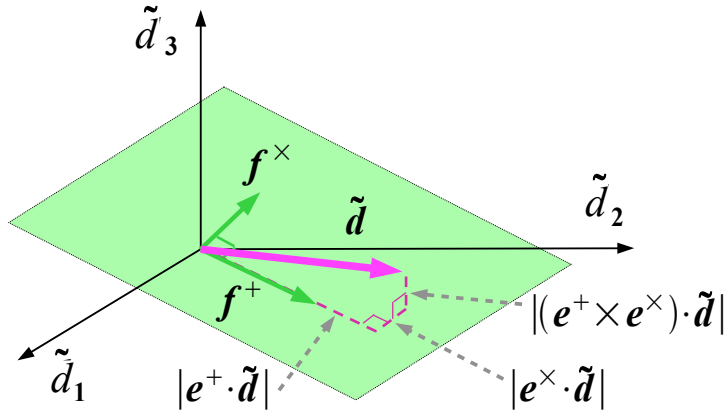


Figure 4.2: Space of noise-weighted detector strains  $\tilde{\mathbf{d}}$ . The GW plane is shown in green. The magenta line represents an example of measured data  $\tilde{\mathbf{d}}$ . The dashed lines show the projection of the data vector into the GW plane and the null space [189].

#### 4.2.4 Dominant Polarisation Frame and Likelihoods

A single time-frequency sample of data  $\tilde{\mathbf{d}}$  from a network of  $D$  detectors can be treated as a vector in a  $D$ -dimensional space.  $\mathbf{F}^+$  and  $\mathbf{F}^\times$  span a two-dimensional subspace, which can be used as a starting point for constructing a convenient basis for writing detection statistics.

Equations (4.6) to (4.8) are valid for any choice of polarisation basis. So we can make the specific choice called the dominant polarisation frame (DPF), which is particularly convenient for coherent analysis. The DPF is constructed from the two-dimensional subspace defined by  $\mathbf{F}^+$  and  $\mathbf{F}^\times$ , referred to as the GW plane. We choose one vector  $\mathbf{f}^+$  along the direction in which the network has maximum antenna response and an orthogonal vector  $\mathbf{f}^\times$  along the direction in which the network has minimum antenna response. In the presence of a GW the data vector  $\tilde{\mathbf{d}}$  will have some component which caused by the GW signal, this can be separated from the rest of the data by the projection of  $\tilde{\mathbf{d}}$  onto the GW plane. Uncorrelated noise between detectors in the data vector  $\tilde{\mathbf{d}}$  can be partially separated from the rest of the data by the projection onto the *null space* which is orthogonal to the GW plane.

In the case of a three detector network this can be visualised as shown in figure 4.2, where the DPF unit vectors are defined as  $\mathbf{e}^+ \equiv \mathbf{f}^+ / |\mathbf{f}^+|$  and  $\mathbf{e}^\times \equiv \mathbf{f}^\times / |\mathbf{f}^\times|$ . The *total energy* in the whitened data is given by

$$E_{\text{tot}} \equiv \sum_k |\tilde{\mathbf{d}}|^2, \quad (4.9)$$

where  $k$  is the sum over all time-frequency pixels analysed. The *plus energy* projection likelihood,

$$E_+ \equiv \sum_k |\mathbf{e}^+ \cdot \tilde{\mathbf{d}}|^2, \quad (4.10)$$

and cross energy projection likelihood,

$$E_{\times} \equiv \sum_k |\mathbf{e}^{\times} \cdot \tilde{\mathbf{d}}|^2, \quad (4.11)$$

give respectively the plus and cross polarisation GW energy in the whitened data that is consistent with the hypothesis of a GW from a known sky position. These are useful for discriminating between signal and noise as large values of  $E_{+}$  or  $E_{\times}$  are inconsistent with Gaussian-noise and imply the presence of a “+” or “ $\times$ ” polarised GW respectively.

The *standard likelihood* is the sum of  $E_{+}$  and  $E_{\times}$ . Physically, it is the maximum energy in the whitened data that is consistent with the hypothesis of a GW of any polarisation from a known sky position

$$E_{\text{SL}} \equiv \sum_k \left[ |\mathbf{e}^{+} \cdot \tilde{\mathbf{d}}|^2 + |\mathbf{e}^{\times} \cdot \tilde{\mathbf{d}}|^2 \right]. \quad (4.12)$$

Projections from  $E_{\text{tot}}$  to  $E_{\text{SL}}$  remove some fraction of the noise with energy  $E_{\text{null}}$  without removing any signal component, as shown in [figure 4.2](#). This component is the *null energy*,

$$E_{\text{null}} \equiv \sum_k |(\mathbf{e}^{+} \times \mathbf{e}^{\times}) \cdot \tilde{\mathbf{d}}|^2. \quad (4.13)$$

$E_{\text{null}}$  can be interpreted as the minimum energy in the whitened data that is inconsistent with the hypothesis of a GW of any polarisation from a known sky position.

Coherent methods [[158](#), [189](#)], which were first introduced to the problem of GW detection in [[191](#)], combine the data streams from multiple detectors before producing a single candidate event list for the whole network. Coherent methods have some advantages over incoherent methods such as improved background rejection [[192](#)] and GWB waveform reconstruction, but they are more computationally costly. This is because the number of coherent combinations is a function of the sky position, of which there are  $\gtrsim 10^3$  resolvable sky positions in the entire sky, and the need for re-analysis of data with unphysical time shifts to estimate the background due to noise. The analysis must be repeated over a grid of positions covering the sky position uncertainty region of the “external trigger” being analysed, such as a GRB. The computational cost is kept modest for an externally triggered analysis as the time and sky position of a trigger is often well constrained. When searching for high frequency GWs from GRBs with large sky position uncertainty regions, we need to use a new method to reduce the computational cost; this is described in [section 4.3.4](#).

#### 4.2.5 Incoherent Energies and Background Rejection

Coherent likelihoods such as  $E_{\text{SL}}$  and  $E_{\text{null}}$  contain both cross-correlation terms  $(\tilde{\mathbf{d}}_{\alpha}^* \tilde{\mathbf{d}}_{\beta}, \alpha \neq \beta)$  and auto-correlation terms  $(\tilde{\mathbf{d}}_{\alpha}^* \tilde{\mathbf{d}}_{\alpha})$ . For each coherent energy  $E$  we define a corresponding incoherent energy  $I$  by discarding the cross-correlation terms in [equations \(4.10\) to \(4.13\)](#). For uncorrelated glitches the cross-correlation

terms are expected to be small compared to the auto-correlation terms. This allows us to use the coherent and incoherent energies to construct veto tests that can be used to separate signal from background.

For GWs the relationship between the coherent and incoherent null energy is given by

$$E_{\text{null}} \ll I_{\text{null}}, \quad (4.14)$$

whereas for glitches

$$E_{\text{null}} \simeq I_{\text{null}}. \quad (4.15)$$

From these behaviours we can construct a simple background rejection test [192]

$$\frac{I_{\text{null}}}{E_{\text{null}}} > r, \quad (4.16)$$

where  $r$  is a constant  $> 1$ . An example can be seen in figure 4.3. This test is efficient at removing large amplitude glitches.

Another test used by X-PIPELINE is the  $\alpha$  test. For a loud signal of amplitude  $A$ , energy dependent quantities have an  $A^2$  dependence,

$$E \propto A^2, \quad (4.17a)$$

$$I \propto A^2, \quad (4.17b)$$

$$E - I \propto A^2. \quad (4.17c)$$

On the other hand, for a glitch of amplitude  $A$  in a single detector, the difference  $E - I$  involves only cross terms between the glitch and Gaussian noise in the other detectors. For large amplitude glitches,

$$E \propto A^2, \quad (4.18a)$$

$$I \propto A^2, \quad (4.18b)$$

$$E - I \propto A. \quad (4.18c)$$

This difference in behaviour for the signal and glitches in the cross-correlation term  $E - I$  can be used to construct a family of functions,

$$\frac{|E - I|}{(E + I)^\alpha} = r. \quad (4.19)$$

Where  $r$  is a constant, and  $\alpha$  takes a values in the range  $[0.5, 1]$ . For  $\alpha = 1$  we find that a constant fraction of all signals are rejected by this cut, and the fraction of glitches rejected decreases with amplitude. For  $\alpha = 0.5$  we find the opposite, that a constant fraction of all glitches are rejected by this cut, and the fraction of signal rejected increases with amplitude. A value of  $\alpha = 0.8$  is chosen to reject loud glitches while keeping the best detection sensitivity for loud signals [193].

Equivalent tests can also be used with the other coherent energies to separate signal from noise as well as other (non-linear) thresholds in the  $I, E$  plane. In this search the linear (straight-line) and  $\alpha$  tests are used.



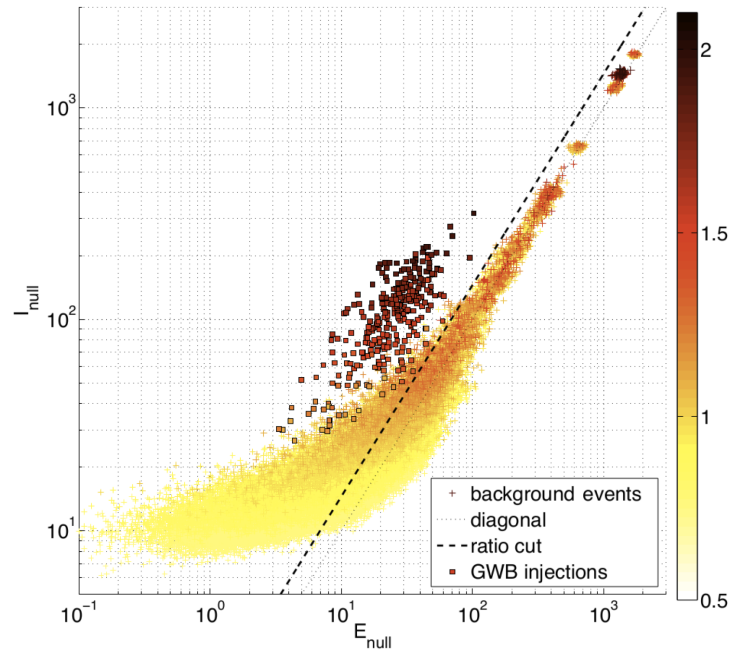


Figure 4.3:  $I_{\text{null}}$  vs.  $E_{\text{null}}$  for background events (+) and simulated gravitational wave bursts (□) for a sample GRB search. The colour of the symbols represents the significance associated with each event, with redder (darker) colours representing higher significance. The dotted line shows the  $I = E$  diagonal. The dashed line shows the threshold selected by X-PIPELINE to separate background and signal; all events that fall below this line are discarded [189]. Note that this test is particularly effective at rejecting high-significance background events (top right)

### 4.2.6 Detection Procedure and upper limits

To make a detection claim, we need to be able to claim with high confidence that a cluster is inconsistent with the background noise. To estimate the distribution of our detection statistic due to background the off source data is artificially time shifted between the detectors by a few seconds up to a few hundred seconds and the time-frequency analysis (cluster identification) process is repeated. The total effective live time analysed typically in time shifts is  $> 1000$  times the on-source duration. This procedure allows estimation of false alarm probabilities at the sub 1% level. The off-source region is analysed by splitting it into chunks of the same duration as the on-source; the loudest surviving cluster in each chunk is identified, which makes up the cumulative background distribution  $C(\mathcal{S}_{\max})$  of loudest significances from all off-source chunks. A threshold is set on  $C(\mathcal{S}_{\max})$  so that the probability of an event being produced with this significance by noise alone is less than 1%. The cluster in the on-source region which has survived veto cuts with the largest significance,  $\mathcal{S}_{\max}^{\text{on}}$ , is compared to the cumulative background distribution  $C(\mathcal{S}_{\max})$  of loudest significances measured using background noise. If the significance  $C(\mathcal{S}_{\max}^{\text{on}})$  of the loudest cluster is above the threshold, then that cluster is considered as a GWB *detection candidate*. The p-value (false-alarm probability) is defined as the probability of obtaining an event with equal or larger detection statistic in the on-source, given the background distribution, under the null hypothesis. The events with the smallest p-value are subjected to additional follow-up studies to determine if the events can be associated with a noise artefact, for example due to environmental disturbances.

If no statistically significant signal is found in the on-source region, then we set a frequentist upper limit on the strength of GWs associated with the GRB. We define the root-sum-squared GW amplitude  $h_{\text{rss}}$  by

$$\begin{aligned} h_{\text{rss}} &= \sqrt{\int_{-\infty}^{\infty} [h_+^2(t) + h_{\times}^2(t)] dt}, \\ &= \sqrt{2 \int_0^{\infty} [\tilde{h}_+^2(f) + \tilde{h}_{\times}^2(f)] df}. \end{aligned} \quad (4.20)$$

Since  $h_{\text{rss}}$  has units of  $\text{Hz}^{-1/2}$ , the same as the amplitude spectra, it is a convenient quantity for comparing to the detector noise curve. For narrow-band signals, the  $h_{\text{rss}}$  can also be linked to the energy emitted in GWs under the assumption of isotropic radiation,

$$E_{\text{GW}}^{\text{iso}} \simeq \frac{\pi^2 c^3}{G} D^2 f_0^2 h_{\text{rss}}^2, \quad (4.21)$$

where  $D$  is the distance to the source and  $f_0$  is the dominant frequency of the radiation [164].

In order to determine the sensitivity of the analysis, simulated GWBs are added into the data. The injections are performed over the  $1\sigma$  sky position uncertainty region following a Fisher distribution. Simulated GW signals are injected into data with a range of different  $h_{\text{rss}}$  amplitudes. The 90% confidence

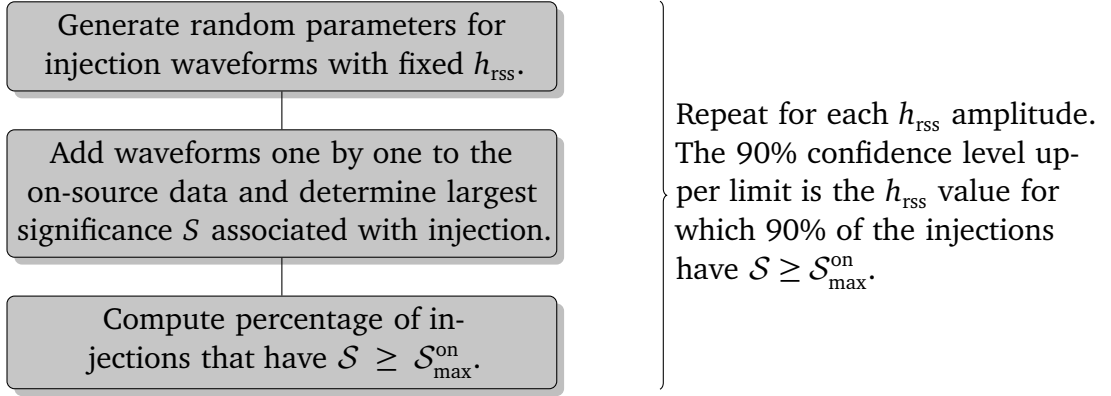


Figure 4.4: The procedure for setting upper limits.

level upper limit is the  $h_{\text{rss}}$  for which 90% of the injections have  $S \geq S_{\text{max}}^{\text{on}}$ . This procedure is shown in [figure 4.4](#).

[Equation \(4.21\)](#) can be re-arranged to be used to calculate the exclusion distance for a particular source model, assuming a value for  $E_{\text{GW}}^{\text{iso}}$ . For GRBs an isotropically distributed energy of  $E_{\text{GW}}^{\text{iso}} = 10^{-2} M_{\odot} c^2$  is often used as an optimistic estimate, see [section 4.1 \[43\]](#). It is also assumed that the GRB is a rotating emitter with the axis of rotation pointing roughly towards the observer, which will yield circularly polarised GWs [\[194\]](#). For a GW at frequency  $f_0$  this gives the exclusion distance

$$D_{\text{exclusion}} \simeq \sqrt{\frac{GE_{\text{GW}}^{\text{iso}}}{\pi^2 c^3 f_0^2 h_{\text{rss}}^2}}. \quad (4.22)$$

#### 4.2.7 Tuning and Closed-box Analysis

We aim to tune the coherent glitch vetoes to optimise the trade off between glitch rejection and signal acceptance. This is done using an exhaustive test of trial thresholds for the coherent veto tests, [equations \(4.16\)](#) and [\(4.19\)](#) and selecting the threshold combination that gives the lowest expected upper limits estimated using injections and off-source segments. This is done using a closed box procedure, where the sensitivity of the pipeline is estimated using an off-source and injection data but not on-source data; this blind tuning avoids biasing the upper limits. For this closed box analysis the off-source segment that gives the loudest even closest to the 95<sup>th</sup> percentile of the off-source  $S_{\text{max}}$  is used in place of the true on-source segment which is referred to as the “dummy on-source”. This procedure is shown in [figure 4.5](#).

### 4.3 Leveraging the GEO 600 Detector to Search for Gravitational Waves from Gamma-Ray Bursts

In this section we report on a search for GWs associated with GRBs using data from the GEO 600, LIGO, and Virgo GW observatories in the frequency range of

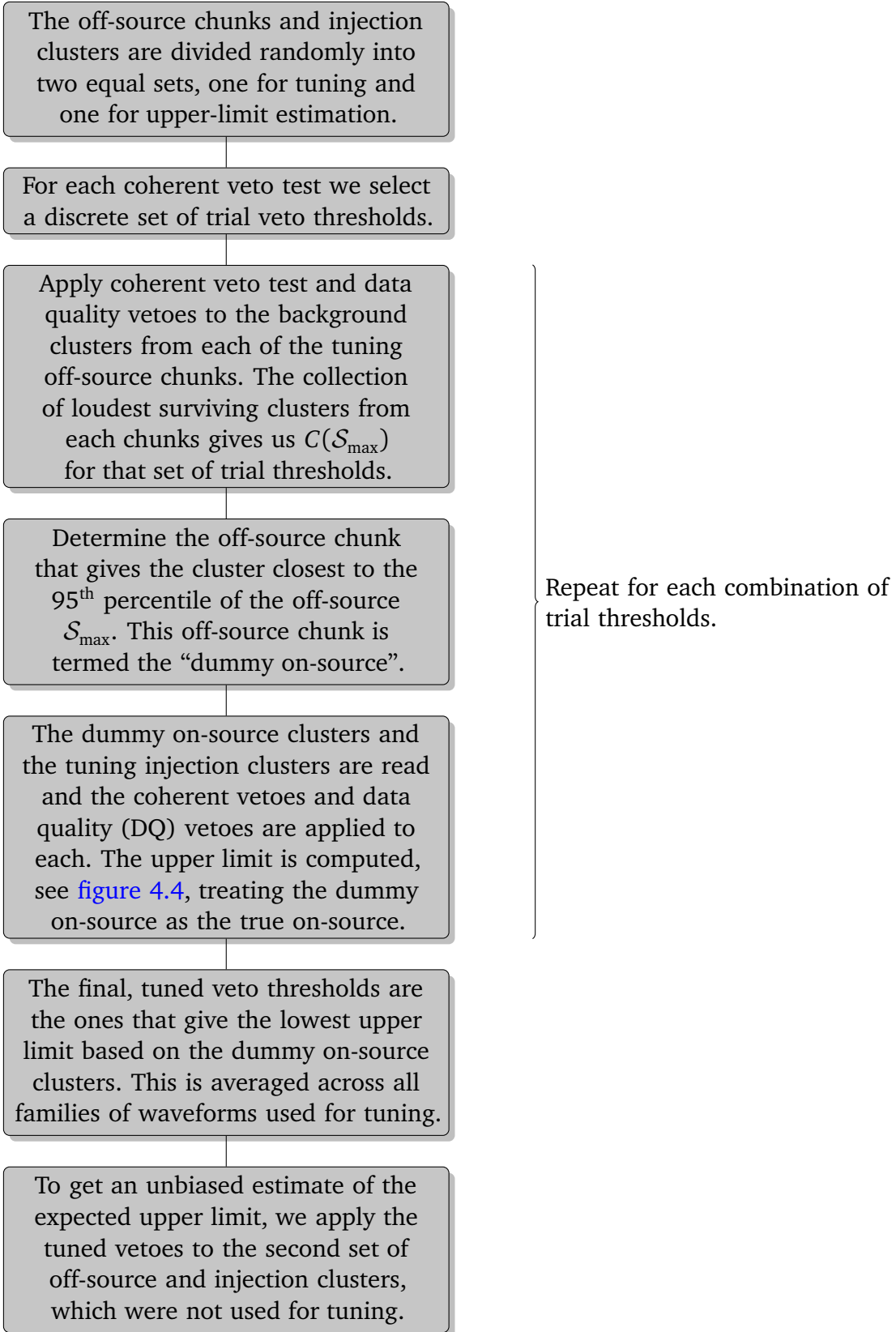


Figure 4.5: The procedure for the closed box analysis.

64 Hz–1792 Hz. The analysis is an externally triggered search for GWBs associated with GRBs which occurred between April 2006 and October 2011, and is the first GRB analysis performed using data from an interferometer implementing squeezing (see [section 2.5.8](#)). The linear sky grid method which is used for the search in this section was implemented into the search pipeline by a number of people included in the author list of [\[153\]](#), particularly Daniel Hoak who co-authored [\[153\]](#) and lead the implementation of the linear sky grid method. This section draws from Ref. [\[153\]](#) which is currently in preparation.

### 4.3.1 Gamma-ray Burst Sample

The GEO 600 detector operated with a high duty cycle from 2006 to 2011, with occasional short breaks for invasive configuration changes and instrumental upgrades. The LIGO and Virgo observatories have taken data in a series of science runs, during which the detector is kept in its most sensitive state, separated by periods of intense commissioning activity. The fifth LIGO science run (S5) started on 1<sup>st</sup> November 2005 and ended on 1<sup>st</sup> October 2007. During S5 the H1, H2, and L1 interferometers operated near their design sensitivity, with duty cycles of approximately 70%. The H2 instrument ceased data-taking operations in July 2009. The sixth LIGO science (S6) run was held from 7<sup>th</sup> July 2009 to 20<sup>th</sup> October 2010. In S6, the H1 and L1 were operated with duty cycles of 52% and 47% respectively, and both surpassed their sensitivities from S5.

The first Virgo science run (VSR1) started 18<sup>th</sup> May 2007 and ended 1<sup>st</sup> October 2007. The second Virgo science run (VSR2) was held from 7<sup>th</sup> July 2009 to 8<sup>th</sup> January 2010, and the third Virgo science run (VSR3) was held from 11<sup>th</sup> August 2010 to 19<sup>th</sup> October 2010. The fourth Virgo science run (VSR4) was held from 20<sup>th</sup> May 2011 to 5<sup>th</sup> September 2011 and was immediately followed by an Astrowatch period that ended on 3<sup>rd</sup> November 2011. Virgo's duty cycle was 71% for VSR2-4. This is summarised in [table 4.1](#).

[Figure 4.6](#) shows typical sensitivities, in terms of noise spectral density, of the GEO 600, LIGO, and Virgo interferometers during these science runs.

The sample of GRBs analysed in this chapter was obtained from the gamma-ray burst coordinates network (GCN) [\[195\]](#), supplemented by the *Swift* and *Fermi* trigger databases [\[196\]](#). Most of the GRBs were detected by *Swift* [\[197\]](#) and *Fermi* [\[198\]](#) satellites, and a single event came from INTEGRAL [\[199\]](#).

### 4.3.2 Including GEO 600 in a Gamma-ray Burst Analysis

GRBs that occurred when two or more of the LIGO or Virgo interferometers were operating in a resonant and stable configuration were previously analysed for GW counterparts [\[64, 43\]](#). GEO 600 was not used in previous searches for GWs associated with GRBs due to its lower sensitivity compared to the LIGO and Virgo detectors. Our first task is to determine if GEO 600 data could improve the limits already set for these GRBs. Here we reprocess the GRBs from the S6D/VSR3

Name	UTC Start time (GPS)	UTC End time (GPS)	Dur. (s)	Network
S5/VSR1	04-11-2005 16:00:00 (815155213)	01-10-2007 00:00:00 (875232014)	60076801	H1H2G1L1V1
S6A/VSR2	07-07-2009 21:00:00 (931035615)	01-09-2009 00:00:00 (935798415)	4762800	H1G1L1V1
S6B	01-09-2009 00:00:00 (935798415)	12-01-2010 22:00:00 (947368815)	11570400	H1L1V1 <sup>†</sup>
S6C	16-01-2010 00:00:00 (947635215)	26-01-2010 01:30:00 (961551015)	13915800	H1G1L1
S6D/VSR3	26-01-2010 00:00:00 (961545615)	21-10-2010 00:00:00 (971654415)	10108800	H1G1L1V1
S6E/VSR4	03-06-2011 21:00:00 (991170015)	03-11-2011 23:14:15 (1004397270)*	13227255	G1V1

Table 4.1: Dates of S5 and S6 science runs including list of available detectors.

<sup>†</sup> G1 was out of commission during S6B due to installation of the OMC.

\* S6E/VSR4 was extended from the official end data 05-09-2011 05:00:00 (999234015) with an Astrowatch period.

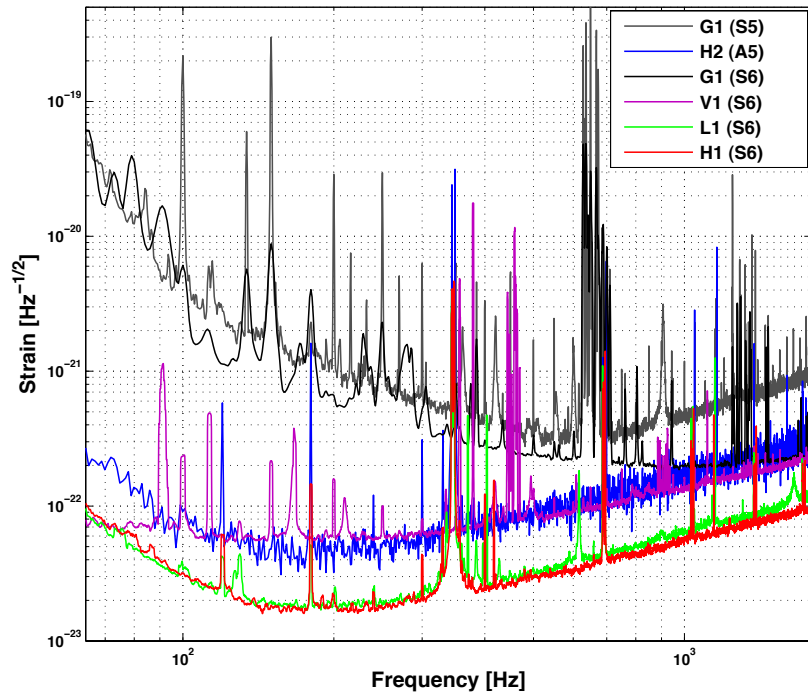


Figure 4.6: Typical strain sensitivity spectrum of the detectors used in this analysis. GEO 600 is shown at two epochs from the S5 (2007-02-09) and S6 (2011-06-03) science runs. The x-axis scale is chosen to match the search bandwidth.

science run including GEO 600 to compare the sensitivity of different detector network combinations including G1.

In figures 4.7 to 4.9 we show the 50% and 90% upper limits for the GRBs analysed in S6D/VSR3 using three different injection waveforms, for different detector networks. We can see that by including G1 in the detector network (comparing the H1L1V1 and G1H1L1V1 network results) there is little difference in the results, which shows that G1 does not help to improve the upper limits of these analyses. The real value of G1 is its large duty cycle; because of this there is a subset of GRBs that were previously un-analysable as only one of the LIGO and Virgo detectors was taking data. In our preliminary tests there were 26 GRBs that were analysable when using only the LIGO and Virgo detectors and 17 GRBs that were “recoverable” by including G1 in the network. These results showed similar upper limits for the high frequency sine-Gaussian injections compared to the 26 H1L1V1 GRBs, figure 4.8, and upper limits an order of magnitude larger for the lower frequency sine-Gaussian and BNS injections, figures 4.8 and 4.9. By including G1 in the network and analysing GRBs with a two detector network the number of observable GRBs in S6D/VSR3 is increased by 65%.

This behaviour matches what we might expect as GEO 600 has a higher frequency sensitive band than the LIGO and Virgo detectors; GEO 600s sensitivity during S6D/VSR3 above 1 kHz was only a factor of 2 away from the other large scale ground-based detectors. At lower frequencies, below 500 Hz, GEO 600 has relatively poor sensitivity so our analyses will be insensitive at these frequencies

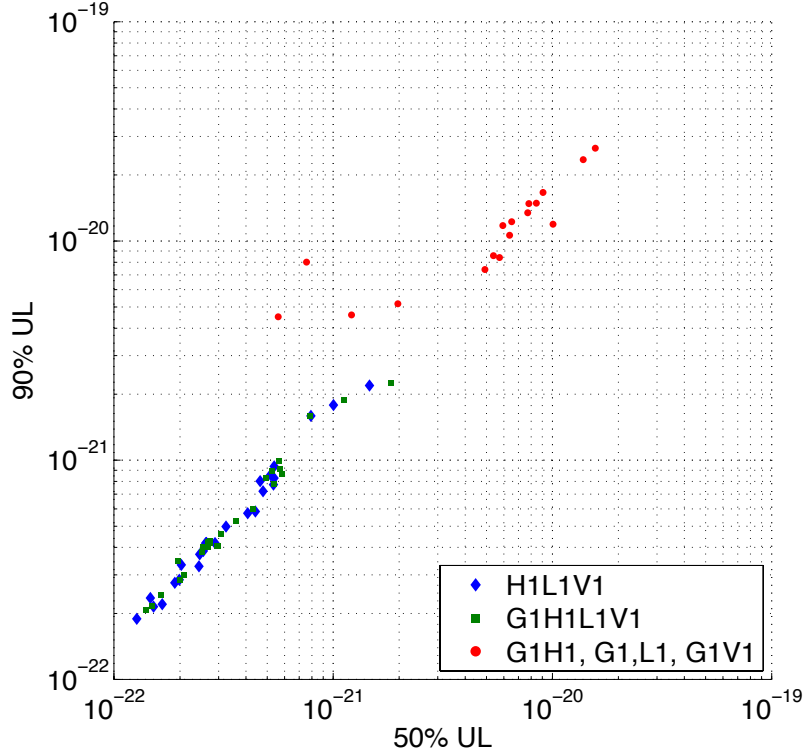


Figure 4.7: The 50% and 90% upper limits for 150 Hz Gaussian modulated sinusoids that are the standard injection waveform type for burst searches. We show the GRBs analysed with the H1, L1 and V1 network (blue diamonds), G1, H1, L1 and V1 network (green squares), and the two detector networks using G1 and one of H1, L1 or V1 (red circles). We see that adding GEO 600 to the analysis does not improve the sensitivity of a search (comparing blue diamonds and green squares), however using GEO 600 allows us to analyse a new population of GRBs (red circles). For the GRBs analysed with G1 plus one other detector we can only set upper limits a factor of  $\sim 10$  larger than for the LIGO-Virgo network analyses for low-frequency circular sine-Gaussian (CSG) waveforms. This is due to the poor low-frequency sensitivity of GEO 600 compared to the LIGO and Virgo detectors, see [figure 4.6](#).



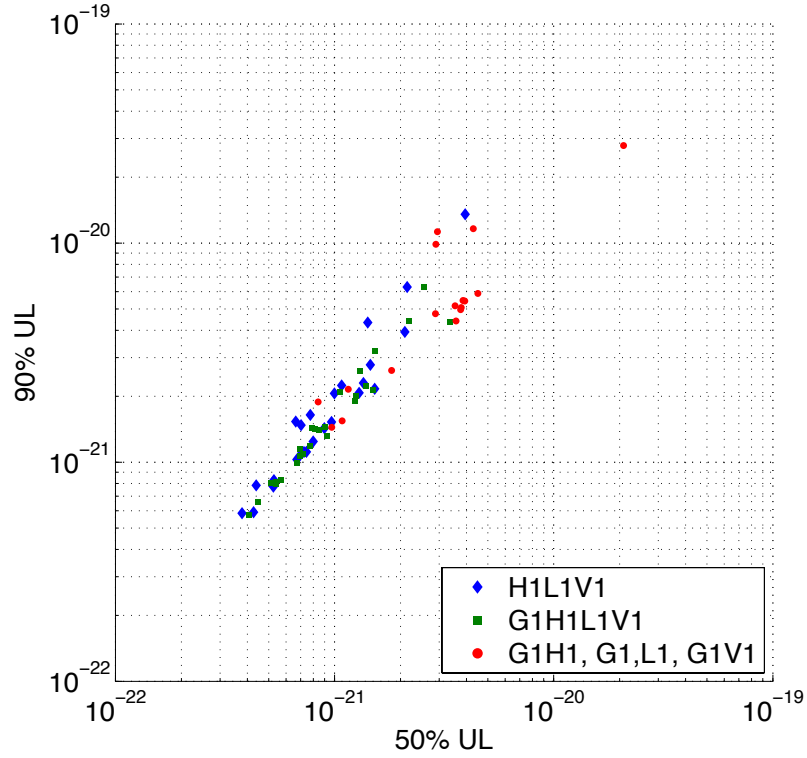


Figure 4.8: The 50% and 90% upper limits for 800 Hz Gaussian modulated sinusoids that are the standard injection waveform type for burst searches. We show the GRBs analysed with the H1, L1 and V1 network (blue diamonds), G1, H1, L1 and V1 network (green squares), and the two detector networks using G1 and one of H1, L1 or V1 (red circles). We see that adding GEO 600 to the analysis does not improve the sensitivity of a search (comparing blue diamonds and green squares), however using GEO 600 allows us to analyse a new population of GRBs (red circles). For the GRBs analysed with G1 plus one other detector we can set upper limits of the same scale as for the LIGO-Virgo network analyses for high-frequency CSG waveforms. This is due to the high-frequency sensitivity of GEO 600 being comparable to the LIGO and Virgo detectors, see [figure 4.6](#).

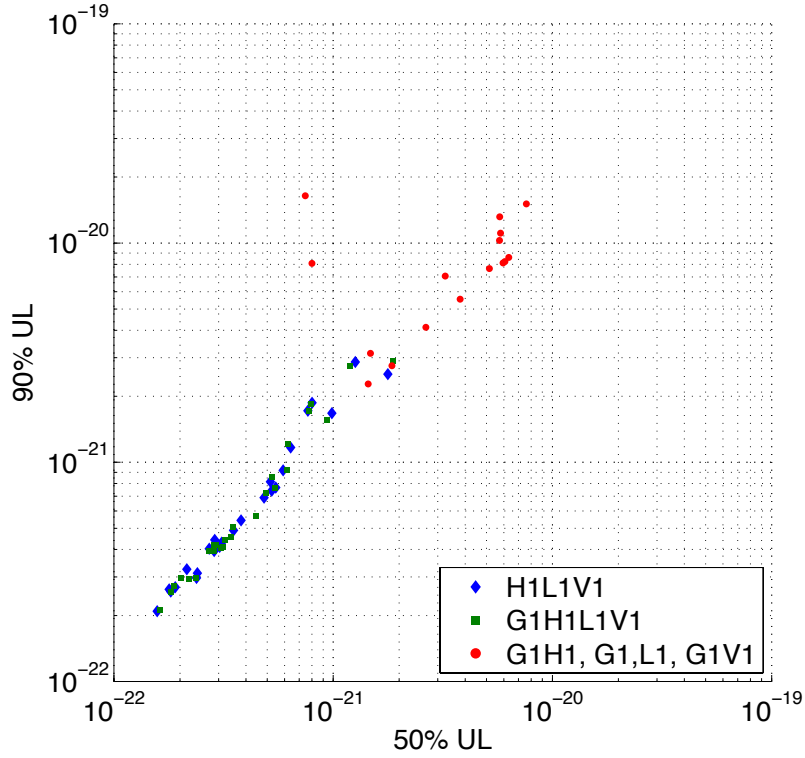


Figure 4.9: The 50% and 90% upper limits for BNS inspiral injections. We show the GRBs analysed with the H1, L1 and V1 network (blue diamonds), G1, H1, L1 and V1 network (green squares), and the two detector networks using G1 and one of H1, L1 or V1 (red circles). We see that adding GEO 600 to the analysis does not improve the sensitivity of a search (comparing blue diamonds and green squares), however using GEO 600 allows us to analyse a new population of GRBs (red circles). For the GRBs analysed with G1 plus one other detector we can only set upper limits a factor of  $\sim 10$  larger than for the LIGO-Virgo network analyses for binary neutron star inspiral injections. This is due to the poor low-frequency sensitivity of GEO 600 compared to the LIGO and Virgo detectors, see [figure 4.6](#).

due to the sensitivity mismatch between GEO 600 and the other detectors. These tests show that because G1 has comparable sensitivity to LIGO, Virgo at high frequencies, networks including GEO 600 are well suited for the detection of high frequency ( $\geq 500$  Hz) GWs. Therefore we decide to analyse these “recoverable” GRBs with the view to search for high frequency GWBs.

Here we analyse GRBs which were observed from 2006–2011 when GEO 600 plus one other observatory was taking science-quality data. GRBs that occurred when two or more of the LIGO or Virgo detectors were observing we previously analysed for GW counterparts [64, 43]. No distinction is made between short GRBs and long GRBs and the analysis is performed without regard to the observed GRB fluence or red shift (if known). GW data segments which are flagged as being of poor quality are excluded from the analysis, and GRBs for which there is insufficient data surrounding the GRB trigger time are not analysed. In total, 78 GRBs were analysed, about  $\sim 5\%$  of which have associated red shift measurements. The results of the analysis of these GRBs is summarised in the [section 4.3.5](#).

### 4.3.3 GEO 600 Data Quality

As GEO 600 had not previously been used for analyses in all of the epochs from S5–S6E, science segments and data quality vetoes had to be constructed for each of the science runs. To do this the state vector, which records information about the status of the detector, was used decomposed into its bit components and used to construct the required segments. For S5/VSR1, S6A/VSR2, S6C, and S6D/VSR3, science segments are defined as times when the detector is in lock and both hardware and software maintenance flags are off.

For S6E/VSR4 science is defined differently due to the data quality vector being updated to incorporate the status of the squeezer after its installation in 2011 [151]; for a brief description of squeezing see [section 2.5.8](#). In this science run, science segments are defined as times when the detector is in lock and both hardware and software maintenance flags are off, and the squeezing flag is either on or off. This final requirement results in there being two distinct science segment lists for GEO 600 during S6E/VSR4. This distinction is made due to the requirement that the off source segment for an analysis gives a good representation of the noise during the on-source segment. In the case that squeezing is turned on or off, this can change the strain sensitivity of GEO 600 in the shot noise limited frequency band by up to 30%. Therefore, by using two separate science segments lists, these two detector states are treated as if they were two separate detectors, thus eliminating this problem. During this analysis we actually found that this did not affect any of our GRB analyses, this was due to the squeezer being either primarily on or off for large blocks of time during the science run and so there were no cases where it changed between these states during the analysis window of a GRB. This is an important point to note for future analyses using the advanced LIGO detectors if they implement squeezing.

#### 4.3.4 Changes to the Search Method for High Frequency analyses

The coherent analysis algorithm used in this search is X-PIPELINE [189], which we give a brief introduction to in section 4.2. The overall search procedure follows that used in previous unmodelled searches for generic GWs signals during the S5-VSR1 [64] and S6-VSR2,3 [43] science runs. In this section we give a brief description of the analysis pipeline and introduce new techniques to accommodate the high frequency sensitivity of the GEO 600 detector and the sky localisation uncertainties of the *Fermi* gamma-ray burst monitor (GBM).

Data from GW detectors surrounding the time of a GRB are divided into an *off-source region*, which is used to characterise the transient signal background around the time of the GRB, and an *on-source region*, which is searched for GW signals. To allow for possible GW precursors from, for example, the core-collapse SN associated with long GRBs, the on-source window is  $[-600, +60]$  s around the onset time of the GRB event. For very long-lasting GRBs, the window is extended to include the entire  $T_{90}$  time of the event. This is the time interval over which 90% of the energy from the GRB is observed. The standard off-source window is  $[-1.5, +1.5]$  hr around the time of the GRB trigger, excluding the on-source window. To estimate the rate of background events with large significance, the analysis of the off-source data is repeated many hundreds of times, with unphysical time-shifts of  $> 3$  s applied to the detector data. A typical search will perform  $\mathcal{O}(1000)$  time-shifts of the off-source region, which robustly estimates the background event rate down to a *false-alarm rate* (FAR) below  $10^{-6}$  Hz. Calculating the background distribution for each GRB is the most computationally intensive portion of the search.

For the *Fermi* GBM, the 95% containment region can cover hundreds square degrees [200], which presents specific difficulties when searching for signals with frequencies larger than a few hundred Hz. In a coherent search for GWs associated with GRBs, performing the analysis with an incorrect sky location can reduce the significance of a GW signal in two ways.

First, the sensitivity of each detector to the polarisations of GWs from the sky location of the GRB will be incorrectly accounted for. This can result in loss of coherent signal energy when the time-frequency maps are combined. Over most of the sky, the antenna factors for GW observatories change slowly as a function of sky location (usually a percent over a few degrees). Empirical tests of the robustness of our coherent detection statistic to variations in sky localisation of several degrees indicate that the loss of signal is of order a few percent, for the majority of positions on the sky. For typical location uncertainties from the GBM, this effect is not large enough to significantly alter the results of our search, and we ignore it in our analysis.

Second, and more significantly, an error in the sky location will lead to an incorrect time-shift of the detector data vectors when accounting for the time-of-arrival of a GW signal. For pairs of ground-based detectors the difference in arrival times are  $\mathcal{O}(10)$  ms, and an error in sky location of a few degrees could introduce errors of a millisecond or more. This can introduce a misalignment of

the signal by several periods for GWs with frequency content above 1 kHz, and when the data vectors are coherently combined the signal strength will be diminished. In the worst case, the waveform will be shifted by a half-period between the detectors, and the signal will cancel entirely in the coherent summation.

The standard solution in coherent GW searches is to repeat the analysis over a discrete grid of sky positions covering most of the uncertainty region. The grid step is chosen so that the timing synchronisation error between any sky position in the sky localisation error box and the nearest analysis grid point is less than 25% of the period for the highest frequency GW signals included in the search. Previous searches have used regular grids of concentric circles around the best estimate of the source location, which covers at least 95% of the sky location probability distribution. A study of search grid efficiency was performed in Ref. [44].

For the *Fermi* GBM, the 95% containment region can cover hundreds square degrees, and a search for signals with frequencies larger than a few hundred Hz would require tiling the search area with many hundreds of search points. At each grid point the coherent signal combination will have to be re-computed using the new time-of-arrival corrections. The background estimation for a GBM event with a search grid for a frequency band extending above 1 kHz will typically require  $\mathcal{O}(10^4)$  CPU hours, depending on the size of the GRB uncertainty region, the sky location, and the GW detectors included in the search. Even on computing clusters with thousands of CPU cores, the analysis for a single GBM event could take several hours to several days to complete.

Our solution is to cover the search region with a linear grid, arranged parallel to the maximum gradient of change in the relative time-of-arrival between detectors; see figure 4.10. In the case of a 2-detector network, we find that such a pattern is sufficient to capture the dominant source of coherent energy variability as the likelihood is calculated across the GRB uncertainty region. Studies performed in [153] show that the linear grid can give a reduction in the computational cost of an analysis by up to a factor of 10 for GRB triggers with large sky position uncertainty regions, such as *Fermi* GBM triggers. This was achieved with negligible change in the analysis upper limits of  $< 5\%$ , which is not statistically significant. A comparison of the circular and linear search grids for the *Fermi* event GRB 080906B is shown in figure 4.10.

For two detectors separated by a distance  $d$ , the difference in time of arrival of the GW is

$$t = \frac{d \cos \theta}{c} \quad (4.23)$$

where  $\theta$  is the angle between the inter-detector baseline and the line-of-sight to the GRB, and  $c$  is the speed of light. For a maximum time-delay error tolerance of  $dt \leq \alpha$ , the corresponding spacing  $d\theta$  between grid points is

$$|d\theta| \leq \frac{2c}{d \sin \theta} \alpha \quad (4.24)$$

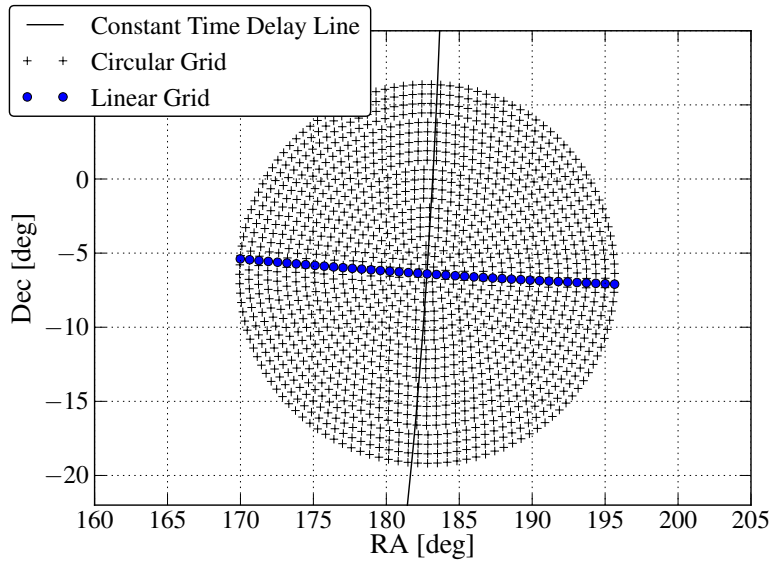


Figure 4.10: Example linear (blue circles) and circular (black crosses) grids for a search for GW signals up to 1792 Hz. The localisation for the *Fermi* GBM event GRB 080906B is shown. The linear search grid contains 41 sky positions, arranged in the direction of the gradient of the time shift between the H2 and G1 detectors. The circular grid contains 1324 sky positions and would require  $\mathcal{O}(10^4)$  cpu-hours. Both search grids cover the  $1.65 \sigma_{stat+sys}$  uncertainty region for the *Fermi* GBM event, which corresponds to 95% containment for a Fisher distribution on a sphere. The GBM statistical error for this event is  $1.6^\circ$ .

For our search band<sup>2</sup> of 64 Hz–1792 Hz, we choose  $\alpha = 0.14$  ms. The extent of the linear grid is determined by the 95% containment radius for the given GRB. For events localised by the *Swift* satellite, we use a search grid of a single point. For events localised by the *Fermi* GBM event, we use  $1.65 \sigma_{stat+sys}$ , where  $\sigma_{stat}$  is the GBM statistical error for the GRB (typically  $2^\circ$ – $3^\circ$ ), and  $\sigma_{sys}$  is a  $7.5^\circ$  systematic error [200, 201, 202, 203].

For a handful of GRBs, direct comparisons were made between the linear grid and the full circular tiling [153]. The results for the two methods were nearly identical: the detection thresholds to simulated GW signals using the linear grid were within a few percent of the thresholds observed when the analysis was performed with the circular grid. Furthermore, the analysis using the linear grid was completed in a fraction of the time required for the circular grid, and typically required  $\mathcal{O}(10^3)$  or fewer CPU hours, depending on the detectors used in the analysis. Using computing clusters with thousands of CPU cores<sup>3</sup>, it was possible to analyse some GRBs localised by the GBM in less than three hours.

One of the primary goals of GW searches is the prompt localisation of the source sky location for follow-ups by optical and x-ray astronomers. Currently, very few GRBs detected by the *Fermi* GBM are searched for optical counterparts, due to the resources necessary to search an uncertainty region of hundreds of square degrees. The detection of a GW signal associated with a GRB will be of tremendous interest to the astronomical community, and any improvement of the GBM localisation will increase the chances that astronomers could detect an optical or x-ray counterpart to the gamma-ray and GW signal.

In the presence of a detected GW signal, X-PIPELINE can localise the source to within a few degrees along the axis of the linear grid, depending on the frequency content of the signal and its duration; this is described in full in Ref. [153]. The reduction in the computational cost from the linear grid can help us to quickly feed back sky localisation information to the astronomical community for EM follow-up observations.

### 4.3.5 Search Results

In the epoch considered for our search (see table 4.1), there were 99 GRBs with sufficient science data to analyse, and for 78 GRBs the closed-box results had good sensitivity to potential GW signals. About half of these GRBs were detected and localised by the *Fermi* GBM; the rest were primarily detected by the *Swift* Burst-Alert Telescope burst alert telescope (BAT). For each of the 78 GRBs with good closed-box results and good sensitivity to potential GW signals we calculated the p-value (false alarm probability) for the loudest event in the on-source [43]. Two GRBs in our sample had on-source events with  $p < 0.01$ :

**GRB 060502A** was analysed using the G1 and L1 detectors. The data from both detectors at the time of the event was reasonably Gaussian. The sky

<sup>2</sup>This low frequency limit was chosen to match previous analyses for which the data conditioning has been well tested. For searches using data from the GEO 600 detector, GW signals are typically only detectable at frequencies above 300 Hz.

<sup>3</sup>LIGO Data Grid, <https://www.lsc-group.phys.uwm.edu/lscdatagrid/>



position of this GRB was not ideal for either detector, both had sensitivity to this sky position of  $\sim 30\%$  of their optimal sensitivity. Cat3 vetoes are applied during event follow up and will remove detection candidates if they are in coincidence with a cat3 veto, this is a blind decision as the vetoes are produced before the analysis is performed. During event follow up for this event we examined the data quality around the time of this GRB. This showed that there was significant noise in the L1 detector, associated with increased ground motion due to a magnitude 5.0 earthquake in Costa Rica, which had been flagged by cat3 vetoes made to monitor above-normal levels of seismic noise. Since 35% of the on-source window for this GRB was flagged by cat3 veto segments and all three on-source events with  $p < 0.01$  occurred during these cat3 veto segments, we do not include this GRB in the cumulative results.

**GRB 090712A** was the event with the smallest p-value in our sample, with a p-value of  $3 \times 10^{-3}$ . GRB 090712A is a *Swift* GRB analysed with data from the V1 and G1 detectors, had an on-source event with  $p = 0.3\%$ . While we find no plausible instrumental or environmental cause for the event, the observed p-value for this GRB, as shown below, is not significant in a data set containing 78 GRBs.

The distribution of p-values for the most significant event found in the on-source window for each of the 78 GRBs is shown in [figure 4.11](#). A weighted binomial test is used to check if the distribution of p-values is compatible with the uniform distribution expected from the null hypothesis (see Appendix A of [\[43\]](#) for details). This test looks for deviations from the null hypothesis in the tail of p-values; here we used the lowest 5%. The probability that our cumulative distribution is due to background is 41%, which indicates that the data is consistent with no sub-threshold GW events being present.

We place upper limits on the amplitude of GW signals associated with our GRB sample by measuring the detection efficiency of simulated GW waveforms at various signal strengths [\[43\]](#). Following the procedure of the S6-VSR2,3 search, we employ a circularly polarised GW signal model; this is motivated by our expectation that the rotation axis of the GRB central engine is likely pointed at the observer, to within  $\sim 10^\circ$ . For this search, we simulate GWs using CSGs with quality factor  $Q = 9$  and a range of central frequencies  $f_0$ ; these *ad hoc* waveforms are the standard ones used for estimating the sensitivity of GW analyses to generic short-duration signals [\[50, 53, 190, 43\]](#):

$$\begin{aligned} h_+(t) &= \frac{A}{D} \cos(2\pi f_0 t) e^{-\frac{(2\pi f t)^2}{2Q^2}}, \\ h_\times(t) &= \frac{A}{D} \sin(2\pi f_0 t) e^{-\frac{(2\pi f t)^2}{2Q^2}}. \end{aligned} \quad (4.25)$$

Where  $A$  is an arbitrary scaling factor,  $D$  is the distance to the source. The distribution of exclusion distances for waveforms with central frequencies of 500 Hz and 1 kHz for the 78 GRBs in this search is shown in [figure 4.12](#). The median exclusion distance for the 500 Hz and 1 kHz waveforms are 0.8 Mpc and 0.4 Mpc



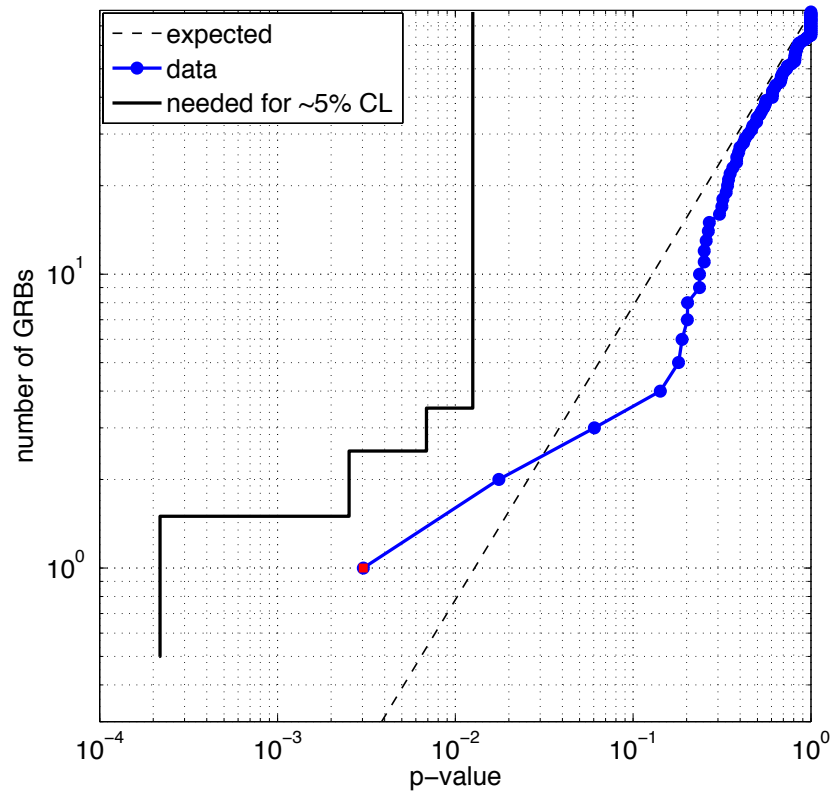


Figure 4.11: Cumulative p-value distribution from the analysis of 78 GRB triggers. The dashed line gives the expected distribution under the null hypothesis. The solid black line shows the threshold for a  $2\sigma$  detection with the binomial test (Appendix. A of [43]). The blue points represent our distribution of measured p-values for the 78 GRBs. Any blue point in our distribution which is above and to the left of the black line would be considered as a candidate for detection.

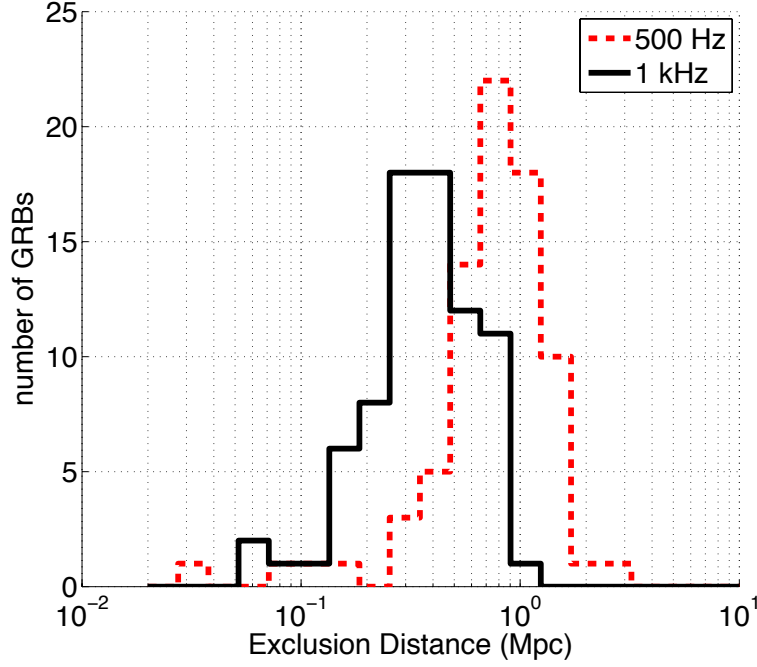


Figure 4.12: Exclusion distances for 500 Hz and 1 kHz CSG waveforms for 78 GRBs. An optimistic total emitted energy of  $10^{-2} M_{\odot} c^2$  is assumed. The median exclusion distance for the 500 Hz and 1 kHz waveforms were 0.8 Mpc and 0.4 Mpc respectively.

respectively, where we have assumed the GRB emission mechanism releases  $10^{-2} M_{\odot} c^2$  energy in GWs. For other emission energies  $E_{\text{GW}}$  the distance limits scale as  $E_{\text{GW}}^{1/2}$ . For example, assuming  $E_{\text{GW}} = 10^{-8} M_{\odot} c^2$  gives a median exclusion distance of 0.8 kpc at 500 Hz. We give a full list of the 90% upper limits for the 500 Hz and 1 kHz CSG waveforms from each GRB in [table 4.2](#).

GRB name	UTC Time	Ra.	Dec.	Network	90% UL ( $\times 10^{-21} \text{ Hz}^{-1/2}$ )		$\gamma$ -Ray Detector
					500 Hz	1 kHz	
S5							
060424	04:16:19	0 <sup>h</sup> 29 <sup>m</sup> 26 <sup>s</sup>	36°47′	G1L1	1.46	3.01	BAT
060512	23:13:20	13 <sup>h</sup> 02 <sup>m</sup> 58 <sup>s</sup>	41°13′	G1L1	1.48	2.53	BAT
060522	02:11:18	21 <sup>h</sup> 31 <sup>m</sup> 49 <sup>s</sup>	2°53′	G1L1	1.93	2.35	BAT
060602A	21:32:12	9 <sup>h</sup> 58 <sup>m</sup> 19 <sup>s</sup>	0°18′	G1L1	2.55	4.39	BAT
060604	18:19:00	22 <sup>h</sup> 28 <sup>m</sup> 54 <sup>s</sup>	−10°56′	G1L1	1.37	2.58	BAT
060708	12:15:59	0 <sup>h</sup> 31 <sup>m</sup> 17 <sup>s</sup>	−33°45′	G1L1	1.61	2.88	BAT
060801	12:16:15	14 <sup>h</sup> 11 <sup>m</sup> 56 <sup>s</sup>	16°59′	G1L1	3.95	3.37	BAT
060929	19:55:01	17 <sup>h</sup> 32 <sup>m</sup> 35 <sup>s</sup>	29°50′	H2G1	2.22	4.93	BAT
061110B <sup>†</sup>	21:58:45	21 <sup>h</sup> 35 <sup>m</sup> 38 <sup>s</sup>	6°52′	G1L1	2.91	7.42	BAT
070328	03:53:53	4 <sup>h</sup> 20 <sup>m</sup> 27 <sup>s</sup>	−34°04′	G1L1	1.42	2.21	BAT
070406	00:50:38	13 <sup>h</sup> 15 <sup>m</sup> 52 <sup>s</sup>	16°28′	G1L1	1.37	2.31	BAT
070509	02:48:27	15 <sup>h</sup> 51 <sup>m</sup> 35 <sup>s</sup>	−78°39′	G1L1	1.49	2.13	BAT
070517	11:20:58	18 <sup>h</sup> 30 <sup>m</sup> 14 <sup>s</sup>	−62°18′	H2G1	2.60	4.12	BAT
070925	15:52:32	16 <sup>h</sup> 52 <sup>m</sup> 52 <sup>s</sup>	−22°02′	G1V1	3.01	3.98	IBIS
S6A							
090712A	03:51:05	4 <sup>h</sup> 40 <sup>m</sup> 22 <sup>s</sup>	22°31′	G1V1	2.21	3.31	BAT
090713A	00:29:28	18 <sup>h</sup> 59 <sup>m</sup> 11 <sup>s</sup>	−3°19′	G1V1	2.85	3.41	GBM
090715B	21:03:15	16 <sup>h</sup> 45 <sup>m</sup> 21 <sup>s</sup>	44°50′	G1V1	1.59	1.64	BAT
090718B	18:17:43	18 <sup>h</sup> 16 <sup>m</sup> 24 <sup>s</sup>	−36°23′	G1H1	0.85	1.58	GBM
090804B	22:33:20	8 <sup>h</sup> 41 <sup>m</sup> 36 <sup>s</sup>	−11°18′	G1V1	1.43	1.95	GBM
090807B	19:57:59	21 <sup>h</sup> 47 <sup>m</sup> 35 <sup>s</sup>	7°13′	G1V1	2.94	5.34	GBM
090810A	18:44:44	7 <sup>h</sup> 45 <sup>m</sup> 43 <sup>s</sup>	−17°28′	G1V1	2.19	3.99	GBM
S6C							
100131A	17:30:58	8 <sup>h</sup> 01 <sup>m</sup> 36 <sup>s</sup>	16°23′	L1G1	3.18	7.57	GBM
100331A	00:30:22	17 <sup>h</sup> 24 <sup>m</sup> 14 <sup>s</sup>	−58°56′	L1G1	2.39	2.58	IBIS
100417A	03:59:44	17 <sup>h</sup> 25 <sup>m</sup> 12 <sup>s</sup>	50°23′	G1L1	26.7	7.05	GBM
100510A	19:27:07	23 <sup>h</sup> 43 <sup>m</sup> 12 <sup>s</sup>	−35°36′	L1G1	2.91	3.76	MAXI
100511A	00:49:56	7 <sup>h</sup> 17 <sup>m</sup> 12 <sup>s</sup>	−4°39′	L1G1	5.66	8.70	GBM
100528A	01:48:01	20 <sup>h</sup> 44 <sup>m</sup> 24 <sup>s</sup>	27°48′	L1G1	2.20	2.43	AGILE
100625A	18:32:28	1 <sup>h</sup> 03 <sup>m</sup> 11 <sup>s</sup>	−39°05′	L1G1	2.56	3.90	BAT
S6D							
100703A	17:43:37	0 <sup>h</sup> 38 <sup>m</sup> 05 <sup>s</sup>	−25°42′	L1G1	3.13	3.89	IBIS
100704A	03:35:08	8 <sup>h</sup> 54 <sup>m</sup> 33 <sup>s</sup>	−24°12′	H1G1	2.60	3.73	BAT
100719C	19:48:08	15 <sup>h</sup> 25 <sup>m</sup> 38 <sup>s</sup>	18°33′	H1G1	65.3	17.0	GBM
100805A	04:12:42	19 <sup>h</sup> 59 <sup>m</sup> 23 <sup>s</sup>	52°37′	L1G1	2.23	2.39	BAT
100807A	09:13:13	3 <sup>h</sup> 41 <sup>m</sup> 07 <sup>s</sup>	67°39′	L1G1	2.04	1.60	BAT
100814B	08:25:26	8 <sup>h</sup> 11 <sup>m</sup> 16 <sup>s</sup>	18°29′	L1G1	3.63	10.0	GBM
100901A	13:34:10	1 <sup>h</sup> 49 <sup>m</sup> 00 <sup>s</sup>	22°45′	G1V1	7.36	6.16	BAT
100906A	13:49:27	1 <sup>h</sup> 54 <sup>m</sup> 47 <sup>s</sup>	55°38′	H1G1	1.16	1.16	BAT
100907A	18:01:12	11 <sup>h</sup> 49 <sup>m</sup> 09 <sup>s</sup>	−40°37′	G1V1	6.40	6.15	GBM
100915B	05:49:38	5 <sup>h</sup> 41 <sup>m</sup> 34 <sup>s</sup>	25°05′	L1G1	2.59	3.18	IBIS
101008A	16:43:15	21 <sup>h</sup> 55 <sup>m</sup> 31 <sup>s</sup>	37°03′	G1V1	4.16	2.79	BAT
101017B	14:51:29	1 <sup>h</sup> 49 <sup>m</sup> 52 <sup>s</sup>	−26°33′	G1V1	4.37	3.37	GBM
S6E							
110604A	14:49:46	18 <sup>h</sup> 04 <sup>m</sup> 00 <sup>s</sup>	18°28′	G1V1	4.70	3.18	BAT
110605A	04:23:32	0 <sup>h</sup> 59 <sup>m</sup> 47 <sup>s</sup>	52°27′	G1V1	1.82	1.49	GBM
110610A	15:21:32	20 <sup>h</sup> 32 <sup>m</sup> 49 <sup>s</sup>	74°49′	G1V1	2.12	1.93	BAT
110616A	15:33:25	18 <sup>h</sup> 17 <sup>m</sup> 48 <sup>s</sup>	−34°01′	G1V1	2.17	1.60	GBM
110618A	08:47:36	11 <sup>h</sup> 47 <sup>m</sup> 13 <sup>s</sup>	−71°41′	G1V1	2.11	1.61	GBM
110624A	21:44:26	4 <sup>h</sup> 20 <sup>m</sup> 04 <sup>s</sup>	−15°57′	G1V1	2.12	1.79	GBM
110625A	21:08:28	19 <sup>h</sup> 07 <sup>m</sup> 00 <sup>s</sup>	6°45′	G1V1	2.96	2.15	BAT
110626A	10:44:54	8 <sup>h</sup> 47 <sup>m</sup> 38 <sup>s</sup>	5°33′	G1V1	3.24	2.32	GBM
110629A	04:09:58	4 <sup>h</sup> 37 <sup>m</sup> 28 <sup>s</sup>	25°00′	G1V1	3.09	2.86	GBM

Table 4.2 continued

GRB name	UTC Time	Ra.	Dec.	Network	90% UL ( $\times 10^{-21} \text{ Hz}^{-1/2}$ )		$\gamma$ -Ray Detector
					500 Hz	1 kHz	
110702A	04:29:29	0 <sup>h</sup> 22 <sup>m</sup> 28 <sup>s</sup>	−37°39′	G1V1	5.70	6.70	GBM
110706A	04:51:04	6 <sup>h</sup> 40 <sup>m</sup> 19 <sup>s</sup>	6°08′	G1V1	5.94	5.64	GBM
110709A	15:24:29	15 <sup>h</sup> 55 <sup>m</sup> 34 <sup>s</sup>	40°55′	G1V1	2.60	2.07	BAT
110709B	21:32:39	10 <sup>h</sup> 58 <sup>m</sup> 40 <sup>s</sup>	−23°28′	G1V1	3.96	3.18	BAT
110709C	11:06:53	10 <sup>h</sup> 21 <sup>m</sup> 31 <sup>s</sup>	23°07′	G1V1	2.59	2.02	GBM
110709D	20:40:50	10 <sup>h</sup> 24 <sup>m</sup> 50 <sup>s</sup>	−41°47′	G1V1	3.07	2.87	GBM
110710A	22:53:51	15 <sup>h</sup> 16 <sup>m</sup> 21 <sup>s</sup>	48°23′	G1V1	1.92	1.61	GBM
110716A	00:25:20	21 <sup>h</sup> 58 <sup>m</sup> 43 <sup>s</sup>	−76°58′	G1V1	2.86	2.48	GBM
110722A	16:39:17	14 <sup>h</sup> 20 <sup>m</sup> 14 <sup>s</sup>	5°00′	G1V1	2.76	2.03	GBM
110729A	03:25:06	23 <sup>h</sup> 33 <sup>m</sup> 33 <sup>s</sup>	4°58′	G1V1	2.04	1.64	GBM
110730B	15:50:44	22 <sup>h</sup> 20 <sup>m</sup> 24 <sup>s</sup>	−2°53′	G1V1	2.86	2.19	GBM
110731A	11:09:30	18 <sup>h</sup> 42 <sup>m</sup> 03 <sup>s</sup>	−28°32′	G1V1	1.98	1.51	BAT
110801A	19:49:42	5 <sup>h</sup> 57 <sup>m</sup> 39 <sup>s</sup>	80°57′	G1V1	2.17	1.99	BAT
110803A	18:47:25	20 <sup>h</sup> 01 <sup>m</sup> 40 <sup>s</sup>	−11°26′	G1V1	6.02	4.13	GBM
110809A	11:03:34	11 <sup>h</sup> 28 <sup>m</sup> 40 <sup>s</sup>	−13°55′	G1V1	3.91	3.48	GBM
110817A	04:35:12	22 <sup>h</sup> 24 <sup>m</sup> 09 <sup>s</sup>	−45°50′	G1V1	3.47	2.77	GBM
110818A	20:37:49	21 <sup>h</sup> 09 <sup>m</sup> 29 <sup>s</sup>	−63°58′	G1V1	3.55	3.01	BAT
110825B	06:22:11	16 <sup>h</sup> 45 <sup>m</sup> 14 <sup>s</sup>	−80°16′	G1V1	2.35	2.14	GBM
110827A	00:01:52	10 <sup>h</sup> 56 <sup>m</sup> 14 <sup>s</sup>	53°49′	G1V1	4.11	3.41	BAT
110828A	13:48:15	7 <sup>h</sup> 22 <sup>m</sup> 19 <sup>s</sup>	−23°48′	G1V1	4.45	4.91	GBM
110831A	06:45:27	23 <sup>h</sup> 29 <sup>m</sup> 24 <sup>s</sup>	33°39′	G1V1	5.34	3.70	GBM
110903A	02:39:55	13 <sup>h</sup> 08 <sup>m</sup> 14 <sup>s</sup>	58°59′	G1V1	3.02	2.96	BAT
110903B	00:13:06	10 <sup>h</sup> 56 <sup>m</sup> 50 <sup>s</sup>	42°04′	G1V1	18.8	5.62	GBM
110904A	02:58:16	23 <sup>h</sup> 58 <sup>m</sup> 45 <sup>s</sup>	35°53′	G1V1	1.86	1.53	GBM
110904C	12:44:19	21 <sup>h</sup> 34 <sup>m</sup> 57 <sup>s</sup>	23°56′	G1V1	14.3	8.70	GBM
111008B	23:49:01	14 <sup>h</sup> 43 <sup>m</sup> 00 <sup>s</sup>	−5°40′	G1V1	3.35	4.31	GBM
111022A	16:07:04	18 <sup>h</sup> 23 <sup>m</sup> 29 <sup>s</sup>	−23°40′	G1V1	3.88	3.03	BAT
111022B	17:13:04	7 <sup>h</sup> 15 <sup>m</sup> 42 <sup>s</sup>	49°39′	G1V1	4.29	3.14	BAT
111103C	22:45:06	13 <sup>h</sup> 26 <sup>m</sup> 19 <sup>s</sup>	−43°09′	G1V1	1.58	1.59	GBM

Table 4.2: Information and limits on associated GW emission for each of the analysed GRBs. The first four columns are: the GRB name in YYMMDD format; the trigger time; and the sky position used for the GW search (right ascension and declination). The fifth column gives the GW detector network used in the analysis. Columns six and seven display the upper limits from each GRB: the 90% confidence upper limits on the strain amplitude for circularly polarised 500 Hz and 1 kHz sine-Gaussian waveforms, in units of  $10^{-21} \text{ Hz}^{-1/2}$ . The last column gives the  $\gamma$ -ray detector that provided the event time, sky location, sky position uncertainty, and  $T_{90}$  used for the search (*Swift* BAT, *Fermi* GBM, *INTEGRAL* IBIS, *SuperAGILE*, or *MAXI*). For three GRBs marked with a †, narrowband non-stationary noise in the GEO 600 detector at frequencies above 1 kHz may have reduced our sensitivity to GW signals.

### 4.3.6 Summary of results

We have reported the results of a search for generic short-duration gravitational wave signals associated with 78 GRBs with data from the GEO 600, LIGO and Virgo detectors, which were not previously analysed. The search covered the frequency range 64 Hz–1792 Hz, and employed a new technique to analyse the large-uncertainty GRB sky localisations from the *Fermi* GBM. This search is the

first GRB analysis performed using data from an interferometer implementing squeezing (see [section 2.5.8](#)), and the first to analyse GBM events for GW signals at frequencies above 500 Hz. No plausible GW event candidates were detected, and the population as a whole does not demonstrate a statistically significant number of low-probability events.

The LIGO and Virgo detectors are currently undergoing a major upgrade, implementing new techniques to greatly increase their sensitivity, and are expected to begin operations in 2015. It is likely that the first direct detection of GWs will occur within a few years of the resumption of science operations with the advanced LIGO detectors [123]. Our analysis demonstrates the potential for extending the search frequency band for GWs associated with GBM events above 1 kHz using two detector networks. The reduced computational cost of this method will be useful for rapid triggered analyses of *Fermi* GBM events in the era of advanced GW detectors, particularly in the first science runs which are likely to use only the two advanced LIGO detectors while advanced Virgo undergoes commissioning [123]. In the event of a GW detection with signal content above 1 kHz, our search method can provide improved localisation for GRBs with large uncertainties in sky location, which can be passed on to optical, radio, and x-ray astronomers for follow-up using wide-field telescopes.



# Gravitational Wave Detection Using Multivariate Analysis (XTMVA)

---

# 5

In this Chapter we give details on the performance of a multivariate analysis pipeline to search for GWBs associated with astrophysical triggers. This is an extension of the standard X-PIPELINE analysis, which will be used for comparison.

The sensitivity of GW transient searches is limited by the ability to distinguish between signals and background. This section draws from Ref. [204]. As described in [section 4.2](#), the standard X-PIPELINE analysis uses a simple pass/fail cut in one or more two-dimensional parameter spaces. These cuts only discriminate between signal and background using a few of the variables associated with each event, and ignore other information such as duration, bandwidth, and time-frequency volume. Multivariate analysis (MVA) techniques can mine the full parameter space of the events to better discriminate between signal and background. Here we explore the efficacy of MVA in GW detection by using the boosted decision tree (BDT) classifier to re-evaluate the significance of events from an X-PIPELINE analysis. We find that the BDT classification of events renders the  $(I, E)$  test redundant, and that BDT improves the amplitude sensitivity of the analysis by up to 50% in some cases.

## 5.1 X-PIPELINE Event Variables

As was explained in [section 4.2](#), X-PIPELINE is a standard analysis package used for LIGO–Virgo searches for generic GW transients associated with GRBs and other astrophysical triggers.

X-PIPELINE processes data from a network of GW detectors. First, the data are time-shifted according to the direction of the GRB trigger so that GW signals will arrive simultaneously in all data streams. Various combinations of the data streams are then formed, split into two groups: those that maximise the signal-to-noise ratio of a GW (signal streams); and those that cancel out GW signals leaving only noise events (null streams). Time-frequency maps of the signal streams are

constructed, and clusters of pixels that have large energy values are selected as candidate signal events [189]. For each event cluster a variety of energy measures and time-frequency information (such as peak frequency, bandwidth, peak time, duration, and number of pixels) are recorded. Each event is also assigned a significance measure based on the energy in the signal stream; in this study we use a Bayesian-inspired likelihood statistic appropriate for circularly polarised GWs [44]. Brief descriptions of the 15 event properties fed into the Multivariate X-PIPELINE (XTMVA) analysis are given in table 5.1.

Background noise fluctuations produce clusters of excess power in the signal streams. For these noise “glitches” there is typically a strong correlation between the energy in the individual detector data streams (incoherent energy  $I$ ) and the corresponding energy in the combined detector data streams (coherent energy  $E$ ) [192]. These incoherent and coherent energies are compared in order to remove events with properties similar to the background noise. The test uses a threshold curve in the two-dimensional  $(I, E)$  space, such as that shown in figure 4.3. The test may be single-sided, vetoing all events on one side of the line, or two-sided, vetoing events inside a band centred on the  $I = E$  diagonal. Two curve shapes are tested (see section 4.2.5):

$$\frac{I}{E} = \text{constant}, \quad (5.1)$$

$$\frac{|E - I|}{(E + I)^{0.8}} = \text{constant}. \quad (5.2)$$

For the studies performed here, there are usually three distinct  $(I, E)$  energy pairs available for testing: one associated with the signal stream, and two associated with null streams. Which pairs will be used for a given analysis and the thresholds to be used are determined by an automated tuning procedure (see Ref. [193] for a discussion).

The thresholds for the background rejection tests are selected to optimise the trade-off between glitch rejection and signal acceptance. Samples of known background events are generated by analysing data with unphysically large ( $> 3$  s) relative time shifts applied to the detector data streams. Known signal events are generated by adding simulated GW signals to the data, known as “injections”. The background and injection events are randomly divided into two equal sets, one that is used for training the pipeline and a second that is used for testing performance. For each  $(I, E)$  pair the background rejection test is applied to both the background and injection training samples using a range of trial thresholds. The cumulative distribution of significance of background events surviving the cuts is computed. We then determine the minimum injection amplitude at which 50% of the injections both survive the cuts and have significance greater than a user-specified fraction of the background (e.g., greater than 99% of the background, for a p-value  $\leq 0.01$ ). The optimum thresholds are then defined as those which yield the lowest minimum injection amplitude at the user-specified p-value (i.e., which make the analysis sensitive to the weakest GW signals at fixed p-value). Finally, unbiased estimates of the background distribution and



Event property	Description
significance	The statistic used to rank events. By default equal to $\text{loghbayesiancirc}$ .
$\text{loghbayesiancirc}$	Bayesian-inspired likelihood ratio for the hypothesis of a circularly polarised GWs versus Gaussian noise [44].
$E_{\text{max}}$	The maximum amount of energy in the whitened data that is consistent with the hypothesis of a GW of any polarisation from a given sky position.
$E_{\text{circ}}$	The circular coherent energy is the maximum amount of energy in the whitened data that is consistent with the hypothesis of a circularly polarised GW from a given sky position.
$I_{\text{circ}}$	The circular incoherent energy is the sum of the autocorrelation terms of $E_{\text{circ}}$ ; i.e., neglecting cross-correlation terms.
$E_{\text{circnull}}$	The circular coherent null energy, $E_{\text{max}} - E_{\text{circ}}$ . Physically, it is the energy in the whitened data that is inconsistent with the hypothesis of a circularly polarised GW from a given sky position, but which could be produced by a GW of a different polarisation.
$I_{\text{circnull}}$	The circular incoherent null energy is the sum of the autocorrelation terms of $E_{\text{circnull}}$ ; i.e., neglecting cross-correlation terms.
$E_{\text{null}}$	The coherent null energy is the minimum amount of energy in the whitened data that is inconsistent with the hypothesis of a GW of any polarisation from a given sky position.
$I_{\text{null}}$	The incoherent null energy is the sum of the autocorrelation terms of $E_{\text{null}}$ ; i.e., neglecting cross-correlation terms.
$E_{\text{H1}}$	The cluster energy in the LIGO-Hanford interferometer.
$E_{\text{L1}}$	The cluster energy in the LIGO-Livingston interferometer.
$E_{\text{V1}}$	The cluster energy in the Virgo interferometer.
number of pixels	The number of pixels in the cluster.
duration	The extent of the cluster in time (s).
bandwidth	The extent of the cluster in frequency (Hz).

Table 5.1: Cluster properties recorded by X-PIPELINE that are fed into the XTMVA analysis. See [189, 193, 44] for more details.

detectable injection amplitudes are made by processing the testing data set with our fixed optimal test thresholds.

## 5.2 Toolkit for Multivariate Analysis

We use the ROOT [205] based software package toolkit for multivariate analysis (TMVA) [206] which was developed by the particle physics community [207]. TMVA takes as input known signal and background events. These events are split randomly into two sets, one for training the classifier and the other for testing its performance. This split ensures that the testing produces an unbiased estimate of the classifier performance, since the events used for testing are independent of those used for training.

The results from the training of the classifier are stored in a “weight” file, that contains all the information needed to evaluate the classifier function for any input event and assign a MVA significance value. This significance is a measure of the likelihood of an event being a signal; events with high values of significance are more likely to be signals, and events with small values of significance are more likely to be background. The TMVA package provides many classifiers such as boosted decision trees (BDTs), neural networks (NNs) and projective likelihood [206]. For a full list and descriptions of all the classifiers variables in TMVA, see [206]. Initial tests, performed by Duncan Meacher in [208], found that a number of the classifiers produced similar results, and that by tuning the classifier parameters an improvement of  $\sim 10\%$  was possible; for simplicity we selected BDT using the default parameters for in-depth testing as it exhibited the best performance in the shortest processing time, as shown in figure 5.1, [208]. However, a more in-depth study should be performed to optimise MVA performance for GW applications.

Using the BDT classifier also outperforms the standard X-PIPELINE post processing procedure. The standard X-PIPELINE post processing takes  $\mathcal{O}(1 \text{ day})$  to complete while the XTMVA post processing takes only a few hours, this is a factor of  $\sim 100$  improvement in computational cost. This improvement is consistent though out our tests, and there is plenty of scope to further optimise the XTMVA to gain further improvements in speed.

## 5.3 Boosted Decision Trees

A decision tree consists of a series of yes/no decisions applied to each event, as shown schematically in figure 5.2. Beginning at the root node, an initial criterion for splitting the full set of events is determined. The split criterion consists of a threshold applied to a single variable, selected to best discriminate signal from background. The split criterion are determined by applying a range of thresholds for each variable in turn to the training data set to determine which combination provides the best separation between signal and background events. This split results in two branches, each containing a subset of the events. The process then repeats, with a new split criterion being determined at each branch node

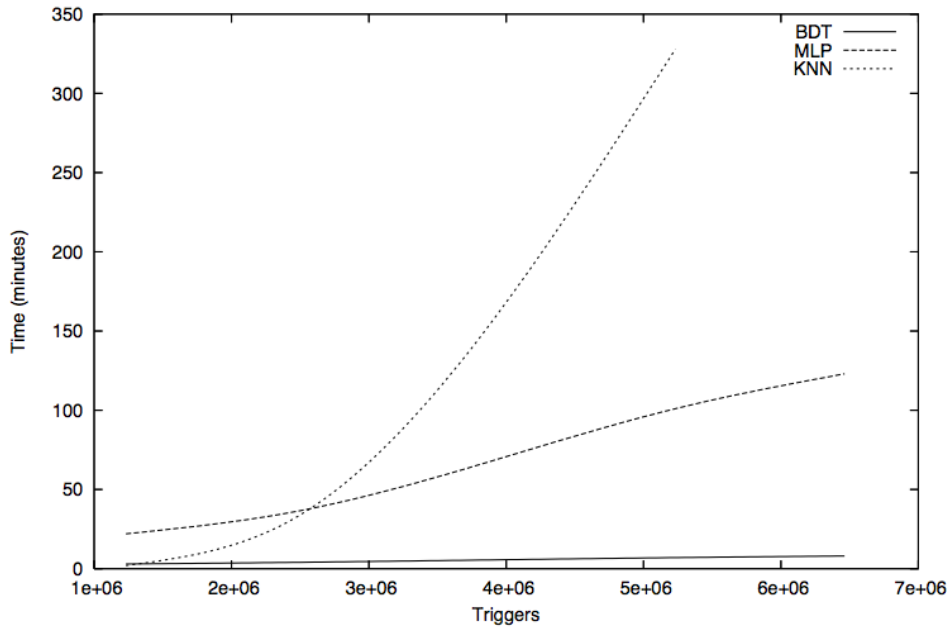


Figure 5.1: Processing time verses number of triggers for different MVA classifiers. BDT is shown as a solid line. This classifier is described in depth in [section 5.3](#). Multilayer perceptron (MLP)/ neural network is shown as a dashed line. This classifier uses a collection of simulated neurons, with each neuron producing a certain response at a given set of input signals. k-nearest neighbour (KNN) is shown as a dotted line. This classifier method compares an observed (test) event to reference events from a training data set to building a model that reproduces the input variables for signal and background.

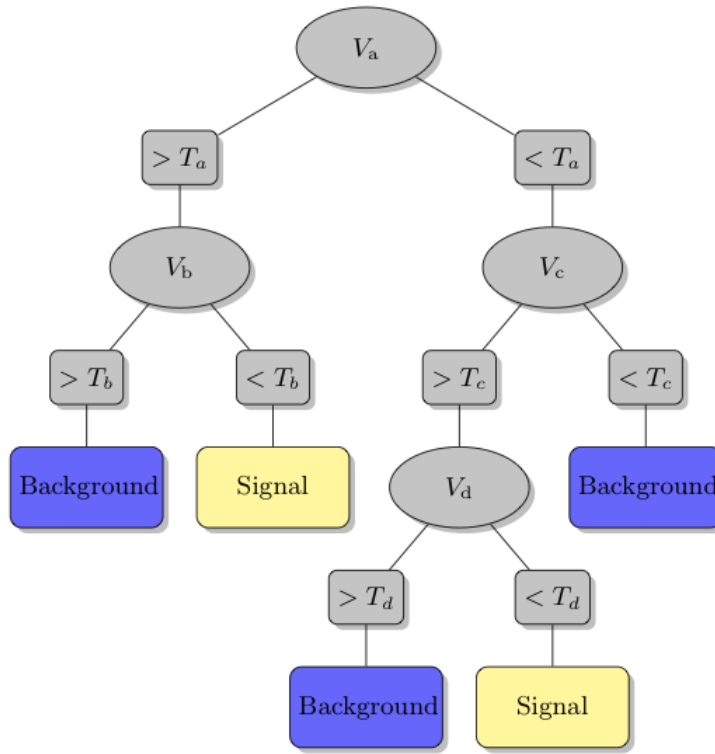


Figure 5.2: Schematic of a decision tree. Decision nodes for each event variable ( $V_a$ ,  $V_b$ ,  $V_c$ , and  $V_d$ ) are grey ellipses, with thresholds ( $T_a$ ,  $T_b$ ,  $T_c$ , and  $T_d$ ) for each branch given in grey rectangles. The events are classified by a majority vote of events in a leaf node as either signal (yellow/ light grey rectangles) or background (blue /dark grey rectangles).

to further separate signal from background. The splitting process ends once a minimum number of events has been reached within a node, which then becomes a leaf node. We use the default value in TMVA of 400 events. Leaf nodes are labelled as either signal or background depending on the class of the majority of training events that fall within it. The user can specify criteria at which the tree stops being grown, such as how many layers a tree can contain and the total number of nodes which may be created.

Decision trees are susceptible to statistical fluctuations within the set of training events used to derive the tree structure. To avoid over training, a whole “forest” of decision trees are created, each generated using a randomly selected subset of the training events. The final classification of events is determined by a majority vote from the classifications of each individual tree within the forest. This procedure stabilises the response of individual trees and enhances overall performance. We use the default forest in TMVA made of 400 BDTs.

Another procedure to statistically stabilise the classifier is “boosting”. During training, signal and background events which are misclassified by one tree are given increased weight when constructing the next tree in the forest. We use the default boosting method in TMVA, “AdaBoost”.

## 5.4 Signal Population

We test BDT for a common GW scenario: the search for a GW burst associated with a GRB.

For our purposes, the GRB trigger provides a known sky position (accurate to within a few degrees) and approximate arrival time (to within a few minutes) of the GW signal, as well as motivating some possible signal models. Furthermore, in each model the GWs are emitted by a quadrupolar mass distribution rotating around the GRB jet axis. Since the GRB is observed at Earth, this implies the observer is near the system axis, which yields circularly polarised GWs [194].

For training and testing the MVA classifier we need to choose a set of simulated GW waveforms to generate our signal data set. Since the expected GW emission is not known with certainty (particularly for long GRBs), we must be careful to avoid training the classifier to find only the waveforms that have been used for training. To do this we use a combination of different waveform classes, which are described below.

**circular sine-Gaussians (CSGs):** These are circularly polarised, Gaussian modulated sinusoids with a fixed central frequency and quality factor (number of cycles); see figure 5.3(a). This simple *ad hoc* waveform is a standard choice for evaluating the sensitivity of burst searches, and is a special case of the chirplets, which are described below.

**binary neutron star inspirals (BNS):** The binary neutron star progenitor model for short GRBs implies an associated “chirp” signal in GWs which can be accurately modelled using a Post-Newtonian (PN) expansion [209]. See figure 5.3(b) for an example. Since the X-PIPELINE analysis is not sensitive to the precise morphology, we use the approximation that is quadrupolar in amplitude and 2 PN in phase and frequency, and cut off the inspiral at the earlier of the coalescence time or the time that the phase second derivative becomes negative.

**chirplets:** Chirplets are a generalisation of the CSG waveforms with a non-zero chirp parameter that causes the instantaneous frequency to increase or decrease linearly with time. See figure 5.3(c) for an example.

**white noise bursts (WNBs):** White noise bursts are stochastic signals: bursts of Gaussian noise which are white over a frequency band  $[f_{\text{low}}, f_{\text{low}} + \delta f]$  and which have a Gaussian time profile with decay time  $\tau$ . See figure 5.3(d) for an example.

The incident sky position is distributed over the GRB sky uncertainty region following a Fisher distribution [44]. The signal arrival time is distributed uniformly over the interval  $[t_{\text{GRB}} - 120 \text{ s}, t_{\text{GRB}} + 60 \text{ s}]$ , known as the *on-source* window. Here  $t_{\text{GRB}}$  is the time of the GRB trigger; this on-source window is wide enough to encompass most plausible scenarios of GW emission associated with GRBs. The polarisation angle is uniformly distributed over  $[0, \pi]$ . For the CSGs and chirplets, the central frequency is distributed uniformly over the search band,

64 Hz to 500 Hz, which is the most sensitive frequency band of the LIGO and Virgo detectors. The signal decay rate  $\tau$  is uniformly distributed between the minimum (1/4 s) and maximum (1/128 s) time resolutions searched by X-PIPELINE. The chirp parameter is distributed uniformly between the values which half or double the central frequency in the time interval from  $-\tau$  to  $\tau$  about the peak time. The BNS signals use a fixed mass of  $1.35 M_{\odot}$  for each of the components of the binary, and an inclination angle between  $0^{\circ}$  and  $30^{\circ}$ . The white noise burst (WNB) waveforms are constructed with fixed values  $f_{\text{low}} = 50$  Hz,  $\delta f = 100$  Hz and decay time  $\tau = 0.1$  s.

The BNS waveforms are physically motivated signal models. While the other waveforms are *ad hoc*, the CSGs are a standard waveform class for evaluating the sensitivity of GWB searches. Therefore we choose to use a combination of BNS and CSG waveforms for our default training signal set. The WNB and chirplet waveforms are used to test the robustness of the analysis, as described in [section 5.5.6](#). In particular, the WNB model, being stochastic, provides a rigorous test of the ability of MVA to detect signals of *a priori* unknown shape.

Each waveform is added to the data, and X-PIPELINE selects the most significant time-frequency cluster (event) that is coincident with the time at which the waveform was added to the data. This is repeated for each waveform set at a number of injection scales to generate our signal population. At small injection scales the injection can be buried by the detector noise at the time of the injection. In this case X-PIPELINE will recover a glitch in place of an event produced by the injection, which causes some contamination of the signal data set. This effect reduces the performance of the classifier to separate signal and background events, as the signal set contains some small number of background events. This can be seen in [figure 5.16](#). The scale of the affect that this has on the performance of the classifier is currently unmeasured, but by cleaning the signal data set of these events we could hope to see an improvement in the classifier performance. This is a subject for investigation in a future publication, as well as investigating the possibility for optimisation of the XTMVA pipeline. The background population is produced using events from the off source period around the time of the trigger being analysed. Our signal and background data sets consist of  $\sim 1.4 \times 10^4$  and  $\sim 1.4 \times 10^6$  events respectively, which are each split randomly into equal sized training and testing sets.

## 5.5 Multivariate X-PIPELINE Performance

We test the efficacy of MVA for GW burst detection by performing a standard analysis of the type used to search for GWs from GRBs. First, X-PIPELINE is used to process the data around the time and sky position of a (simulated) GRB trigger. The sensitivity of the analysis is characterised by the minimum amplitude at which at least 50% of simulated signals survive the analysis cuts and have  $p$  values of 1% or less, as discussed in [section 4.2](#). This amplitude is denoted by  $h_{\text{rss}}^{50\%}$ . The BDT classifier is then applied to the events recorded by X-PIPELINE to re-evaluate the significance of each event. The procedure of

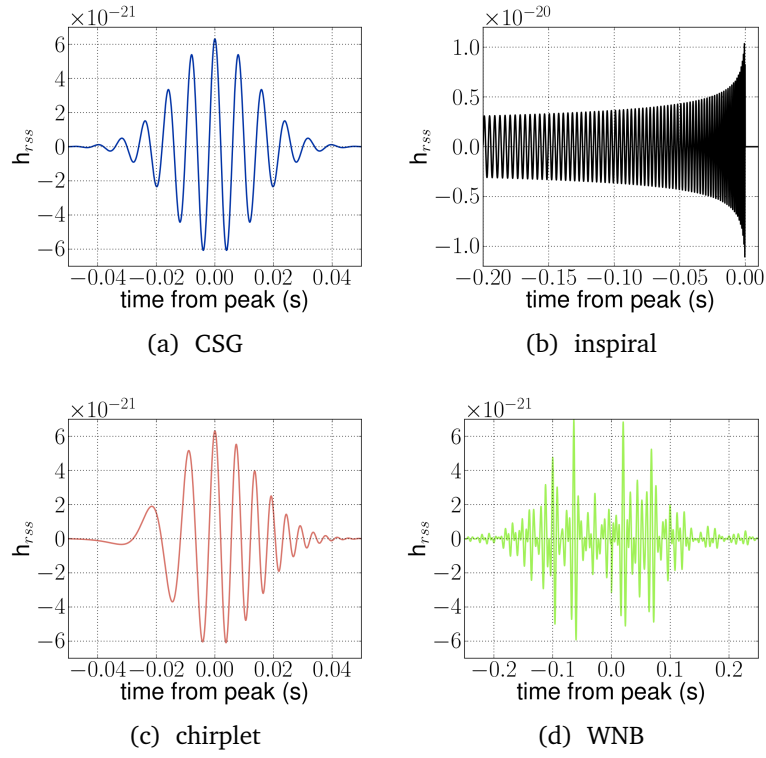


Figure 5.3: Time series of waveforms used for signal injections. For clarity, only one of the two polarisations is plotted.

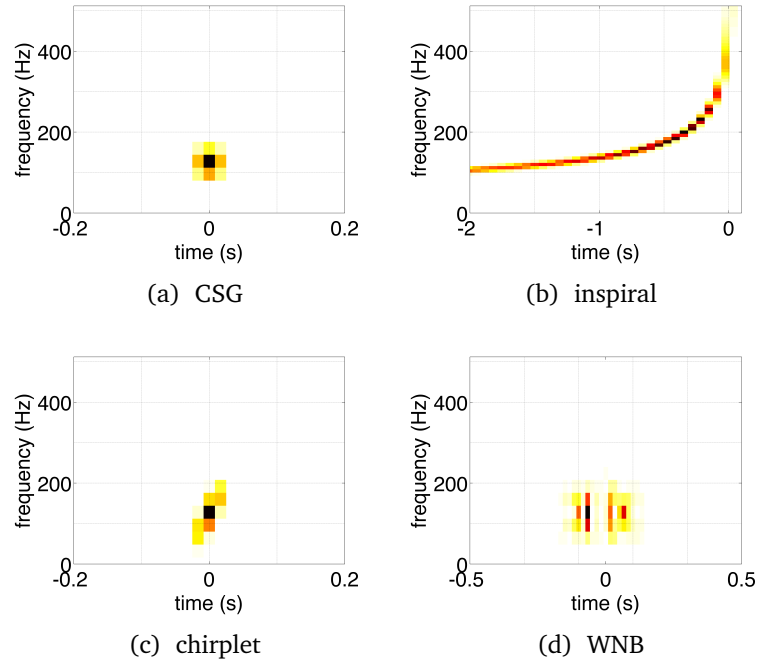


Figure 5.4: Time-frequency spectrograms of waveforms used for signal injections. For clarity, only one of the two polarisations is plotted.

cut threshold tuning and sensitivity estimation is then repeated using the BDT measure of significance to rank events. The relative performance is measured as the ratio of  $h_{\text{rss}}^{50\%}$  for the standard X-PIPELINE analysis and the XTMVA analysis. A ratio greater than unity indicates that the XTMVA analysis is more sensitive to a particular waveform type than the standard X-PIPELINE analysis.

To verify that the performance improvement of MVA is robust, we repeat the GRB analysis for a number of different scenarios. Specifically, we test different GRB sky positions covering a range of network sensitivities, and both large and small sky position uncertainty regions. We also repeat the analysis for a period of particularly poor data quality, and using simulated Gaussian noise to approximate ideal data quality. We find that the relative improvement of BDT to X-PIPELINE is consistent across all of these scenarios. We also explore the affect of training using only two types of waveform (CSGs, BNSs) or all four types of waveform. We find that even when searching for signal types that are not included in the training set, the XTMVA analysis is consistently at least as sensitive as the X-PIPELINE analysis, and typically more sensitive. Furthermore, in all cases we find that after processing events with BDT, the X-PIPELINE background rejection tests do not improve the sensitivity further; i.e., the BDT has effectively incorporated the signal/background discrimination power of the X-PIPELINE background rejection test. Since the test typically requires some assumption about the signal polarisation (in this study we assume circular polarisation), the replacement of the test by BDT actually broadens the range of signals to which the analysis is sensitive.

The following subsections describe each of these tests in turn. We give a full table of the  $h_{\text{rss}}^{50\%}$  results for all analyses and all waveforms in [table 5.3](#).

### 5.5.1 Baseline GRB 060223A Analysis

For our baseline test we perform an analysis using the parameters (time, sky position) of GRB 060223A, as given in [table 5.2](#). GRB 060223A was detected by the *Swift* satellite [[197](#)] during a period of operation of the LIGO H1, LIGO L1, and Virgo V1 detectors, and localised by *Swift* to a well-defined sky position. We generate signal events by adding simulated CSG and BNS signals to the three minute on-source window  $t_{\text{GRB}} - 120 \text{ s}$ ,  $t_{\text{GRB}} + 60 \text{ s}$  around the GRB. We generate background events by analysing a three-hour off-source window surrounding the GRB time. These events were split randomly into two sets for training and testing the BDT.

The plot of background rejection against signal efficiency for the BDT test sample, using the CSG waveforms, is given in [figure 5.5](#). We see that the BDT classifier is very powerful at rejecting background events, even up to very high signal efficiencies (above 0.94) we still obtain  $\sim 100\%$  background rejection.

As can be seen in [figure 5.6](#), for CSG signals the XTMVA analysis gives a substantial improvement in sensitivity – of order 50% – over the standard X-PIPELINE analysis. However, there is no significant improvement in the sensitivity to BNS signals (differences of order 5% are not statistically significant).



Test name	UTC time	Ra.	Dec.	Sky position uncertainty
GRB 060223A (default)	2006-02-23 06:04:23	55.19°	−17.13°	0.03°
sky position 1	2006-02-23 06:04:23	299.56°	44.16°	0.03°
sky position 2	2006-02-23 06:04:23	311.02°	32.70°	0.03°
sky position 3	2006-02-23 06:04:23	345.40°	−1.67°	0.03°
sky position 4	2006-02-23 06:04:23	31.23°	−47.51°	0.03°
large sky position uncertainty 1	2006-02-23 06:04:23	345.40°	−1.67°	9.0°
large sky position uncertainty 2	2006-02-23 06:04:23	31.23°	−47.51°	9.0°
highly non-Gaussian background	2007-06-20 03:05:40	319.52°	−57.67°	0.03°
detection challenge	2007-09-22 03:05:40	33.44°	16.94°	0.03°

Table 5.2: Trigger parameters used during test analyses. The waveform robustness and Gaussian noise tests used the default GRB 060223A parameters.

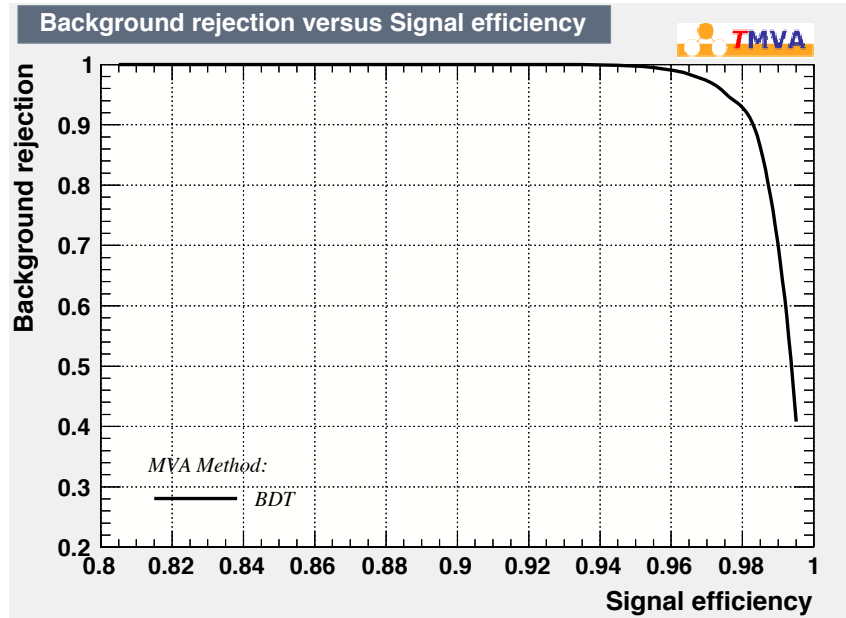


Figure 5.5: Background rejections against signal efficiency for the BDT test sample in the GRB 060223A analysis. Note the x-axis scale, where we focus on the region of interest at large signal efficiencies. The threshold used in the BDT significance is the parameter which is used to select a point on this curve.

### 5.5.2 Sky Position

To verify that the results of the BDT–X-PIPELINE comparison are robust, we repeat the test for a variety of other cases. First, we vary the sky position of the GRB trigger. We test four additional sky positions, as listed in [table 5.2](#). These positions were chosen to cover a range of different relative detector network sensitivities [44].

As can be seen in [figure 5.6](#), for CSG waveforms the XTMVA analysis gives a consistent improvement in sensitivity of 30 – 50%, for all tested sky positions, compared to the standard X-PIPELINE analysis. Again there is no significant change in the sensitivity to BNS signals.

### 5.5.3 Large Sky Position Uncertainty

The previous tests have assumed the GRB sky position to be known to high accuracy ( $\ll 1^\circ$ ). By contrast, GRBs detected by the GBM instrument on the Fermi satellite have relatively large sky location systematic uncertainties of a few degrees [200] and statistical errors of up to  $\sim 10$  degrees. This requires analysing the GW data over a grid of trial sky positions covering the error region [44]. We test the performance of the XTMVA analysis in this scenario using two different sky positions with sky position uncertainties of  $\approx 9^\circ$  (see [table 5.2](#)), which is typical for Fermi-GBM GRBs [198].

As can be seen in [figure 5.6](#), the BDT performance is consistent with previous tests: for CSG waveforms BDT improves the sensitivity by 40 – 50%, with no significant change in the sensitivity to BNS signals.

### 5.5.4 Highly Non-Gaussian (Glitchy) Background

Excess power noise transients can be introduced into the detector data streams by a wide range of known and unknown sources. These glitches are artefacts of the detectors and can be difficult to distinguish from real weak signals. To test the performance of the XTMVA analysis, we analyse a trigger which is at a time of unusually poor data quality.

As can be seen in [figure 5.6](#), for CSG waveforms the XTMVA analysis again gives a  $\sim 30\%$  improvement in sensitivity, with no notable change for BNS signals compared to the standard X-PIPELINE analysis.

### 5.5.5 Gaussian Background

As a best-case scenario, the performance of the XTMVA analysis was tested using simulated Gaussian noise with a spectral density coloured to match that of the real detector noise at the time of our default GRB 060223A trigger. All other parameters are kept the same as in the default analysis.

As can be seen in [figure 5.6](#), for CSG waveforms the XTMVA analysis gives an improvement in sensitivity of 40% compared to the standard X-PIPELINE analysis. There is no notable change in the sensitivity to BNS signals.

### 5.5.6 Waveform Robustness

In GW burst searches the signal waveform is usually not known *a priori*. It is therefore of the utmost importance to verify that MVA is able to detect waveforms with morphologies that differ from those used for training; at the very least, MVA should not have *worse* sensitivity for unknown waveforms than the standard analysis. We study this issue by repeating our analysis using different waveform sets for training and testing. Specifically, we evaluate the BDT performance for detecting chirplet and WNB waveforms in two cases: one in which the BDT is trained using CSG and BNS signals *only* (and not chirplet or WNB signals) and again after training on all four waveform types (CSG, BNS, chirplet, WNB). We refer to these as the two-waveform and four-waveform robustness tests.

Figure 5.6 shows that in the two-waveform test (training on CSG and BNS only) the XTMVA analysis shows the same performance for CSG and BNS as was seen in the default GRB 060223A analysis. This is expected, as the tests are identical as far as these waveforms are concerned. However, BDT also gives an improvement in sensitivity of order 50% for chirplet waveforms compared to the standard X-PIPELINE analysis. This implies that the CSGs and chirplets are sufficiently similar in terms of a time-frequency analysis that an MVA trained to detect one can detect the other. More surprising is the BDT performance for WNBs. These waveforms are not detectable by the standard X-PIPELINE analysis. This happens because the two GW polarisations are uncorrelated for a WNB, whereas the X-PIPELINE background rejection test applied to the signal stream (discussed in section 4.2) assumes the two polarisations are related by  $90^\circ$  phase shift, as expected for a circularly polarised signal. The XTMVA analysis is able to recover these waveforms, albeit with an  $h_{\text{rss}}^{50\%}$  value about twice as high as for the case of training with WNBs (discussed below).

The four waveform robustness test used independent samples of all four waveform types (CSG, BNS, chirplet, and WNB) for both training and testing. From figure 5.6 we again see the same performance from BDT for the CSG and BNS signals. However, with training extended to include chirplet and WNB waveforms, we see slightly *less* improvement of sensitivity to chirplets (only 30% compared to the standard X-PIPELINE analysis). This is partly due to a small improvement in the sensitivity of the X-PIPELINE analysis to chirplets when they are included in the training. However, most of the change is due to a decrease in sensitivity of the XTMVA analysis ( $\sim 15\%$  drop) from the two-waveform case; we attribute this to the inclusion of WNBs in the training. The classifier in this case finds a compromise between the sensitivity to circularly polarised signals and unpolarised signals in the training. This can be seen as the sensitivity to WNBs is dramatically improved, by more than a factor of two compared to the two-waveform XTMVA analysis. The standard X-PIPELINE analysis can also detect WNBs when trained with all four waveform types; in this case the automated background rejection tuning places less emphasis on the tests that assume circular polarisation and more on the polarisation-independent null stream test. We find a net sensitivity improvement of  $\sim 15\%$  by BDT relative to X-PIPELINE for WNBs when training includes these waveforms.

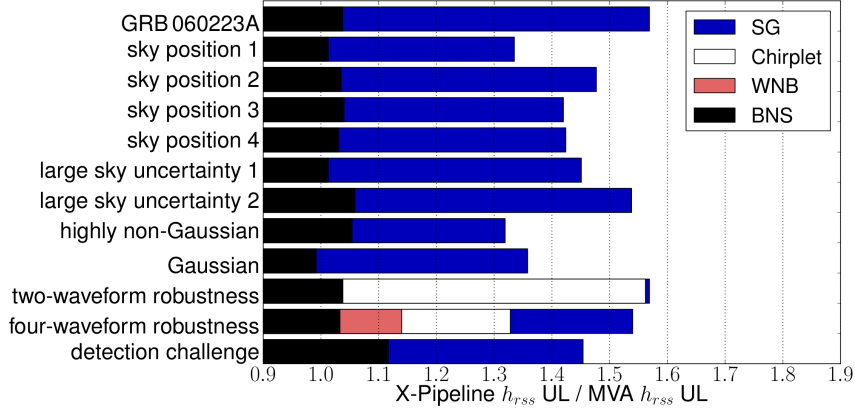


Figure 5.6: Ratio of the minimum-detectable signal amplitudes  $h_{\text{rss}}^{50\%}$  for the standard X-PIPELINE analysis and the XTMVA analysis for each of the signal waveforms and scenarios described in [section 5.5](#). Ratios greater than 1 indicate the XTMVA analysis is more sensitive than the standard X-PIPELINE analysis. (Equivalently, for a fixed signal amplitude the distance reach of the BDT search is greater than that of the X-PIPELINE search by this ratio.) CSG performance is given in blue (dark grey), BNS performance is given in black, chirplet performance is given in white, and WNB performance is given in red (light grey). The standard X-PIPELINE analysis is unable to recover WNB signals in the robustness two-waveform test, so the sensitivity ratio is ill-defined in this case. All  $h_{\text{rss}}^{50\%}$  values of results can be found in [table 5.3](#).

### 5.5.7 Detection Challenge Case

Recent science runs of the LIGO and Virgo detectors have included a “blind injection challenge” wherein a small number of simulated signals are secretly added to the data via the interferometer control systems [210, 64, 43, 63]. These signals are used to test the analysis procedures. Our final test is to analyse one of these signals, to demonstrate that the improvement in sensitivity extends to false-alarm rates low enough to permit a detection claim at the  $3\sigma$  level.

For this test we select the “equinox event”, an injection performed on 22 September 2007. The simulated waveform was approximately a single-cycle sine-Gaussian with a central frequency of approximately 60 Hz and an amplitude of  $h_{\text{rss}} = 1.0 \times 10^{-21} \text{ Hz}^{-1/2}$ ; see [figure 5.7](#). The relative amplitudes of the plus and cross polarisations were consistent with an inclination angle of approximately  $30^\circ$ . The sky position is shown in [table 5.2](#).

We analysed this injection using the standard GRB procedure; i.e., assuming the sky position and approximate time of the event were known *a priori* due to observation of an electromagnetic counterpart. In our previous tests we evaluated the minimum detectable signal amplitude at a fixed false alarm probability of 1%. This follows the standard use of X-PIPELINE in GRB searches [53, 43]. However, in order to claim the detection of a GW signal, much lower false-alarm probabilities are required. In particular, a  $3\sigma$  significance requires a false-alarm probability of  $p \leq 0.0027$ . Furthermore, a typical search includes 100–150 GRB

Analysis	Waveform	$h_{\text{rss}}^{50\%} (10^{-21} \text{ Hz}^{-1/2})$		Ratio
		X-PIPELINE	BDT	
GRB 060223A (default)	CSG	4.90	3.12	1.569
	BNS	10.9	10.5	1.038
sky position 1	CSG	8.70	6.51	1.335
	BNS	20.5	20.2	1.013
sky position 2	CSG	6.43	4.36	1.477
	BNS	14.2	13.7	1.035
sky position 3	CSG	4.07	2.86	1.420
	BNS	9.08	8.73	1.040
sky position 4	CSG	3.91	2.74	1.424
	BNS	9.03	8.76	1.031
large sky position uncertainty 1	CSG	4.19	2.89	1.451
	BNS	9.39	9.26	1.013
large sky position uncertainty 2	CSG	4.04	2.63	1.538
	BNS	9.21	8.70	1.059
Very non-Gaussian background	CSG	5.70	4.32	1.319
	BNS	13.8	13.1	1.054
Gaussian background	CSG	4.48	3.30	1.358
	BNS	10.1	10.2	0.992
two-waveform robustness	CSG	4.90	3.12	1.569
	BNS	10.9	10.5	1.038
	chirplet	50.3	3.22	1.562
	WNB	nan	16.5	nan
four-waveform robustness	CSG	4.91	3.19	1.540
	BNS	11.0	10.6	1.033
	chirplet	4.81	3.62	1.328
	WNB	7.45	6.54	1.140
detection challenge case	CSG	4.92	3.38	1.454
	BNS	7.65	6.85	1.117

Table 5.3: Sensitivity of the standard X-PIPELINE and XTMVA analyses for each test scenario and waveform type.  $h_{\text{rss}}^{50\%} (\text{Hz}^{-1/2})$  is the minimum amplitude for which at least 50% of simulated signals survive the analysis cuts and have p-value  $\leq 0.01$  or less. The last column is the ratio of  $h_{\text{rss}}^{50\%}$  for X-PIPELINE and XTMVA analyses; values greater than unity indicate that XTMVA is more sensitive. Equivalently, for a fixed signal amplitude the distance reach of the XTMVA search is greater than that of the X-PIPELINE search by this ratio.

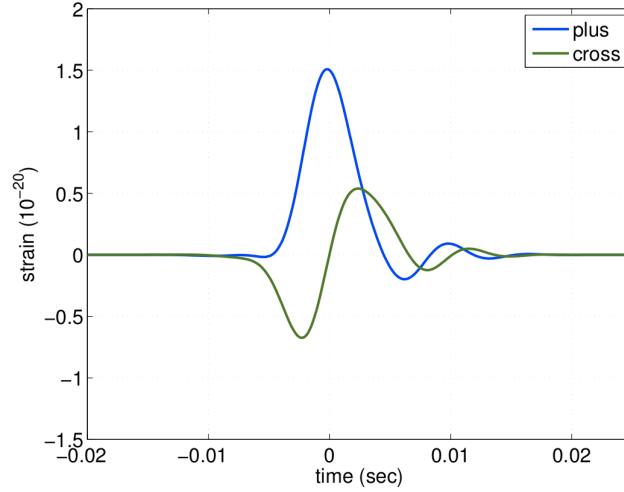


Figure 5.7: Time series of the “equinox event” signal in the detection challenge test.

triggers, which must be accounted for in the trials factor. A  $3\sigma$  significance with 150 trials requires  $p \lesssim 2 \times 10^{-5}$  for an individual event. For this analysis we therefore generate extra background samples and tune the background rejection tests to yield the lowest minimum injection amplitude at a p-value of  $p = 10^{-5}$ . Since the blind injection was not added to the Virgo detector data, we analyse the event using the LIGO H1 and L1 detectors only. All other analysis parameters are the same as for the GRB 060223A test, including training and testing with CSG and BNS waveforms.

Figure 5.8 shows the cumulative distribution of the detection statistic for the loudest background event per three minute interval (the on-source interval) returned by the standard X-PIPELINE analysis and the XTMVA analysis. Both distributions are consistent with a power-law relationship between false alarm probability and detection statistic down to the lowest false alarm probabilities measured,  $p \simeq 10^{-5}$ . From figure 5.6 we can see that the XTMVA analysis gives an improvement in sensitivity compared to the standard X-PIPELINE analysis that is consistent with previous tests. This demonstrates that the benefits of the XTMVA analysis extend down to false alarm rates sufficient for  $3\sigma$  detections in GRB triggered searches.

Of particular interest is the significance assigned to the equinox event itself. The vertical lines in figure 5.8 indicate the value of the detection statistic returned by X-PIPELINE and BDT. In both analyses the equinox event is clearly detected, with a significance higher than any of the background events. In order to estimate the approximate false alarm probability for the equinox event, we extrapolate the background distributions using a best-fit power law. This yields  $p \simeq 7 \times 10^{-8}$  ( $5.4\sigma$ ) for the standard X-PIPELINE analysis and  $p \simeq 1 \times 10^{-10}$  ( $6.5\sigma$ ) for the XTMVA analysis. The shaded bands indicate the plausible extrapolations from using a varied number of data points to determine the best-fit parameters, which can be taken as an estimate of the uncertainty in the extrapolation. While these are estimates, the XTMVA analysis assigns a false alarm

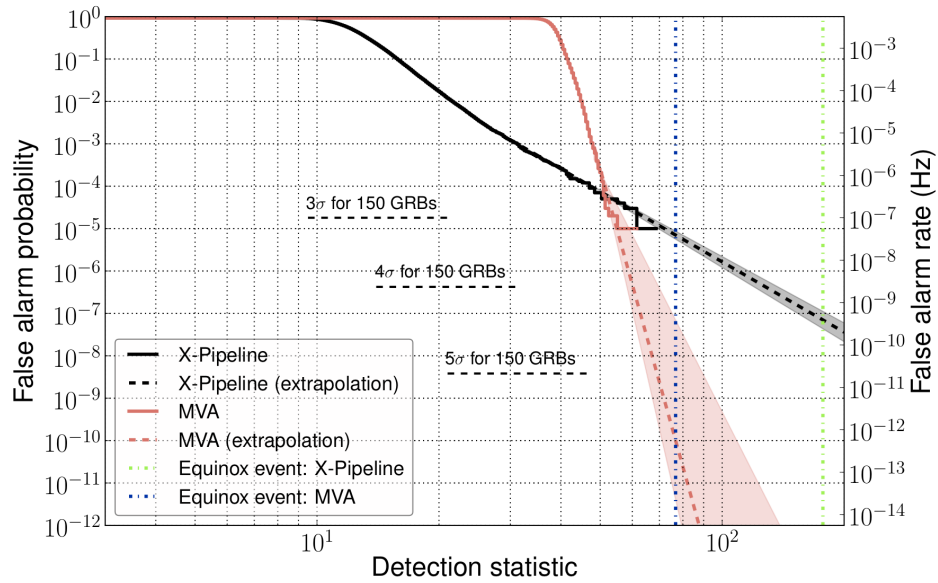


Figure 5.8: Background distributions for the X-PIPELINE and BDT analyses of the equinox event. The background distributions are shown as solid lines. The power-law extrapolations are shown as dashed lines, with the shading indicating the estimated uncertainty in the extrapolations. The value of the detection statistic of the equinox event is shown by the green and blue vertical lines for the X-PIPELINE and BDT analyses respectively.

probability which is at worst consistent with the X-PIPELINE result, and the range of possible extrapolations suggest that the false alarm probability could be significantly lower.

## 5.6 Discussion and Conclusions

The tests shown in [section 5.5](#) and [figure 5.6](#) demonstrate that the XTMVA analysis yields a consistent improvement in sensitivity to some signal types at fixed false-alarm rate with respect to the standard X-PIPELINE analysis. The improvement holds regardless of the incident direction of the signal or its sky location uncertainty, the data quality, and the network of detectors. Most importantly, the XTMVA analysis is always at least as sensitive as X-PIPELINE, even to signals of different morphology to those used in training, and the sensitivity improvement extends down to false alarm probabilities required for detection.

The degree to which the XTMVA analysis outperforms the standard X-PIPELINE analysis depends on the signal waveform. For CSGs, which have compact time-frequency distributions, we find a consistent improvement in sensitivity of 35 – 55%. By contrast, for BNS signals, which are long-duration and have extended time-frequency distributions, the average improvement in sensitivity is only 4%. The XTMVA analysis also yields improved sensitivity to chirplet and WNB waveforms, regardless of whether they were included in the training set or not. The



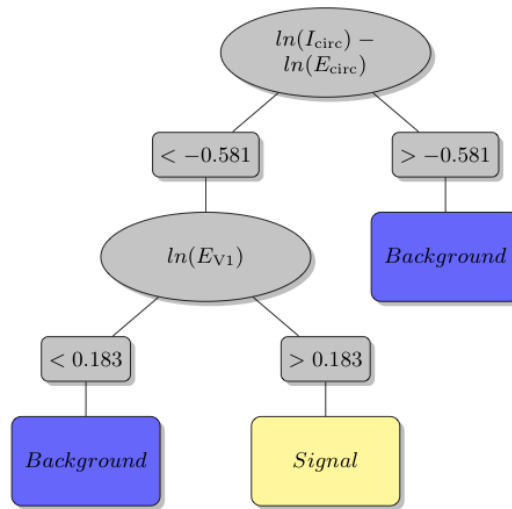


Figure 5.9: Example decision tree used in the GRB 060223A XTMVA analysis.

Decision nodes are grey ellipses, with thresholds for a branch given in grey rectangles. Leaf nodes for signal events are light yellow rectangles and for background events are dark blue rectangles.

large increase in sensitivity to chirplet waveforms seen in the two-waveform robustness test is likely due to these waveforms being very similar to the CSGs. The smaller improvement seen in the four-waveform test is likely due to the classifier compromising performance between the mix of waveforms; the effect of this is a decrease in sensitivity gain for both the CSG and chirplet waveforms, but a dramatic improvement in sensitivity to WNB waveforms.

The robustness of the XTMVA analysis to signals of different morphology from those used in training is crucial, because accurate signal waveforms are not known in most burst searches. (In fact, the WNB results from the two-waveform robustness test show that BDT can actually improve the sensitivity to *a priori* unknown waveforms by removing the need for X-PIPELINE’s polarisation-specific background rejection tests.) The robustness of BDT may be due to the fact that the MVA does not have access to the raw GW data, but rather only to characteristics passed on by X-PIPELINE. In particular, the only time-frequency information that is available to BDT are the time and frequency extent of the event, its peak time and frequency, and the number of time-frequency pixels; no shape information is recorded. In principle shape information could be used to improve signal/background discrimination, e.g. by recognising the characteristic chirp shape of inspiral signals (see [figure 5.3\(b\)](#)). However, this would presumably also make the XTMVA analysis more waveform-specific, and less sensitive to signals not included in the training. Further study of the waveform dependence of MVA analyses is warranted.

[Figure 5.9](#) and [figure 5.11](#) show sample decision trees that were used in the default GRB 060223A analysis. Decision nodes for each variable are shown as grey ellipses with the thresholds for a branch shown in grey rectangles. The leaf nodes are light yellow rectangles for signal and dark blue rectangles for background.



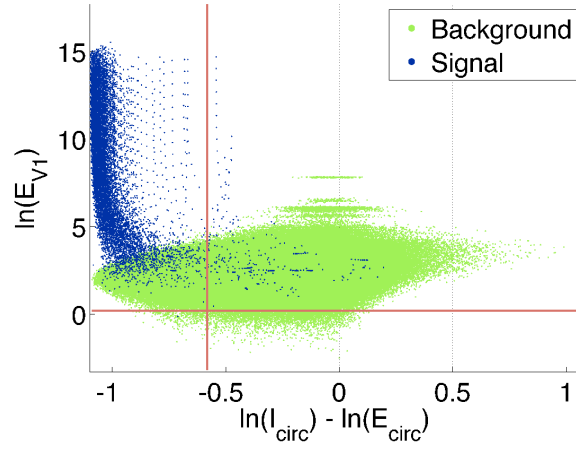


Figure 5.10: Scatter plot of signal and background events from the GRB 060223A analysis. The red lines indicate the cuts applied by the decision tree shown in figure 5.9.

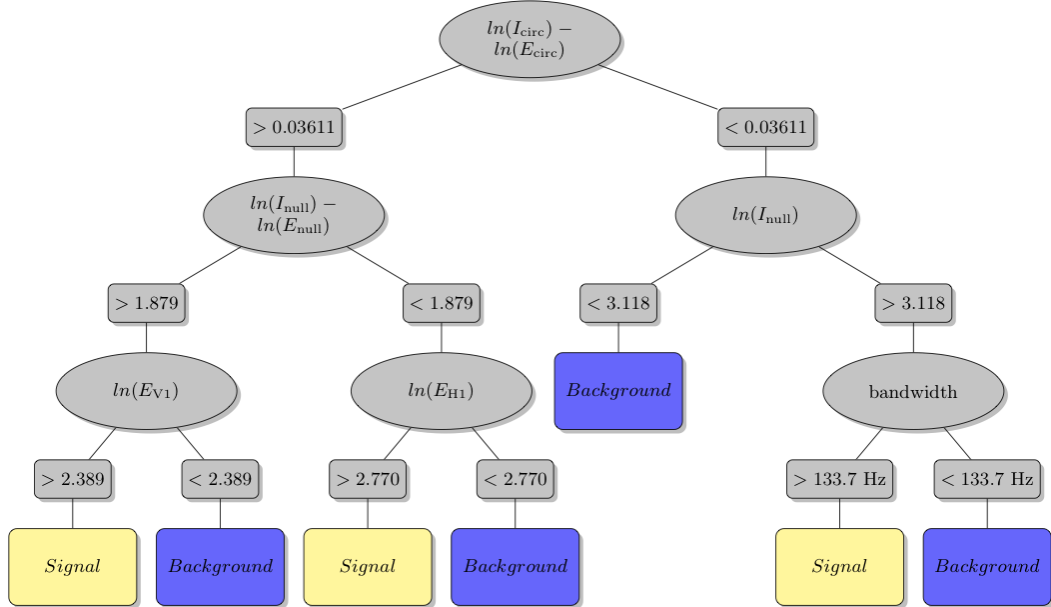


Figure 5.11: Example decision tree used in the GRB 060223A XTMVA analysis. Decision nodes are grey ellipses, with thresholds for a branch given in grey rectangles. Leaf nodes for signal events are light yellow rectangles and for background events are dark blue rectangles.

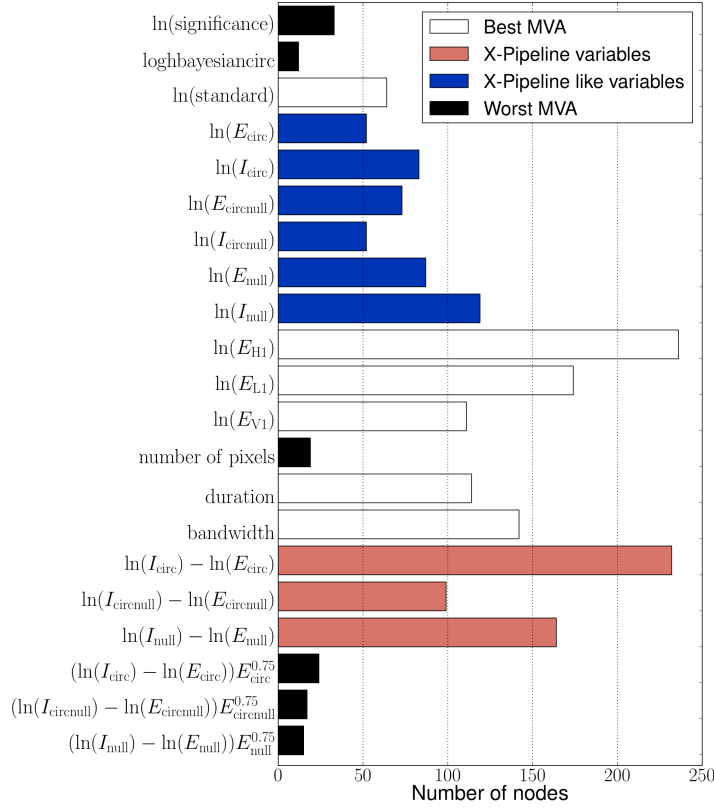
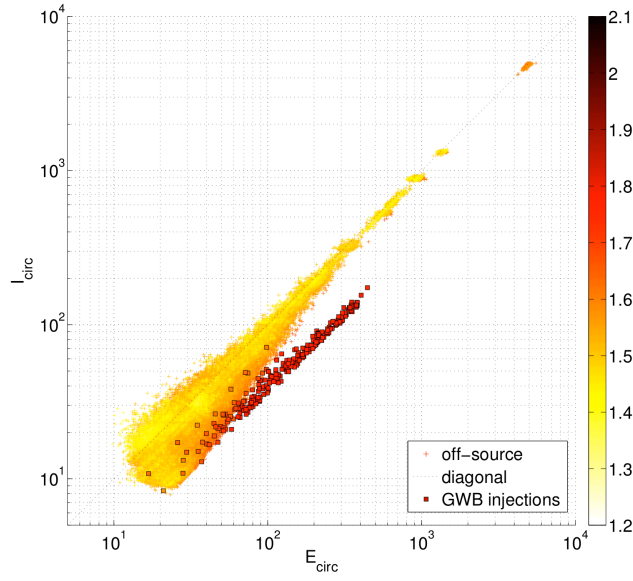


Figure 5.12: Histogram of the number of times each variable or variable combination is used at decision tree nodes in the BDT forest for the GRB 060223A analysis. The “X-PIPELINE variables” are combinations of variables that precisely match those used in the X-PIPELINE background rejection test of [section 5.1](#), while the “X-PIPELINE like variables” can be used to construct the cut of [section 5.1](#). Together these are among the variables most frequently selected by the XTMVA analysis, accounting for half of all nodes. The single-detector energies, duration, and bandwidth are selected for 40% of all nodes. These variables are not used by X-PIPELINE demonstrating how MVA makes use of the full dimensionality of the data. The remaining variables collectively account for approximately 10% of all nodes. See [table 5.1](#) for definitions of the variables.

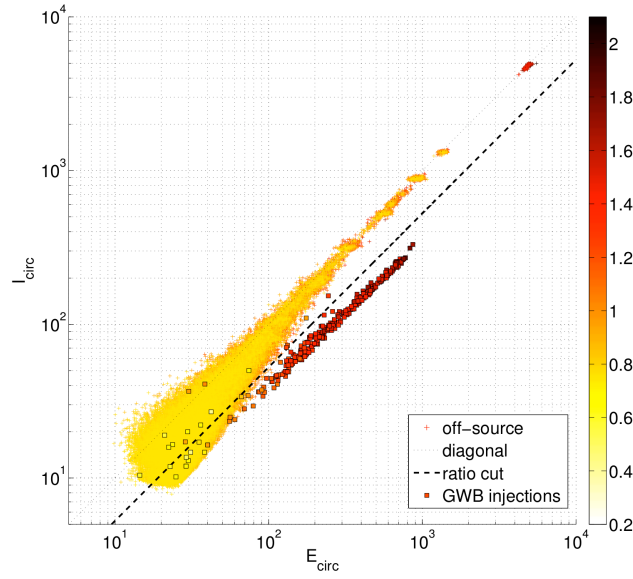
We first consider the simple decision tree shown in [figure 5.9](#). In this example the first cut is applied to the difference between the incoherent and coherent energies,  $\ln(I_{\text{circ}}) - \ln(E_{\text{circ}})$ , at a threshold of  $-0.581$ . Events above this threshold are classified as background, while events below this threshold are then cut on the energy in the Virgo detector,  $\ln(E_{\text{V1}})$ , which has a threshold of  $0.183$ . Events above this second threshold are classified as signal, while events below are classified as background. The logic behind these choices can be understood from [figure 5.10](#), which shows a scatter plot of  $\ln(E_{\text{V1}})$  versus  $\ln(I_{\text{circ}}) - \ln(E_{\text{circ}})$  for the training events. The red lines are the thresholds used in the example decision tree to separate the signal events from the majority of the background events. While this single tree assigns a large fraction of the background events to the signal leaf node (the upper-left rectangle), the final significance of events is determined collectively by 400 such trees, each generated from a random subset of the training data. A more complicated tree is shown in [figure 5.11](#), which classifies events based on 6 of their properties.

We gain further insight into the performance of the XTMVA analysis by considering how frequently different event variables are used in the classification. [Figure 5.12](#) is a bar chart of the total number of times each variable or combination of variables reported by X-PIPELINE is used in one of the decision nodes for the GRB 060223A analysis. We take this as an indicator of the value of each variable for signal/background discrimination. The X-PIPELINE background rejection tests are based on combinations of  $E_{\text{circ}}$  and  $I_{\text{circ}}$ ,  $E_{\text{circnull}}$  and  $I_{\text{circnull}}$ , and  $E_{\text{null}}$  and  $I_{\text{null}}$ , as given in [section 5.1](#) and [section 5.1](#). The pairwise differences  $\ln(I) - \ln(E) = \ln(I/E)$  are labelled as “X-PIPELINE variables” in the chart, because thresholding on these differences is equivalent to applying the X-PIPELINE test of [section 5.1](#). We see that these are some of the most frequently used combinations, selected for approximately 26% of all nodes. The individual  $\ln(I)$  and  $\ln(E)$  variables are labelled as “X-PIPELINE like variables” because the remaining X-PIPELINE cut of [section 5.1](#) can be constructed from them. These are selected for a total of 24% of the nodes. The selection of these variables by BDT for approximately 50% of the nodes affirms their usefulness for signal/background discrimination, as expected from their demonstrated value in X-PIPELINE’s background rejection tests. However, close to half of the BDT nodes use variables that are *not* used by X-PIPELINE. This is a clear demonstration of an MVA making use of the full dimensionality of the data. In particular, the single-detector energies are selected for approximately 27% of all nodes. Thresholding on these values is equivalent to thresholding on the event signal-to-noise ratio in the individual detectors [[189](#)], which is not done in X-PIPELINE. The event duration and the bandwidth are also useful, selected for 13% of all nodes. The remaining variables collectively account for approximately 10% of all nodes. Interestingly, the number of pixels (time-frequency area of the event) is one of the variables that is not particularly useful for signal/background discrimination.

Another view of the merits of BDT classification is given by [figure 5.13](#). These show scatter plots of  $I_{\text{circ}}$  versus  $E_{\text{circ}}$  for testing data from the default GRB 060223A analysis. The squares represent simulated CSG events at the amplitude for which the detection efficiency is approximately 90%. [Figure 5.13\(a\)](#)



(a) X-Pipeline



(b) BDT

Figure 5.13: (a) - Scatter plot of  $I_{\text{circ}}$  versus  $E_{\text{circ}}$  for testing data from the default GRB 060223A X-PIPELINE analysis. The squares represent simulated CSG events at the amplitude for which the X-PIPELINE detection efficiency is approximately 90%. Events are coloured by their significance in the X-PIPELINE analysis. The dashed line is the threshold line for the X-PIPELINE background rejection test; events above this line are discarded. (b) - Scatter plot of  $I_{\text{circ}}$  versus  $E_{\text{circ}}$  for testing data from the default GRB 060223A XTMVA analysis. The squares represent simulated CSG events at the amplitude for which the BDT detection efficiency is approximately 90%. Events are coloured by their significance in the XTMVA analysis.

shows the events coloured by their significance in the X-PIPELINE analysis, as well as the threshold line for the X-PIPELINE background rejection test. Event significance increases with  $I_{\text{circ}}$  or  $E_{\text{circ}}$ ; i.e., along the diagonal, whereas the signal and background are separated primarily in the orthogonal direction. Signals become detectable when they do not overlap the background distribution in  $I_{\text{circ}}$  versus  $E_{\text{circ}}$  space. [Figure 5.13\(b\)](#) shows the same background events as ranked by BDT. By contrast with the X-PIPELINE analysis, significance increases with distance from the diagonal, so that no additional background rejection test is required. Simulated CSG events are detectable at lower amplitudes, even though they overlap the background distribution in  $I_{\text{circ}}$  versus  $E_{\text{circ}}$  space, because the XTMVA analysis takes account of other event properties such as the single-detector energies.

It is also useful to look at the standard plots used in the TMVA package to understand the performance of the BDT classifier in the XTMVA analysis. For the default GRB 060223A analysis the linear correlation matrices of the event variables for the signal and background training samples are shown in [figure 5.14](#) and [figure 5.15](#) respectively. From the correlations we could decide to remove the variables of the form  $X^{0.75}$ , where  $X$  represents combinations of the various coherent-incoherent energy pairs, shown in [figure 5.12](#) from our analysis. As can be seen in [figure 5.12](#) these variables were not used for many of the nodes in the default GRB 060223A analysis. Reducing the number of variables used, will help to optimise the analysis and reduce computational cost. In [figure 5.14](#) we see that for the signal training sample there are strong correlations for many of the event variables, particularly between all of the event coherent and incoherent energies. In comparison in [figure 5.15](#) we see that for the background training sample the correlations between event variables is weaker, although there is still reasonably high correlation between each of the coherent/ incoherent energy pairs. The histograms of BDT response distributions of the signal and background testing samples, overlaid with the response of the signal and background training samples, is given in [figure 5.16](#). We see that there is good separation between the signal and background testing samples in the BDT responses, which demonstrates the performances of the BDT for discriminating between signal and background events. We see a feature around BDT response of 0 in the signal training sample. This is likely due to low amplitude injections being buried by the detector noise, and X-PIPELINE selecting glitches in time coincidence with the waveform injection (see [section 5.4](#)). It was found that this effects the BNS waveforms the most, which were used in combination with the CSG waveforms in the signal training sample. This does not affect the performance of discrimination for the CSG testing sample, and the classifier gives good discrimination between the signal and background testing samples. By adding a signal cleaning step to the XTMVA analysis for the signal training, this would provide the classifier with a cleaner signal training set of just signal event by removing this contamination, which could help the BDT classifier achieve better discrimination between the signal and background testing samples.

The results presented here indicate that multivariate analysis techniques may be valuable for improving the sensitivity of searches for unmodelled GWB.

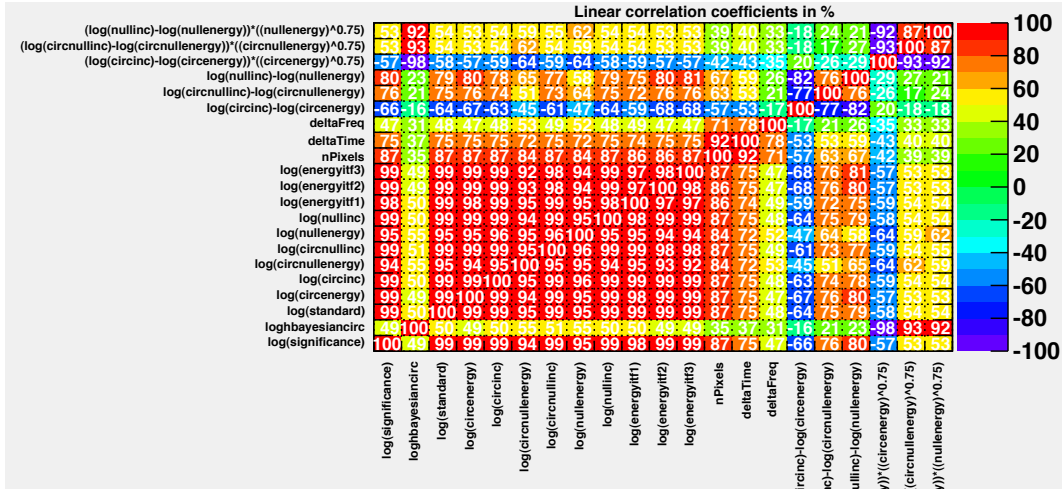


Figure 5.14: Linear correlation matrix for the event variables in the training sample for signal events. We see strong correlations between event variables, particularly between all of the event coherent and incoherent energies. Due to plotting limitations the x-axis labels are cut off, these are the same as the y-axis labels.

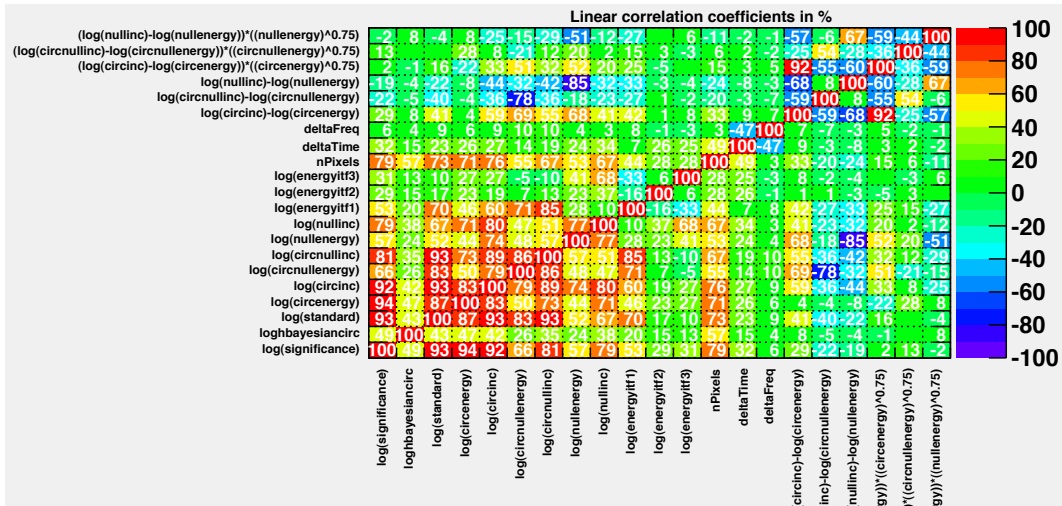


Figure 5.15: Linear correlation matrix for the event variables in the training sample for background events. We see weak correlations between event variables. Due to plotting limitations the x-axis labels are cut off, these are the same as the y-axis labels.

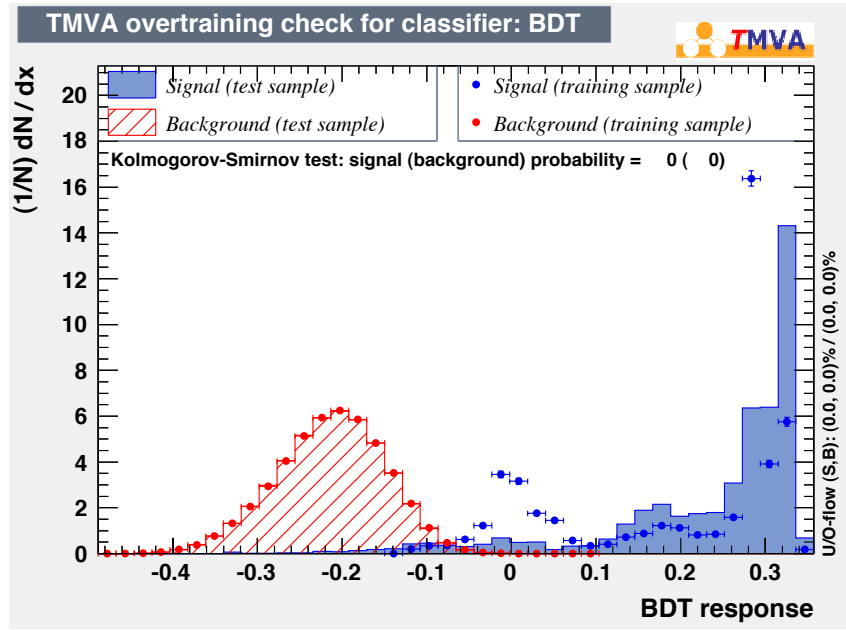


Figure 5.16: Histogram of BDT response for the CSG signal and background testing samples, overlaid with the combined CSG/BNS signal and background training samples response for the default GRB 060223A analysis. We see good separation of the test samples for the signal and background. There is a feature in the response of the signal training sample around BDT response of 0, this is due to the contamination of the signal sample explained in [section 5.4](#).

Additional studies are merited, particularly using a wider range of waveform morphologies, larger background samples and lower false alarm rates, and extending to all-sky untriggered searches.





# Gravitational Wave Detection Using a Single Detector

---

# 6

In this chapter we demonstrate the feasibility of performing a single detector burst search using GEO 600, by performing an example analysis for a single astrophysical trigger to demonstrate the procedure. We compare the sensitivity of this single detector analysis to a comparable two detector analysis of the same trigger. Demonstrating this procedure is important due to GEO 600 currently being the only ground-based GW interferometer in operation while the LIGO and Virgo detectors are out of operation for upgrades to their advanced detector configurations. Standard burst searches rely on coincidence in two or more detectors, or correlations between two or more detectors, to reject non-Gaussian background events as noise. These techniques are not available for a single detector analysis, so we test if a one detector search for GWBs is possible and employ advanced detector characterisation and analysis methods to assist.

## 6.1 Single Detector Analysis Trigger

The single detector era started when the last of the LIGO and Virgo detectors went off line in 2010–2011 for upgrades to the advanced detector configurations. Since this time GEO 600 has been the only GW detector taking astrophysical data. Therefore a single detector search was developed to be ready should there be an extraordinary astrophysical event, such as a Galactic supernova, during this period.

There is good reason to prepare for the case of an extraordinary event. In the case of Galactic SNs they occur once per 30–100 years [25, 26]. For example Betelgeuse, which is at a distance of 197 pc, is expected to go supernova in the next million years; soon in astrophysical terms. This makes it an excellent potential source for a triggered GW analysis, in fact Betelgeuse could have already gone supernova producing a strong GW signal that is now travelling towards us that we should make sure we are prepared to detect.

However, at the time of writing no extraordinary Galactic event has been observed. We have chosen to test our analysis on a high energy neutrino (HEN) observed by IceCube [211]. This is one of a pair of events detected by IceCube

Name	Bert
Time UTC (GPS)	2011-08-08 12:23:15 (996841410)
Right ascension (°)	261.01
Declination (°)	-29.0
1- $\sigma$ position uncertainty (°)	0.5

Table 6.1: Table of parameters for the Bert IceCube event.

which are the first accepted astrophysical HENs ever detected. The two events are nicknamed “Bert” and “Ernie” by IceCube, and occurred on August 8<sup>th</sup> 2011 and January 3<sup>rd</sup> 2012 respectively. They had the largest recorded neutrino energies to date, which an estimated deposited energy in the IceCube detector of  $1.04 \pm 0.16$  PeV and  $1.14 \pm 0.17$  PeV with a combined p-value of  $2.9 \times 10^{-3} (2.8\sigma)$ . GEO 600 was out of lock during the Ernie event, but was recording data around the Bert event. Specifically, GEO 600 had re-entered science mode after a  $\sim 20$  minute lock loss which ended 254 s before the event time, and then remained in science mode for many hours. Over the two days surrounding the HEN event GEO 600 had a duty cycle of  $\sim 93.9\%$ . The Bert event occurred during the S6E/VSR4 science run which ran from June 3<sup>rd</sup> until November 3<sup>rd</sup>, and so Virgo was also in lock during the Bert event. This allows us to make a direct comparison of a two detector analysis and a single detector analysis using only GEO 600, to gauge the possible performance.

The parameters for the Bert event are given in [table 6.1](#). The sky position of this event is consistent with the source being in the Galactic centre, which makes this event particularly interesting as it could plausibly be due to a Galactic source. The distance to the Galactic centre is approximately  $8.33 \pm 0.35$  kpc [[212](#)].

As there are a number of astrophysical scenarios in which both HENs and GWs may be emitted, this makes HEN interesting for GW searches [[190](#)]. HEN emission is expected from baryon-loaded relativistic astrophysical outflows, which could occur in SGRs [[213](#)]. Significant energy could be emitted as GWs in SGR giant flares, this could occur during excitation of the stars non-radial modes, producing GWs with kHz-frequencies [[181](#), [182](#), [183](#)]. Theoretical upper limits have been set on the emitted energy in GWs from SGRs of  $10^{-7} M_{\odot} c^2$  [[182](#)] and  $10^{-6} M_{\odot} c^2$  [[184](#)]. For a more complete discussion of possible joint sources of HEN and GWs see Ref. [[190](#)].

## 6.2 Single Detector Analysis Procedure

The Bert IceCube event was chosen for a single detector study using GEO 600. However, this event occurred during the S6E science run and fortunately both GEO 600 and Virgo were taking data at the time of the trigger. The availability of Virgo data allows us to compare the single detector search performance to a standard two detector search.

We run four tests for our methods study:

**Standard X-PIPELINE two detector analysis.** Two detector analysis using the

G1V1 network. This is a baseline analysis, replicating the procedure used in standard triggered analyses such as [43], and in section 4.3.

**XTMVA two detector analysis.** Two detector analysis using the G1V1 network. This is the best analysis we would consider if there were two detectors on-line for an event. Here we use the same set up as the previous analysis, but use the BDT MVA classifier to gain improved discrimination between signal and noise events. This has previously shown great potential to improve the analysis performance as shown in chapter 5 [204]; MVA techniques could become a part of the standard X-PIPELINE analysis in the advanced detector era.

**Standard X-PIPELINE single detector analysis.** Single detector analysis using G1 only. This is the simplest analysis that could be performed with a single detector, i.e. our single detector baseline analysis. This is using the same parameters and data quality vetoes as the first tests analysis, but using data from only the G1 detector to simulate the case where an event occurred during the single detector era. We expect the sensitivity of this analysis to be limited because the standard X-PIPELINE background rejection tests require correlations between two or more detectors.

**XTMVA single detector analysis.** Single detector analysis using G1 only. This analysis is a single detector analysis which uses a number of advanced analysis and data quality techniques to try to improve the analysis sensitivity. We use a range of combinations of a low frequency cut off thresholds on events from the analysis and vetoes generated from environmental auxiliary channels to find the best performance, this is described in section 6.3. In this test we use the XTMVA analysis pipeline and targeted vetoes to clean the detector background; since the standard X-PIPELINE coherent consistence tests are not available.

All of these analyses use the standard data quality vetoes produced at GEO 600 from the data quality vector, as well as veto segments produced by HVeto [162]. The set up of these analyses is shown in table 6.2.

To obtain a p-value low enough to find statistically interesting events, we use a large off-source and smaller on-source than the standard X-PIPELINE GRB analysis. We have chosen to use a  $[-2, +2]$  s on source around the time of the trigger and a  $[-1, +1]$  day off-source. This is motivated by likely Galactic models for joint GW–HEN emission (e.g. SGR giant flares). This will allow us to obtain values of p-value down to  $\sim 2 \times 10^{-5}$  with the single detector analysis. An event with a p-value of order  $2 \times 10^{-5}$  would need to be considered carefully as a detection candidate and follow up investigations would be performed. Unlike for a multi-detector analysis, we can not expand our on source using time slides to decrease the obtainable p-value. We could however perform an in depth study of the detector stability around the time of an event to extend the background period, which would allow us to obtain slightly smaller p-values.

A single detector analysis will only be performed in coincidence with an external trigger. For a given p-value ( $P$ ) we can find the maximum number of

Name	Detector Network	MVA	HVeto	Targeted vetoes
Two detector standard X-PIPELINE	G1V1	No	Yes	No
Two detector XTMVA	G1V1	Yes	Yes	No
Single detector standard X-PIPELINE	G1	No	Yes	No
Single detector XTMVA	G1	Yes	Yes	Yes

Table 6.2: Set up of the test analyses for the Bert IceCube event.

triggers to analyses in an Astrowatch period from a simple rearrangement of

$$P = \frac{N_{\text{trigs}}}{T} \frac{T_{\text{on}}}{T_{\text{off}}}. \quad (6.1)$$

Where  $N_{\text{trigs}}$  is the number of triggers analysable,  $T$  is the length of the Astrowatch period,  $T_{\text{on}}$  is the length of the on source window (4 s), and  $T_{\text{off}}$  is the length of the off source window (2 days). For  $P = 2 \times 10^{-5}$  ( $4.23\sigma$ ) in a Astrowatch period of length  $T$ , we can analyse only 1 trigger during the Astrowatch period to obtain an event with this p-value. Therefore we must be very careful about which events to analyse and would only perform a single detector analysis for an exceptional astrophysical event, such as a Galactic supernova within the sensitive range for GEO 600. For example, GEO 600 has a sensitive range to SNs (assuming  $E = 10^{-8} M_{\odot} c^2$ ) of  $\sim 200$  pc makes the expected SN from Betelgeuse (which is at a distance of 197 pc) a prime candidate for a GEO 600 single detector analysis. In the case of performing such an analysis, if a coincident detection of a GW candidate was made this would be at best a  $4\sigma$  detection, a twice in a life time event.

However, in the case that there are multiple exceptional astrophysical events during an Astrowatch period we will only be able to make a weaker detection statement and obtain a larger p-value, given by [equation \(6.1\)](#).

For testing the sensitivity of our analysis we use a selection of different waveforms. We use a single CSGs which are the standard waveform chosen for evaluating the sensitivity of burst searches. The parameters of this waveform are jittered in the same way as in [chapter 5](#) to avoid over training the MVA classifier on a particularly signal model. We also use the same BNS and WNB waveforms as were used in [chapter 5](#). In addition, we use a cosmic string cusp with a cut off frequency at 1 kHz because it is a hypothetical source of HENs and GWs [[214](#), [215](#), [216](#)]. In all analyses we will use only the CSG and BNS waveforms for training and all four waveforms for testing performance. Due to the relatively small number of background jobs available for a single detector analysis, as there is no possibility of time shifting the data between multiple detector to produce extra background, we determine the minimum injection amplitude at which 50%

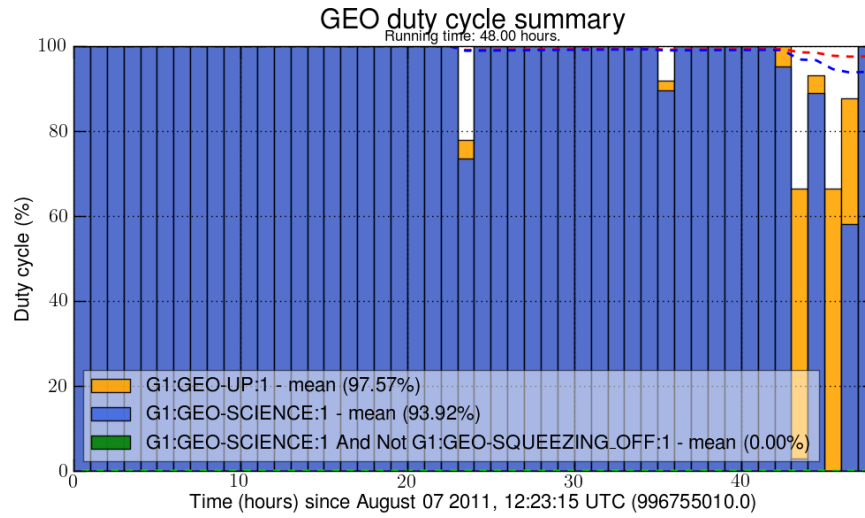


Figure 6.1: Duty cycle histogram against time in hours of the two day off source around the Bert trigger. Orange denotes times when GEO 600 was locked, Blue denotes times when GEO 600 was recording science. The lack of green reflects the fact that the squeezer was not on during this off source period.

of the injections both survive the cuts and have significance greater than 95% of the background (e.g.  $p \leq 0.05$ ).

The results for these tests are shown in [table 6.5](#).

## 6.3 Analysis Segments and Veto Methods

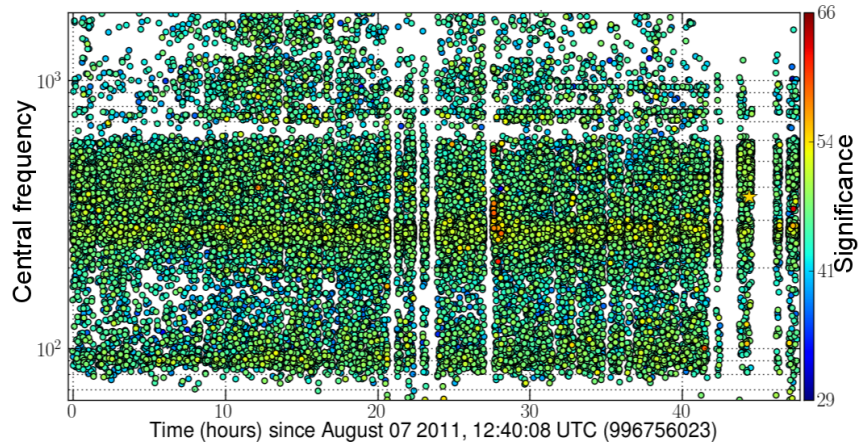
In this section we will give details of the science segments and vetoes that were used in our tests. We focus primarily on GEO 600 here, as the main aim of these tests is to find the performance available from a single detector analysis. The V1 science and veto segments are the same as those produced for the analyses in [section 4.3](#) for the S6E/VSR4 science run.

### 6.3.1 Science segments

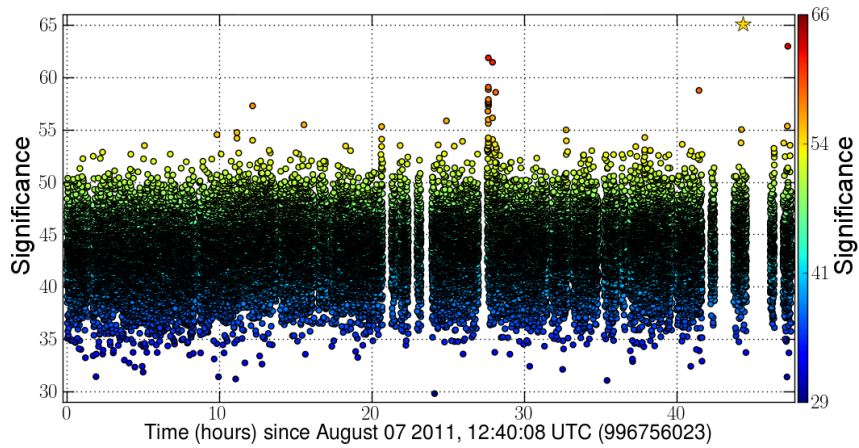
The Bert trigger occurred at the start of a GEO 600 science segment which lasted several hours. The detector had just reacquired science mode 254 s before the trigger after a 20 min lock loss. GEO 600 has a duty cycle of 93.9% for the two day off source period around this trigger. The duty cycle is shown in [figure 6.1](#). GEO 600 ran without squeezing for the entire time used for these tests.

The events recorded by X-PIPELINE in the two day off source before applying any vetoes are shown in [figure 6.2\(a\)](#) and [figure 6.2\(b\)](#).

Here all of these analyses use the standard category 2 vetoes that are produced using the GEO 600 data quality vector, these reduce the duty cycle to 93.6%.



(a) Time versus frequency triggergram



(b) Time-SNR triggergram

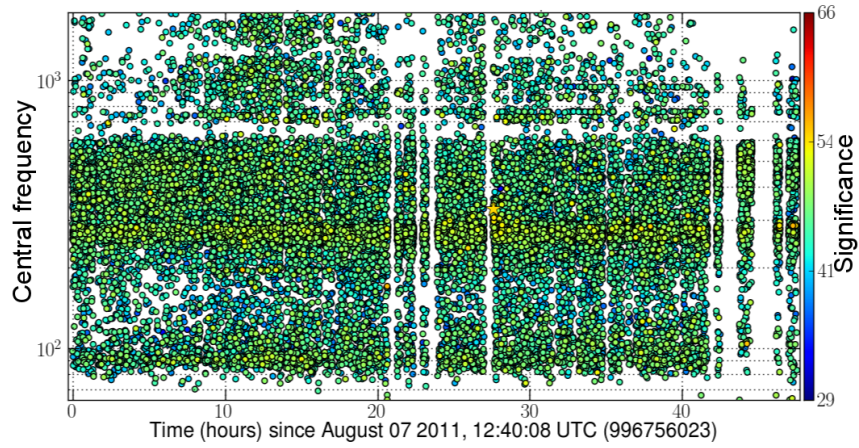
Figure 6.2: Time versus frequency and time versus SNR triggergrams before applying any vetoes segments. The yellow star represents the loudest trigger.



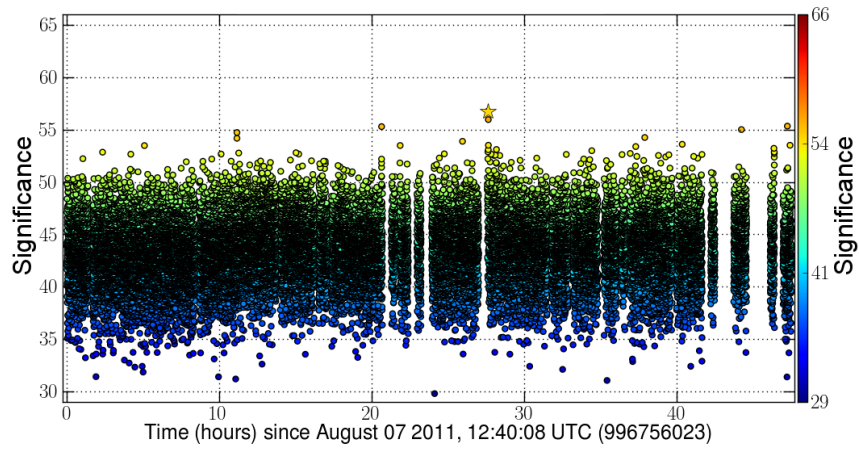
### 6.3.2 HVeto Segments

The HVeto algorithm [162] was described in [section 3.2.1](#). In brief, this algorithm finds the auxiliary channel with the most significant coupling to the GW data channel, testing a number of different coincidence windows and minimum SNR thresholds, and removes data from the GW channel using coincidence with glitches in that auxiliary channel. This process is then repeated until the maximum significance channel does not pass some pre-set threshold. For the Bert trigger HVeto was run for the entire two day off source; the results of this are presented in [table 6.3](#). In [table 6.3](#) we can see that the most significant channel is G1:PSL\_PWR\_EASTARM-BSAR, this gave an efficiency of 8.5% with just 2.7% dead time. The subsequent rounds did not give as large an effect as the first, but the combined results gave a cumulative efficiency of  $\sim 14.2\%$  and cumulative dead time of  $\sim 5.7\%$ . The duty cycle of GEO 600 after applying the HVeto segments was 88.3%.

The effect of the HVeto triggers on the events recorded by X-PIPELINE in the two day off source are shown in [figure 6.3\(a\)](#) and [figure 6.3\(b\)](#).



(a) Time versus frequency triggergram



(b) Time-SNR triggergram

Figure 6.3: Time versus frequency and time versus SNR triggergrams after applying HVeto segments. The yellow star represents the loudest trigger.



Round number	Channel (event trigger generator (ETG)) [Bandwidth]	Significance	$t_{\text{window}}$	SNR threshold	Efficiency % (number)	Dead time % (s)
1	G1:PSL_PWR_EASTARM-BSAR (HACR) [20 Hz–100 Hz]	412.03	1.0	6.0	8.507 (2233)	2.655 (4293.78)
2	G1:ASC_MCN_SPOT-PWR (HACR) [5 Hz–20 Hz]	63.36	1.0	6.0	0.911 (219)	0.222 (350.04)
3	G1:ASC_MCN_SPOT-PWR (HACR) [0.5 Hz–5 Hz]	58.12	1.0	6.0	1.126 (268)	0.345 (541.62)
4	G1:PEM_CBCLN_ACOU-M (HACR) [100 Hz–500 Hz]	29.74	0.2	8.0	0.412 (97)	0.097 (152.13)
5	G1:SEI_TCC_STS2x (HACR) [20 Hz–100 Hz]	15.25	1.0	20.0	0.286 (67)	0.088 (138.0)
6	G1:LSC_MIC_FP-MMC2B (HACR) [500 Hz–4096 Hz]	14.96	0.2	8.0	2.756 (644)	1.955 (3055.58)
7	G1:PSL_SL_PWR-AMPL-OUTLP (HACR) [500 Hz–4096 Hz]	11.42	5.0	8.0	0.316 (72)	0.112 (170.96)
8	G1:LSC_MIC_VIS (HACR) [100 Hz–500 Hz]	6.76	0.1	10.0	0.543 (123)	0.329 (503.45)
9	G1:ASC_MCN_SPOT-X (HACR) [20 Hz–100 Hz]	6.32	5.0	15.0	0.049 (11)	0.007 (10.0)

Table 6.3: HVeto results for the Bert IceCube event single detector GEO 600 analysis. The significance quantifies how unlikely the number of time coincidences between triggers in the GW data channel and triggers in an auxiliary channel are, compared with the number expected from the intersection of two random Poisson time distributions with the same numbers of triggers and  $t_{\text{window}}$ .  $t_{\text{window}}$  is the coincidence time window used around auxiliary triggers when testing coincidences with the GW data channel and to produce veto segments. The SNR threshold is the minimum SNR of triggers in the auxiliary channel that are used to construct vetoes. Efficiency is the fraction of triggers in the GW data channel falling inside veto segments, relative to the total number of triggers. Dead time is the amount of time for which a given veto was active, relative to the total duty cycle.

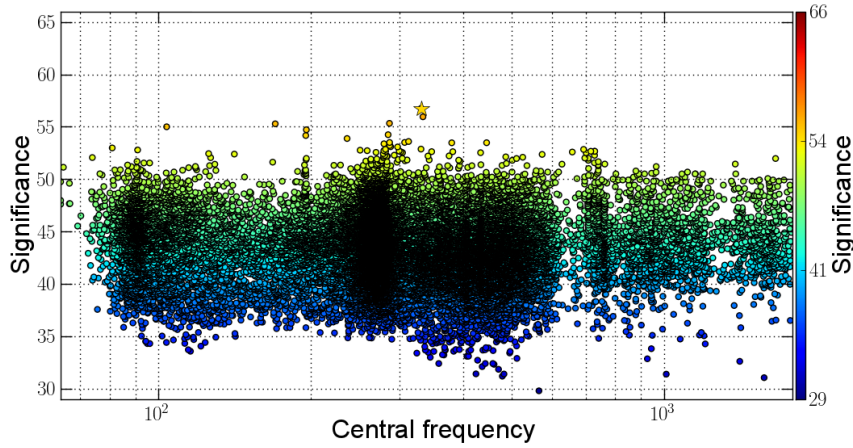


Figure 6.4: Frequency-SNR triggergram after applying HVeto segments.

### 6.3.3 Targeted Vetoes

Targeted investigations were performed on the noise around the time of the event to try to better characterise the background. To do this Omega-scans were made of the 50 loudest events in the off-source, as ranked by the single detector XTMVA analysis using the standard vetoes and HVeto segments. Omega-scans take as an input the time of a glitch in the GW data channel and find coincidence events in auxiliary channels. Omega-grams are then produced for each auxiliary channel which contains coincident noise for a range of different time periods. This tool is often very useful for tracking down possible causes of glitches by quickly reducing the information from all the auxiliary channels to short coincidence windows for just the ones which contain useful information. Using this it is easy to compare the shape and distribution glitches in the GW channel time-frequency plane and coincident glitches in auxiliary channels.

The first class of targeted vetoes we consider is a low frequency cut off of events. Due to the limited sensitivity of GEO 600 below a few hundred Hz we tested a number of different low frequency cut-offs at 100 Hz, 200 Hz, and 300 Hz. This was not previously an issue for two detector analyses using GEO 600 as the coherent cuts would work well at removing events that were at these low frequencies. While the 100 Hz and 200 Hz cuts are conservative tests, the 300 Hz cut is motivated by the noise features observed in the GEO 600 spectrum (see [figure 6.5](#)). There is also a high density glitch feature which can be seen in the distribution of glitches in [figure 6.4](#) that extends from around 200 Hz to 300 Hz.

It was found that the cut at 300 Hz gave the greatest improvement to the analysis upper limits. The off source after applying this veto is shown in [figure 6.6\(a\)](#) and [figure 6.6\(b\)](#). This type of veto causes zero dead time, but we must accept zero sensitivity below the frequency cut off in exchange for better sensitivity at higher frequencies due to an reduced noise background.

The second class of targeted veto which we considered uses trend data from auxiliary channels to find times of excess noise and remove them from the analyses. The first channel that we considered was an auxiliary channel recording

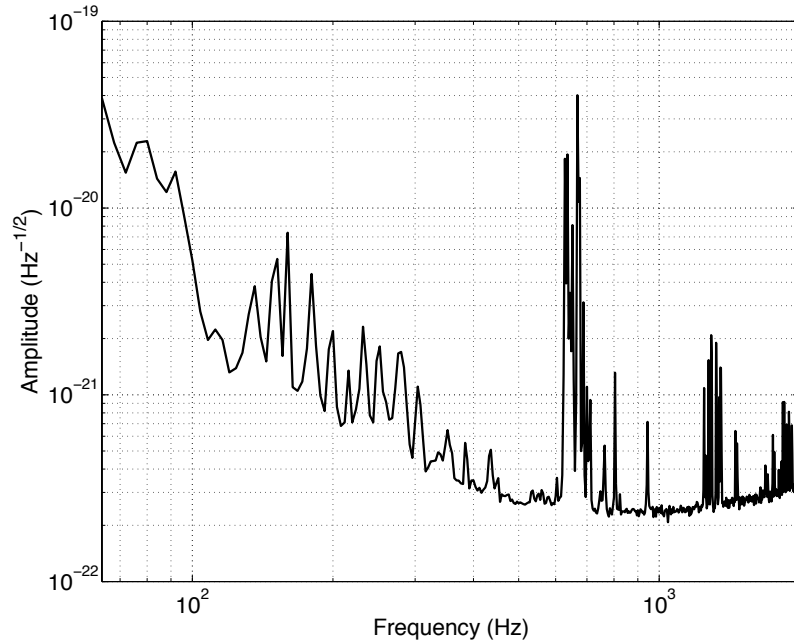
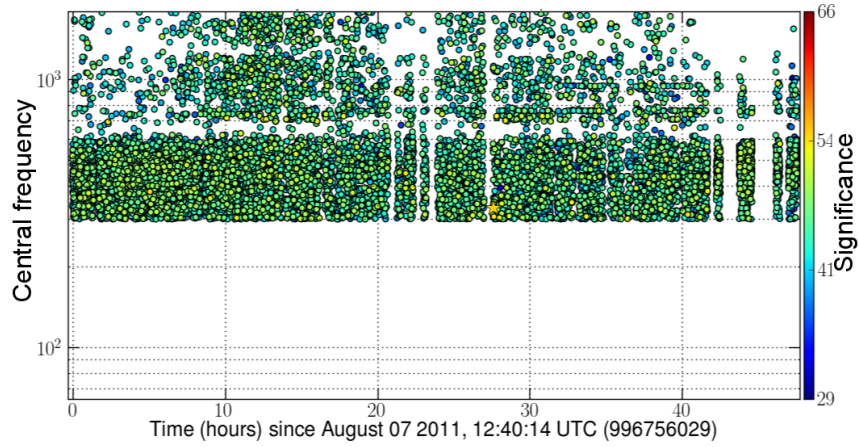


Figure 6.5: GEO 600 noise amplitude spectral density for the single detector Bert IceCube event analysis.

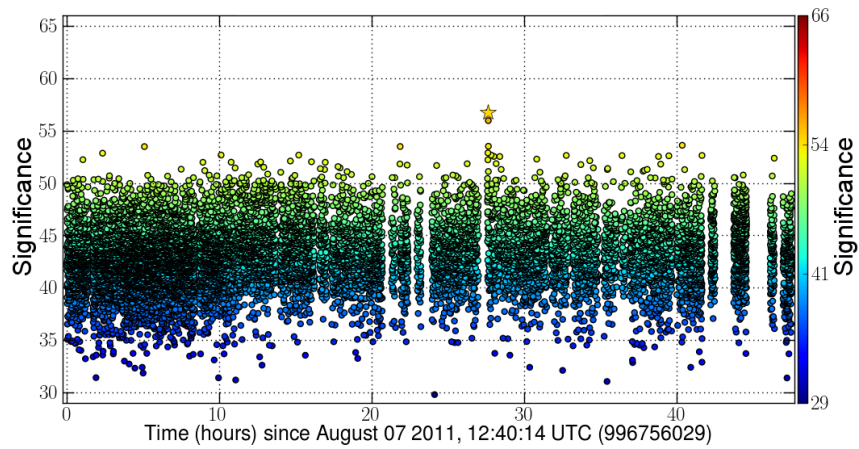
a microphone in the central building. This channel was prominent in a number of the Omega-scans for the 50 loudest background events. Looking at the trend data it was easy to separate times when the central building was quiet, and times when people were inside performing commissioning work although these times are not in science. Using these levels as a guide we applied a threshold to define times when the detector was sufficiently quiet to not cause glitches. We produced segments for all of the times that this channel went above this threshold, with a  $[-2, +2]$  s padding. After applying these veto segments to GEO 600 we have a duty cycle of 86.2%; the resulting off source triggers are shown in [figure 6.7\(a\)](#) and [figure 6.7\(b\)](#). We see that a number of the loudest background events are removed by this veto.

The next auxiliary channel we considered was recording a seismometer in the central building. This channel also showed prominently in the Omega-scans of the 50 loudest background events, and showed clear coincidence with some of the loudest remaining off source event seen in [figure 6.7\(b\)](#). From the trends of this seismometer we set a threshold to select times of high seismic noise. We produced segments for all of the times that this channel went above this threshold, with a  $[-2, +4]$  s padding. After applying these veto segments to GEO 600 we have a duty cycle of 78.8%; the resulting off source triggers are shown in [figure 6.8\(a\)](#) and [figure 6.8\(b\)](#).

The final channel which we considered was the circulating power inside the interferometer east arm. This channel also showed consistently in the Omega-scans of the 50 loudest background events, and showed clear coincidence with some of the loudest remaining off source event seen in [figure 6.8\(b\)](#). From

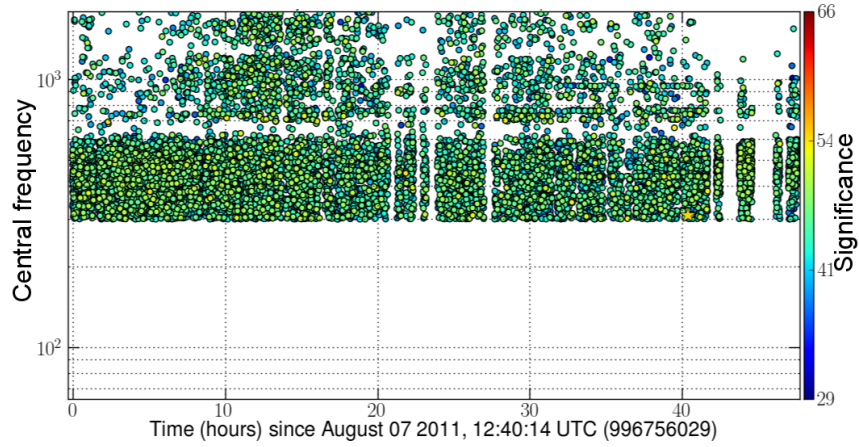


(a) Time versus frequency triggergram

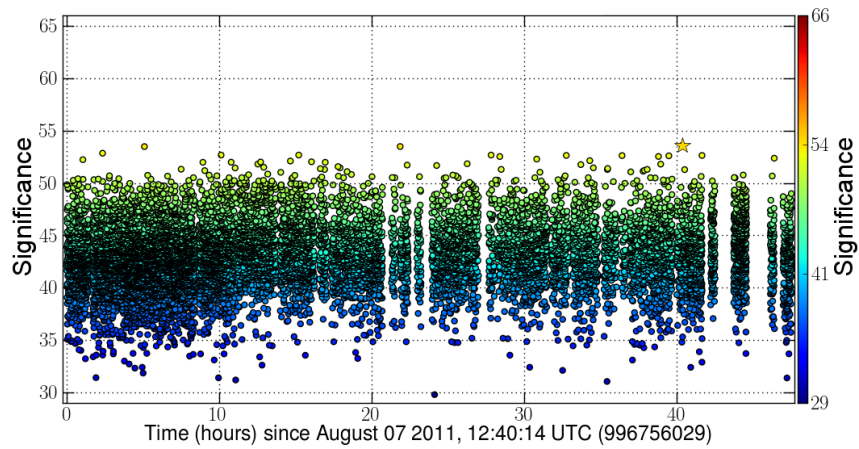


(b) Time-SNR triggergram

Figure 6.6: Time versus frequency and time versus SNR triggergrams after applying HVeto segments and  $> 300$  Hz low frequency cut-off. The yellow star represents the loudest trigger.

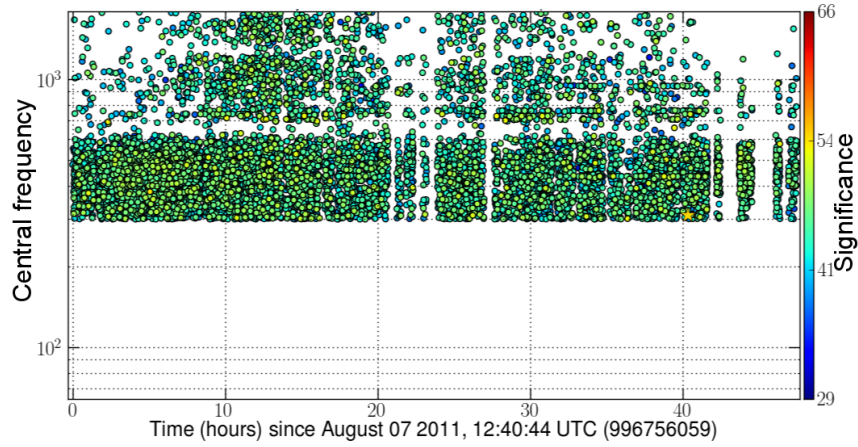


(a) Time versus frequency triggergram

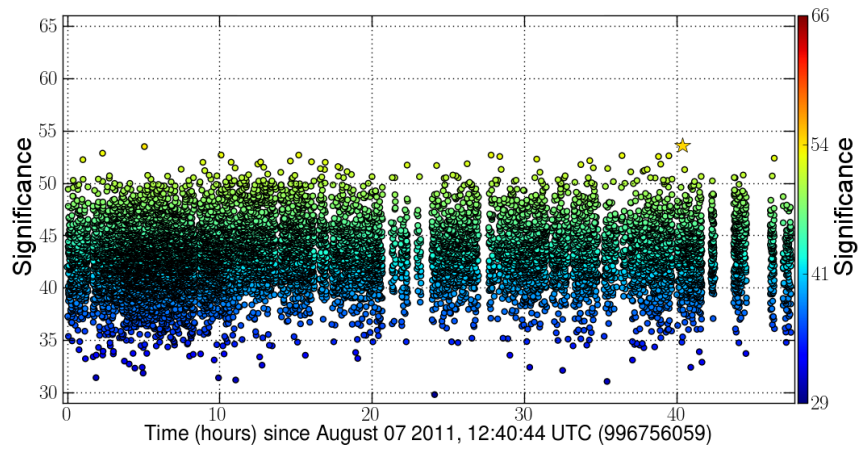


(b) Time-SNR triggergram

Figure 6.7: Time versus frequency and time versus SNR triggergrams after applying HVeto segments,  $> 300$  Hz low frequency cut-off, and acoustic channel trends. The yellow star represents the loudest trigger.



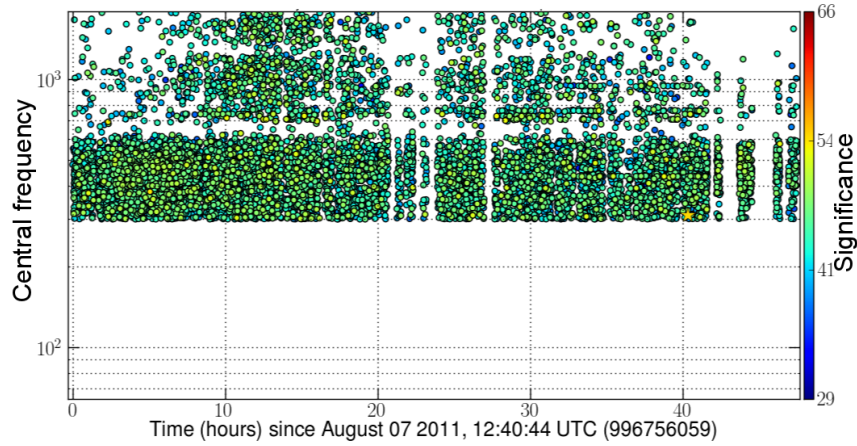
(a) Time versus frequency triggergram



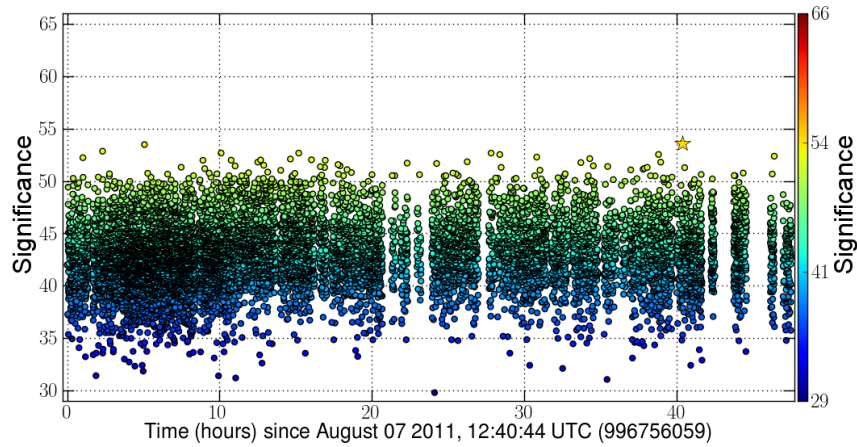
(b) Time-SNR triggergram

Figure 6.8: Time versus frequency and time versus SNR triggergrams after applying HVeto segments,  $> 300$  Hz low frequency cut-off, acoustic channel, and seismometer trends. The yellow star represents the loudest trigger.





(a) Time versus frequency triggergram



(b) Time-SNR triggergram

Figure 6.9: Time versus frequency and Time versus SNR triggergram after applying HVeto segments,  $> 300$  Hz low frequency cut-off, acoustic channel, seismometer, and east arm power trends.

the trends of this channel we set a threshold to select times of excess noise. We produced segments for all of the times that this channel went above this threshold, with a  $[-2, +2]$  s padding. After applying these veto segments to GEO 600 we have a duty cycle of 78.4%; the resulting off source triggers are shown in [figure 6.9\(a\)](#) and [figure 6.9\(b\)](#).

We summarise the duty cycle for each combination of vetoes considered in [table 6.4](#).

## 6.4 Analysis Results

For each of our tests analyses we calculate the  $h_{\text{rss}}^{50\%}$  upper limits for a number of different waveforms, the results are presented in [table 6.5](#).

Veto	Duty cycle
No vetoes	93.9%
Data quality vector and Hveto	88.3%
ACOU trends	86.2%
ACOU and SEI trends	78.8%
ACOU, SEI and PWR trends	78.4%

Table 6.4: GEO 600 duty cycle for different combinations of vetoes for the Bert IceCube event single detector analysis. ACOU trends are produced from an auxiliary channel recording a microphone in the central building. SEI trends are produced from an auxiliary channel recording a seismometer in the central building. PWR trends are produced from an auxiliary channel recording the circulating power in the interferometer east arm.

**Standard X-PIPELINE two detector analysis.** This analysis performed well for the CSG and BNS injections, but did not recover the WNB or cusp signals well. This is due to the coherent analysis requiring circularly polarised signals, the WNB is unpolarised and the cosmic string cusp waveforms is linearly polarised.

**XTMVA two detector analysis.** This analysis showed an improvement that is consistent with what was observed in [chapter 5](#) and [\[204\]](#). There is a factor of 2–3 improvement for the CSG and BNS waveforms. There is a factor of  $\sim 20$  improvement for the cusp waveform and a factor of  $\sim 200$  improvement for the WNB, this is due to there being no requirement for signals to be circularly polarised when using the XTMVA analysis, unlike for the standard X-PIPELINE analysis which assumes circularly polarised signals. To understand where this improvement comes from, we can look at the event variables usage in the nodes of the BDTs which were used in this analysis, shown in [figure 6.10](#). We see that the X-PIPELINE-like variables perform well, as well as the  $\ln(\text{power law})$ , duration, and bandwidth.

**Standard X-PIPELINE single detector analysis.** This analysis is a factor of  $\sim 4$ , for the CSG and BNS injections, less sensitive than the standard X-PIPELINE two detector analysis. This analysis was a factor of  $\sim 2$  less sensitive than the standard X-PIPELINE two detector analysis for the WNB injection, due to there being no coherent cuts for the single detector analysis which apply a circular polarisation requirement. However, the performance of both of these analyses for this waveform type are poor.

**XTMVA single detector analysis.** From the targeted veto investigations performed in [section 6.3](#) we have a range of different veto segments to apply to the data for our analysis. We break down our final test into multiple analyses, each using a different combination of the targeted vetoes to find which gives the best performance. The best result was found using a low frequency cut on events at 300 Hz, as well as the standard HVeto segments,



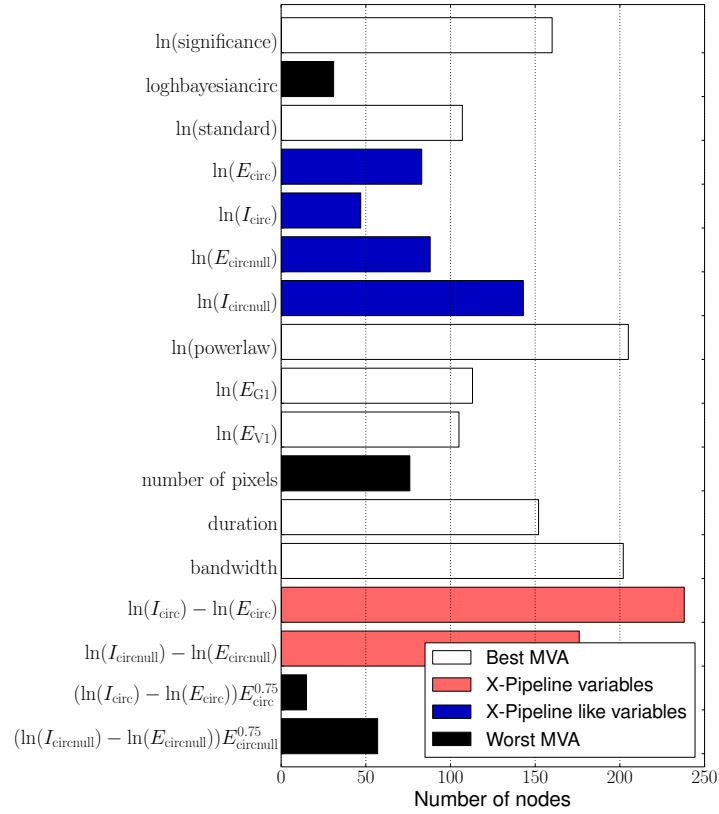


Figure 6.10: Bar chart of the number of times each variable is used at decision tree nodes in the BDT forest for the two detector XTMVA analysis. The “X-PIPELINE variables” are combinations of variables that precisely match those used in the X-PIPELINE background rejection test of [section 5.1](#), while the “X-PIPELINE like variables” can be used to construct the cut of [section 5.1](#). Together these are among the variables most frequently selected by the BDT analysis, accounting for  $\sim 38\%$  of all nodes. The power law, single-detector energies, duration, and bandwidth are selected for  $\sim 38\%$  of all nodes. These variables are not used by X-PIPELINE demonstrating how MVA makes use of the full dimensionality of the data. The remaining variables collectively account for approximately 24% of all nodes. See [table 5.1](#) for definitions of the variables.

as shown in [table 6.5](#). This gives us an improvement over the standard X-PIPELINE single detector analysis of a factor of 2 for the CSG injections, and brings the single detector search sensitivity to within a factor of 2 of the standard two detector search. For the BNS waveform we see a factor of 1.4 improvement over the standard X-PIPELINE single detector analysis, and brings the single detector search sensitivity to within a factor of 3 of the standard two detector search. We see a factor of  $\sim 2.6$  improvement for the cusp and WNB waveforms over the standard X-PIPELINE single detector analysis. Compared to the standard two detector analysis, the cusp waveform is of comparable sensitivity and the WNB waveform is a factor of  $\sim 3$  more sensitive. This is due to the coherent analysis requiring circularly polarised signals for the two detector analysis. To understand where this improvement comes from, we can look at the event variables usage in the nodes of the BDTs which were used in this analysis, shown in [figure 6.11](#). We see that the single detector energy and the log significance perform well, along with the event bandwidth.

Secondly we add to this previous test the simple 300 Hz low frequency cut off. This gave an improvement of  $\sim 14\%$  for the CSG upper limits.

Next we show the performance of the targeted vetoes from trends. We find that these *reduce* the performance of the analysis, as shown in [table 6.5](#). Even though these vetoes do well to remove the loudest background events as shown in [section 6.3](#), they also incur extra dead time. In fact, these tests all performed worse than just using the XTMVA pipeline with a 300 low frequency cut off.

The lack of utility of the ACOU-SEI-PWR vetoes appears to be due to the loudest events that were removed by these vetoes already having been down weighted by the XTMVA analysis, and so the removal of them does not greatly change the background distribution of glitches. This can be seen in the comparison of the background event histograms from each of the tests shown in [figure 6.12](#).

The MVA significance runs on a scale from 0–100, where events with low values are classified as noise and events with large values are classified as signals. The combination of the standard data quality veto category 2 veto segment and HVeto segments cut out the tail of the background noise well. The 300 Hz low frequency cut gives a small improvement, but does not remove the few loudest events; this is done without any loss of duty cycle. Finally the combination of trend vetoes gives a slight improvement, and removes the loudest events, however incurring an extra  $\sim 10\%$  dead time. Also, looking at these events we can see that the MVA significance values are of order 50, on a scale from 0–100, and so these events are already down weighted to relatively low significance by the MVA classifier.

It is also useful to look at the standard plots used in the TMVA package to understand the performance of the BDT classifier in the XTMVA analysis. For the single detector XTMVA analysis we show the linear correlation matrices of the event variables for the signal and background training samples are shown in

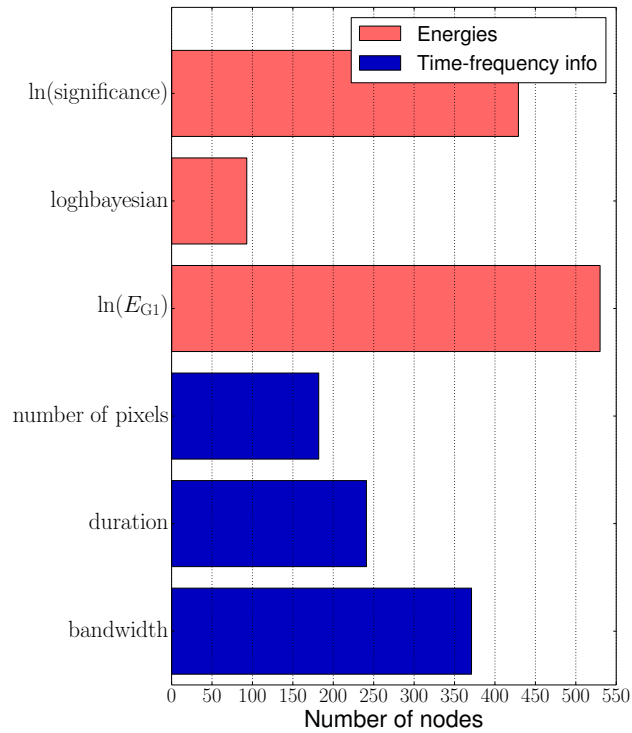


Figure 6.11: Bar chart of the number of times each variable is used at decision tree nodes in the BDT forest for the single detector XTMVA analysis. The “Energies” are different measures of the power in a cluster, these are selected for  $\sim 57\%$  of all nodes, with the  $\ln(\text{significance})$  and  $\ln(E_{G1})$  accounting for half of all nodes. The number of pixels, duration, and bandwidth are selected for  $\sim 43\%$  of all nodes. See [table 5.1](#) for definitions of the variables.

<b>Test name</b>	50% UL ( $\times 10^{-21} \text{ Hz}^{-1/2}$ )			
	<b>CSG</b>	<b>BNS</b>	<b>cusp</b>	<b>WNB</b>
Two detector standard X-PIPELINE	4.20	13.5	24.0	471
Two detector XTMVA	2.08	4.18	1.15	2.39
Single detector standard X-PIPELINE	16.7	56.9	65.0	374
Single detector XTMVA	8.07	48.4	25.6	187
Single detector XTMVA > 300 Hz	7.07	40.4	24.3	139
Single detector XTMVA > 300 Hz ACOU	9.16	49.6	35.3	197
Single detector XTMVA > 300 Hz ACOU-SEI	9.07	48.3	34.7	197
Single detector XTMVA > 300 Hz ACOU-SEI-PWR	9.07	48.3	34.7	197

Table 6.5: Results from test analysis of Bert trigger. The best single detector analysis using advanced detector characterisation and analysis methods is the single detector XTMVA > 300 Hz analysis. This analysis give upper limits within a factor of 2 of the standard two detector analysis for the CSG waveform.

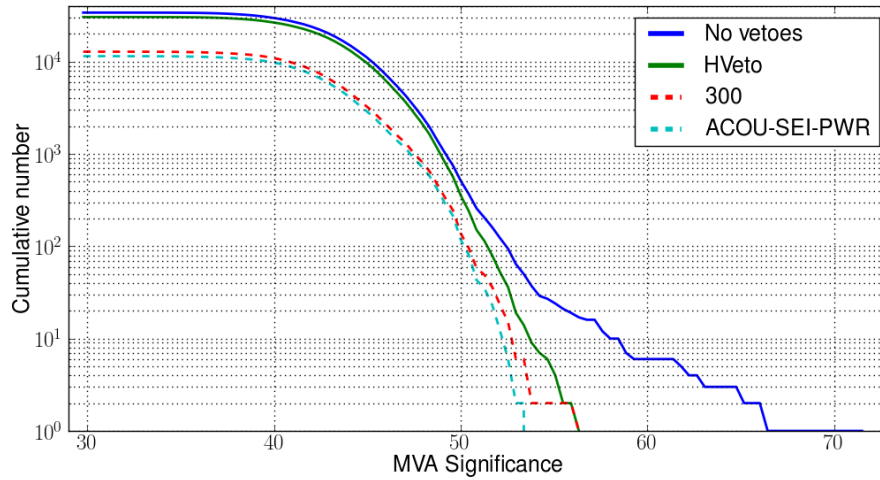


Figure 6.12: Histogram of off-source triggers for a number of the different single detector XTMVA test analyses. Although the trend vetoes do remove the loudest events left over after HVeto segments and 300 Hz low frequency cut have been applied, these events are already down weighted by the MVA classifier.

figure 5.14 and figure 5.15 respectively. In figure 6.13 we see that for the signal training sample there are strong correlations for many of the event variables, particularly between the various energy measures for the events. In figure 6.14 we see that for the background training sample the correlations between event variables is slightly weaker. The difference in these correlation plots is less significant that was seen in figure 5.14 and figure 5.15. For the single detector XTMVA analysis we show a plot of background rejection against signal efficiency for the BDT test sample, using the CSG waveforms, in figure 6.15. We can see in figure 6.15 that we are unable to obtain a signal efficiency of 1. This is due to the overlap of the signal and background testing samples in figure 6.16 for all thresholds on the BDT significance. The histograms of BDT response distributions of the CSG signal and background testing samples, overlaid with the response of the signal and background training samples, is given in figure 6.16. We see that there is some separation between the signal and background testing samples in the BDT responses. Only  $\sim 50\%$  of the signal testing set is distinguishable from the background testing set using the BDT response in figure 6.16. We see a significant feature around BDT response of 0 in the signal training sample. This is possibly due to low amplitude injections being buried by the detector noise, and X-PIPELINE selecting glitches in time coincidence with the waveform injection (see section 5.4). It was found that this effects the BNS, cusp, and WNB waveforms the most, which were used in combination with the CSG waveforms in the signal training sample. By adding a signal cleaning step to the XTMVA analysis for the signal training the classifier would be provided with a cleaner signal training set of just events associated with the signal injections by removing this contamination, which could help the classifier to achieve better discrimination between signal and background. Caution should be applied when

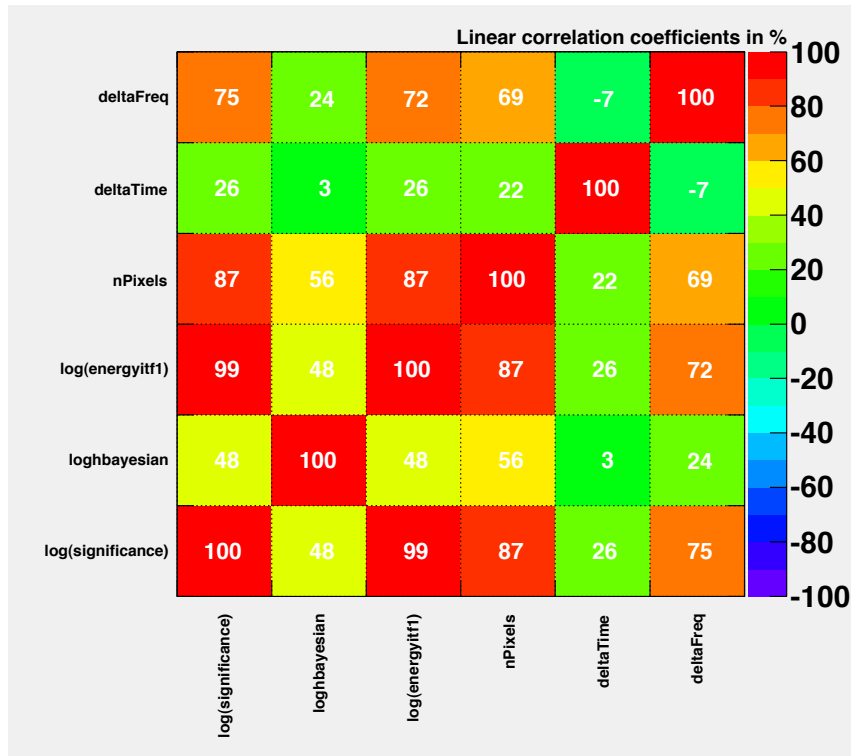


Figure 6.13: Linear correlation matrix for the event variables in the training sample for signal events. There are strong correlations for the different measures of the event energy, npixels, and deltaFreq.

interpreting these results due to the overtraining illustrated in [figure 6.16](#), this motivates future work to remove this contamination.

The XTMVA analysis gives a consistent improvement of a factor of  $\sim 2$  for both the single detector and two detector analyses for the CSG waveforms and an improvement for all other waveforms over the standard X-PIPELINE analysis. The poor performance of the standard X-PIPELINE two detector analysis for the cusp and WNB injections was because the two GW polarisations are uncorrelated for these injections, whereas the X-PIPELINE background rejection test applied to the signal stream (discussed in [section 4.2](#)) assumes the two polarisations are related by  $90^\circ$  phase shift, as expected for a circularly polarised signal. This is the same effect as we observed in [section 5.5.6](#). The XTMVA analysis does not assume anything about the polarisation of the expected signals and so detects these injections. For the single detector analysis this is also not a problem as we are not applying the background rejections tests. Therefore, these injections are recovered with comparable sensitivity to the two detector X-PIPELINE analysis. However, the sensitivity to these injections is still modest compared to the XTMVA two detector analysis which obtains upper limits a factor of  $\sim 20$  smaller for both the cusp and WNB injections compared to the standard X-PIPELINE two detector analysis. The comparison of these results can be seen in [table 6.5](#).

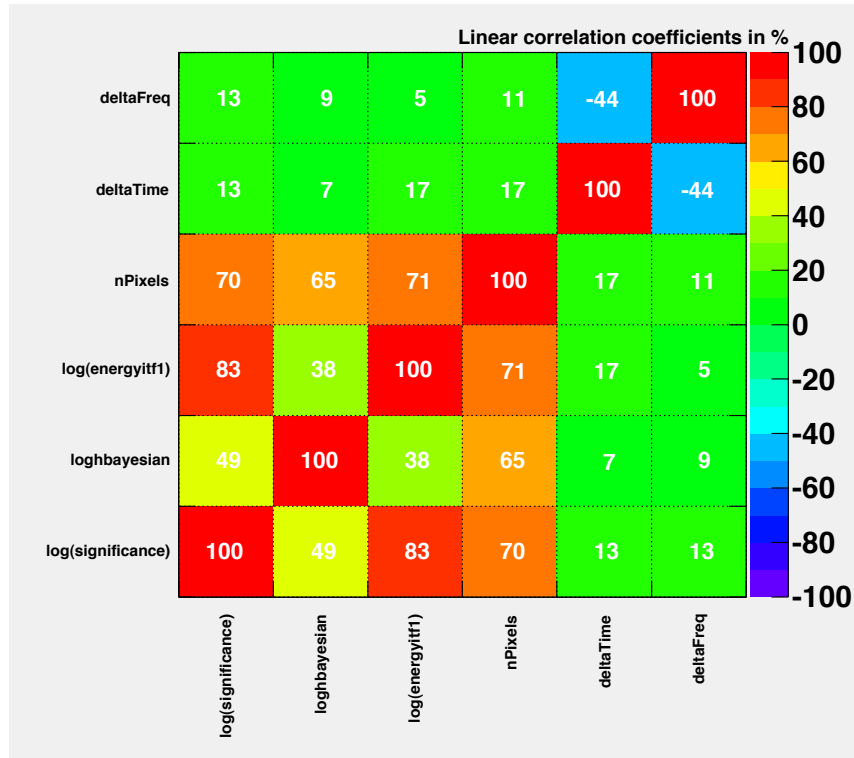


Figure 6.14: Linear correlation matrix for the event variables in the training sample for background events. The correlations for the background events are weak compared to the signal correlations seen in [figure 6.13](#).

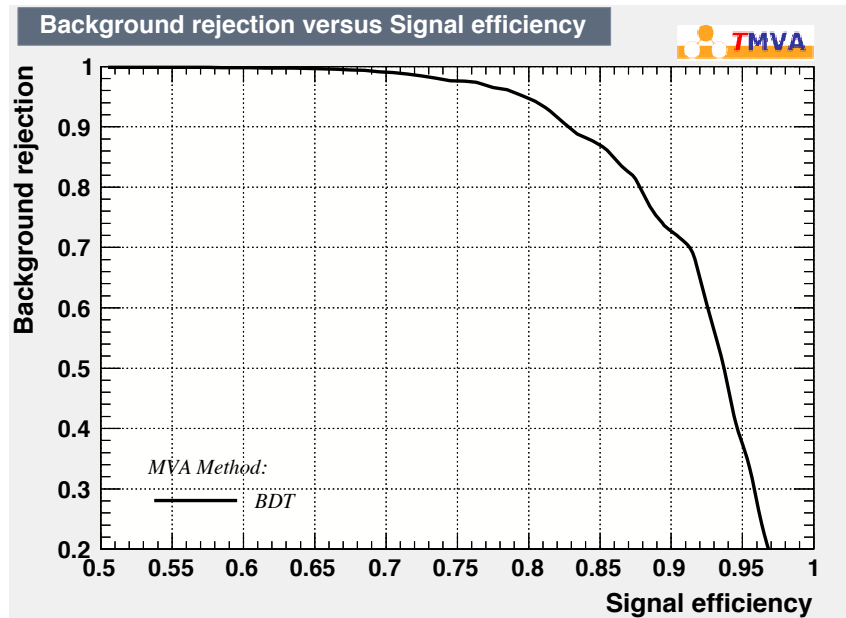


Figure 6.15: Background rejections against signal efficiency for the BDT test sample in the single detector analysis. Note the x-axis scale, where we focus on the region of interest at large signal efficiencies. The threshold on the BDT significance is the parameter which is used to select a point on this curve.

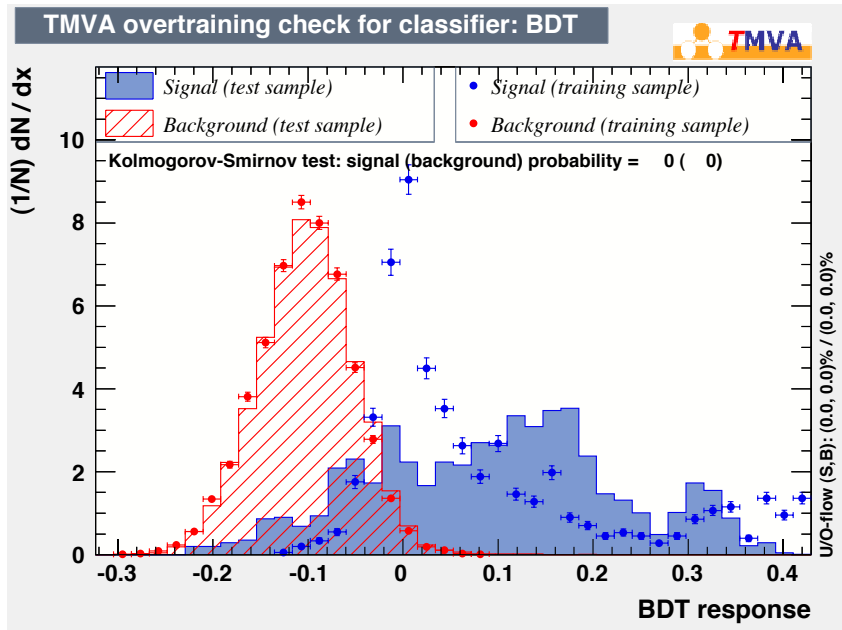


Figure 6.16: Histogram of BDT response for the CSG signal and background testing samples, overlaid with the signal and background training samples response for the single detector XTMVA analysis. We see some separation of the test samples for the signal and background, although there is also a large discrepancy between the signal training and signal testing sets. The overtraining feature in the response of the signal training sample around BDT response of 0, this is likely similar to the effect seen in [figure 5.16](#) due to the contamination of the signal sample described in [section 5.4](#) but should be investigated further. The results from this single detector XTMVA analysis should be viewed with caution due to this contamination of the signal training set, and the poor classification.



### 6.4.1 Interpretation of Results

We can translate the  $h_{\text{rss}}^{50\%}$  closed box upper limits into approximate sensitive ranges by assuming an energy emission and central frequency for the GW burst. Assuming an emission energy in GWs of  $10^{-2} M_{\odot} c^2$  at 1 kHz, we find an exclusion distance for the two detector XTMVA analysis of 543 kpc for the CSG waveform. The standard X-PIPELINE two detector analysis gives an exclusion distance of 258 kpc. The standard X-PIPELINE single detector analysis gives an exclusion distance of 68 kpc. The most sensitive XTMVA single detector analysis gives an exclusion distance of 154 kpc. The exclusion distance scales as  $E^{1/2}$ , and so for a less optimistic energy emission of  $10^{-8} M_{\odot} c^2$  the above limits become pc rather than kpc. These limits are not astrophysically interesting.

We have demonstrated that a single detector analysis aided by MVA can reach comparable sensitivity to a two detector network using the standard X-PIPELINE analysis. However, caution should be applied when interpreting these results due to the overtraining seen in [figure 6.16](#). This result shows that during the single detector period while only GEO 600 is recording data and the LIGO and Virgo detectors are undergoing commissioning we could perform an analysis using GEO 600 of any extraordinary astrophysical events, such as a Galactic supernova.



# Discussion and Conclusions

---

# 7

The first direct detection of gravitational waves (GWs) is expected within the decade once the advanced detectors come online. This will be an exciting and important moment in the history of astronomy, opening up a new window to the Universe. To make this a reality however, we must first make sure that the advanced detectors reach their design sensitivities, and remove transient noise sources.

This will require a large amount of detector characterisation, particularly in the build up to and during the first science runs which are expected in 2015. We showed in [chapter 3](#) the importance of detector characterisation, demonstrated the use of some of the currently available software tools, and showed some of the challenges involved in performing this work. In particular, we demonstrated in [section 3.6](#) a method which could be used to efficiently guide commissioning activities using detector characterisation to maximise the number of observable sources.

Gamma-ray bursts (GRBs) are some of the most exciting potential sources for gravitational-wave bursts (GWBs), and will be a prime source for targeted analyses in the advanced detector era. In [chapter 4](#) we outlined the flagship triggered GWB analysis pipeline X-PIPELINE. Using X-PIPELINE we demonstrate a new method for tiling the sky position uncertainty regions of GRBs. This can reduce the computational cost of an analysis by up to a factor of 10 for triggers with large sky position uncertainty regions, such as *Fermi* GBM events, when using a search frequency band which extends above 1 kHz. This new method could be useful in the advanced detector era to speed up analyses, and with improved localisation feed back to the astronomical community for electromagnetic follow up. In [section 4.3](#) this method is applied to a sample of 78 GRBs which were observed from April 2006 to October 2011 by GEO 600 and one of the LIGO or Virgo detectors. No plausible GW event candidates were detected, and the population as a whole does not demonstrate a statistically significant number of low-probability events.

In [chapter 5](#) we demonstrate an advanced method for GWB searches: multivariate analysis (MVA). The standard X-PIPELINE analysis uses a simple pass/fail cut in one or more two-dimensional parameter spaces. These cuts only

---

discriminate between signal and background using a few of the variables associated with each event, and ignore other information such as duration, bandwidth, and time-frequency volume. MVA techniques can mine the full parameter space of the events to better discriminate between signal and background. We perform a number of robustness tests on the Multivariate X-PIPELINE (XTMVA) analysis pipeline which uses the boosted decision tree MVA classifier. We find an improvement of up to a factor of 50% in range, which translates to an increase of a factor of 3 in observable volume. MVA classifiers will play a key role in future analyses pipelines due to their power at pulling weak signals out from background noise, and this method could become a standard element of the X-PIPELINE analysis for future searches.

In [chapter 6](#) we apply a combination of detector characterisation techniques and the XTMVA pipeline to test the potential performance of a single detector analysis using the GEO 600 detector. This is important, as during the upgrade of the LIGO and Virgo detectors to the advanced detector configurations GEO 600 is the only GW interferometer taking astrophysical observations as it operates in Astrowatch mode. Any potential searches would be using an EM trigger to reduce the time over which we expect a signal, and we are only sensitive to signals within our own Galaxy. At the time of writing no exceptional events have occurred so we use a HEN burst that was observed from the direction of the Galactic centre to test the performance of our analyses. During this event both the GEO 600 and Virgo detectors were online so we perform a number of tests to compare different analysis configurations. We find that using the XTMVA pipeline and aggressive data characterisation with a single detector analysis using GEO 600 we can obtain upper limits within a factor of 2 of the standard two detector X-PIPELINE analysis for the circular sine-Gaussian (CSG) waveform. This method could be useful in the case of an extraordinary astrophysical event, such as a Galactic supernova, while only one of the advanced detectors is operating. GEO 600 will now continue to run in Astrowatch mode at least until the advanced detectors come online in 2015.



# Optical Layout of GEO 600

---



Here we show the schematic of the GEO 600 optical layout, draw with the Optocad program [217]. This shows the main optical components such as the BS, MPR, MSR, IMC, OMC and squeezer. Also the main beams in the detector are show as well as the vacuum tanks, optical benches and a number of photo detectors which are used for local control of the interferometer optics. Note that the interferometer arms are folded vertically, this is more clearly seen in the north arm optics.

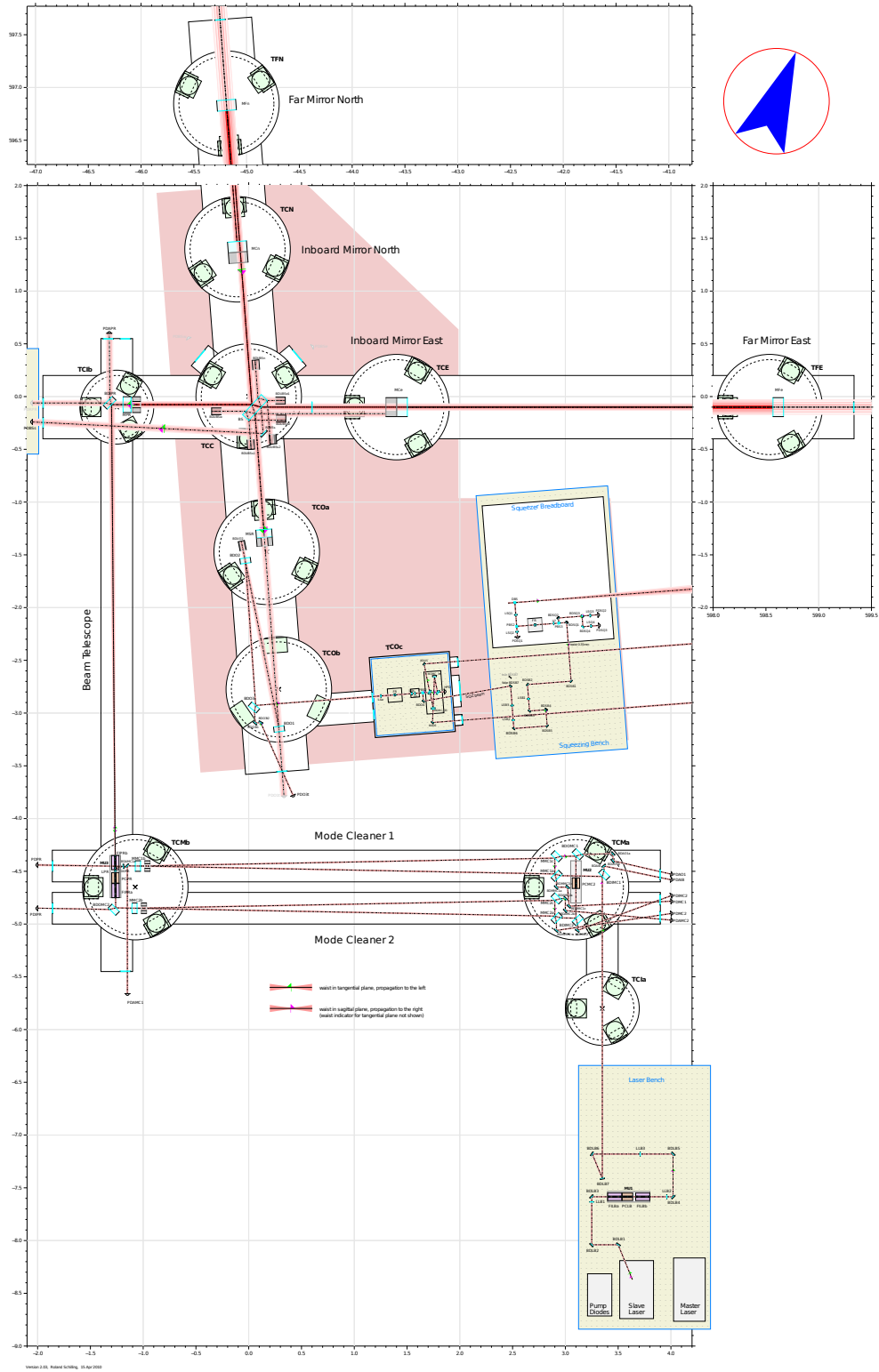


Figure A.1: Schematic of the GEO 600 detector showing the main optics, vacuum tanks, sensors and laser paths. Drawn using the OptoCad program.





# Bibliography

---

- [1] A. Einstein. The Formal Foundation of the General Theory of Relativity. *Sitzungsber.Preuss.Akad.Wiss.Berlin (Math.Phys.)*, 1914:1030–1085, 1914.
- [2] A. Einstein. Approximative Integration of the Field Equations of Gravitation. *Sitzungsber.Preuss.Akad.Wiss.Berlin (Math.Phys.)*, 1916:688–696, 1916.
- [3] R. A. Hulse and J. H. Taylor. Discovery of a pulsar in a binary system. *Astrophysical Journal*, 195:L51–L53, January 1975.
- [4] J. M. Weisberg and J. H. Taylor. The Relativistic Binary Pulsar B1913+16: Thirty Years of Observations and Analysis. *Binary Radio Pulsars*, 328:25, July 2005.
- [5] J. H. Taylor, L. A. Fowler, and P. M. McCulloch. Measurements of general relativistic effects in the binary pulsar PSR 1913+16. *Nature*, 277:437–440, February 1979.
- [6] J. M. Weisberg, D. J. Nice, and J. H. Taylor. Timing Measurements of the Relativistic Binary Pulsar PSR B1913+16. *The Astrophysical Journal*, 722(2):1030–1034, October 2010.
- [7] I. H. Stairs, et al. Studies of the Relativistic Binary Pulsar PSR B1534+12. I. Timing Analysis. *The Astrophysical Journal*, 581(1):501–508, December 2002.
- [8] M. Burgay, et al. The Highly Relativistic Binary Pulsar PSR J0737-3039A: Discovery and Implications. *Binary Radio Pulsars*, 328:53, July 2005.
- [9] C. L. Wong, K. W. Yoon, and B. Collaboration. BICEP2 I: Detection Of B-mode Polarization at Degree Angular Scales. *arXiv.org*, 2014.
- [10] M. Maggiore. *Gravitational Waves: Volume 1*, volume 1 of *Theory and Experiments*. Oxford University Press, USA, November 2007.
- [11] B. F. Schutz. *A First Course in General Relativity*, January 1985.
- [12] É. É. Flanagan and S. A. Hughes. The basics of gravitational wave theory. *New Journal of Physics*, 7(1):204, September 2005.

- 
- [13] P. R. Saulson. *Fundamentals of Interferometric Gravitational Wave Detectors*. World Scientific Publishing Company Incorporated, 1994.
  - [14] B. S. Sathyaprakash and B. F. Schutz. Physics, Astrophysics and Cosmology with Gravitational Waves. *Living Reviews in Relativity*, 12:2, March 2009.
  - [15] E. Mueller and W. Hillebrandt. The collapse of rotating stellar cores. *Astronomy and Astrophysics*, 103:358–366, 1981.
  - [16] E. Mueller. Gravitational radiation from collapsing rotating stellar cores. *Astronomy and Astrophysics*, 114:53–59, October 1982.
  - [17] H. Dimmelmeier, J. A. Font, and E. MULLER. Relativistic simulations of rotational core collapse II. Collapse dynamics and gravitational radiation. *Astronomy and Astrophysics*, 393:523–542, October 2002.
  - [18] M. Shibata and Y.-i. Sekiguchi. Gravitational waves from axisymmetric rotating stellar core collapse to a neutron star in full general relativity. *Physical Review D*, 69(8):84024, April 2004.
  - [19] P. Mösta, et al. Magnetorotational Core-collapse Supernovae in Three Dimensions. *The Astrophysical Journal Letters*, 785(2):L29, April 2014.
  - [20] A. V. Filippenko. Optical Spectra of Supernovae. *Annual Review of Astronomy & Astrophysics*, 35:309–355, 1997.
  - [21] E. B. Abdikamalov, et al. Axisymmetric general relativistic simulations of the accretion-induced collapse of white dwarfs. *Physical Review D*, 81(4):44012, February 2010.
  - [22] L. Dessart, et al. Multidimensional Simulations of the Accretion-induced Collapse of White Dwarfs to Neutron Stars. *The Astrophysical Journal*, 644(2):1063–1084, June 2006.
  - [23] C. D. Ott. The gravitational-wave signature of core-collapse supernovae. *Classical and Quantum Gravity*, 26(6):3001, March 2009.
  - [24] J. Abadie, et al. All-sky search for gravitational-wave bursts in the second joint LIGO-Virgo run. *Physical Review D*, 85(1):122007, June 2012.
  - [25] G. A. Tammann, W. Löffler, and A. Schröder. The Galactic supernova rate. *The Astrophysical Journal Supplement Series*, 92:487–493, 1994.
  - [26] E. Cappellaro, R. Evans, and M. Turatto. A new determination of supernova rates and a comparison with indicators for galactic star formation. *Astronomy and Astrophysics*, 351:459–466, November 1999.
  - [27] R. Narayan, B. Paczynski, and T. Piran. Gamma-ray bursts as the death throes of massive binary stars. *Astrophysical Journal*, 395:L83–L86, August 1992.

- [28] R. Mochkovitch, et al. Gamma-ray bursts as collimated jets from neutron star/black hole mergers. *Nature (ISSN 0028-0836)*, 361:236–238, January 1993.
- [29] P. Mészáros. Gamma-ray bursts. *Reports on Progress in Physics*, 69(8):2259–2321, August 2006.
- [30] C. Kouveliotou, et al. Identification of two classes of gamma-ray bursts. *Astrophysical Journal*, 413:L101–L104, August 1993.
- [31] J. N. Reeves, et al. The Signature of Supernova Ejecta in the X-ray Afterglow of the  $\gamma$ -ray Burst 011211. *Nature*, 416(6880):512–515, 2002.
- [32] S. E. Woosley and J. S. Bloom. The Supernova Gamma-Ray Burst Connection. *Annual Review of Astronomy & Astrophysics*, 44(1):507–556, September 2006.
- [33] J. Hjorth and J. S. Bloom. The Gamma-Ray Burst - Supernova Connection. *arXiv.org*, April 2011.
- [34] R. C. Duncan and C. Thompson. Formation of very strongly magnetized neutron stars - Implications for gamma-ray bursts. *Astrophysical Journal*, 392:L9–L13, June 1992.
- [35] E. Nakar. Short-hard gamma-ray bursts. *Physics Reports*, 442(1):166–236, April 2007.
- [36] A. Corsi and P. Mészáros. Gamma-ray Burst Afterglow Plateaus and Gravitational Waves: Multi-messenger Signature of a Millisecond Magnetar? *The Astrophysical Journal*, 702(2):1171–1178, September 2009.
- [37] M. B. Davies, et al. Gamma-Ray Bursts, Supernova Kicks, and Gravitational Radiation. *The Astrophysical Journal*, 579(2):L63–L66, November 2002.
- [38] S. Kobayashi and P. Mészáros. Gravitational Radiation from Gamma-Ray Burst Progenitors. *The Astrophysical Journal*, 589(2):861–870, June 2003.
- [39] S. E. Woosley and A. Heger. The Progenitor Stars of Gamma-Ray Bursts. *The Astrophysical Journal*, 637(2):914–921, February 2006.
- [40] C. L. Fryer, D. E. Holz, and S. A. Hughes. Gravitational Wave Emission from Core Collapse of Massive Stars. *The Astrophysical Journal*, 565(1):430–446, January 2002.
- [41] A. L. Piro and E. Pfahl. Fragmentation of Collapsar Disks and the Production of Gravitational Waves. *The Astrophysical Journal*, 658(2):1173–1176, April 2007.
- [42] G. E. Romero, M. M. Reynoso, and H. R. Christiansen. Gravitational radiation from precessing accretion disks in gamma-ray bursts. *Astronomy and Astrophysics*, 524:4, December 2010.

- 
- [43] J. Abadie, et al. Search for Gravitational Waves Associated with Gamma-Ray Bursts during LIGO Science Run 6 and Virgo Science Runs 2 and 3. *The Astrophysical Journal*, 760(1):12, November 2012.
  - [44] M. Was, et al. Performance of an externally triggered gravitational-wave burst search. *Physical Review D*, 86(2):22003, July 2012.
  - [45] B. P. Abbott, et al. First joint search for gravitational-wave bursts in LIGO and GEO 600 data. *Classical and Quantum Gravity*, 25(2):5008, December 2008.
  - [46] B. P. Abbott, et al. Search for high frequency gravitational-wave bursts in the first calendar year of LIGO's fifth science run. *Physical Review D*, 80(1):102002, November 2009.
  - [47] B. P. Abbott, et al. Search for gravitational-wave bursts in the first year of the fifth LIGO science run. *Physical Review D*, 80(1):102001, November 2009.
  - [48] J. Abadie, et al. All-sky search for gravitational-wave bursts in the first joint LIGO-GEO-Virgo run. *Physical Review D*, 81(1):102001, May 2010.
  - [49] B. P. Abbott, et al. Search for gravitational-wave bursts in LIGO data from the fourth science run. *Classical and Quantum Gravity*, 24(2):5343–5369, November 2007.
  - [50] B. P. Abbott, et al. Search for gravitational waves associated with 39 gamma-ray bursts using data from the second, third, and fourth LIGO runs. *Physical Review D*, 77(6):62004, March 2008.
  - [51] B. P. Abbott, et al. Implications for the Origin of GRB 070201 from LIGO Observations. *The Astrophysical Journal*, 681(2):1419–1430, July 2008.
  - [52] B. P. Abbott, et al. Search for Gravitational-Wave Bursts from Soft Gamma Repeaters. *Physical review letters*, 101(2):211102, November 2008.
  - [53] B. P. Abbott, et al. Search for gravitational-wave bursts associated with gamma-ray bursts using data from LIGO Science Run 5 and Virgo Science Run 1. *Astrophysical Journal*, 715(2):1438, 2010.
  - [54] J. Abadie, et al. Search for Gravitational Wave Bursts from Six Magnetars. *The Astrophysical Journal Letters*, 734(2):L35, June 2011.
  - [55] J. Abadie, et al. Implications for the Origin of GRB 051103 from LIGO Observations. *The Astrophysical Journal*, 755(1):2, August 2012.
  - [56] J. Aasi, et al. Search for long-lived gravitational-wave transients coincident with long gamma-ray bursts. *Physical Review D*, 88(1):122004, December 2013.
-

- [57] J. Aasi, et al. Search for Gravitational Waves Associated with Gamma-Ray Bursts Detected by the Interplanetary Network. March 2014.
- [58] L. Blanchet. Gravitational Radiation from Post-Newtonian Sources and Inspiralling Compact Binaries. *Living Reviews in Relativity*, 9:4, June 2006.
- [59] L. A. Waistein and V. D. Zubakov. *Extraction of signals from noise*. Prentice Hall, 1962.
- [60] J. Abadie and others. Sensitivity Achieved by the LIGO and Virgo Gravitational Wave Detectors during LIGO’s Sixth and Virgo’s Second and Third Science Runs. *arXiv.org*, gr-qc, 2012.
- [61] J. Aasi, et al. Gravitational waves from known pulsars: results from the initial detector era. September 2013.
- [62] J. Abadie, et al. TOPICAL REVIEW: Predictions for the rates of compact binary coalescences observable by ground-based gravitational-wave detectors. *Classical and Quantum Gravity*, 27(1):3001, September 2010.
- [63] J. Abadie, et al. Search for gravitational waves from low mass compact binary coalescence in LIGO’s sixth science run and Virgo’s science runs 2 and 3. *Physical Review D*, 85(8):82002, April 2012.
- [64] J. Abadie, et al. Search for Gravitational-wave Inspiral Signals Associated with Short Gamma-ray Bursts During LIGO’s Fifth and Virgo’s First Science Run. *The Astrophysical Journal*, 715(2):1453–1461, June 2010.
- [65] J. Aasi, et al. Search for gravitational waves from binary black hole inspiral, merger, and ringdown in LIGO-Virgo data from 2009-2010. *Physical Review D*, 87(2):22002, January 2013.
- [66] P. Jaranowski, A. Królak, and B. F. Schutz. Data analysis of gravitational-wave signals from spinning neutron stars: The signal and its detection. *Physical Review D (Particles)*, 58(6):63001, September 1998.
- [67] B. P. Abbott, et al. Searches for Gravitational Waves from Known Pulsars with Science Run 5 LIGO Data. *The Astrophysical Journal*, 713(1):671–685, April 2010.
- [68] J. Abadie, et al. First Search for Gravitational Waves from the Youngest Known Neutron Star. *The Astrophysical Journal*, 722(2):1504–1513, October 2010.
- [69] J. Aasi, et al. Einstein@Home all-sky search for periodic gravitational waves in LIGO S5 data. *Physical Review D*, 87(4):42001, February 2013.
- [70] J. Aasi, et al. Directed search for continuous gravitational waves from the Galactic center. *Physical Review D*, 88(1):102002, November 2013.

- 
- [71] B. P. Abbott, et al. Beating the Spin-Down Limit on Gravitational Wave Emission from the Crab Pulsar. *The Astrophysical Journal*, 683(1):L45–L49, August 2008.
- [72] J. Abadie, et al. Beating the Spin-down Limit on Gravitational Wave Emission from the Vela Pulsar. *The Astrophysical Journal*, 737(2):93, August 2011.
- [73] V. Ferrari, S. Matarrese, and R. Schneider. Gravitational wave background from a cosmological population of core-collapse supernovae. *Monthly Notices of the Royal Astronomical Society*, 303(2):247–257, February 1999.
- [74] T. Regimbau and J. A. de Freitas Pacheco. Cosmic background of gravitational waves from rotating neutron stars. *Astronomy and Astrophysics*, 376:381–385, September 2001.
- [75] T. Regimbau and J. A. de Freitas Pacheco. Gravitational wave background from magnetars. *Astronomy and Astrophysics*, 447(1):1–7, February 2006.
- [76] T. Regimbau and J. A. de Freitas Pacheco. Stochastic Background from Coalescences of Neutron Star-Neutron Star Binaries. *The Astrophysical Journal*, 642(1):455–461, May 2006.
- [77] Grishchuk, L. P. Relict gravitons and possibilities of their detection. *Pis'ma v ZhurnEhTF*, 23:326–330, 1976.
- [78] B. P. Abbott, et al. An upper limit on the stochastic gravitational-wave background of cosmological origin. *Nature*, 460(7):990–994, August 2009.
- [79] M. Maggiore. Gravitational Wave Experiments and Early Universe Cosmology, 2000.
- [80] T. L. Smith, E. Pierpaoli, and M. Kamionkowski. New Cosmic Microwave Background Constraint to Primordial Gravitational Waves. *Physical review letters*, 97(2):21301, July 2006.
- [81] B. P. Abbott, et al. Searching for a Stochastic Background of Gravitational Waves with the Laser Interferometer Gravitational-Wave Observatory. *The Astrophysical Journal*, 659(2):918–930, April 2007.
- [82] J. Abadie, et al. Upper limits on a stochastic gravitational-wave background using LIGO and Virgo interferometers at 600-1000 Hz. *Physical Review D*, 85(1):122001, June 2012.
- [83] A. A. Michelson and E. W. Morley. On the Relative Motion of the Earth and of the Luminiferous Ether. *Sidereale Messenger*, 6:306–310, November 1887.
-

- [84] P. R. Saulson. If light waves are stretched by gravitational waves, how can we use light as a ruler to detect gravitational waves? *American Journal of Physics*, 65(6):501–505, June 1997.
- [85] B. F. Schutz and M. Tinto. Antenna patterns of interferometric detectors of gravitational waves. I - Linearly polarized waves. *Monthly Notices of the Royal Astronomical Society (ISSN 0035-8711)*, 224:131–154, January 1987.
- [86] B. F. Schutz. Networks of gravitational wave detectors and three figures of merit. *Classical and Quantum Gravity*, 28(1):5023, June 2011.
- [87] A. Freise and K. Strain. Interferometer Techniques for Gravitational-Wave Detection. *Living Reviews in Relativity*, 13:1, February 2010.
- [88] R. W. P. Drever, et al. Laser Phase and Frequency Stabilization Using an Optical-Resonator. *Applied Physics B-Photophysics and Laser Chemistry*, 31(2):97–105, 1983.
- [89] E. Black. Notes on pound-drever-hall technique. *LIGO Technical notes*, 1998.
- [90] C. M. Caves. Quantum-mechanical noise in an interferometer. *Physical Review D (Particles and Fields)*, 23(8):1693–1708, April 1981.
- [91] C. M. Caves. Quantum-Mechanical Radiation-Pressure Fluctuations in an Interferometer. *Physical review letters*, 45(2):75–79, July 1980.
- [92] S. Goßler. *The Suspension Systems of the Interferometric Gravitational-wave Detector GEO 600*. PhD thesis, 2004.
- [93] R. Brown. A Brief Account of Microscopical Observations Made ... on the Particles Contained in the Pollen of Plants, and on the General Existence of Active Molecules in Organic and Inorganic Bodies, 1828.
- [94] A. Einstein. Investigations on the theory of the Brownian movement. page 119, 1956.
- [95] P. R. Saulson. Thermal noise in mechanical experiments. *Physical Review D (Particles and Fields)*, 42(8):2437–2445, October 1990.
- [96] K. Somiya and K. Yamamoto. Coating thermal noise of a finite-size cylindrical mirror. *Physical Review D*, 79(1):102004, May 2009.
- [97] Y. Levin. Internal thermal noise in the LIGO test masses: A direct approach. *Physical Review D (Particles)*, 57(2):659–663, January 1998.
- [98] G. M. Harry, et al. Thermal noise from optical coatings in gravitational wave detectors. *Applied Optics IP*, 45(7):1569–1574, March 2006.

- 
- [99] G. I. González and P. R. Saulson. Brownian motion of a mass suspended by an anelastic wire. *The Journal of the Acoustical Society of America*, 96:207, 1994.
- [100] G. González. Suspensions thermal noise in the LIGO gravitational wave detector. *Classical and Quantum Gravity*, 17(2):4409–4435, November 2000.
- [101] K. Somiya. Thermal noise of GEO’s beamsplitter. 2009.
- [102] B. Benthem and Y. Levin. Thermorefractive and thermochemical noise in the beamsplitter of the GEO600 gravitational-wave interferometer. *Physical Review D*, 80(6):62004, September 2009.
- [103] C. I. E. Torrie. *Development of Suspensions for the GEO 600 Gravitational Wave Detector*. PhD thesis, 1999.
- [104] IndIGO. Proposal for an Interferometric Gravitational-Wave Observatory, November 2011.
- [105] M. Punturo, et al. The Einstein Telescope: a third-generation gravitational wave observatory. *Classical and Quantum Gravity*, 27(1):4002, October 2010.
- [106] M. V. Plissi, et al. Aspects of the suspension system for GEO 600. *Review of Scientific Instruments*, 69(8):3055–3061, August 1998.
- [107] R. Abbott, et al. Seismic isolation enhancements for initial and Advanced LIGO. *Classical and Quantum Gravity*, 21(5):915, March 2004.
- [108] B. F. Schutz. Gravitational wave astronomy. *Classical and Quantum Gravity*, 16(12A):A131, 1999.
- [109] B. P. Abbott, et al. LIGO: the Laser Interferometer Gravitational-Wave Observatory. *Reports on Progress in Physics*, 72(7):6901, July 2009.
- [110] F. Acernese, et al. Status of Virgo. *Classical and Quantum Gravity*, 25(1):4045, June 2008.
- [111] F. Acernese, et al. Virgo status. *Classical and Quantum Gravity*, 25(1):4001, September 2008.
- [112] T. Accadia, et al. Virgo: a laser interferometer to detect gravitational waves. *Journal of Instrumentation*, 7(03):P03012–P03012, March 2012.
- [113] H. Grote and The LIGO Scientific Collaboration. The status of GEO 600. *Classical and Quantum Gravity*, 25(1):4043, June 2008.
- [114] K. Arai and T. Collaboration. Recent progress of TAMA300. *Journal of Physics: Conference Series*, 120(3):2010, July 2008.
-



- [115] M. Ando and T. Collaboration. Current status of TAMA. *Classical and Quantum Gravity*, 19(7):1409–1419, April 2002.
- [116] The LIGO Scientific Collaboration. Advanced LIGO Reference Design. March 2011.
- [117] G. Losurdo and D. Shoemaker. Possible Scenarios for Commissioning and Early Observing with the Second Generation Detectors, 2010.
- [118] G. M. Harry and The LIGO Scientific Collaboration. Advanced LIGO: the next generation of gravitational wave detectors. *Classical and Quantum Gravity*, 27(8):4006, April 2010.
- [119] J. R. Smith and The LIGO Scientific Collaboration. The path to the enhanced and advanced LIGO gravitational-wave detectors. *Classical and Quantum Gravity*, 26(1):4013, June 2009.
- [120] The Virgo Collaboration. Advanced Virgo Technical Design Report. *Virgo internal document VIR-0128A-12*, April 2012.
- [121] The Virgo Collaboration. Advanced Virgo Baseline Design, August 2009.
- [122] The Virgo Collaboration. Advanced virgo baseline design note vir027a0(2009). <https://tds.ego-gw.it/itf/tds/file.php?callFile=VIR-0027A-09.pdf>, April 2009.
- [123] The LIGO Scientific Collaboration, et al. Prospects for Localization of Gravitational Wave Transients by the Advanced LIGO and Advanced Virgo Observatories. *arXiv.org*, page 670, April 2013.
- [124] B. Willke, et al. The GEO-HF project. *Classical and Quantum Gravity*, 23(8):207, April 2006.
- [125] K. Somiya and KAGRA Collaboration. Detector configuration of KAGRA—the Japanese cryogenic gravitational-wave detector. *Classical and Quantum Gravity*, 29(12), 2012.
- [126] P. Amaro-Seoane, et al. eLISA: Astrophysics and cosmology in the millihertz regime. *GW Notes*, 6:4–110, May 2013.
- [127] J. Hough, et al. Proposal for a joint German-British interferometric gravitational wave detector. 1989.
- [128] K. Danzmann. GEO 600: proposal for a 600m laser interferometric gravitational wave antenna. page 18, 1994.
- [129] B. Willke, et al. The GEO 600 gravitational wave detector. *Classical and Quantum Gravity*, 19(7):1377–1387, April 2002.
- [130] B. Willke and The LIGO Scientific Collaboration. GEO600: status and plans. *Classical and Quantum Gravity*, 24(1):389, October 2007.

- 
- [131] H. Grote and The LIGO Scientific Collaboration. The GEO 600 status. *Classical and Quantum Gravity*, 27(8):4003, April 2010.
- [132] H. Lück, et al. The upgrade of GEO 600. *Journal of Physics: Conference Series*, 228(1):2012, May 2010.
- [133] H. Grote. *Making it Work*. PhD thesis, 2003.
- [134] I. Zawischa, et al. The GEO 600 laser system. *Classical and Quantum Gravity*, 19(7):1775–1781, April 2002.
- [135] R. X. Adhikari, P. Fritschel, and S. Waldman. Enhanced LIGO. *LIGO document, LIGO-T060156-01*, <http://www.ligo.caltech.edu/docs>, 2006.
- [136] H. Wittel, et al. Thermal Correction of Astigmatism in the Gravitational Wave Observatory GEO 600. *arXiv.org*, page 5367, November 2013.
- [137] M. Lorenzini and The Virgo Collaboration. The monolithic suspension for the Virgo interferometer. *Classical and Quantum Gravity*, 27(8):4021, April 2010.
- [138] A. V. Cumming, et al. Design and development of the advanced LIGO monolithic fused silica suspension. *Classical and Quantum Gravity*, 29(3):5003, February 2012.
- [139] G. Heinzel. *Advanced Optical Techniques for Laser Interferometric Gravitational Wave Detectors*. PhD thesis, 1999.
- [140] B. J. Meers. Recycling in laser-interferometric gravitational-wave detectors. *Physical Review D (Particles and Fields)*, 38(8):2317–2326, October 1988.
- [141] G. Heinzel, et al. Experimental demonstration of a suspended dual recycling interferometer for gravitational wave detection. *Physical review letters*, 81(25):5493–5496, 1998.
- [142] J. Mizuno, et al. Resonant sideband extraction: a new configuration for interferometric gravitational wave detectors. *Physics Letters A*, 175(5):273–276, April 1993.
- [143] G. Heinzel, et al. An experimental demonstration of resonant sideband extraction for laser-interferometric gravitational wave detectors. *Physics Letters A*, 217(6):305–314, 1996.
- [144] M. Prijatelj, et al. The output mode cleaner of GEO 600. *Classical and Quantum Gravity*, 29(5):5009, March 2012.
- [145] S. Hild, et al. DC-readout of a signal-recycled gravitational wave detector. *Classical and Quantum Gravity*, 26(5):055012, February 2009.
- [146] J. Mizuno. *Comparison of optical configurations for laser-interferometric gravitational-wave detectors*. PhD thesis, 1995.
-

- [147] P. Fritschel, et al. Readout and Control of a Power-Recycled Interferometric Gravitational-Wave Antenna. *Applied Optics*, 40(2):4988–4998, October 2001.
- [148] J. Degallaix, et al. Commissioning of the tuned DC readout at GEO 600. *Journal of Physics: Conference Series*, 228(1):2013, May 2010.
- [149] T. T. Fricke, et al. DC readout experiment in Enhanced LIGO. *Classical and Quantum Gravity*, 29(6):065005, February 2012.
- [150] H. Grote, et al. First Long-Term Application of Squeezed States of Light in a Gravitational-Wave Observatory. *Physical review letters*, 110(1):181101, May 2013.
- [151] J. Abadie, et al. A gravitational wave observatory operating beyond the quantum shot-noise limit. *Nature Physics*, 7(12):962–965, September 2011.
- [152] H. Vahlbruch, et al. The GEO 600 squeezed light source. *Classical and Quantum Gravity*, 27(8):4027, April 2010.
- [153] J. Aasi, et al. Methods and results of a search for gravitational waves associated with gamma-ray bursts using the GEO600, LIGO, and Virgo detectors. May 2014.
- [154] J. Gea-Banacloche and G. Leuchs. Squeezed states for interferometric gravitational-wave detectors. *Journal of Modern Optics*, 1987.
- [155] C. Caves. Quantum mechanics of measurements distributed in time. A path-integral formulation. *Physical Review D*, 33(6):1643–1665, March 1986.
- [156] I. S. Heng, et al. First steps towards characterizing the hierarchical algorithm for curves and ridges pipeline. *Classical and Quantum Gravity*, 21(5):S821–S826, February 2004.
- [157] S. Chatterji, et al. Multiresolution techniques for the detection of gravitational-wave bursts. *Classical and Quantum Gravity*, 21(2):1809, October 2004.
- [158] S. K. Chatterji. *The Search for Gravitational Wave Bursts in Data from the Second LIGO Science Run*. PhD thesis, 2005.
- [159] A. Parameswaran. *On Aspects of Gravitational-wave Detection*. PhD thesis, 2007.
- [160] J. G. Rollins. *Multimessenger Astronomy with Low-latency Searches for Transient Gravitational Waves*. PhD thesis, 2011.
- [161] J. Aasi, et al. The characterization of Virgo data and its impact on gravitational-wave searches. *Classical and Quantum Gravity*, 29(1):5002, August 2012.

- 
- [162] J. R. Smith, et al. A hierarchical method for vetoing noise transients in gravitational-wave detectors. *Classical and Quantum Gravity*, 28(2):5005, December 2011.
- [163] M. Was, et al. A fixed false alarm probability figure of merit for gravitational wave detectors. . . . *and Quantum Gravity*, 2014.
- [164] P. J. Sutton. A rule of thumb for the detectability of gravitational-wave bursts. *arXiv preprint arXiv:1304.0210*, 2013.
- [165] T. S. Adams and others. Characterisation Directed Commissioning of the GEO600 Detector. 2014.
- [166] S. Klimenko, et al. A coherent method for detection of gravitational wave bursts. *Classical and Quantum Gravity*, 25(11):114029, 2008.
- [167] N. R. Tanvir, et al. A ‘kilonova’ associated with the short-duration  $\gamma$ -ray burst GRB130603B. *Nature*, 500(7):547–549, August 2013.
- [168] E. Berger, W. Fong, and R. Chornock. An r-Process Kilonova Associated with the Short-Hard GRB 130603B. *eprint arXiv:1306.3960*, June 2013.
- [169] K. S. Thorne. Gravitational Radiation. In S. W. Hawking and W. Israel, editors, *Three Hundred Years of Gravitation*, pages 330–458. Cambridge University Press, 1987.
- [170] K. Kiuchi, et al. Long-term general relativistic simulation of binary neutron stars collapsing to a black hole. *Physical Review D*, 80(6):64037, September 2009.
- [171] Y. Sekiguchi, et al. Gravitational Waves and Neutrino Emission from the Merger of Binary Neutron Stars. *Physical review letters*, 107(5):51102, July 2011.
- [172] R. Oechslin and H. T. Janka. Gravitational Waves from Relativistic Neutron-Star Mergers with Microphysical Equations of State. *Physical review letters*, 99(1):121102, September 2007.
- [173] K. Hotokezaka, et al. Remnant massive neutron stars of binary neutron star mergers: Evolution process and gravitational waveform. *Physical Review D*, 88(4):44026, August 2013.
- [174] N. R. Tanvir, et al. An origin in the local Universe for some short  $\gamma$ -ray bursts. *Nature*, 438(7):991–993, December 2005.
- [175] K. Hurley, et al. A new analysis of the short-duration, hard-spectrum GRB 051103, a possible extragalactic soft gamma repeater giant flare. *Monthly Notices of the Royal Astronomical Society*, 403(1):342–352, March 2010.
- [176] E. P. Mazets, et al. A Giant Flare from a Soft Gamma Repeater in the Andromeda Galaxy (M31). *The Astrophysical Journal*, 680(1):545–549, June 2008.
-

- [177] T. J. Galama, et al. An unusual supernova in the error box of the  $\gamma$ -ray burst of 25 April 1998. *Nature*, 395(6):670–672, October 1998.
- [178] J. S. Bloom, et al. The unusual afterglow of the  $\gamma$ -ray burst of 26 March 1998 as evidence for a supernova connection. *Nature*, 401(6):453–456, September 1999.
- [179] C. D. Ott, et al. A New Mechanism for Gravitational-Wave Emission in Core-Collapse Supernovae. *Physical review letters*, 96(2):201102, May 2006.
- [180] C. D. Ott. Probing the core-collapse supernova mechanism with gravitational waves. *Classical and Quantum Gravity*, 26(2):4015, October 2009.
- [181] J. A. de Freitas Pacheco. Do soft gamma repeaters emit gravitational waves? *Astronomy and Astrophysics*, 336:397–401, August 1998.
- [182] K. Ioka. Magnetic deformation of magnetars for the giant flares of the soft gamma-ray repeaters. *Monthly Notices of the Royal Astronomical Society*, 327(2):639–662, October 2001.
- [183] J. E. Horvath. Energetics of the superflare from SGR1806-20 and a possible associated gravitational wave burst. *Modern Physics Letters A*, 20(36):2799–2804, 2005.
- [184] A. Corsi and B. J. Owen. Maximum gravitational-wave energy emissible in magnetar flares. *Physical Review D*, 83(10):104014, May 2011.
- [185] M. H. van Putten. Proposed Source of Gravitational Radiation from a Torus around a Black Hole. *Physical review letters*, 87(9):91101, August 2001.
- [186] M. H. van Putten, et al. Gravitational radiation from gamma-ray burst-supernovae as observational opportunities for LIGO and VIRGO. *Physical Review D*, 69(4):44007, February 2004.
- [187] M. Shibata and K. Taniguchi. Merger of black hole and neutron star in general relativity: Tidal disruption, torus mass, and gravitational waves. *Physical Review D*, 77(8):84015, April 2008.
- [188] A. L. Piro and E. Thrane. Gravitational Waves from Fallback Accretion onto Neutron Stars. *The Astrophysical Journal*, 761(1):63, December 2012.
- [189] P. J. Sutton, et al. X-Pipeline: an analysis package for autonomous gravitational-wave burst searches. *New Journal of Physics*, 12(5):3034, May 2010.
- [190] S. Adrian-Martinez, et al. A first search for coincident gravitational waves and high energy neutrinos using LIGO, Virgo and ANTARES data from 2007. *Journal of Cosmology and Astroparticle Physics*, 06(0):008, June 2013.

- [191] Y. Gürsel and M. Tinto. Near optimal solution to the inverse problem for gravitational-wave bursts. *Physical Review D (Particles and Fields)*, 40(1):3884–3938, December 1989.
- [192] S. Chatterji, et al. Coherent network analysis technique for discriminating gravitational-wave bursts from instrumental noise. *Physical Review D*, 74(8):82005, October 2006.
- [193] M. Was. *Searching for gravitational waves associated with gamma-ray bursts int 2009-2010 ligo-virgo data*. PhD thesis, Université Paris Sud-Paris XI, 2011.
- [194] S. Kobayashi and P. Mészáros. Polarized Gravitational Waves from Gamma-Ray Bursts. *The Astrophysical Journal*, 585(2):L89–L92, March 2003.
- [195] S. D. Barthelmy. GCN and VEvent: A status report. *Astronomische Nachrichten*, 329(3):340, March 2008.
- [196] A. von Kienlin, et al. The Second Fermi GBM Gamma-Ray Burst Catalog: The First Four Years. *The Astrophysical Journal Supplement*, 211(1):13, March 2014.
- [197] N. Gehrels, et al. The Swift gamma-ray burst mission. *Astrophysical Journal*, 611(2):1005, 2004.
- [198] C. Meegan, et al. The Fermi Gamma-ray Burst Monitor. *The Astrophysical Journal*, 702(1):791–804, September 2009.
- [199] C. Winkler, et al. The INTEGRAL mission. *Astronomy and Astrophysics*, 411(1):L1–L6, November 2003.
- [200] M. S. Briggs, et al. The accuracy of GBM GRB locations. 1133:40, 2009.
- [201] K. Hurley, et al. The Interplanetary Network Supplement to the Fermi GBM Catalog of Cosmic Gamma-Ray Bursts. *The Astrophysical Journal Supplement*, 207(2):39, August 2013.
- [202] L. P. Singer, et al. Discovery and Redshift of an Optical Afterglow in 71 deg2: iPTF13bxi and GRB 130702A. *The Astrophysical Journal Letters*, 776(2):L34, October 2013.
- [203] V. Connaughton. New feature in Fermi GBM GRB ground position notices., 2011.
- [204] T. S. Adams, et al. Gravitational-wave detection using multivariate analysis. *Physical Review D*, 88(6):62006, September 2013.
- [205] CERN. *ROOT: an object-oriented data analysis framework: User’s guide*. An object-oriented data analysis framework. CERN, Geneva, 2006.

- [206] A. Hoecker, et al. TMVA - Toolkit for Multivariate Data Analysis. *arXiv.org*, March 2007.
- [207] T. Aaltonen and others. Search for a Low-Mass Standard Model Higgs Boson in the  $\tau\tau$  Decay Channel in pp  $\sqrt{s}$  Collisions at  $\sqrt{s}=1.96$  TeV. *Physical review letters*, 108(18):181804, 2012.
- [208] D. Meacher. *Distinguishing gravitational wave signals from detector noise using multivariate analysis*. PhD thesis.
- [209] L. Blanchet, et al. Gravitational waveforms from inspiralling compact binaries to second-post-Newtonian order. *Classical and Quantum Gravity*, 13(4):575–584, April 1996.
- [210] B. P Abbott, et al. Search for gravitational waves from low mass compact binary coalescence in 186 days of LIGO’s fifth science run. *Physical Review D*, 80(4):047101, 2009.
- [211] M. G. Aartsen, et al. First Observation of PeV-Energy Neutrinos with IceCube. *Physical review letters*, 111(2):21103, July 2013.
- [212] S. Gillessen, et al. Monitoring stellar orbits around the Massive Black Hole in the Galactic Center. *Astrophysical Journal*, 692(2):1075, 2009.
- [213] F. Halzen, H. Landsman, and T. Montaruli. TeV photons and Neutrinos from giant soft-gamma repeaters flares. *arXiv.org*, page 3348, March 2005.
- [214] V. Berezhinsky, E. Sabancilar, and A. Vilenkin. Extremely high energy neutrinos from cosmic strings. *Physical Review D*, 84(8):085006, 2011.
- [215] T. Damour and A. Vilenkin. Gravitational Wave Bursts from Cosmic Strings. *Physical review letters*, 85(1):3761–3764, October 2000.
- [216] X. Siemens, et al. Gravitational wave bursts from cosmic (super)strings: Quantitative analysis and constraints. *Physical Review D*, 73(1):105001, May 2006.
- [217] R. Schilling. OptoCad, a Fortran 95 module for Gaussian beam tracing through an optical set-up. January 2002.